Targeting Extracellular Vesicles and Tumour-Mediated Signalling in Brain Metastasis

Emma Rigg

Thesis for the degree of Philosophiae Doctor (PhD)
at the University of Bergen

2025

Scientific Environment

The work presented in this thesis was carried out at the Translational Cancer Research Group, Department of Biomedicine, Faculty of Medicine, University of Bergen. I have taken part in the Bergen Biomedical Research School. The work presented in the thesis was funded by the University of Bergen and the Norwegian Regional Health Authorities (Helse Vest).

UNIVERSITY OF BERGEN
Faculty of Medicine

HELSE VEST

Acknowledgements

I am grateful to the Faculty of Medicine at the University of Bergen for funding my PhD and research stay at the Universitätsklinikum Freiburg, along with the valuable support from Helse Vest that made this work possible.

To my main supervisor, Frits Thorsen, your guidance and unwavering support have been instrumental in my development as a scientist. Throughout this journey, your trust in my abilities and dedication to my future have made the challenging path of a PhD more manageable. Your constant willingness to provide opportunities has shaped my growth as a researcher. To Rolf Bjerkvig, your insights and guidance during the writing process were crucial in bringing our major paper to publication.

I extend my sincere gratitude to our collaborators in Luxembourg, Jinan, and Tromsø for their valuable contributions to this thesis, as well as Henrik Heiland and his team for welcoming me for a research stay at their lab in Freiburg. Special thanks to Endy Spriet, Hege Avsnes Dale, and Hans Olav Rolfsnes at the Molecular Imaging Center in Bergen for their technical expertise, countless hours of training, troubleshooting assistance, and methodological support. I deeply appreciate the essential contributions of the Flow Cytometry Core Facility and the Vivarium staff (and mice), as well as the Department of Neurosurgery staff and patients whose tissue donations make our research possible.

To the TCR group, you've made these four years truly extraordinary. Thank you to our exceptional technicians, Halala and Aurea, for keeping the lab running smoothly and for all the coffee pods, chocolate and other snacks I’ve stolen from you over the years. To my office mates Victoria and Ege, thank you for making work fun and being there for our reciprocal PhD stress therapy. To my master’s students Birgitte and Sunniva, you made my first experience as a supervisor incredibly rewarding - thank you for your patience and dedication. To our forskerlinjer students - Christina, Agathe, Tobias, Erlend, Magnus, and Annabeth - your enthusiasm and hard work make our lab environment a joy to work in.

Finally, to my personal support system: Tyler and Andreas, your friendship has been invaluable. To Sayintha in Oslo and to Cons and Cath in Toronto, thank you for always being there despite the distance from Bergen. My parents, biological, step and sviger-Mom and Rick, Dad and Ann, Tom og Bente-for your endless encouragement. My brothers Cooper and Jackson who are always available around the clock. And finally to min kjære Ole - your support, advice, understanding and encouragement throughout this journey has been immeasurable.

To all of you involved, I am forever grateful.

Bergen, February 2024

-Emma Rigg

Abstract

Brain metastasis is one of the most severe complications of cancer, occurring ten times more frequently than primary brain tumours and affecting up to 40% of solid tumour patients. The blood-brain barrier, a complex tumour microenvironment, and the adaptive capabilities of tumour cells limit therapeutic strategies. This thesis aimed to investigate the role of tumour-derived extracellular vesicles in brain metastasis progression and explore alternative second-line therapies for brain metastasis.

We investigated tumour-brain interactions and potential therapeutic strategies in melanoma brain metastases (MBM). Our findings reveal that extracellular vesicles (EVs) derived from MBM reprogram astrocytes through the delivery of miR-146a-5p, activating the Notch pathway and promoting a tumour-supportive environment. Targeting miR-146a-5p via genetic knockdown or deserpidine treatment reduced metastatic burden and improved survival *in vivo*. Additionally, we developed a novel method for labelling EVs from brain metastasis cell lines using superparamagnetic iron oxide nanoparticles, enabling their visualization through magnetic resonance imaging. Finally, we demonstrated that CCT196969, a pan-RAF and Src family kinase inhibitor (SFK), effectively suppressed growth in treatment naïve and BRAF inhibitor-resistant MBM cell lines, highlighting its potential as a therapeutic agent.

Our findings not only shed light on intricate tumour-brain communication mechanisms but also introduce an innovative tool for further studying the role of EVs in the brain metastasis tumour microenvironment. Furthermore, we propose a promising second-line treatment strategy, highlighting the potential of a pan-RAF and SFK inhibitor to target resistant metastasis.

Sammendrag

Hjernemetastaser er blant de mest alvorlige komplikasjonene ved kreft og forekommer ti ganger oftere enn primære hjernesvulster, og rammer opptil 40 % av pasienter med solide svulster. Blod-hjerne-barrieren, et komplekst tumormikromiljø og tumorcellers evne til tilpasning begrenser effekten av tilgjengelige terapeutiske strategier. Denne avhandlingen undersøker rollen tumor-deriverte ekstracellulære vesikler spiller i utviklingen av hjernemetastaser og utforsker alternative andrelinjebehandlinger for denne tilstanden.

Vi har undersøkt tumor-hjerne-interaksjoner og potensielle terapeutiske tilnærminger ved melanom-hjernemetastaser (MHM). Våre funn viser at ekstracellulære vesikler (EV) fra MHM omprogrammerer astrocytter ved å levere miR-146a-5p, som aktiverer Notch-signalveien og fremmer et tumor-vennlig mikromiljø. Ved å målrette miR-146a-5p gjennom genetisk nedregulering eller behandling med deserpidine, reduseres metastasebyrden og overlevelsen forbedres i dyremodeller. Videre utviklet vi en ny metode for merking av EV fra hjernemetastase-cellelinjer ved bruk av superparamagnetiske jernoksid-nanopartikler, som gjør det mulig å visualisere disse ved hjelp av magnetisk resonansavbildning. Til slutt viste vi at CCT196969, en hemmer av både pan-RAF og Src-familiekinaser (SFK), effektivt hemmet vekst i både behandlingsnaive og BRAF-hemmer-resistente MHM-cellelinjer, noe som understreker potensialet som terapeutisk middel.

Gjennom dette arbeidet har vi ikke bare observert komplekse kommunikasjonsmekanismer mellom tumor og hjerne, men vi introduserer også et innovativt verktøy for å studere EVs sin rolle i tumormikromiljøet ved hjernemetastaser. Vi foreslår så videre en lovende andrelinjebehandlingsstrategi, som fremhever potensialet til en pan-RAF og SFK-hemmer for resistente metastaser.

List of Articles

This thesis has been based on the following:

Paper I: **Inhibition of extracellular vesicle-derived miR-146a-5p decreases progression of melanoma brain metastasis via Notch pathway dysregulation in astrocytes**
Emma Rigg*, Jiwei Wang*, Zhiwei Xue, Taral R. Lunavat, Guowei Liu, Tuyen Hoang, Himalaya Parajuli, Mingzhi Han, Rolf Bjerkvig, Petr V. Nazarov, Nathalie Nicot, Stephanie Kreis, Christiane Margue, Miléne Tetsi Nomigni, Jochen Utikal, Hrvoje Miletic, Terje Sundstrøm, Lars A. R. Ystaas, Xingang Li, Frits Thorsen
Journal of Extracellular Vesicles 12.10 (2023): 12363.
* Equal Contributions

Paper II: **Multimodal imaging of brain metastasis-derived extracellular vesicles using superparamagnetic iron oxide nanoparticle labeling**
Birgitte Feginn Berle*, Sunniva Juliussen*, Aurea Castilho, Ege Solel, Halala Sdik Saed, Oliver Vanderpoorten, Taral R. Lunavat, Emma Rigg[#], Frits Thorsen[#]
Submitted to: International Journal of Nanomedicine
*,[#] Equal Contributions

Paper III: **CCT196969 effectively inhibits growth and survival of melanoma brain metastasis cells**
Agathe Reigstad, Christina Frantzen Herdlevær, Emma Rigg, Tuyen Hoang, Ole Vidhammer Bjørnstad, Synnøve Nymark Aasen, Jasmin Preis, Claude Haan, Terje Sundstrøm, Frits Thorsen
PLOS ONE 17.9 (2022): e0273711.

Publications or manuscripts in preparation/ submission process not for evaluation in the thesis:

Repurposing neuroleptics: clozapine as a novel, adjuvant therapy for melanoma brain metastases

Tobias Wikerholmen, Erlend Moen Taule, Emma Rigg, Birgitte Feginn Berle, Magnus Sættem, Katharina Sarnow, Halala Sdik Saed, Terje Sundstrøm, Frits Thorsen.

Clinical & Experimental Metastasis 42.2 (2025): 12.

Repurposing thioridazine as a novel treatment of melanoma brain metastasis.

Erlend Moen Taule, Tobias Wikerholmen, Katharina Sarnow, Emma Rigg, Birgitte Feginn Berle, Terje Sundstrøm, Jian Wang, Frits Thorsen.

(Manuscript in preparation).

GSDME in glioblastoma –pyroptosis resistance and tumour-promoting functions

Ege Solel, Egil Brudvik, Lars Andreas Rømo Ystaas, Yahaya A. Yabo, Emma Rigg, Romi Roy Choudhury, Halala Sdik Saed, Dieter Henrik Heiland, Rolf Bjerkvig, Jubayer Hossain, Hrvoje Miletic.

Cell Death Discovery (Minor Revisions)

Table of Contents

Abbreviations

ALK - Anaplastic lymphoma kinase
BBB - Blood-brain barrier
BRAF - B-Raf proto-oncogene
BEC - Brain endothelial cell
BM - Brain metastasis
BMDC - Bone marrow-derived myeloid cells
bMN - Brain metastatic niche
bPMN - Brain pre-metastatic niche
BrBM - Breast cancer brain metastasis
BTB - Blood-tumour barrier
BTBC - Brain trophic breast cancer cell lines
CCM - Cell-conditioned media
CNS - Central nervous system
CSF - Cerebrospinal fluid
CTC - Circulating tumour cell
CXCR/CXCL - C-X-C Motif Chemokine Receptor /Ligand
DAMP - Damage-associated molecular pattern
ECM - Extracellular Matrix
EGFR - Epidermal growth factor receptor
EMP - Epithelial-mesenchymal plasticity
EMT - Epithelial-mesenchymal transition
EV - Extracellular vesicle
FBS - Fetal Bovine Serum
GEMM - Genetically engineered mouse model
GFAP - Glial fibrillary acidic protein
ICI - Immune Checkpoint Inhibitors
IFN - Interferon
IL - Interleukin
ILV - Intraluminal vesicle
JAK - Janus kinase
JAM - Junctional adhesion molecule
LBM - Non-small cell lung cancer brain metastasis
MAPK - Mitogen-activated protein kinase
MBM - Melanoma brain metastasis
MEK - MAP/ERK kinase
MET - Mesenchymal-epithelial transition factor
MMP - Matrix metalloprotease
MN - Metastatic niche
mRNA - Messenger RNA
MRI - Magnetic resonance imaging
MVB - Multivesicular body
ncRNAs - Non-coding RNAs
NH cells - Natural Killer cells
NRAS - Neuroblastoma RAS viral oncogene homolog
NSCLC - Non-small cell lung cancer
PA - Plasminogen activator
PAMP - Pathogen-associated molecular pattern
PD-1 - Programmed cell death protein 1
PDC - Patient-derived cell line
PET - Positron Emission Tomography
PI3K - Phosphoinositide 3-kinase
PMN - Pre-metastatic niche
PTEN - Phosphatase and TENsin homolog
RTK - Receptor tyrosine kinase
SEC - Size exclusion chromatography
SFK - Src family kinase
SPION - Superparamagnetic iron oxide nanoparticle
STAT - Signal transducer and activator of transcription
TEM - Transmission Electron Microscopy
TGF - Transforming Growth Factor
TKI - Tyrosine kinase inhibitor
TME - Tumour Microenvironment
TNF - Tumor Necrosis Factor
VEGF - Vascular endothelial growth factor
VWF - Von Willebrand factor
WBRT - Whole brain radiotherapy

1. Introduction

1.1 Cancer and metastasis

Cancer is one of the leading causes of death worldwide, accounting for one-sixth of all mortalities[1]. While often considered a singular disease, it refers to a group of diseases characterized by abnormal cell growth and invasion beyond tissue borders[2]. Although hundreds of cancer types from various cells and tissues of origin have been identified, genomic instability is a consistent and defining characteristic. The instability leads to the accumulation of 'driver' mutations, which confer a clonal growth advantage through two mechanisms. Activating mutations in **oncogenes** increase protein function and overactivate cellular growth pathways[3]. In contrast, **tumour suppressor genes,** which normally act to inhibit cell pathways and development, are often inactivated[4].

Figure 1: Hallmarks of Cancer from Hanahan 2022. Reprinted with permissions.

In 2000, Douglas Hanahan and Robert Weinberg introduced the "Hallmarks of Cancer," which outline the defining characteristics of cancer, including genomic instability[5]. These six traits were initially intended to summarize the complexity of how normal cells transform into cancerous cells and guide research and therapeutic targeting. Over the years, these hallmarks have been updated several times to incorporate additional hallmarks and enabling characteristics. The most recent update presents a comprehensive summary of 14 hallmarks of cancer (**Fig. 1**)[6–9].

One of the key hallmarks of cancer that contributes directly to patient mortality is the activation of invasion and metastasis. This process enables cancer cells to spread beyond their primary site and establish tumours in distant organs, causing further illness. Primary tumours do not cause the majority of cancer-related deaths; rather, they result from the spread of cancer cells beyond their original site, colonizing distant organs and causing widespread complications, which is the leading cause of cancer-related mortality. In Norway, metastasis is responsible for 66.7% of solid cancer deaths, rising to 82.6% in the United States[10,11].

Common sites of metastasis include the lungs, liver, bone, lymph nodes and brain. The brain is a frequent and fatal site for metastasis in many cancers. Historically, 10-40% of patients with solid tumours may eventually develop brain metastasis, making it the most common type of neural malignancy—occurring at a rate 10 times higher than primary brain tumours[12]. Median survival typically ranges from 4 to 12 months, though this can vary significantly based on factors like age, the number of metastases, and the extent of extracranial disease. Patients present with neurological symptoms such as seizures, headaches, changes in speech or vision, nausea, ataxia, and drowsiness. Notably, up to 52% of brain metastasis (BM) patients will die of progressive neurologic dysfunction[13,14]. Treatment of BM remains a challenge due to the high risk associated with radiation and surgery in the brain, as well as poor penetration of systemic drugs through the blood-brain barrier (BBB)[15]. Despite recent advances in new therapeutic avenues, the 5-year survival rate remains below 10%[16]. Understanding the mechanisms behind BM and its clinical challenges is essential for developing new treatment options and improving patient outcomes.

1.2 Clinical perspectives on brain metastasis

1.2.1 Incidence and risk factors

BM is the most common central nervous system (CNS) malignancy, yet data on its prevalence remains limited and less comprehensive than that of primary tumours. Historically, many countries have not mandated reporting secondary lesions in the brain, and accurate documentation of cases can be challenging, especially in late-stage patients with multiple secondary malignancies.

Annual diagnoses of BM in the United States are estimated to range from 70,000 to 400,000 cancer patients, and approximately 12% of these patients are diagnosed with BM simultaneously with their primary cancer[17–20]. The incidence of BM is increasing for several reasons. Improved reporting systems, such as the Surveillance, Epidemiology, and End Results program (SEER), systematic screening of cancer patients at high risk for BM, and improved imaging techniques, such as magnetic resonance imaging (MRI) and positron emission tomography (PET) scanning, have enhanced the detection and reporting of BM[21,22]. Additionally, advances in molecular profiling and systematic treatments have effectively controlled extracranial disease and increased life expectancy. This improved survival paradoxically creates more opportunity for intracranial disease to develop, as current therapies offer little protection against BM. Consequently, patients living longer with controlled systemic disease are more likely to develop BM[23]. Finally, the increasing incidence of primary tumours with a predilection for BMs further contributes to the growing number of cases[24].

Primary cancer type is the key determinant of BM risk, with three primary cancers accounting for most BM cases. These are melanoma (6, 16.4-28.2%), non-small cell lung cancer (NSCLC) and other lung cancers (43.2-52.4, 60%), and breast cancer (15.7, 11%), with colon cancer in fourth place and is increasing in incidence[19,20,25,26]. BMs in men are most commonly from lung cancer, although the spreading pattern appears to be similar across sexes. Women most frequently develop BMs from breast cancer, and those with

HER2+ or triple-negative receptor status are at a higher risk for BM than their progesterone+ and estrogen+ counterparts[27]. Certain mutational variants within each primary tumour source increase the risk for BM. For example, in NCSLC, mutations in the epidermal growth factor receptor (*EGFR)* or anaplastic lymphoma kinase (*ALK*) oncogenes elevate the risk[28]. In melanoma, mutations in the B-Raf proto-oncogene *(BRAF*) or neuroblastoma RAS viral oncogene homolog *(NRAS*) genes increase the risk of developing BM[29]. Regardless of the primary cancer site, advanced-staged primary cancers and increased age elevate the risk of developing BM[30].

Melanoma, a cancer originating in skin melanocytes and rarely in the eyes or mucosa, has the highest propensity for BM among all cancers[31,32]. While melanoma represents only 1-5% of cancer cases, it accounts for over 10% of BM cases, with up to 50% of late-stage patients developing BM[33]. This neurotropism remains incompletely understood. NSCLC, comprising over 80% of lung cancer cases, includes several subtypes, with adenocarcinoma—affecting the lung's epithelial lining—being the most prevalent[34]. Although small cell lung cancer is considered more aggressive, NSCLC is responsible for over 50% of BM cases[12,25]. In summary, while NSCLC patients have the highest absolute number of BM cases, melanoma patients face the highest relative risk[19]. This thesis, therefore, focuses on both NSCLC-BM (LBM) and melanoma BM (MBM).

1.2.2 Molecular characteristics in MBM and LBM

Specific molecular subtypes, or mutations, found in primary tumours play a significant role in the development of BM, with certain signatures being more prevalent in BM than others. These mutations affect cell signalling pathways through two primary mechanisms: activating mutations that leave proteins constitutively 'on,' driving excessive proliferation, survival, and migration, or loss-of-function mutations that disable critical regulatory proteins, removing natural brakes on these pathways **(Table 1).**

Table 1: Overview of common oncogenic mutations in MBM and LBM patients. NF-κB, nuclear factor kappa-light-chain-enhancer of activated B cells. Compiled from[13,22,28,32,35–38]

Cancer Type	Gene	Prevalence (%)	Pathway	Mutation Type	Overall Survival (months)
Melanoma	*BRAF*	51	MAPK	Missense mutation, activating	9-30
	NRAS	22	MAPK PI3K	Missense mutation, activating	10-14
	c-KIT	11	MAPK PI3K	Missense, activating	9
NSCLC	*EGFR*	47-51	MAPK PI3K JAK/STAT	Deletion, point mutation, activating	30
	ALK	7	MAPK PI3K JAK/STAT	Translocation fusion protein, activating	50
	KRAS	16	MAPK PI3K JAK/STAT NF-κB	Point mutation, activating	22

As shown in **Fig. 2**, the mitogen-activated protein kinase (MAPK) pathway is crucial in oncogenic signalling, driving uncontrolled proliferation, differentiation, and survival in cancer cells. This signalling cascade is initiated when growth factors bind to cell surface receptors, often receptor tyrosine kinases (RTK), and trigger activation events through phosphorylation or direct binding of adapter proteins. These subsequently activate key proteins rat sarcoma (RAS), rapidly accelerated fibrosarcoma (RAF), mitogen-activated protein kinase kinase (MEK) and extracellular signal-regulated kinase (1/2 ERK)[39]. This activation chain leads to transcription factors that induce the promotion of genes involved in tumour growth, cell death avoidance, and resistance to therapy[40]. In MBM, activating mutations in *BRAF*, *NRAS*, and c-*KIT* keep proteins perpetually 'on,' leading to upregulation[29,41].

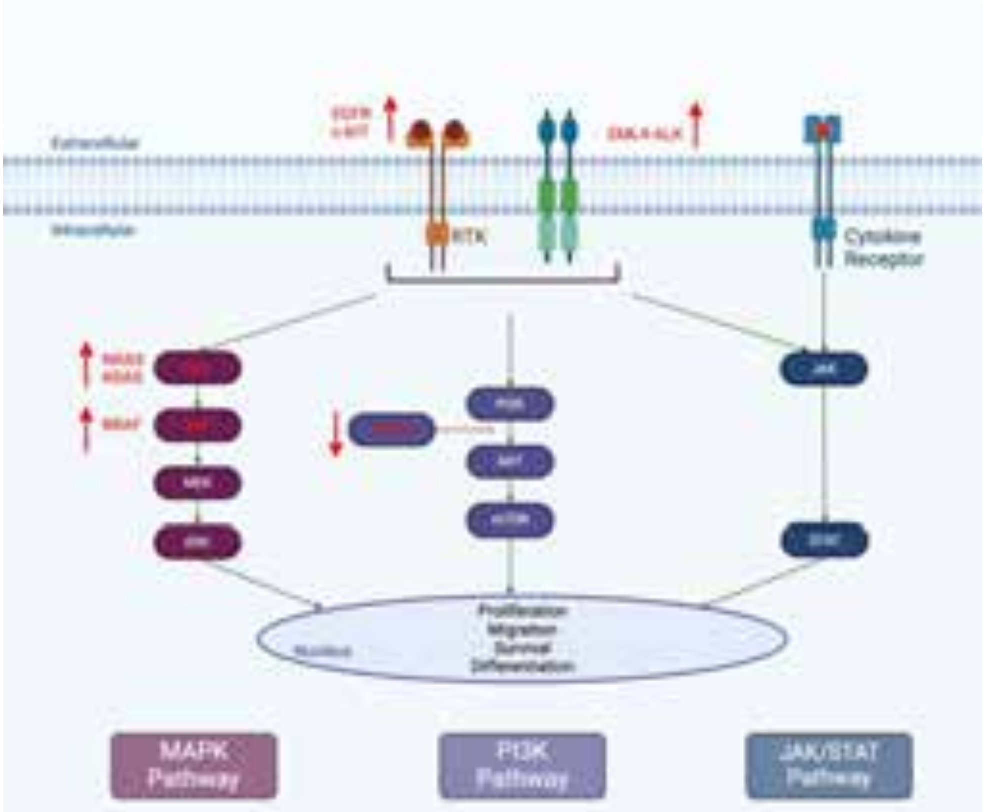

***Figure 2: Simplified outline of upregulated pathways in MBM and LBM**. MAPK, PI3K and JAK/STAT pathways with commonly mutated proteins marked in red with arrows indicating an activating (up) or deactivating (down) mutation. MAPK and PI3K pathways are canonically activated by RTKs, and JAK/STAT is activated by cytokine receptors. All pathways can be activated by the EML4-ALK fusion protein. Activation of effector proteins by phosphorylation or other activating events leads to upregulation of transcription factors initiating transcription of genes involved in important cell functions. Based on principles from references [39,42, 45] and Table 1.*

In addition to MAPK, the phosphoinositide 3-kinase (PI3K) pathway also contributes to cancer progression and therapy resistance. In healthy cells, PI3K activation through an RTK leads to the activation of mammalian target of rapamycin (mTOR) and protein kinase B (AKT) and is mediated by phosphatase and tensin homolog (PTEN)[42]. PTEN, a phosphatase, normally acts as an inhibitor in the pathway and is, therefore, a tumour suppressor. Complete loss or inactivating mutations of *PTEN* are often accompanied by *BRAF* mutations, which drive tumorigenesis through aberrant signalling[42,43]. While MAPK mutations are more common and, therefore, more commonly targeted in clinical therapies, MAPK and PI3K have several nodes of overlap. PI3K and MAPK can stimulate and amplify each other in a bidirectional format, leading to a feedback loop with sustained signalling[44].

The MAPK and PI3K pathways are also activated in LBM through *KRAS*, *EGFR* driver mutations, and *ALK*/*EML4* fusion proteins. These oncogenic drivers further upregulate the Janus kinase/ signal transducer and activator of transcription pathway (JAK/STAT). In the canonical pathway, JAK proteins associate with cytokine receptors to phosphorylate STAT proteins, which act as nuclear transcription factors[45]. In LBM, constitutively active EGFR either indirectly activates JAKs via cytokine production or directly phosphorylates STAT, bypassing JAK[46]. The EML4-ALK fusion protein primarily signals through JAK by forming a complex with JAK proteins while promoting cytokine expression for autocrine pathway activation[47]. Phosphorylated STAT then dimerizes and translocates to the nucleus, regulating genes involved in cell survival, proliferation, differentiation, and immune evasion.

1.2.3 Diagnosis, prognosis and clinical presentation

In acute cases where patients present with neurological symptoms or at diagnoses of high-risk primary cancers, an initial computed tomography (CT) scan is employed to rule out other intracerebral conditions and visualize larger tumours or hemorrhaging. CT is a rapid imaging technique that uses a rotating X-ray beam to produce cross-sectional tomographic images of the scanned area that can be combined to generate a 3D visualization of the brain[48]. MRI is the gold standard for imaging of BM, as it allows for precise soft tissue mapping that is not possible with CT[49]. MRI is used for non-invasive screening, diagnosis, treatment planning, and disease monitoring without ionizing radiation. For more information on the theory of MRI, please refer to **Section 3.5**.

EANO recommends using contrast-enhanced T1 weighted MRI with gadolinium-based contrast agents to diagnose BM, improve detection, and strengthen differential diagnosis[50]. Similarly, the *Response Assessment in Neuro-Oncology-Brain Metastases* and the *Brain Tumour Imaging Protocol for Glioma Research* proposed a standardized imaging protocol to ensure consistency across patients and treatment centers[51]. This protocol includes pre- and post-contrast 3D T1-weighted scans and high-resolution T2-weighted fluid-attenuated inversion recovery (FLAIR) imaging for better visualization of vasogenic edema, with example images shown in **Fig. 3**.

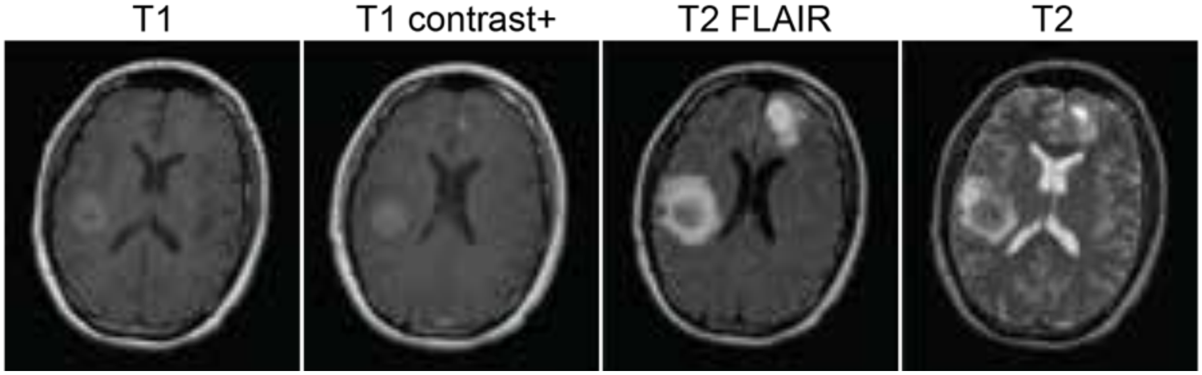

Figure 3: MRI of the brain showing MBM lesions*. Axial scans of a patient presenting with multiple hemorrhagic MBM tumours. Case provided by Prof F. Gaillard, Radiopaedia.org rID: 29116.*

BM exhibit distinct imaging characteristics in MR images that aid in diagnosis, though their appearance can vary based on primary tumour origin. These lesions often develop where vasculature is small, and blood flow is slow, particularly at grey-white matter junctions and in "watershed zones" between cerebral arteries[52,53]. While lung cancer and melanoma often spread as multiple lesions, breast cancer usually presents as a single metastasis[54].

On non-contrast T1-weighted MRI, most BMs appear darker (hypointense) than surrounding tissue, except for hemorrhagic and MBM, which appear bright (hyperintense) due to blood products and melanin content[55,56]. Morphologically, BMs are typically well-defined spherical lesions that may show central necrosis[57]. They predominantly occur in the cerebrum (80% of cases), followed by the cerebellum (15%) and basal ganglia (3%)[54,55]. A distinctive feature of BMs is their tendency to hemorrhage, causing significant vasogenic edema around the tumour. This edema appears bright on T2-weighted FLAIR images and is often disproportionately large compared to the tumour size – a key characteristic that helps distinguish BMs from primary brain tumours[55,58,59].

1.2.4 Treatment strategies

Given the brain's vital function and its distinctive nature, treatments for BMs require a delicate balance between therapeutic benefit and potential harm. The primary aim of treatment is generally not to cure but to prevent or delay neurological decline and to extend survival while maintaining an acceptable quality of life. To achieve this, a combination of surgery, radiotherapy and pharmacotherapy is employed, each with recommendations based on multiple factors. Generally, the tumours are resected surgically, followed by adjuvant radiation and pharmacotherapy, either targeted therapy or immunotherapy. Treatment regimens vary greatly, depending on individual circumstances. The following section will describe the recommendations from the North American (ASCO-SNO-ASTRO) and the European (EANO–ESMO) Clinical Practice Guidelines, along with the challenges each strategy faces[60,61].

1.2.4.1 Physical and radiological strategies

Surgery

Surgical resection, whether partial or complete, is recommended for patients with large, solitary tumour masses and for patients with multiple BMs who develop acute neurological symptoms from increased intracranial pressure[61]. For long-term management, surgery has limited evidence of effectiveness in patients with poor performance status and extensive systemic disease. Still, it may be beneficial for relieving symptoms and prolonged survival in recurrent BMs[62]. Tumours located in inaccessible locations, such as the brain stem or the basal ganglia, are usually not resected due to a high risk of morbidity[63].

Radiotherapy

Radiotherapy effectively treats BMs by delivering high-energy radiation to tumour sites. This treatment damages cancer cell DNA, disrupting their ability to proliferate and spread. Tumour cells are particularly vulnerable to radiation due to their high rates of proliferation and defective DNA repair mechanisms, but surrounding healthy tissue can also be affected.

Whole brain radiotherapy (WBRT) is the broad administration of radiation to the brain. It is fundamentally nonselective and, therefore, does not differentiate between healthy and tumour tissue, leading to severe neurologic side effects such as cognitive deficits, nausea, and vomiting[64]. Due to the high risk of radiation-related side effects, WBRT is mainly recommended for patients with advanced disease and multiple BMs due to its broad coverage in brain tissue[60,61].

Stereotactic radiosurgery (SRS) delivers high-dose radiation with sub-millimeter accuracy and a steep dose fall-off between tumour and normal brain tissue. A stereotactic frame attached to the head of the patient and image guidance enables precise targeting of lesions. SRS has become the standard of care due to its sound effects on BM and fewer radiation-related side effects. The treatment is recommended for patients with up to four BMs and may be considered for patients with five to ten BMs if the combined tumour volume is less than 15 mL[65]. While SRS effectively treats visible metastases, new lesions can develop from a pre-existing microscopic disease that was undetectable at the time of treatment and should be combined with other therapies[66].

1.2.4.2 Pharmacotherapy

Pharmacotherapy for BMs aims to control tumour growth and relieve symptoms through drug administration. However, the BBB (**Section 1.3.1**) is a highly selective barrier that protects the brain, preventing the penetration of almost all large-molecule drugs and up to 98% of small-molecule drugs[15,67]. This presents a significant challenge for treating BMs. Despite this, emerging strategies are promising to improve the effectiveness and penetration of small-molecule drugs in BM patients. See **Table 2** for current guidelines on pharmacotherapies.

Corticosteroids

Corticosteroids are commonly administered to patients not as a primary treatment but for symptom management. In cases of symptomatic BM, corticosteroids help reduce swelling (edema) and intracranial pressure, alleviating symptoms such as headaches, nausea, and neurological deficits[60,61].

Immunotherapy

Immunotherapy uses the body's immune system to identify, target, and eliminate cancer cells. Immune checkpoint inhibitors (ICI) are antibodies designed to block proteins, such as cytotoxic T-lymphocyte-associated antigen 4 (CTLA-1) and programmed cell death protein 1 (PD-1), that suppress immune activity[68]. These proteins are often upregulated by tumour cells to evade immune detection. The clinical trial CheckMate evaluated the efficacy of combining the ICIs nivolumab (anti-PD-1) and ipilimumab (anti-CTLA-4) in treating various types of BMs. Remarkably, asymptomatic MBM patients had an impressive intracranial response of up to 60% and a 3-year progression-free survival rate of 54.1%, establishing this regimen as the first-line treatment for asymptomatic MBMs[69,70]. LBM patients evaluated in the same or similar studies had less impressive but still clinically meaningful response rates of around 28-40% and a 3-year progression-free survival of around 30%, leading to adopting the same regimen for LBM patients[71,72].

Unfortunately, response rates were much lower in symptomatic or advanced-stage patients. The reasons for this are still unknown, but they are likely linked to corticosteroid use, which suppresses the immune response for symptom management[73].

Tyrosine kinase inhibitor therapy

Small molecule inhibitors like tyrosine kinase inhibitors (TKIs) can partially penetrate the BBB, while larger chemotherapeutic agents typically cannot. TKIs, developed following the discovery of oncogenic driver mutations, are widely used as first-line therapy in managing the majority of BM patients. These inhibitors selectively target overactive proteins and shut down upregulated signalling pathways that promote tumour growth. For MBM, a combination of BRAF (dabrafenib) and MEK (trametinib) inhibitors is used to address potential resistance[60,61]. However, despite frequent activation of the NRAS protein and the PI3K pathway in MBM, no successful targeted therapies for these pathways have been established in clinical practice. MEK inhibitors are used as an indirect approach[60,61]. KRAS mutations are common in LBM but are not considered first-line actionable (targetable) mutations. The KRAS-targeting drugs sotorasib and adagrasib recently received approval for clinical use[74,75]. However, additional studies are needed before first-line adoption[76]. Patients with activating *EGFR* mutations are typically treated with osimertinib or icotinib, and those with *ALK* rearrangements have several treatment options, including alectinib, brigatinib, and ceritinib[61,76].

Table 2: *Outline of first-line treatment recommendations for LBM and MBM according to EANO-ESMO and ASCO-SNO-ASTRO Guidelines. Adapted from* [60,61]**.**

Cancer Type	Treatment Recommendations
Melanoma	BRAF wild type and BRAF mutant patients: ipilimumab and nivolumab are preferred first-line treatment
	Patients with multiple symptomatic BRAF-mutated BMs or patients requiring 4 mg steroids or higher: dabrafenib plus trametinib
	NRAS - no clinically approved targeting therapies
Lung	KRAS most frequent activating mutation- no clinically approved first-line targeting therapies
	NSCLC without targetable oncogenic driver mutations and PD-L1 positivity: monotherapy with anti-PD-1 or PD-L1 immune checkpoint inhibitors
	Patients with NSCLC with targetable oncogenic driver mutations Osimertinib or icotinib for EGFR mutants Alectinib, brigatinib, or ceritinib for ALK rearrangements

Alternative and experimental therapies

Traditional cytotoxic chemotherapy has historically shown poor effectiveness in treating BM, primarily due to poor BBB penetration. Cisplatin, temozolomide, and pemetrexed studies have disappointing clinical results in treating BM and are typically reserved for patients with extensive, refractive, treatment-resistant disease[77,78].

Anti-angiogenesis drugs, such as bevacizumab targeting vascular endothelial growth factor A (VEGF-A), have proven successful in various cancers and shown efficacy in LBM but demonstrate limited effects in MBM[79]. Phase III trials have historically excluded BM patients for fear of intracranial bleeding, although this concern has been disputed[79,80]. Several ongoing Phase II/III trials are now evaluating bevacizumab's safety and efficacy in BM in combination with TKIs or immunotherapy[81–83].

Alternative TKI targets, such as PI3K and MET receptor tyrosine kinase, have been of interest due to the involvement of multiple pathways and activating mutations in signalling pathways in both MBM and LBM. Buparlisib, a pan-PI3K inhibitor, was initially an attractive potential therapy in LBM and MBM. As monotherapy in the clinic, no intracranial response was observed in MBM or LBM[84]. Combination studies *in vitro* are promising however have ahigh toxicity profile in the clinic [84–86]. Therefore, further research is needed to determine its effectiveness and toxicity[77]. MET inhibitors are another novel option and are still in the experimental phase but show promise as a potential secondary target in preclinical studies[88,89].

1.2.4.3 Resistance in the treatment of brain metastasis

While TKIs have significantly improved short-term response rates in patients, acquired resistance and subsequent progression are almost inevitable in MBM and LBM[90]. In MBM, secondary mutations in the *BRAF* gene, upregulation of compensatory pathways such as PI3K, and switching between RAF family proteins ultimately render TKI therapy ineffective[90–93]. In LBM, common mechanisms include MET amplification and secondary mutations such as $\mathrm{EGFR}^{\mathrm{T790M}}$, which reduce the binding affinity of TKI due to protein structure change[94,95]. Efforts to overcome resistance by targeting secondary mutations can paradoxically result in the loss of the secondary mutation, leading to another treatment-resistance stage[96].

Current approaches rely on combining treatments while managing toxicities, extending survival by months. The path forward lies in early detection, prevention and a deeper understanding of the BM microenvironment to find better actionable targets. Understanding the temporal dynamics of brain colonization, stromal cell interactions, and treatment resistance mechanisms could enable more effective intervention. Progress demands better characterization of this complex biology to enable targeted prevention and treatment, ultimately improving outcomes.

1.3 The healthy brain microenvironment

1.3.1 Blood-brain barrier

Circulating tumour cells (CTCs) must penetrate the BBB to successfully metastasize into the brain. The BBB is a specialized microvascular structure of the brain that strictly regulates both transcellular and paracellular passage of molecules and cells from the circulation system into the brain parenchyma. The BBB is built from a neurovascular unit comprised of specialized brain endothelial cells (BECs) anchored to a basement membrane and encircled by pericytes and astrocytic end-feet (**Fig. 4**). These components work together to efficiently remove toxic cellular waste, transport essential macromolecules and ions necessary for CNS function, and restrict entry of cells or pathogens that may cause harm to the neuroparenchyma[97].

The BECs of the BBB are characterized by their absence of gap junctions, connected exclusively through tight junctions formed by transmembrane proteins such as occludin, claudin, and junctional adhesion molecules. These proteins anchor to their counterparts on adjacent cells and connect to peripheral membrane proteins, such as zonula occludens (ZO), to maintain a robust connection between cells. BECs are classified as non-fenestrated, as their membranes contain limited pores and pinocytosis capabilities, therefore transcellular movement across the BBB must be either vesicle-, receptor- or protein carrier-mediated[98]. BECs contain many ATP-binding cassette transporters that protect the brain by effluxing toxins. Unfortunately these efflux pumps recognize many therapeutic drugs as substrates, resulting in low drug delivery[97].

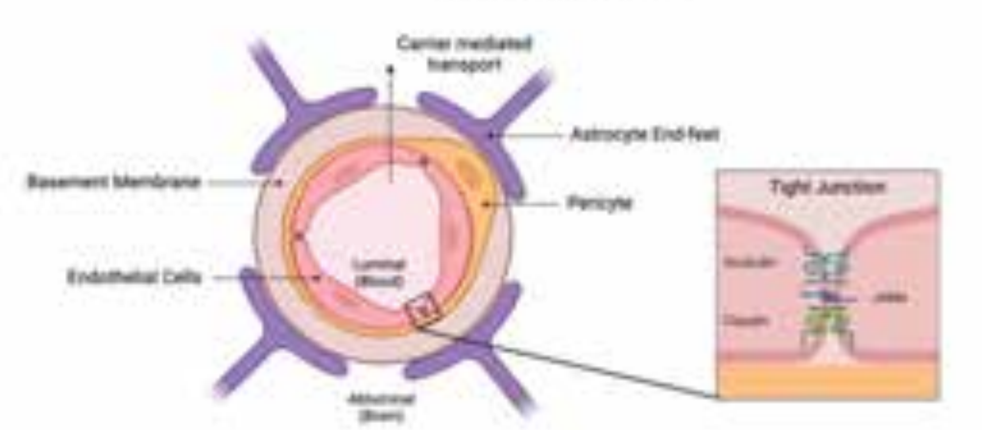

Figure 4: Cell types and structure of blood-brain barrier. *Brain endothelial cells are connected to each other through tight junctions made up of occludins, claudins and junctional adhesion proteins (JAMs), and surrounded by a layer of pericytes. A basement membrane made up of ECM proteins surrounds endothelial cell layer, pericytes and associates with astrocyte-end feet. Based on principles from reference* [97].

Surrounding the layer of BECs is another layer of cells known as pericytes. These cells cover approximately 80% of brain microvasculature and play a critical role in regulating BBB permeability[99]. In addition to structural support, pericytes secrete glycoproteins that constitute the basal lamina surrounding the BBB and regulate the expression of transporters on the BECs[100].

Finally, astrocytes provide additional structural integrity to the BBB by covering a large portion of the abluminal surface with protrusions called end-feet and secreting extracellular matrix proteins[97]. In addition to directly supporting the vasculature, astrocytes act as a bridge between blood vessels and neurons, ensuring the exchange of nutrients and waste products between the bloodstream and neurons to facilitate homeostasis within the brain[101,102].

The highly specialized and efficient BBB is crucial for maintaining neuronal homeostasis and protecting the brain by tightly regulating the movement of essential molecules and blocking harmful substances. However, while vital for brain health, the BBB is a formidable obstacle in the treatment of brain tumours, as it severely restricts the delivery of potentially life-saving therapies.

1.3.2 Cell types of the brain

The brain microenvironment consists of two primary groups of cells: **neurons** and **glial cells,** which include microglia, astrocytes, ependymal cells and oligodendrocytes. Glial cells are vital for supporting neuronal function and maintaining brain health.

Neurons are the fundamental units of the brain. They transmit information and enable communication over long distances through action potentials that propagate along axons, projections that extend from the neuronal cell body[103]. Together, neurons form the intricate neural network of the brain, which is essential for cognitive processes. There is a diverse range of specialized types, and each neuron plays a unique role in functions like memory, learning, sensory processing, motor control, and cognition[103].

Ependymal cells are ciliated neuroepithelial cells that line cerebrospinal fluid (CSF)-filled ventricles and the central canal of the spinal cord. They help maintain CSF circulation through ciliary movement and are an essential component of the brain-CSF barrier[104].

Oligodendrocytes insulate and protect neuronal axons by wrapping their processes around them, forming the myelin sheath essential for efficient signal transmission[105].

Astrocytes are the most abundant and versatile glial cells, providing structural support to the BBB through their end feet and maintaining homeostasis within the parenchyma. Their membranes contain high amounts of aquaporins and ion transporters to aid fluid transport. They supply nutrients to neurons via the lactate shuttle, regulate extracellular ion and pH balance, and secrete factors to support endothelial cells[106]. Using calcium signalling networks, astrocytes communicate with other astrocytes and neurons to mediate synaptic plasticity while maintaining synaptic function by recycling excess glutamate into glutamine for neuronal reuse[106]. In response to damage-associated molecular patterns (DAMPs) or pathogen-associated molecular patterns (PAMPs), which are released during cell death, damage, or tissue injury, astrocytes can undergo reactive astrogliosis. These reactive astrocytes, characterized by increased glial fibrillary acidic protein in combination with other protein markers and an increased proliferation potential, form glial scars at sites of injury, phagocytose synapses and secrete pro- or anti-inflammatory cytokines and neurotrophins[107,108].

Microglia, described as the brain's resident macrophages, are distributed throughout the brain parenchyma. They patrol and migrate to injury sites to promote repair and modulate synaptic signalling by pruning damaged or unnecessary synapses[109]. Like astrocytes, microglia undergo reactive microgliosis in response to DAMPs and PAMPs. Reactive microglia clear pathological or dead cell debris through phagocytosis, secrete cytokines to recruit immune cells and promote healing, present antigens to T cells, and release neurotrophic factors supporting neuronal repair[110].

The roles of reactive astrocytes and microglia often overlap, as their activation frequently occurs in tandem[111]. Microglia are typically activated first, triggering astrocytes, which can be followed by additional astrocyte-mediated stimulation of distant microglia[111,112]. Moreover, recent research reveals that astrocyte and microglial activation states exist along a spectrum rather than as discrete phases, further blurring the distinction between their roles[107,113]. If the glial cell response to damage is insufficient or becomes excessive, sustained activation can lead to peripheral immune cell infiltration and prolonged neuroinflammation, hindering recovery and contributing to various neurological conditions[114].

Immune System

While the brain parenchyma lacks resident immune cells other than microglia, recent research has challenged the long-held belief that the CNS and brain are ‘immuno-privileged.’ Studies have identified lymphatic vessels within the meninges, particularly around the dural sinuses, which facilitate the transport of antigens from the brain parenchyma through CSF and the lymphatic system to cervical lymph nodes[115]. The choroid plexus, CSF, and meninges contain a small but dispersed population of border-associated immune cells, including monocytes, neutrophils, natural killer (NK) cells, B cells, regulatory T cells, conventional T cells, and border-associated macrophages[116]. Under normal conditions, the blood-meningeal barrier maintains control over restricting these immune cells to areas outside the parenchyma. During pathological events, signalling through chemokines, cytokine, and complement proteins enables their infiltration into the brain parenchyma, interacting with reactive microglia and astrocytes to coordinate an immune response[117].

These specialized cells and mechanisms work to maintain the brain as a highly functional and protected environment. However, in the context of cancer, profound alterations in the brain's microenvironment reshape the brain parenchyma, changing its role from supporting neural health to promoting tumour growth and progression.

1.4 The metastatic cascade

Metastasizing tumour cells employ various cancer hallmarks to increase motility and establish secondary tumours. From unlocking cell plasticity to accessing vasculature, metastasizing cancer cells take full advantage of their chromosomal instability to invade and disseminate throughout the body. The metastatic cascade is a complex, multi-step process that follows a consistent sequence across solid tumours (**Fig. 5**)[118,119].

The **formation of the primary tumour** represents the first step towards potential metastasis. Tumour cells accumulate mutations that enhance their growth potential, trigger a process of uncontrolled proliferation and survival, and lead to the development of a primary tumour with invasive properties. While it is still not determined what triggers cancer cell dissemination from the initial tumour, it is hypothesized that stress from nutrient and oxygen deficiencies may play a role once the tumour outgrows its location[119]. Notably, tumour cells have been shown to disseminate even during the early stages of primary tumour development, so there may be alternative factors[120].

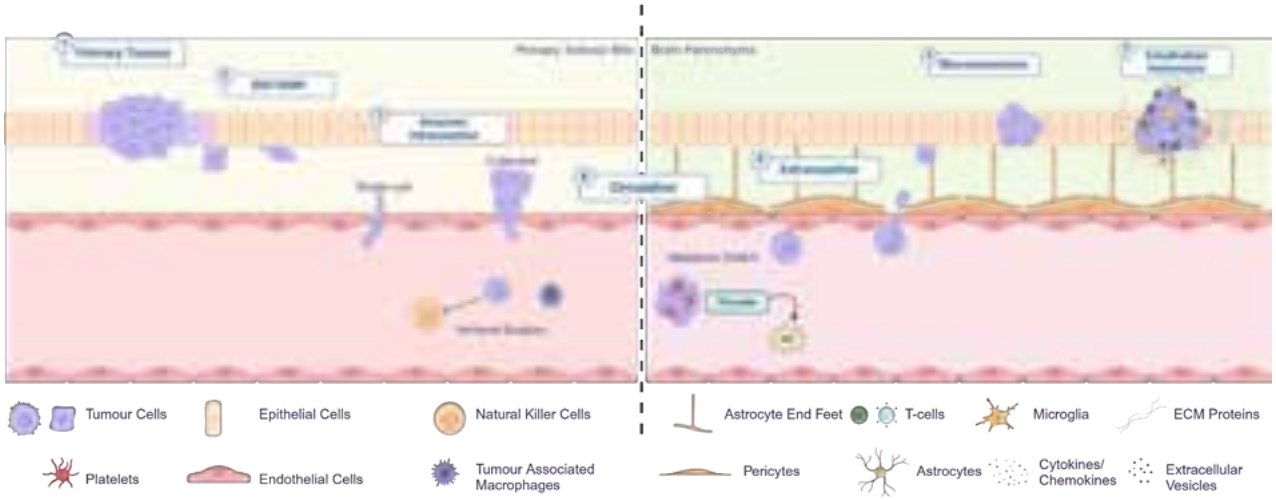

***Figure 5**: **Metastatic cascade to the brain.** The metastatic cascade from primary tumour to brain metastasis follows a defined progression. Step 1: Primary tumour establishment. Step 2: Select tumour cells undergo epithelial-mesenchymal plasticity, enhancing their motility and migratory capacity. Step 3: Cells breach the basement membrane and extracellular matrix through MMP secretion to access the circulation. Step 4: As CTCs navigate the vasculature, they form platelet associations for immune evasion and mechanical protection, while shifting to adenosine triphosphate (ATP) production through pyruvate metabolism rather than glucose-dependent proliferation. Step 5: Cells arrest at the secondary site, adhere to specific proteins, and traverse the BBB through enzymatic secretion. Step 6: Resulting micrometastases enter a dormant state, characterized by immunologic, metabolic, and proliferative quiescence. Step 7: Local cell support enables tumour cells to resume proliferation, establishing an expanding metastatic lesion. Based on principles described in reference[117,118].*

Cancer cells must undergo **epithelial to mesenchymal transition/plasticity (EMT/EMP)** to begin dissemination from the primary tumour mass. This process enables tumour cells with invasive potential to acquire stem-like properties, weakening cell-cell connections and increasing their migrational capabilities[121]. Transcription factors such as Snail, FOXC2, Slug and Twist drive the downregulation of epithelial markers involved in cell adhesion and structural integrity, such as E-cadherin, occludin, and cytokeratin[122–125]. These are replaced by mesenchymal markers such as N-cadherin and vimentin, which drive motility[126,127]. Research has suggested that this process is not strictly unidirectional, and metastatic cells may often exist in a transitional state, giving rise to the concept of epithelial to mesenchymal plasticity (EMP)[128]. These hybrid cell populations have higher metastatic potential, tumour-initiating capacity, and therapeutic resistance [129,130].

These motile cells then begin **invasion and intravasation** through the extracellular matrix (ECM) and into the vasculature, which may occur in either a single-cell or collective fashion toward blood vessels, guided by nutrient and growth factor gradients[128]. Collective invasion involves a group of heterogeneous cells adhering to each other through cadherins. A mesenchymal-like leading edge remodels the ECM through matrix metalloproteases (MMPs) secretion. It rearranges the cytoskeleton through integrin-β1, while the epithelial-like follower cells maintain polarity and structured intermediate filaments that withstand the mechanical stress of migration[131]. In contrast, single-cell invasion typically involves only mesenchymal-type cells that manage structural support and ECM reorganization. These cells utilize flexible stress fibres composed of laminin and vimentin to resist mechanical stress as they enzymatically degrade the ECM[132,133].

The **circulation** of the tumour cells through the vasculature is the most selective step in the metastatic process. A combination of immune detection, sheer stress, metabolic deficiencies, and the risk of anoikis-cell death following detachment from the ECM- leads to fewer than 0.01% of CTCs successfully exiting the vasculature into secondary organs[134]. To mediate this, CTCs undergo a metabolic switch, prioritizing ATP production for energy production through pyruvate metabolism, in contrast to actively proliferating tumour cells, which focus on growth and depend on glucose metabolism[135]. CTCs also associate with platelets for structural protection and to shield from NK cells. They release soluble factors such as VEGF, interleukin (IL)-10 and transforming growth factor (TGF) β to recruit tumour-associated dendritic cells and macrophages, thereby avoiding detection[136].

The challenge of **extravasation** takes place for the small population of cells that survive the journey through the vasculature and arrest at a secondary site. In the brain, CTCs must cross the BBB, the most selective and restrictive barrier in the human body, as detailed in **Section 1.3.1.** The extravasation of CTCs is not a random process. These resilient cells arrest within the narrow capillaries and interact with BECs through cell adhesion molecules such as integrins and selectins. They then proteolytically disrupt the tight junctions between endothelial cells and migrate through the endothelial layer[137,138].

The invasive cells then form **micrometastases,** which often enter a state of dormancy. This can be related to cellular dormancy, where proliferative mechanisms remain suppressed; angiogenic dormancy, where the angiogenic switch remains 'off,' or immune dormancy, influenced by immunological factors to evade the immune system[128]. The micrometastases may remain dormant for extended periods or, under suitable conditions, progress to form **established metastases.**

The local environment must evolve into a supportive niche for cancer cells to thrive. Tumour cells recruit and modify local cells through signalling pathways to promote angiogenesis, enhance nutrient availability, and suppress immune responses. This creates what is known as the pre-metastatic niche (PMN) and metastatic niche (MN), which are essential for the successful establishment and progression of metastasis[139]. This process is hypothesized to lead to organotropic metastasis, where certain cancers are directed to specific secondary organs.

1.5 The tumour microenvironment

The BM tumour microenvironment (TME) can be categorized into two temporal phases: the PMN and the MN. These phases refer to the microenvironment of the metastatic site before and after the arrival of tumour cells, respectively. The PMN primarily aid CTCs by promoting access, anchorage, and initial survival at the metastatic site and in contrast, the MN supports prolonged survival, protection, and proliferation of established metastases[140]. Although well-characterized in the literature, distinguishing these phases is challenging clinically and experimentally, especially in the brain, due to technical limitations[139]. The PMN and MN are influenced by paracrine signalling mediated by tumour-secreted factors, including cytokines, chemokines, growth factors, proteases, and extracellular vesicles (EVs).

1.5.1 Extracellular vesicles

EVs are a key component when discussing the PMN. They play a critical role in intercellular signalling under healthy and pathological conditions. EVs are lipid bilayer structures released from cells and are highly heterogeneous in composition and size, ranging from approximately 20 nm to 1 µm. While terms like exosomes, microvesicles and apoptotic bodies are historically the main components of EV populations, many additional kinds of EVs, including oncosomes, ectosomes, supermeres and exomeres, have been described[141]. According to recent guidelines from the International Society for Extracellular Vesicles (ISEV), the more generic term EV is now recommended in studies to avoid attributing functions to specific EV populations without definite confirmation of their origin[142].

1.5.1.1 Biogenesis of extracellular vesicles

Under both physiological and pathophysiological conditions, EVs are typically produced by two main mechanisms, as shown in **Fig. 6**.

EVs known as exosomes are formed through the endosomal pathway. Here, an early endosome is generated through the **inward budding** of the plasma membrane, facilitated by endosomal sorting complex required for transport (ESCRT) proteins. The endosome then undergoes a second inward budding, forming intraluminal vesicles (ILVs) within a late endosome/multivesicular body (MVB). These MVBs are then transported to the cell

Figure 6: Cellular vesicle formation mechanisms. *The left panel shows the endosomal pathway, where an early endosome forms through inward budding from the cellular membrane. A second inward budding leads to the formation of ILVs of 30-150nm contained in a MVB or late endosome. This then fuses with the cellular membrane to release the EVs into the extracellular space. The right panel illustrates plasma membrane budding, where vesicles of 150nm-1µm form through outward budding from the cell surface. Based on principles described in references* [143-145].

surface, fusing with the plasma membrane, mediated by Rab GTPases. Then, the EVs are released into the extracellular space[143].

Larger EVs (including microvesicles, ectosomes, microparticles or endosomes) are created independently of MVBs through **outward budding** of the plasma membrane[144]. The genesis of these particles typically involves the shuffling of lipid components at the plasma membrane and the rearrangement of the actin cytoskeleton mediated by small GTPases. During this process, the plasma membrane buds outwards, pinches off, and releases the vesicle into the extracellular space[145].

Once formed, EVs exert their function primarily through their cargo. Target cells interact with EVs through membrane-bound receptors, initiating signalling through receptor-ligand interactions. These interactions can also facilitate the internalization of EV through mechanisms such as clathrin-mediated endocytosis, other forms of endocytosis, phagocytosis, or membrane fusion[145]. These processes enable EVs to efficiently and precisely alter the physiological state of the recipient cells by delivering their cargo.

1.5.1.2 Extracellular vesicle cargo

During biogenesis, EVs are selectively enriched with bioactive cargo, including transmembrane and cytosolic proteins, RNA, DNA, and lipids. While the composition of EVs often reflects their parent cells—for instance, EVs derived from mesenchymal stem cells exhibit intrinsic therapeutic properties and are being explored for applications in wound healing and immunosuppression—the cargo is selectively packaged for specific functions[146]. Certain molecules found abundantly in EVs may only be present at low levels in their parent cells, underscoring the active sorting mechanisms involved in EV formation.

Proteins in EVs are often related to their biogenesis, making them valuable markers for EV characterization[141,142]. ESCRT or ESCRT-associated proteins (ALIX, TSG101, FLOT-1/2), release-regulating proteins (RAB27a), and membrane tetraspanins (CD81, CD63, and CD9) are commonly found in EVs[144]. EVs from malignant cells have distinct profiles based on the cancer of origin, containing oncoproteins contributing to tumour progression through the initiation of tumour-related signalling, adhesion, and cell motility[147,148].

The **lipid** composition of EVs resembles that of their parent cells but is enriched in certain lipids including sphingomyelin, cholesterol, and phosphatidylserine. The lipid signature on EVs tends to reflect their origin through either the endosomal or membrane budding process. For example, MVB-derived vesicles have more phosphatidylserine on their outer surface, which helps them be taken up by other cells[143,149].

While **DNA** is packaged into EVs, its mechanics and biological role remain understudied. It has been shown that EVs, specifically tumour-derived EVs, contain single stranded DNA, genomic DNA, and mitochondrial DNA, although their purpose has yet to be fully described[150,151].

Finally, **RNA** represents one of the most enriched cargos in EVs[152]**.** Many assortments of RNAs, primarily small RNAs, have been characterized by next-generation sequencing. microRNA (miRNA), ribosomal (rRNA), long and short non-coding (lnRNA and snRNA), transfer (tRNA) fragments and other less well-known short RNAs have been described[144]. The majority of RNAs found in EVs are under 200 nucleotides in length, but longer messenger (mRNA) and lncRNAs are also present. RNA cargo is often stabilized by proteins such as argonaute 2 (AGO2) or lipoproteins. Through the delivery of RNA, EVs can modulate the post-transcriptional regulation of receptor cells and enact significant alterations in the physiology of the cell. miRNAs are of particular interest in cancer research as they regulate upwards of 60% of protein-coding genes in the human genome[153]. Due to their stability in human biofluids within EVs and association with tumour progression, tumour-delivered miRNAs represent a potential biomarker or actionable target for therapeutics[154].

1.5.1.3 Extracellular vesicles in cancer

There is overwhelming evidence that EVs are a major contributor to cancer establishment, metastasis, and other related processes[148,155–157]. EVs are produced in larger amounts by cancer cells than healthy cells, and some proteins involved in EV biogenesis and release, such as RAB proteins, are found to be upregulated in cancer cells[158,159]. Crosstalk between cancer cells and their environment is critical in cancer progression, as manipulating the conditions around them is a prerequisite to ensure their survival and progression. Tumour-derived EVs have been shown to induce angiogenesis, promote cell migration, reprogram bone marrow-derived myeloid cells (BMDCs) and other immune cells to suppress the immune response, trigger differentiation of cancer-associated fibroblasts and even determine organotropic-directed metastasis[148,160–165]. It is, therefore, no surprise that these EVs are involved in constructing the PMN and facilitating the MN, given their ability to travel long distances in the body and enact alterations on recipient cells. Consequently, their potential in therapeutic interventions is a large topic of study, in addition to mechanistic insight. Drug delivery, discovery of biomarkers, and inhibition studies are of interest for potential alternative routes of therapy[148,166].

1.5.2 The pre-metastatic niche

In 1889, Stephen Paget introduced the concept of preferential cancer spread in *The Lancet*, postulating why metastases target specific organs. Observing that breast cancer frequently spreads to specific organs, Paget proposed the "seed and soil" theory, suggesting that both cancer cells (the "seed") and the organ environment (the "soil") determine the pattern of metastasis[167]. His theory was challenged by James Ewing, who suggested that metastatic spread was entirely related to hematogenous and lymphatic spread[168]. While not entirely incorrect, Ewing's view accounts for only part of the process. Paget's theory laid the groundwork for the modern concept of the PMN, and it remains a subject of study and has been well-established for over a century. In modern research, the PMN refers to an abnormal, tumour-supportive microenvironment distant from the primary tumour. In this niche, the local cells are altered to facilitate metastatic growth, even in the absence of tumour cells[139]. These alterations are driven by the systemic release of factors secreted by the primary tumour, which promote the molecular and cellular changes responsible for the establishment of the PMN.

1.5.2.1 General characteristics of the pre-metastatic niche

The first proof-of-principle study that established that tumours can induce the distant formation of a tumour-supporting microenvironment via non-neoplastic cells was published in 2005. Here, Kaplan et al. described that clusters of VEGFR1^{+} expressing hematopoietic stem cells interacted with resident fibroblasts at a secondary site, stimulating the production of fibronectin and MMP9. This, in turn, created a leaky vasculature and a PMN for disseminating C-X-C chemokine receptor type (CXCR) 4 positive tumour cells[169]. Since then, a set of defining characteristics of a PMN have been determined across multiple sites of metastasis[170].

Like the metastatic cascade, the formation of the PMN is thought to be a stepwise process, beginning with the **induction of vascular leakiness and angiogenesis.** Cancer cells secrete factors like TGF-α, TGF-β and VEGF to induce distant upregulation of proteins that break down cell-cell junctions and basement membranes to increase the extravasation ability of incoming CTCs directly[171,172]. Following this, cancer-derived factors and EVs initiate **stromal remodelling** at the metastatic site, a highly specific process to the target organ and cell types. Finally, a hallmark of PMN establishment is the **recruitment of immune cells** to the pre-metastatic sites to induce a supporting environment for the arriving CTCs[139]. While these hallmarks are typically common to all sites of a PMN, it should be noted that a large portion of PMN studies describe the process in the lungs, given the frequency of metastases *in vivo* and the clinic[173].

1.5.2.2 Pre-metastatic niche in the brain

While the PMN is an established concept in commonly metastasized organs such as the lungs, lymph nodes, bone, and liver, the brain PMN (bPMN) remains one of the least studied, with limited empirical evidence supporting its existence[139,173–177]. Unlike other at-risk organs that can be easily biopsied, obtaining pre-colonized brain tissue from patients is unfeasible. The brain's specialized access to the lymphatic and immune system, complex vasculature, and unique cell types make the bPMN a distinct and challenging frontier in metastatic research, requiring the adaptation of PMN hallmarks to the brain's specific characteristics[115]. Due to the limited evidence on the bPMN, the mechanisms discussed here and described and **Fig. 7** draw from combined findings in melanoma, lung, and breast cancer studies.

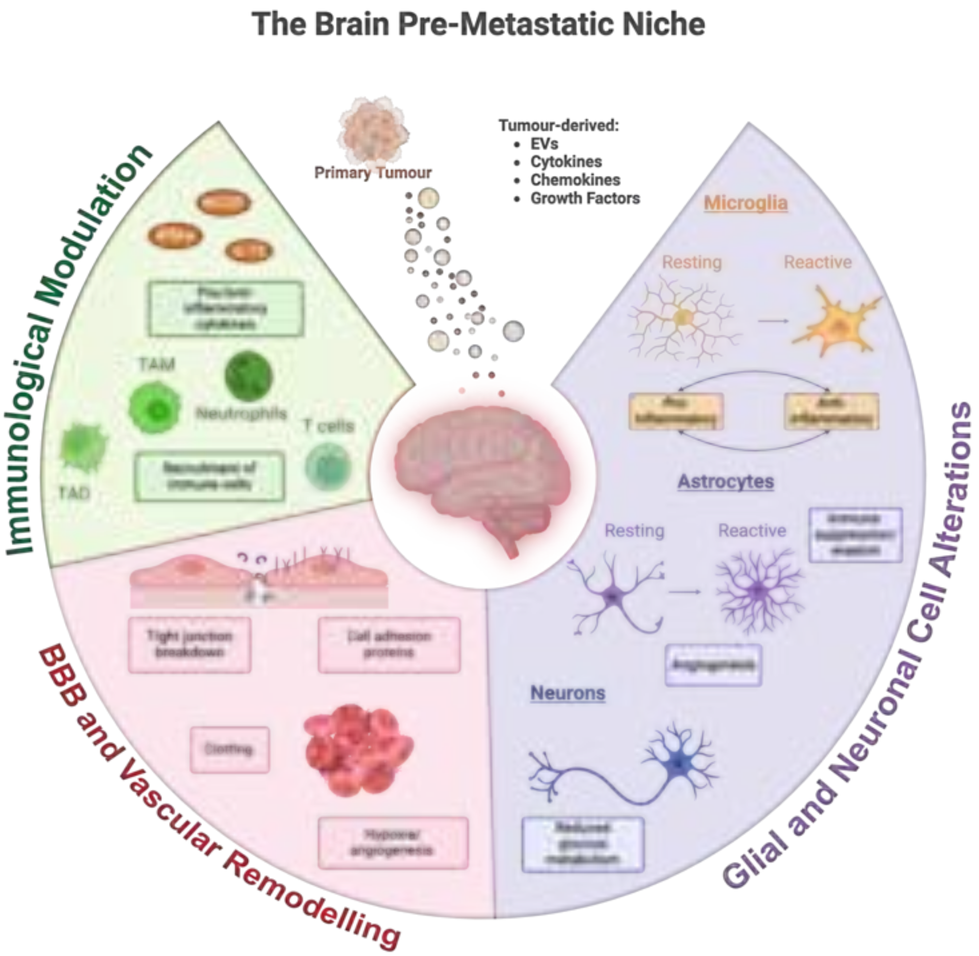

Figure 7: The brain pre-metastatic niche. *Tumour-derived cytokines, chemokines, and growth factors shape a pro-metastatic environment in the brain by modulating immune responses, disrupting the BBB, and altering glial and neuronal function. Based on information from references[178-192].*

The pre-metastatic blood-brain barrier

The BBB presents significant challenges for both research and treatment. Yet, its role as the primary gateway into the brain makes it an evident focus for understanding and studying the bPMN. Evidence from multiple primary cancer types has demonstrated mechanisms that enhance BBB permeability and promote cellular adhesion as part of bPMN formation to aid CTCs in extravasation.

Several EV-delivered ncRNAs have been implicated in compromising BBB integrity through distinct mechanisms, primarily through targeting tight junctions. In animal models using brain trophic breast cancer cell lines (BTBC), EV-delivered miRNAs disrupted tight junctions by directly downregulating tight junction protein expression or inducing abnormal localization through actin fibre dysregulation[178,179]. In an LBM model, lnc-MMP2-2 delivered by tumour EVs was found to sequester the tight junction stabilizer, miR-1207-5p, resulting in dysregulated cell-cell adhesion in BECs[180].

In addition to compromising the structural stability of the BBB to facilitate the transmigration of CTCs, clotting and adhesion protein expression is altered and upregulated in the bPMN to aid in arresting CTCs. For example, in a mouse model of MBM, Von Willebrand factor (VWF) accumulation was observed, produced by both platelets and BECs. These VWF fibres promoted platelet clustering and microthrombi that support CTC retention within blood vessels. Notably, similar levels of VWF expression were found in metastatic and peri-metastatic regions and in the brains of tumour-bearing mice without established BM[181]. Studies in breast cancer BM (BrBM) mouse models have shown that specific adhesion molecules, such as activated leukocyte cell adhesion molecule (ALCAM) and vascular cell adhesion molecule-1 (VCAM-1), are upregulated on BECs. These proteins are critical for the early seeding of metastases and may also promote interactions between tumour cells and monocytes, contributing to immune evasion and further supporting metastatic progression[182].

Glial cell alterations

In the brain microenvironment, BMDC infiltration and immune changes are tightly linked to stromal remodelling due to the interplay between glial cells and the immune system[183]. Neuroinflammation through reactive gliosis was traditionally considered a defensive response aimed at eliminating tumour cells. However, tumour cells orchestrate a dynamic reprogramming of neuroinflammation throughout the metastatic process, balancing pro-inflammatory BBB disruption with immunosuppressive immune evasion before ultimately hijacking inflammatory pathways to promote growth[183]. To achieve this complex reprogramming, tumours strategically activate and exploit glial cells within the bPMN[140]. MBM and LBM models have shown that paracrine signaling and tumour secreted-EVs can activate astrocytes *in vivo* and *in vitro*[184,185]. In response, reactive astrocytes overproduce chemokines and cytokines that contribute to immune cell recruitment (CXCL1), angiogenesis (VEGF, platelet-derived growth factor; PDGF), tumour survival (macrophage colony-stimulating factor; M-CSF), and resistance to immune responses (interferon-γ; IFN-γ, IL-15)[185–187]. Reactive astrocytes also overexpress chemokine C-X-C motif ligand (CXCL) 10 *in vitro* and *in vivo*, which acts as a homing signal to chemoattract melanoma cells expressing the CXCR3 receptor to the brain[188]. Furthermore, after guiding CTCs to the brain, increased secretion of IL-23 by reactive astrocytes was also shown to upregulate MMP2 production in CTCs upon arrival, aiding in their ECM degradation and extravasation[189].

Microglia undergo activation similar to astrocytes in the bPMN, though evidence of this remains somewhat contradictory. In a BrBM model, tumour EVs enriched with cell migration-inducing and hyaluronan-binding protein (CEMIP) were taken up by BECs and microglia, triggering a pro-inflammatory response and contributing to neuroinflammation and vascular leakiness[190]. In an LBM model, EVs carried LINC00482, promoting an ‘M2’ microglial phenotype, which is more anti-inflammatory *in vitro* and *in vivo* by inducing TGF-β1 overexpression. These ‘M2’ microglia were shown to enhance the growth of lung cancer cells by secreting cytokines that enhanced proliferation, colony formation, migration, and invasion of LBM cells *in vitro*[191].

While alterations in glial cells within the bPMN destabilize the BBB or drive neuroinflammation, tumour cells have also been shown to manipulate the metabolic environment in the bPMN to suit their needs. EVs from a BrBM model delivered miR-122, which suppressed glucose uptake by astrocytes and neurons by downregulating pyruvate kinase, a process found to be reversible by miR-122 inhibition *in vivo*. This created an abundance of glucose to meet the high energy demands of incoming tumour cells, without which tumour cells would likely remain in dormancy upon arrival[192].

1.5.3 The metastatic niche

The conceptual distinction between the bPMN and the brain MN (bMN) lies in the timing-with bPMN preceding bMN- and the presence of tumour cells. In practice, there is an overlap in mechanisms. The bPMN primes the brain microenvironment to support the entry, initial survival, and establishment of CTCs, while the bMN primarily facilitates the sustained survival, growth, and expansion of established metastases[140]. Given this, a defining characteristic of the bMN is bidirectional tumour-stromal interactions, by which the tumour cells continuously communicate with the local environment to modify it to suit their needs.

1.5.3.1 The blood-tumour barrier

Once a metastasis has established itself, the compromised, heterogeneous and leaky remnants of the BBB are referred to as the blood-tumour barrier (BTB)[34]. Arriving CTCs utilize cell surface ligands and proteases, such as cathepsin S and MMPs, to mediate transmigration and disrupt junctional complexes, which further implements damage[193,194]. High energy demand from expanding tumours results in hijacking the vasculature, often through vessel co-option instead of sprouting angiogenesis, to meet the metabolic requirements of the tumour cells[195,196]. Ever-expanding tumours physically disrupt the BBB and compromise the connections between the BECs, astrocytes and neural cells[97].

In BrBM, BTB vessels are dilated and contain high levels of VEGF, activated astrocytes, and microglia[197]. Astrocytic end-feed supporting the BTB lack aquaporin channels, which disrupts their polarization, and notably[197]. Unfortunately, although the BTB seems to be leaky to pharmacotherapeutics and contrast agents in experimental models, the BTB is highly heterogeneous in terms of permeability, and experimental results most often fail to translate into the clinics[198]. Leakage is insufficient for a meaningful clinical response to drugs, especially given the enhanced pro-survival signalling in BM cells[198–201].

1.5.3.2 Tumour-neuronal interactions

There is limited evidence to suggest that neuronal cells are anything other than passive bystanders in metastasis. Neuronal cell death often occurs due to extended neuroinflammation, lack of nutrients, and reduced blood flow, serving as collateral damage to the growth of tumour cells[202]. In BrBM tissue samples, tumour cells had a phenotype similar to that of GABAergic neurons and expressed several of the same receptors to confer a proliferative advantage[203]. This suggests that tumour cells gain more from co-opting resources essential to neurons than from any direct support the neurons could provide.

Interestingly, a similar perspective was held regarding interactions between tumours and nerves outside the brain. Recent research has suggested that neural progenitor cells may contribute to cancer cell aggressiveness in tumours outside the brain, although this phenomenon is relatively unexplored in the CNS[204,205]. Oligodendrocytes are also compromised in the bMN, leading to further neuronal dysfunction and subsequent cell death through loss of the myelin sheath[111].

1.5.3.3 Neuroinflammation and tumour-immune interactions

Myeloid cells

In established BMs, it has been estimated that up to 30% of the tumour mass consists of macrophages and microglia, making them the most abundant non-neoplastic cell type in the tumours[193]. These cells have been found to form a boundary around the tumour mass, both in animal experiments and in patient brain slices[117,206,207].

Upon detection of even a single circulating tumour cell, microglia mount an initial defence response through rapid recruitment and activation. However, tumour cell mechanisms quickly shut down the anti-tumour response and recruit the macrophages into a tumour-supporting phenotype[208]. In BrBM cell lines, toll-like receptor (TLR) and Wnt signalling can interfere with microglia's DAMP responses while increasing the BM progression marker CXCR4 expression to recruit more cancer cells and promote their proliferation[209]. In MBM, reciprocal communication between tumour cells and microglia decreases their phagocytic response through c-Jun N-terminal kinase (JNK) dephosphorylation, while upregulating ERK and STAT3 signaling in tumour cells to increase proliferation[210].

Lymphocytes

The role of lymphocytes in BM is complex and contradictory. Tumour-infiltrating lymphocytes have been identified in BM from all common primary cancers, with the highest frequencies observed in renal cell carcinoma and melanoma[211]. Increased density of specific CD3+ or CD8+ T cell populations has been correlated with improved overall survival. However, certain T cell subsets paradoxically promote BM progression through immunosuppression[25,212,213]. Regulatory T cells infiltrate both MBM and LBM, mediating immunosuppressive functions[214]. Though the precise mechanisms of lymphocyte-tumour cell crosstalk require further investigation, their presence and dysregulation in the brain metastatic microenvironment has been demonstrated.

1.5.3.4 Tumour-astrocyte interactions

Reactive astrocytes initially defend against extravasating CTCs by producing plasminogen activators (PAs), which generate plasmin to trigger cell death in invading CTCs. However, CTCs can circumvent this defence through the production of anti-PA serpins[196]. If successful in avoiding the defence mechanisms, tumour cells engage with astrocytes to induce a cancer-promoting phenotype. These tumour-promoting astrocytes localize around metastasizing cells to create a protective niche for secondary tumour formation[215]. This initial interaction evolves into a complex bidirectional relationship, where direct cell-cell contact and secreted factors facilitate metastatic progression[216]. Through this reciprocal exchange, tumour cells activate astrocytes to enhance chemoprotection, proliferative signalling, and immune evasion.

Gap junctions between activated astrocytes in both LBM and BrBM models transfer cGAMP, triggering IFNα and TNF release from astrocytes. This activation of STAT and NF-κB pathways enhances tumour growth and chemoresistance[217]. Notch signalling to promote self-renewal of tumour cells is stimulated by direct signalling to activated astrocytes by IL-1β secretion from tumour cells[218]. These direct cell interactions can also contribute to survival, whereby in MBM mouse models, gap junctions formed between astrocytes and tumour cells transfer intracellular calcium from tumour cells, preventing pro-apoptotic signalling[219].

Beyond direct cellular interactions, astrocyte-derived factors significantly influence metastatic progression. In an impressive paper by Zhang et al., it was discovered that human and mouse BM cells lost tumour suppressor PTEN expression after dissemination to the brain. This loss was mediated by EVs released from the reactive astrocytes containing miR-19a, targeting PTEN mRNA for degradation. This subsequently increased C-C motif chemokine ligand (CCL) 2 expression in tumour cells to recruit myeloid cells, enhancing tumour cell proliferation[220]. Recent research suggests that BMs from lung, melanoma and breast cancer are surrounded by a subpopulation of BM-induced pSTAT3 positive reactive astrocytes in patient brains[221]. These astrocytes influence various immune system components, including the innate immune system (microglia/macrophages) and the acquired immune system (T cells). The subpopulation of $pSTAT3^+$ astrocytes was reduced *in vivo* upon blocking STAT3 signaling[221].

As summarized, evidence demonstrates that tumour cells influence the brain microenvironment before and during metastatic spread. While research has elucidated some key mechanisms in this process, significant knowledge gaps remain in our understanding of how the bPMN and bMN are established and persist. Given the impact of BM and its resistance to current therapies, further investigation of the tumour microenvironment and how cancer adapts to ensure its survival is warranted.

2. Aims

This thesis aims to deepen our understanding of BM establishment and progression by investigating tumour influence on the metastatic site and tumour-mediated signalling pathways. This will encompass mechanistic studies of EV-mediated tumour microenvironment alterations and therapeutic intervention strategies.

1) To investigate the functional impact of MBM-EV-derived miRNAs on astrocytes and their subsequent contribution to MBM progression.

2) To establish an *in vivo* tracking system by loading BM-EVs with superparamagnetic iron oxide particles (SPIONs) to understand their biodistribution patterns and cellular targets within the brain during the pre-metastatic phase

3) To evaluate the therapeutic potential of a combined pan-RAF and Src family kinase (SFK) inhibitor as a novel second-line treatment strategy for MBM.

3. Methodological Considerations

3.1 Cell culture: patient-derived cell lines

We use *in vitro* cell culture in **Papers I-III** for various mechanistic, functional and drug studies. Our research group collaborates with neurosurgeons in the Department of Neurosurgery at Haukeland University Hospital, who provide brain tumour samples from patients with written consent for research. From here, our lab has generated around 30 BM patient-derived cell lines (PDCs) from varying primary tumour types. PDCs offer a more representative *in vitro* model than commercially available cell lines and, therefore, are the main cell culture models used in **Papers I-III**.

Cell culture, in general, is not always straightforward in translation to clinical or *in vivo* studies but is a worthy starting point for mechanistic and drug studies. Commercial cell lines provide a standardized, ethical research tool that enables consistent comparison and, thus, reproducibility across different studies and laboratories. However, despite their widespread use, they can have significant limitations. Such cell lines typically have high passage numbers and numerous cell divisions, resulting in accumulated mutations that deviate from the original tumour cells. They frequently fail to accurately reflect human cancer characteristics, with documented issues including misalignment with actual cancer behaviours, reduced drug sensitivity, potential cell line contamination, and even misdiagnosis of original cancer types[222].

In contrast, PDCs derived from resected tumour material and used at consistent and limited passages maintain the original tumour's driver mutations. This unique characteristic enables more reliable anti-cancer drug testing, comprehensive tumour mutation sequencing, and personalized medicine approaches through individual tumour sample screening[223,224]. PDC culture remains challenging, with a low percentage of tumour samples successfully establishing *in vitro* cell lines and an even smaller percentage producing reliable mouse models. Despite their advantages, both commercial and PDCs have a critical limitation: 2D cultures lack the complex cell interactions and environment in 3D models[224].

Several PDCs generated in our laboratory were used in **Papers I-III**. Their driver mutations and characteristics are listed below in Table 3. Majority of MBM cell lines contain a BRAF mutation, with all but two harbouring a V600E mutation, which helps in clinical translation for drug studies.

Table 3: Summary of cell lines used in Papers I-III.

Melanoma Origin				
Cell line	Site of Metastasis	Driver mutation status	Origin	Papers
H1/H1_Dl2	Brain	$BRAF^{V600E}$	Patient-derived	I, III
H2	Brain	$BRAF^{V600E}$	Patient-derived	I,III
H3	Brain	$BRAF^{L577F}$	Patient-derived	I, III
H6	Brain	$BRAF^{V600E}$	Patient-derived	III
H10	Brain	$BRAF^{V600E}$	Patient-derived	I, III
H16	Brain	$BRAF^{wild\text{-}type}$	Patient-derived	II
Melmet 1	Subcutaneous	$BRAF^{V600E}$	Patient-derived	I, III
Melmet 5	Lymph node	$BRAF^{V600E}$	Patient-derived	I, III
Wm3248	Not metastasis, cutaneous	$BRAF^{V600E}$	Purchased cell line	III

NCSLC Origin				
Cell line	Site of Metastasis	Driver mutation status	Origin	Papers
LBM1	Brain	$KRAS^{G12C}$	Patient-derived	II

Normal cells		
Cell line	Origin	Papers
Human astrocytes	Purchased cell line	I
Human melanocytes	Purchased cell line	I

3.2 *In vivo* models BM research

Current *in vivo* research on BM commonly uses three model systems: syngeneic mouse models, cell/tissue xenografts, and genetically engineered mouse models (GEMMs)[223,225]. It should be noted that humanized mice models, where human peripheral cells are implanted into immunodeficient mice strains, are an exciting way to model patient-derived cells or tissues combined with an intact immune system. However, it has yet to be fully introduced into BM research[226].

Syngeneic mouse models utilize tumour cells that share genetic identities with the host organism. The B16 melanoma line and its brain-seeking variants, which naturally metastasize to the lung and brain, serve as one of the most widely used experimental models in BM research. Originally derived from C57BL/6 mice, these cells have proven particularly valuable for studying the mechanisms of melanoma brain tropism[227]. Others include spontaneous, transgenic, and carcinogen-induced systems. These models are ideal for immunological studies as they maintain intact immune responses. However, the rapid development of brain lesions and extracranial tumours restrict their utility for studying early colonization events, and limited mutational diversity hinders their translational potential[225].

GEMMs are models in which oncogenic mutations are introduced into mice to allow for the spontaneous generation of tumours. For example, a $BRAF^{V600E}/Cdkn2a^{Null}$ melanoma model has a 17% chance of developing BMs[228]. These models accurately represent BM, following the metastatic process and including an intact immune system. However, they also present significant challenges[227,229]. Slow secondary tumour development can conflict with rapid primary tumour growth, leading to premature endpoint requirements before meaningful data can be collected[230]. Additionally, developing the models is costly and time-consuming, and the low BM generation in current models does not align well with the Replacement, Reduction and Refinement (3R) principles of *in vivo* research[231].

Patient-derived cell or tissue xenografts- as employed in **Papers I and II** - involve implanting human tumour cells or tissue into immunocompromised mice, most commonly non-obese diabetic/severe combined immunodeficiency (NOD/SCID) or NOD SCID gamma (NSG) mice. These models maintain genetic stability and tumour heterogeneity while providing realistic microenvironments with physiologically relevant nutrient and hormone levels. Their high predictive value for therapeutic responses to anti-cancer agents bridges preclinical and clinical research and often complements *in vitro* experiments[232].

In this thesis, PDC xenograft models complement PDC data and translate our *in vitro* work into *in vivo* applications.

Intracardiac Injections

For this thesis, an ultrasound-guided intracardiac injection of PDCs was employed in **Papers I and II**. This approach enables direct translation of *in vitro* PDC findings into an *in vivo* model. Intracardiac injection provides reliable and consistent brain colonization; tumour cells undergo the demanding process of circulation and extravasation while avoiding the limitations of intravenous and orthotopic methods where extracranial lung tumours often cause premature mortality (**Fig. 8 A,B**) [233].

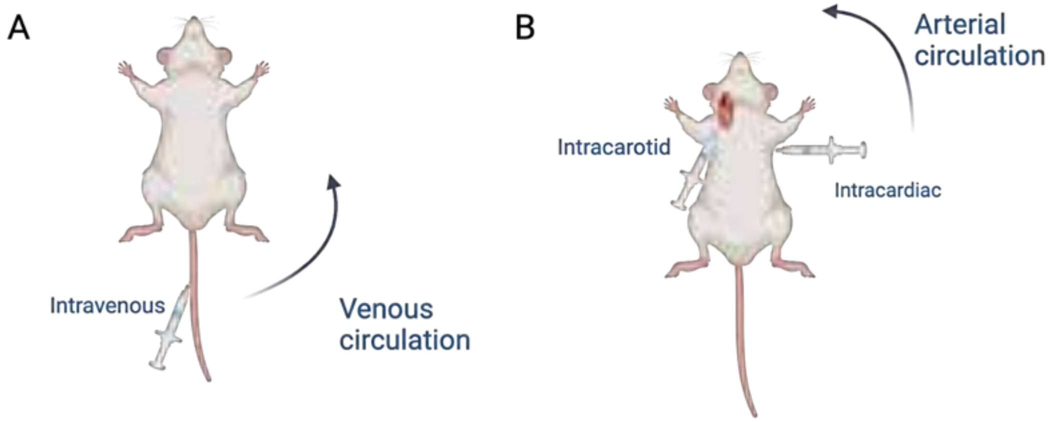

Figure 8: Routes of administration for BM models. *(A) Intravenous cell injection via the tail vein leads cells through the venous system, right ventricle, and lungs before entering arterial circulation to reach the brain. (B) Both intracarotid (surgical) and intracardiac (non-surgical) injections deliver cells directly into the arterial circulation, allowing them circulate through the brain before entering the venous and pulmonary systems.*

While intracarotid injections offer similar reliability and a more direct route to the brain, they require invasive surgery and, thus, the additional risk for failure and extended recovery for the mice (**Fig. 8B**). In contrast, our ultrasound-guided approach ensures precise injection into the left cardiac ventricle through a cross-sectional overview of the heart chambers. Using H1 cells, as detailed in **Paper I**, this technique consistently achieves

100% brain colonization when properly executed. The intracardiac route directs cells through the cerebral vasculature, circumventing initial lung circulation and effectively facilitating BM establishment. Mice are followed up with MRI, and initial tumours can be detected as early as four weeks post-injection.

3.3 Separating extracellular vesicles from cell culture media

In **Papers I** and **II**, we isolated EVs derived from MBM or LBM cell lines for mechanistic, characterization, functional, and disease modelling studies. EVs can be separated from cell culture media using various techniques. In this thesis, we employed differential ultracentrifugation (**Paper I**) and size exclusion chromatography (SEC) **(Paper II**), adhering to the 'Minimal information for studies of extracellular vesicles' (MISEV) recommendations for EV isolation for both studies[141,142].

Regardless of the separation method, certain precautions must be taken while culturing cells to successfully separate a clean and pure EV sample. Standard fetal bovine serum (FBS) or serum derivatives contain bovine EVs that contaminate isolates. Cells must be cultured in serum-free conditions or EV-depleted FBS to avoid this. Both serum-free media and EV-depleted FBS are commercially available at premium costs. Therefore, we depleted FBS of EVs in-house by ultracentrifugation (18h at 120,000 × g) followed by filtration through a 0.22 µm membrane.

Differential ultracentrifugation is a method that involves centrifuging the cell-conditioned media (CCM) at various speeds to sequentially collect populations of particles of different sizes (**Fig. 9**). Initial low-speed centrifugation at 2,000 × g removes cell debris and apoptotic bodies, followed by 20,000 × g for larger EVs (>200nm) and ultra-speeds of 120,000 × g for smaller vesicles (<200nm). While ultracentrifugation is cost-effective and straightforward when equipment is available, it has limitations. This technique co-isolates large proteins like BSA, yields lower quantities of EVs, and is time-intensive for processing large volumes of CCM. It is suboptimal for low-volume samples, such as patient-derived serum, plasma, or CSF.

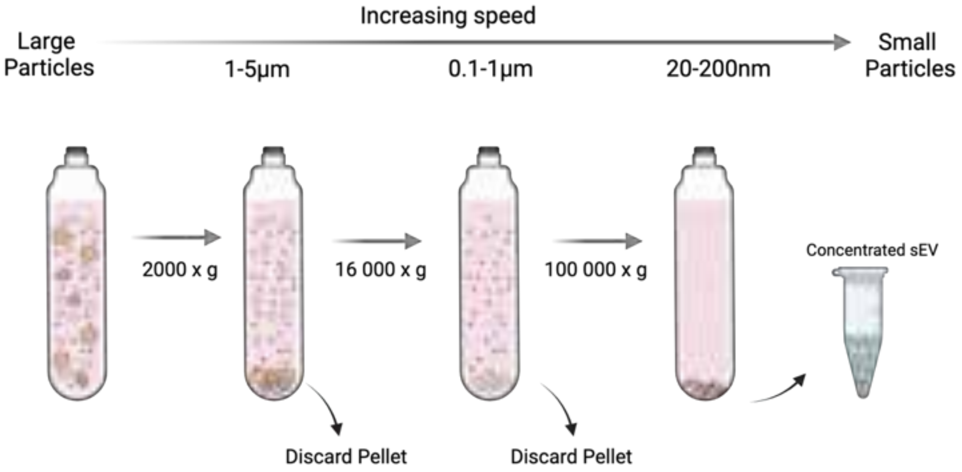

Figure 9: Principle of Differential Ultracentrifugation for isolating small EVs*. Cell-conditioned media (CCM) is collected and spun at low speed, pelleting larger apoptotic bodies and debris. This is discarded before spinning a second time at 16 000 x g, pelleting larger EVs, which are again discarded. A final spin at 100 000 x g pellets small EVs under 200mm. This is resuspended in filtered 1x PBS for further use.*

As used in **Paper II**, SEC separates particles based on size using a gel matrix column. Larger particles elute in earlier fractions, while smaller particles, such as proteins and molecules, become trapped in the matrix pores, eluting in later fractions (**Fig. 10**). This method offers flexibility in collecting high-purity individual EV-rich fractions or pooled populations to improve yield. Our lab demonstrated nearly 10-fold higher yields compared to DUC. The technique can be scaled up for multiple separations per day, unlike DUC, which is limited by rotor tube capacity and processing time.

In **Paper II**, the Izon Automatic Fractionator was used for EV separation from CCM. This instrument is optimized for EV separation and can be tailored for various sample types and volumes. We utilized 0.5 mL columns for CCM separation after concentrating samples using centrifugal filters, allowing for scalability. This system proved particularly effective

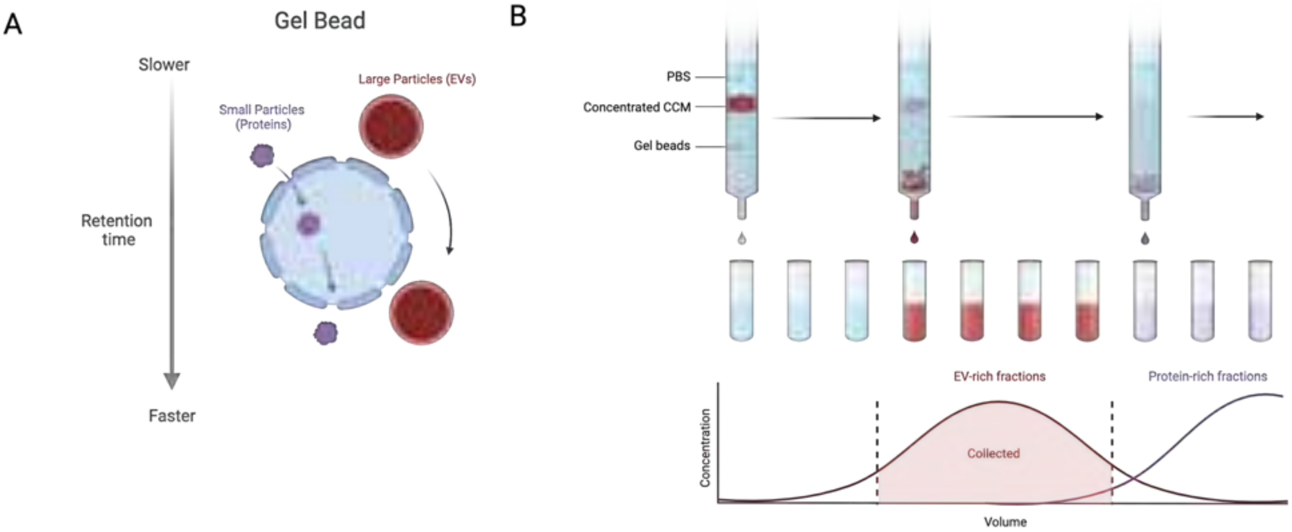

Figure 10: Principe of Size exclusion chromatography for isolation of small EVs*.** ***A *Gel beads in a column contain pores that cause smaller particles (proteins) to travel slowly through the column, while larger particles (EVs) bypass the pores and travel down the column faster.* ***B*** *CCM is spun at 2000 x g to remove debris before being concentrated in a centrifugal filter. Concentrated CCM is added to the column where the EVs move through the beads faster. EV-rich fractions are collected earlier than protein-rich fractions, allowing the collection of fractions containing the highest yield of EVs while avoiding contamination from larger proteins.*

for removing excess SPIONs (5 nm) from EV samples through size-based fractionation, ensuring high-purity EV isolates.

3.4 Labeling extracellular vesicles with superparamagnetic iron oxide nanoparticles

Different imaging modalities require specific EV labelling approaches, with each method optimized for research objectives. In **Paper II**, we developed a strategy enabling nanoscale and *in vivo* visualization.

Lipophilic membrane dyes, such as PKH67, are among the most common methods for EV labelling. These dyes are cost-effective and easy to use in, for instance, cellular uptake studies by confocal microscopy. However, their limitations - such as non-specific binding, aggregate formation, and signal loss within 24-48 hours - make them unsuitable for *in vivo* applications[234]. More robust alternatives include fluorescent-fusion proteins (CD63-GFP) or metabolic labelling with tagged lipids, providing specific, sustained tracking capabilities. Despite being an effective labelling method, fluorescent imaging *in vivo* remains restricted by tissue penetration depth (1-2 mm) unless invasive techniques such as intravital microscopy through cranial windows are used[235,236].

In **Paper II**, SPIONs were identified as the optimal choice for EV labelling due to their compatibility with our established BM mouse model, access to MRI facilities, and availability of transmission electron microscopy (TEM) instrumentation. These particles offer versatile, multimodal visualization capabilities: Prussian blue staining for light microscopy, electron-dense properties for nanoscale TEM analysis, and superparamagnetic characteristics that provide stable, biocompatible T2-weighted MRI contrast.

Our lab has previously successfully labelled MBM cells with SPIONs to study brain colonization[237]. Building on this, we wanted to adopt a similar strategy for labelling and tracking EVs. We implemented passive loading over electroporation to preserve membrane integrity and prevent aggregation. Although passive loading - where cells naturally incorporate SPIONs into EVs – can exhibit variable loading efficiency and potentially modify EV properties, its broad applicability across cell lines makes it particularly valuable for our PDC models *in vitro* and *in vivo*. Size-based separation through SEC removes free SPIONs (5nm) from EVs (50-200nm), ensuring high sample purity for cell culture studies and animal experiments.

3.5 Magnetic resonance imaging

MRI is the gold standard for brain tumour imaging in clinical and preclinical studies. MRI provides high-resolution visualization of fine structures in soft tissues as a non-invasive imaging modality, making it particularly well-suited for detailed brain imaging. MRI provides sub-millimetre resolution, can differentiate between healthy tissue, tumours and edemas, and does not require radioactive tracers, allowing frequent imaging[49]. In **Papers I and II**, MRI was used to visualize our BM mouse model to assess and quantify tumour burden. In **Paper II** MRI was used to visualize SPION-loaded EVs in mouse tissues.

MRI exploits the magnetic properties of water molecules in the body, particularly the hydrogen atoms within them. A hydrogen nucleus, consisting of a single proton, behaves like a tiny magnet with a north and south pole. This is due to its spin, which generates a magnetic field[238]. Usually, these protons spin in random orientations (**Fig. 11**). However, when an object is placed in the strong magnetic field (B0) of an MR scanner, its protons align either parallel (the lower energy state) or anti-parallel to B_0. This alignment generates a net magnetization in the direction of B_0. By applying brief radio frequency (RF) pulses at 90^{o}, these aligned protons are knocked into the transverse plane (B_1), commonly at a 90^{o} angle to their original position, and synchronize their spin[238].

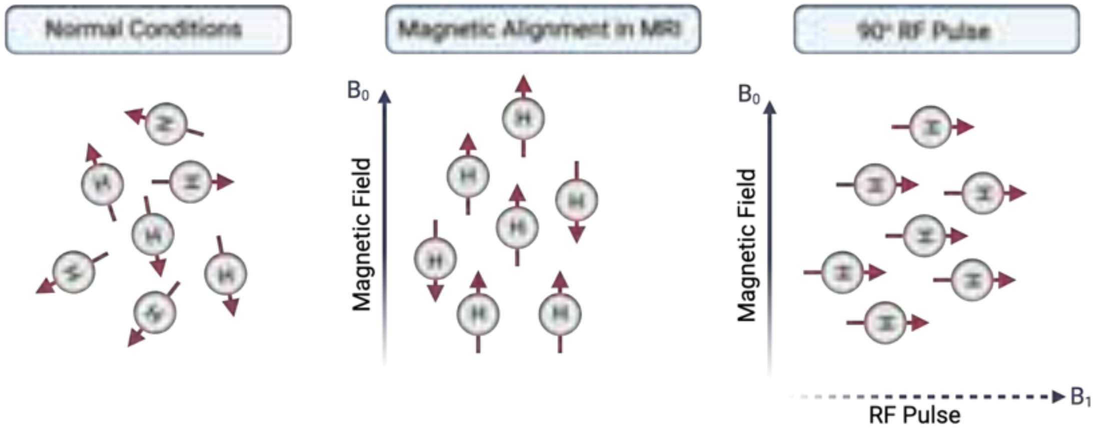

Figure 11: Overview of MRI theory, proton alignment. *Under normal conditions in the body, hydrogen atoms (protons) will spin in random directions and orientations. Under magnetic alignment in the MRI, protons will align either parallel or anti-parallel with magnetic field* B_0*. During* 90^{o} *RF pulses, protons will briefly align at a* 90^{o} *angle to* B_0 *before realigning. Based on principles described in reference* [238].

After the RF pulse, protons realign with B_0 and release energy in two independent and measurable processes: T1 and T2 relaxation. During the relaxation process, the protons return to their original state, and their changing magnetic fields induce signals in a receiver coil. These signals are processed to create an MR image. Stronger signals produce brighter areas in the final image. These different modalities are used based on which tissues you want to highlight.

In T1-weighted imaging, the **recovery of longitudinal magnetization** along the B_0 magnetic field is measured (**Fig. 12A**). The T1 time constant represents the time required for the recovery of 63% of the longitudinal magnetization energy[239]. Tissues with shorter T1 relaxation times (such as fat and protein-rich tissues) efficiently transfer energy to their surroundings, resulting in a brighter appearance on T1 images[240]. On the other hand, water molecules found in CSF move too rapidly to transfer energy efficiently, resulting in a darker appearance in these regions.

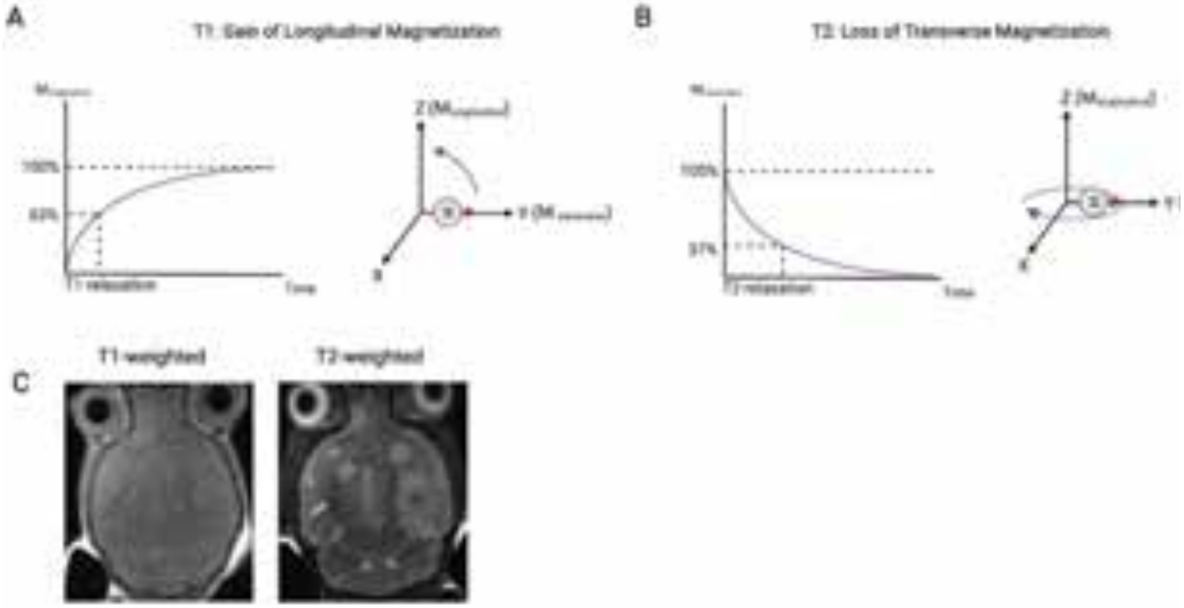

__Figure 12: Principle of T1 and T2 imaging modalities.__ __A__ T1 measures the relaxation time constant (in milliseconds) required for protons in tissue to recover 63% of their longitudinal magnetization. Following a 90° radiofrequency pulse that directs protons to the transverse plane along the Y-axis, the protons gradually return to the longitudinal plane along the Z-axis. __B__ T2 measures the relaxation time constant (in milliseconds) required for protons in tissue to lose 63% of their transverse magnetization. Following a 90° radiofrequency pulse that directs protons to the transverse plane along the Y-axis. Protons initially spin together in phase but gradually dephase and lose their coherent spin while remaining in the transverse plane, resulting in the decay of the transverse magnetization. __C__ Mouse brain with tumours with either T1- or T2-weighted imaging. Based on principles described in references[239, 240].

In T2-weighted MRI, the **loss of transverse magnetization**, which is perpendicular to B_0, is measured (**Fig. 12B**). The T2 time constant is taken when 37% of the original transverse magnetization remains (or 63% has decayed)[239]. Tissues with short T2 relaxation times (muscle or liver) appear darker on T2-weighted images. This effect is due to water molecules in these tissues being highly constrained and frequently interacting with surrounding structures or substances that create magnetic field inhomogeneities, causing the molecules to lose synchronization quickly[239]. For our mouse BM models, T2-weighted imaging is used, as tumours may be easily differentiated from healthy tissue compared to in T1-weighted imaging (**Fig. 12C**). Tumours often have high water content due to vascularization and edema and thus appear as bright areas.

In some cases, contrast agents are used to enhance tissue differentiation. In **Paper II**, we used SPIONs as a contrast agent to visualize EVs *in vivo,* as it complements our T2-weighted imaging of BMs in mice. SPIONs act as a potent negative contrast agent in T2-weighted images, creating dark regions of signal loss. When subjected to RF pulses, their superparamagnetic properties create magnetic field inhomogeneities, influencing nearby protons by shortening their T2 relaxation times[241]. This effect reduces the signal intensity, resulting in darker (hypointense) areas and facilitating precise visualization of SPION-labeled EVs. T2*-weighted imaging is an even more effective modality for visualizing iron as it accounts for both T2 decay and magnetic field inhomogeneities and, therefore, is especially sensitive to visualizing iron**;** however, due to its sensitivity, imaging requires extensive optimization.

3.6 Ethical approvals

For patient-derived material utilized in **Papers I-III**, patients provided written consent for collecting tumour samples and using them to develop cell lines. The Regional Ethical Committee (REC) approved all aspects of this process, including tissue collection, biobank storage of tumour biopsies, and the development and use of cell lines. REC Approvals: 2013/720 and 2020/65185. For animal work done in **Paper I**, The Norwegian National Animal Research Authority (Application #14751, approved Feb 6th, 2018, and Application #28740, approved Dec 21st, 2021) and The Institutional Animal Care and Use Committee (IACUC) of Shandong University, Jinan, China (Approval number: KYLL-2020(KS)-515) approved all animal procedures before all experiments. For animal work done in **Paper II**, The Norwegian National Animal Research Authority approved all procedures prior to performing experiments (Application #30011, approved May 10th, 2023).

4. Results

Paper I

This study examined the impact of EVs from MBM cells on BM development by exploring their effects on astrocytes in the brain. We found that MBM-derived EVs contain high levels of miR-146a-5p, which is transferred to brain astrocytes. Once taken up by astrocytes, miR-146a-5p targets and inhibits *NUMB* mRNA, upregulating the Notch signalling pathway. This activates astrocytes and triggers production of high levels of tumour-promoting cytokines, including IL-6, IL-8, CCL2 (MCP-1), and CXCL1. MiR-146a-5p was highly expressed in MBM cell lines and EVs, and patients' MBM samples. When miR-146a-5p was inhibited in mice, either through genetic knockdown or treatment with the drug deserpidine, we observed reduced formation of MBM and improved animal survival. The study demonstrates that MBM cells use EV-packaged miR-146a-5p to establish a favourable environment for metastasis by reprogramming normal brain astrocytes. Further, we show that deserpidine is a promising therapeutic candidate for preventing or treating MBM by targeting this pathway.

Paper II

This study established a method to visualize BM-EVs *in vivo* via SPIONs as the labelling and MRI contrast agent. Uncoated 5 nm SPIONs showed optimal cellular uptake without toxicity, while dextran-coated SPIONs showed signs of cell death, and carboxyl-coated variants showed poor uptake. Iron content within SPION-EVs derived from labelled LBM and MBM was validated using electron microscopy, colorimetric assays and nanoparticle tracking analysis (Nanospacer). Dynamic light scattering and Nanospacer analysis confirmed EV size population was unchanged after SPION labelling. The SPION-EVs remained biologically active, successfully transferring iron to brain organoids. Furthermore, MRI detected these EVs in both agar phantoms and mouse muscle tissue, presenting a cost-effective and reliable approach for tracking EVs and investigating PMN formation.

Paper III

This study investigated the effects of CCT196969, an SRC family kinase (SFK) and pan-RAF inhibitor, on MBM cells. The findings revealed that CCT196969 effectively inhibited MBM cell growth, migration, and survival across multiple MBM cell lines, with IC_{50} doses for viability ranging from 0.2-2.6 µM. The drug worked through various mechanisms: decreased expression of key signalling proteins (p-ERK, p-MEK, p-STAT3, and STAT3), induced apoptosis in 90-95% of cells at 4 µM concentration, and reduced cell migration. Importantly, CCT196969 was also effective against BRAF inhibitor-resistant cell lines, suggesting its potential as a second-line treatment for patients who develop resistance to standard BRAF inhibitors. The drug was particularly effective in 3D tumour sphere models, showing 15-47 times higher effectiveness than in 2D cultures. While these *in vitro* results are promising, further studies are needed to evaluate the therapeutic potential of CCT196969, particularly regarding its ability to cross the BBB.

5. Discussion

Treatment strategies for BM remain inadequate. Although immunotherapy has shown promising results in asymptomatic patients, the prognosis for those with established BM remains poor. First-line therapies frequently prove ineffective, and second-line treatment options are limited. The primary challenges in treating BM include the complex TME and the frequent development of drug resistance. Thus, research has shifted focus toward understanding the microenvironment beyond tumour cells and exploring alternative therapeutic approaches.

In this thesis, we investigated novel mechanistic aspects of the BM process, primarily in melanoma, to identify potential therapeutic interventions. We describe a mechanism through which MBM-EVs influence the brain metastatic environment by altering local astrocytes **(Paper I**) and present a model that could advance our understanding of BM-EV routing and uptake (**Paper II**). Finally, we propose a novel approach to second-line MBM intervention (**Paper III**).

5.1 Mediators of the pre-metastatic and metastatic niche

Since Kaplan's seminal work in 2005 introduced the concept of the PMN, extensive research has characterized its key components and underlying mechanisms[169]. While PMN formation in organs such as the liver, lymph nodes, omentum, and lungs has been well described, our understanding of PMN development in the brain remains limited. Nevertheless, studies have identified common underlying mechanisms across different metastatic sites, including the brain microenvironment, alongside brain-specific pathways[242]. These shared mechanisms include vascular disruption, clot formation, extracellular matrix and glial cell remodelling, and neuroinflammation, all collectively transforming the pre-metastatic environment into a permissive niche that facilitates tumour cell extravasation and metastatic colonization[139]. In the brain, these processes are uniquely modified by the presence of the BBB and the distinct responses mediated by resident glial cells. These brain-specific adaptations present unique challenges for studying the brain PMN in preclinical and clinical contexts.

5.1.1 Tumour-derived extracellular vesicles in brain metastasis development

PMN formation can be studied through complementary biopsy samples in ‘high-risk’ pre-metastatic tissues to identify distinct pre-metastatic signatures compared to healthy samples[243]. However, similar investigations in the brain are particularly challenging due to the lack of access to clinical brain samples for pre-metastatic analysis. Tumour-derived EVs have emerged as key mediators in PMN formation, orchestrating nearly all hallmarks of PMN establishment through multiple mechanisms. These mechanisms include metabolic reprogramming, organ-specific targeting, BMDC recruitment, glial cell alteration, and extracellular matrix and vascular remodelling[160,161,180,192]. Given the demonstrated ability of EVs to cross the BBB, there is little doubt about their contribution to bPMN transformation. Therefore, we focused our investigation in **Paper I** on the role of tumour-derived EVs in modulating the brain environment throughout the metastatic process.

We demonstrate for the first time that mice preconditioned with MBM-EVs resulted in increased BM burden, both in number and size, suggesting that EVs contribute to colonization and subsequent proliferation. These findings align with previous studies where EVs from brain-seeking MDA-MB-231-BR cells enhanced BM formation after retro-orbital injections. Notably, EVs from the parental MDA-MB-231 cell line, which has only moderate brain metastatic potential, did not affect metastasis sizes compared to untreated controls[244]. The BM efficiency of our H1 cell line, comparable to the brain-seeking MDA-MB-231-BR variant, suggests the presence of a brain-tropic signature in the EVs inherited from parent cells with organotropic potential. This phenomenon was also confirmed in our own BM cell lines in the brain organoid co-culture study in **Paper II**. These findings led us to investigate the specific molecular mechanisms, focusing on EV-miRNA cargo, driving this process.

5.1.2 Extracellular vesicle-delivered miR-146a-5p in the bPMN and MN

Astrocytes play a critical regulatory role in the brain, maintaining BBB integrity, recycling neurotransmitters, maintaining ion and nutrient balance, and responding to injury. Therefore, it is unsurprising that cancer cells hijack these functions in the tumour environment for their own purposes[220,245,246]. Given this, we focused in **Paper I** on the effects of MBM-EVs on astrocytes and the specific cargo within the EVs targeting them.

MiRNAs regulate up to 60% of protein-coding genes in humans and are implicated as major regulators in cancer[154]. Given this, we investigated the miRNA cargo of our MBM-EVs in **Paper I** to identify potential miRNA candidates affecting astrocytic phenotype and behaviour. We found that MBM-EVs containing high levels of miR-146a-5p are uptaken into astrocytes, directly driving them into a reactive phenotype that promotes melanoma establishment and progression. Literature indicates that miR-146a-5p is highly expressed in primary melanoma and that its expression is induced by oncogenic NRAS and BRAF mutations[247]. However, its levels decrease in CTCs but increase again in the metastatic sites[248]. In **Paper I**, we found MBM patients had significantly less expression of miR-146a-5p in serum EVs than healthy controls, corroborating that its expression is dynamically regulated throughout metastasis. As further confirmation, we found that patient MBM tumour samples had a significantly higher miR-146a-5p expression than healthy brain slices. However, we were unable to compare to matched primary samples.

We found that MBM-derived EVs activated astrocytes through miR-146a-5p delivery, leading to upregulated Notch signalling via NUMB inhibition. This activation triggered astrocytes to upregulate the production of IL-6, IL-8, CCL2 (MCP-1), and CXCL1. Interestingly, these same cytokines are typically expressed by melanoma and MBM cells themselves, suggesting a potential amplification of their effects in the TME[249,250].

These cytokines have the potential to promote BM through multiple mechanisms. IL-6 and CCL2 from reactive astrocytes can disrupt endothelial cell adhesion, increasing BBB permeability and enhancing CTC transmigration[251]. CCL2 further enhances this effect by recruiting CCR2-expressing cells, including peripheral monocytes, tumour-associated macrophages, and even MBM cells themselves[243,244]. Previous research has shown that CCL2 release from MBM cells can be induced by loss of PTEN[253]. Interestingly, tumour-activated astrocytes have been shown to induce PTEN loss in tumour cells[220]. Combining these two mechanisms, there is the potential for a ‘feed-forward’ mechanism where the initial activation of astrocytes could eventually lead to increased expression of CCL2 from both astrocytes and MBM cells. However, this complex mechanism would have to be confirmed in its entirety.

These cytokines promote tumor proliferation through distinct mechanisms. IL-8 can establish a feedback loop by enhancing Notch signaling in MBM through interactions with VEGF receptors, while CXCL1 drives tumor progression via activation of the NF-κB pathway [250,254]. All four cytokines can activate important pathways in MBM, including PI3K, MAPK and JAK/STAT[210,255–257].

Although miR-146a-5p levels are lower in MBM patient serum compared to healthy controls, its high expression in patient tumors suggests significant effects on the brain microenvironment. Our findings indicate that astrocyte modification, hypothesized to be an early event in bPMN establishment, contributes to PMN formation through cytokine secretion and thus can promote CTC extravasation, vasculature/oxygen demands, and recruiting BMDCs[184]. The direct growth-promoting effects of IL-6 and IL-8 on MBM cells further emphasize their role in sustained tumour proliferation. Given the demonstrated influence of MBM-EVs on BBB permeability, immune modulation, and vascular remodelling, our results suggest that MBM-EVs and miR-146a-5p initially contribute to establishing a pre-metastatic niche through astrocyte activation and likely continue to facilitate the transition into a supportive metastatic environment.

5.2 Advanced strategies for investigating extracellular vesicles in brain metastasis

Experimental modelling of BM involves several challenges. The limited availability of commercial cell lines often requires artificial brain-seeking selection, potentially altering their original properties, and hospital partnerships are required for access to human cell lines. The rapid disease progression and the occurrence of secondary metastases in mouse models restrict study windows, complicating mechanistic research. Even BM models *in vivo* all come with certain disadvantages. Studying specific stages of the disease, such as PMN formation, adds yet another layer of complexity. In this thesis, we addressed experimental challenges by developing a novel experimental model for studying these specific aspects of BM. In **Papers I** and **II**, we focused on the role of EVs and studied their effects on healthy brain cells.

5.2.1 Visualization and tracking of extracellular vesicles

In **Paper I**, we focused on the role of MBM-derived EVs on astrocytes in the brain. While this approach provided valuable insights into astrocyte-specific responses, understanding the broader potential of these EVs in the metastatic process requires comprehensive knowledge of their biodistribution, temporal dynamics, and cell-type uptake patterns. To address these knowledge gaps, we developed a labelling protocol in **Paper II** to visualize and track BM-EVs *in vitro* and *in vivo*. After evaluating various tracking methods, we selected SPIONs for labelling due to their versatility in multimodal imaging. With SPIONs, we can track BM-EVs *in vivo* with MRI, with Prussian blue for light microscopy and TEM for detailed cellular localization studies.

EV tracking methodologies can be broadly classified into direct and indirect labelling approaches. Direct labelling involves the modification of isolated EVs, which is particularly valuable for clinical applications where parent cell manipulation is undesirable[234]. Indirect labelling involves modifying parent cells that subsequently release labelled EVs. As employed in our study, this can be achieved by utilizing techniques such as transduced fluorescent proteins, reporter genes, or SPION incubation[234]. Our aim in **Paper II** was to develop a model system that simulates BM-EVs in their native state. Therefore, we employed an indirect approach where parent cells internalized SPIONs and incorporated them during natural EV biogenesis to avoid possible disruption of EV integrity and properties.

We faced several interrelated challenges when developing methods to label EVs with SPIONs. The primary concern was maintaining cell health throughout the labelling process. Although SPIONs are generally considered non-toxic, higher concentrations can induce cell stress by producing reactive oxygen species[258]. Our studies revealed that SPION size, concentration, and coating significantly influenced cell viability and uptake efficiency. Cells treated with 5 nm particles maintained over 90% viability compared to controls, while 35nm particles showed significant cytotoxicity at similar concentrations.

The size of SPIONs also affects purity after EV isolation, as larger SPIONs can co-sediment with EVs during isolation, a limitation demonstrated in Toomangian et al. seen with TEM imaging of free SPIONs alongside EVs[259]. Although cytotoxicity varies depending on the cell line, SPION size, and coating, concentrations below 100 µg/mL generally proved safe across literature reports[260,261]. This is similarly reflected in our MBM and LBM cells. However, reducing SPION concentration to minimize toxicity directly decreased EV-SPION yields, highlighting a fundamental challenge: achieving adequate labelling while minimizing biological interference.

Our EV size population remained consistent after SPION labelling, suggesting that the basic physical properties were preserved. This is supported by other reports showing that fundamental EV characteristics are largely maintained across labelling methods[234]. However, most studies focus on standard characterization techniques when comparing labelled and native EVs. Comprehensive proteomic and transcriptomic analyses are needed to fully understand potential changes in EV cargo and function after labelling. Beyond physicochemical properties, managing the impact of labelling on EV biological function is essential for functional applications. A previous study by Sancho-Albero et al. showed that cell-targeting mechanisms remain intact post-labeling EVs with gold nanoparticles, and that the parent cell signature dictating EV targeting is preserved[262]. We verified this in

Paper II, where the H16 cell line, previously shown to not produce tumours in mouse brains, had no EV uptake in brain organoids. In contrast, the brain-tropic signature of LBM1-EVs was maintained, as evidenced by their uptake into brain organoids, indicating the preservation of parental cell tropism after SPION labelling.

In vivo imaging of EVs is challenging across all imaging modalities due to their ultrasmall size. For MRI, several inherent limitations must be considered when analyzing images. **Paper II** shows that SPION-loaded EVs produce a dark, hypointense signal on MRI. This is called 'indirect' contrast, as dark areas could also be interpreted as artifacts, noise or other structures with a low signal, such as bone or air-filled cavities.

Our SPION-EVs were visible in agar phantoms and bulk injections into the thighs of mice, confirming the success of our SPION-loading into EVs and subsequent imaging. The brain is a much more complicated tissue. Therefore, extensive dosing, timing, and toxicity optimization must be performed with proper controls to ensure that brain scans are interpreted correctly. The findings must also be corroborated with *ex vivo* techniques, such as Prussian blue staining, to validate MRI findings.

5.3 Novel strategies for therapeutic intervention in brain metastasis

5.3.1 Targeting alternative pathways

Melanoma is highly chemoresistant. Around 20% of patients have tumours with intrinsic resistance, while those who initially respond to treatment typically acquire BRAF-inhibitor resistance within months of starting TKI therapy[90]. Cancer cells exploit several mechanisms to develop resistance, many of which reactivate the MAPK/ERK pathway. These include the acquisition of secondary amplifying or activating mutations in RTKs such as *NRAS*, alternative splicing of *BRAF* mRNA, and activating mutations of *MEK*[90]. In BRAF wild-type tumours, including both primary and metastatic melanoma, BRAF inhibitors can paradoxically upregulate MAPK/ERK signalling by inducing dimerization between drug-bound BRAF and drug-free CRAF, thus stimulating further signalling through MEK and ERK[263–265]. Due to these escape mechanisms, the first-line treatment for MBM patients shifted from single BRAF inhibition to dual BRAF and MEK inhibition. However, relapse still occurs after an average of 9 months, often through acquired MEK2 mutations[266]. There is a severe need for second-line treatment options when TKI therapy or immunotherapy fails. In **Paper III**, we tested CCT196969, a novel pan-RAF and SRK inhibitor, as a potential second-line therapy for tumours with acquired BRAF-inhibitor resistance.

CCT196969 was developed through a drug discovery program at The Institute of Cancer Research in London, which holds the patent[267]. However, no drug approval or clinical trial information is available to date. Initially tested in metastatic melanoma patient xenografts and cell lines, CCT196969 was found to target and inhibit the activity of pan-RAF proteins and SFKs, both of which are regulators of both MAPK and PI3K signalling pathways. This dual inhibition significantly suppressed tumour growth in patient-derived samples previously treated with vemurafenib, effectively overcoming resistance mechanisms such as intrinsic resistance and acquired mutations mediated by RTK/SFK signalling and NRAS. Building on the success of CCT196969 in metastatic melanomas, we tested its efficacy in our MBM cell lines. We found that pMEK and pERK were significantly downregulated at concentrations as low as 1 μM.

Interestingly, CCT196969 demonstrated equivalent efficacy against the H3 cell line, which harbours a novel $BRAF^{L577F}$ mutation in a rare combination with an $NRAS^{Q61H}$ mutation and our $BRAF^{V600E}$ cell lines. Our results confirm that pan-RAF and SFK inhibition can counteract even complex mutation patterns and effectively inhibit the growth of drug-resistant cell lines.

We also discovered that CCT196969 effectively downregulated STAT3 phosphorylation and expression, a mechanism which had not been previously explored. JAK/STAT signalling in cancer is involved in proliferation, immunomodulation, and survival[268]. STAT3 is activated by the membrane receptor JAK or non-receptor tyrosine kinases such as SRC[269]. Often upregulated in primary melanoma, STAT3 plays a particularly critical role in the progression of MBM, with higher activity in MBM cells compared to cutaneous melanoma[255]. STAT3 activation promotes MBM by inducing the expression of VEGF and MMP-2, with a strong correlation between STAT3 activity and brain metastatic potential[255,270]. Although mutations in the *STAT3* gene are rare in MBM, the pathway itself is often upregulated by upstream signals, particularly SRC family kinases[271]. This suggests that targeting upstream regulators like SRC could provide an effective strategy for modulating STAT3 signalling in melanoma, as demonstrated in **Paper III**.

STAT signalling is dysregulated in MBM cells and has been shown to be important in the TME. STAT3+ reactive astrocytes are subpopulations that contribute to MBM cell survival by modulating the immune response[221]. In neurodegenerative diseases, Notch signalling has been shown to influence the JAK/STAT pathway, particularly STAT3 activation, although the precise mechanisms remain unclear[272]. In **Paper I**, we demonstrate a clear relationship between astrocyte reactivity, Notch signalling, and MBM progression, although we did not investigate this with STAT3 activity.

Cytokines like IL-6 can trigger STAT3 signalling[182]. Although we did not investigate the JAK/STAT3 pathway in this context, we did see an MBM-mediated increase of IL-6 expression in astrocytes in **Paper I**. While IL-6 predominantly activates STAT3 via JAK, constitutive SRC activation and dual JAK/SRC activation of STAT3 have been reported in some cancers, suggesting that SRC inhibition could potentially impact this pathway[45,273]. Given this, **Papers I** and **III** results indicate that CCT196969 could indirectly suppress tumour growth by downregulating critical pathways in MBM and potentially in non-tumour cells like astrocytes. However, further studies, especially *in vivo*, are necessary to confirm these findings.

5.3.2 Crossing the blood-brain barrier

A significant challenge in treating any brain cancer is overcoming the BBB. To cross this barrier, drug compounds typically must be lipophilic (Log *P* 1–4) and have a low molecular weight of under 400–600 Da[274]. Even with these properties, some drugs fail to penetrate the BBB or are removed from the brain by efflux pumps. In this thesis, we tested two potential drugs targeting BM, deserpidine in **Paper I** and CCT196969 in **Paper III**.

Deserpidine is a small molecule drug previously used as an antipsychotic and antihypertensive agent, with a molecular weight of 578 Da and a Log *P* of 3.7–4.25[275]. It is an analogue of reserpine, modified by removing a methoxy group to reduce harmful side effects while maintaining potency[276]. While there is no direct experimental evidence proving the ability of deserpidine to penetrate the BBB, its parent compound, reserpine, is confirmed to do so[277]. Computational predictions about the BBB penetration ability of deserpidine are conflicting. Saini et al. (2022) predicted that the drug would not cross the BBB, while in **Paper I**, our drug docking study suggested otherwise, highlighting the limitations of computational approaches[278]. The successful reduction of brain tumour size by deserpidine *in vivo* in **Paper I** indicates sufficient brain availability for therapeutic effect. However, this could be further verified using radiolabeling and PET imaging techniques.

The molecular weight of CCT196969 is 513.52Da, and a predicted Log *P* value of 5.5 indicates high lipophilicity[279]. In a study evaluating the distribution and efflux of CCT196969 in the mouse brain, the delivery of the drug was limited. However, the oral bioavailability of the drug was relatively high at 70%, and the brain plasma ratio was slightly higher than that of vemurafenib (0.006 CCT196969 to 0.004 vemurafenib)[279]. Given that the IC_{50} doses of our H1 cell line are 0.679 µM for vemurafenib vs 0.705 µM for CCT196969, it does not entirely rule out the possibility of the drug being effective in MBM, even if the uptake through the BBB is limited[280]. This has notably not been tested in animals with established tumours where the permeability of the BBB may be compromised. However, the permeability of the BTB is heterogeneous, and consensus on drug uptake in established metastases is unclear[281].

BBB penetration is critical for therapies targeting BM and should always be considered when undertaking preclinical drug investigations. While both drugs tested in this thesis show effectiveness (**Paper I**) or potential effectiveness (**Paper II**) in the brain, experimental confirmation of their ability to cross the BBB is required. Additionally, strategies such as ligand conjugation, membrane coating, BBB disruption, and nanoparticle-based delivery could enable drugs that do not typically penetrate the BBB to reach the brain[274].

5.3.3 Extracellular vesicles as a clinical tool

EVs are present in all human bodily fluids, making them particularly attractive as potential biomarkers due to cancer's ability to spread through these fluids. Their utility spans a range of clinical applications, including early cancer detection, metastasis monitoring, therapy response assessment, and prognosis evaluation. Cancer cells produce significantly more EVs than healthy cells, further supporting their potential as liquid biopsy candidates. Building on their role in fundamental cancer processes, researchers have identified several promising EV-based biomarkers. For instance, up- or downregulation of certain EV-derived miRNAs have been used as diagnostic and prognostic markers in various cancers, such as oral cancer, hepatic carcinoma, NCSLC, and colon cancer[282–284]. In head and neck squamous cell carcinoma, EV quantity and cargo composition are reliable indicators of therapeutic response[285–287]. These examples represent just a fraction of the growing evidence supporting EVs' diagnostic and prognostic potential[288]. In **Paper I**, we investigated whether miR-146a-5p could serve as a liquid biopsy candidate to determine the risk or presence of a BM from melanoma using patient serum EVs. We found that miR-146a-5p expression in serum EVs was higher in healthy controls compared to MBM patients but was significantly expressed in patient MBM samples vs healthy brain sections, confirming its clinical importance. This led us to shift our focus from exploring miR-146a-5p as a diagnostic or prognostic marker to investigating its potential as a therapeutic target.

Targeting the biogenesis and release of EVs has been investigated from several angles to prevent their function and inhibit cancer growth. This includes inhibiting components in the endosomal pathway that prevent biogenesis and release of cancer-derived EVs [288,289]. Recent innovative approaches have expanded the therapeutic potential of EVs, such as novel strategies designed to capture and remove cancerous EVs. However, these broad treatments could interfere with fundamental cellular processes, raising concerns about potential side effects. Thus, we pursued a more targeted approach in **Paper I**, focusing on specific mechanisms and molecules involved in EV-mediated cancer progression.

5.3.4 MiRNA as a clinical target

Targeting miRNA as an anti-cancer therapy is still in its infancy in the clinic but is gaining momentum in preclinical research. Cobomarsen is currently one of the few approved anti-cancer miRNA inhibitor drugs on the market, inhibiting miR-155 for various rare forms of T-cell lymphoma[290]. While cobomarsen demonstrated low toxicity and reduced lesion size in Phase I trials, the Phase II trial was unfortunately cancelled due to financing issues[291,292]. Most anti-miRNA therapeutics are variants of antisense oligonucleotides designed to inhibit miRNA function, commonly called antagomirs.

In **Paper I**, we employed a drug repurposing strategy to find a compound capable of binding mirR-146a-5p to prevent its activity without going through the lengthy process of a new drug application if successful. Additionally, we aimed to avoid possible off-target effects associated with antagomirs[293]. Deserpidine was predicted to bind to the structure of miR-146a-5p and was shown to effectively reduce the expression of miR-146a-5p in MBM cells *in vitro.* Moreover, the amount of miR-146a-5p present in the EVs derived from the MBM was decreased to an even greater extent, suggesting that drug-bound miR-146a-5p was not loaded into the EVs. *In vivo,* deserpidine treatment reduced the number of metastases in the mice, increased survival, and altered the astrocyte behaviour in the brain. Thus, we were able to target the intrinsic effects of miR-146-5pa on the cancer cells and suppress the supportive role astrocytes play in promoting tumour growth and progression.

Interestingly, TTX-MC138, another clinically available miR-10b inhibitor, is an antagomir conjugated to dextran-coated iron oxide nanoparticles designed to enhance targeted delivery to tumour sites[294]. The drug has completed Phase 0 testing and is undergoing Phase 1 trials to assess its safety profile[294]. If successful, this therapeutic approach represents an innovative application of results from **Papers I** and **II**. To further enhance specificity and potential BBB penetration, loading these inhibitors into EVs is a promising future research direction. While loading EVs with anti-cancer drugs to improve delivery has been explored in previous studies, the potential for creating a targeted treatment with an integrated tracking system remains an exciting avenue for investigation[295].

6. Conclusions

This thesis has explored two critical aspects of brain metastasis: the microenvironment and aberrant signalling pathways, both of which present significant treatment challenges. Our findings contribute to a better understanding of the complexities and mechanisms throughout the metastatic process and offer potential strategies for intervention.

1. In **Paper I**, we demonstrated that MBM-EV priming increases tumour burden in mice. We identified a key mechanism in which MBM-EVs deliver miR-146a-5p to astrocytes, enhancing Notch signalling and inducing a tumour-supportive reactive phenotype.
2. We further showed that targeting miR-146a-5p, either through genetic knockdown or pharmacological approaches, effectively reduces tumour burden, highlighting its potential as a therapeutic target.
3. In **Paper II**, we developed a reliable and reproducible protocol for loading BM-EVs with trackable SPIONs, enabling their visualization and tracking *in vivo*.
4. Additionally, we demonstrated the efficacy of CCT196969 in drug-naïve and -resistant MBM cells and underscored the potential of targeting alternative signalling pathways as a second-line treatment for MBM in **Paper III**.

7. Future Perspectives

By understanding the bPMN and bMN, clinical strategies for BM patients could be shifted from reactive treatment to predictive intervention. Our research has revealed how melanoma primes brain astrocytes to promote metastatic growth, but this represents only one facet of the complex communication networks between primary tumours, CTCs, and the brain microenvironment. The relative success of immunotherapy in early-stage patients underscores the importance of understanding bPMN development and formation and identifying biomarkers that could predict BM before clinical manifestation.

Moving forward, we propose a comprehensive temporal and spatial mapping of how the brain microenvironment evolves from healthy to pre-metastatic to fully colonized states. This requires integrating cutting-edge technologies like spatial transcriptomics and single-cell sequencing to capture the dynamic interplay between all cell types within the TME. However, these approaches alone cannot differentiate between the direct effects of MBM and secondary signals from cells already modified by tumour-derived EVs. Our development of SPION-labeled EVs for *in vivo* tracking provides a foundation for understanding specific targeting and distribution patterns, but requires optimization of dosing regimens, imaging windows, and MRI protocols. Complementary validation approaches combining Prussian blue staining with immunohistochemistry will be essential to confirm target cell identity. Advancing this technology alongside other biomarker detection methods could transform our ability to detect BM before clinical manifestation.

The BBB and adaptive resistance present fundamental challenges for therapeutic intervention. While our work with CCT196969 shows promising *in vitro* efficacy as a second-line therapy for resistant disease, translating these findings requires determining whether sufficient drug concentrations can accumulate in brain tissue. The development of effective second-line treatments represents a critical unmet need, as most BM patients inevitably develop resistance to first-line therapies. Our identification of CCT196969's efficacy against resistant MBM contributes vital knowledge to the limited arsenal of treatment options. Future studies must focus on drug distribution and pharmacokinetics. Additionally, medicinal chemistry approaches could optimize CCT196969's properties through structure-activity relationship studies, potentially yielding analogues with enhanced brain penetration while preserving inhibitory activity.

Ultimately, our goal is to transform BM from a devastating complication into a manageable, or even preventable, condition. This vision builds upon our findings while addressing fundamental challenges in early detection and effective treatment if early detection is not possible. By understanding how tumour cells manipulate the brain microenvironment and evolve themselves, and developing strategies to counteract these processes, we aim to disrupt the metastatic cascade before clinical manifestation—potentially sparing patients the devastating consequences of established brain metastases.

8. References

1. Bray F, Laversanne M, Sung H, et al. Global cancer statistics 2022: GLOBOCAN estimates of incidence and mortality worldwide for 36 cancers in 185 countries. *CA: A Cancer Journal for Clinicians*. 2024;74(3):229-263. doi:10.3322/caac.21834
2. Pecorino L. *Molecular Biology of Cancer: Mechanisms, Targets, and Therapeutics*. Oxford University Press; 2021.
3. Todd R, Munger K. Oncogenes. In: *eLS*. John Wiley & Sons, Ltd; 2006. doi:10.1002/9780470015902.a0006006
4. Cooper GM. Tumor Suppressor Genes. In: *The Cell: A Molecular Approach. 2nd Edition*. Sinauer Associates; 2000. Accessed September 26, 2024. https://www.ncbi.nlm.nih.gov/books/NBK9894/
5. Hanahan D, Weinberg RA. The Hallmarks of Cancer. *Cell*. 2000;100(1):57-70. doi:10.1016/S0092-8674(00)81683-9
6. Fouad YA, Aanei C. Revisiting the hallmarks of cancer. *American Journal of Cancer Research*. 2017;7(5):1016.
7. Welch DR, Hurst DR. Defining the Hallmarks of Metastasis. *Cancer Research*. 2019;79(12):3011-3027. doi:10.1158/0008-5472.CAN-19-0458
8. Hanahan D. Hallmarks of Cancer: New Dimensions. *Cancer Discov*. 2022;12(1):31-46. doi:10.1158/2159-8290.CD-21-1059
9. Hanahan D, Weinberg RA. Hallmarks of Cancer: The Next Generation. *Cell*. 2011;144(5):646-674. doi:10.1016/j.cell.2011.02.013
10. Dillekås H, Rogers MS, Straume O. Are 90% of deaths from cancer caused by metastases? *Cancer Medicine*. 2019;8(12):5574-5576. doi:10.1002/cam4.2474
11. Mani K, Deng D, Lin C, Wang M, Hsu ML, Zaorsky NG. Causes of death among people living with metastatic cancer. *Nat Commun*. 2024;15(1):1519. doi:10.1038/s41467-024-45307-x
12. Parker M, Jiang K, Rincon-Torroella J, et al. Epidemiological trends, prognostic factors, and survival outcomes of synchronous brain metastases from 2015 to 2019: a population-based study. *Neuro-Oncology Advances*. 2023;5(1):vdad015. doi:10.1093/noajnl/vdad015
13. Cagney DN, Martin AM, Catalano PJ, et al. Implications of Screening for Brain Metastases in Patients With Breast Cancer and Non–Small Cell Lung Cancer. *JAMA Oncology*. 2018;4(7):1001-1003. doi:10.1001/jamaoncol.2018.0813
14. Neal MT, Chan MD, Lucas JT, et al. Predictors of Survival, Neurologic Death, Local Failure, and Distant Failure After Gamma Knife Radiosurgery for Melanoma Brain Metastases. *World Neurosurgery*. 2014;82(6):1250-1255. doi:10.1016/j.wneu.2013.02.025
15. Banks WA. From blood–brain barrier to blood–brain interface: new opportunities for CNS drug delivery. *Nat Rev Drug Discov*. 2016;15(4):275-292. doi:10.1038/nrd.2015.21
16. Steindl A, Brunner TJ, Heimbach K, et al. Changing characteristics, treatment approaches and survival of patients with brain metastasis: data from six thousand and thirty-one individuals over an observation period of 30 years. *European Journal of Cancer*. 2022;162:170-181. doi:10.1016/j.ejca.2021.12.005
17. Kohler BA, Ward E, McCarthy BJ, et al. Annual Report to the Nation on the Status of Cancer, 1975–2007, Featuring Tumors of the Brain and Other Nervous System. *JNCI: Journal of the National Cancer Institute*. 2011;103(9):714-736. doi:10.1093/jnci/djr077
18. Miccio JA, Tian Z, Mahase SS, et al. Estimating the risk of brain metastasis for patients newly diagnosed with cancer. *Commun Med*. 2024;4(1):1-12. doi:10.1038/s43856-024-00445-7
19. Cagney DN, Martin AM, Catalano PJ, et al. Incidence and prognosis of patients with brain metastases at diagnosis of systemic malignancy: a population-based study. *Neuro-Oncology*. 2017;19(11):1511-1521. doi:10.1093/neuonc/nox077
20. Lamba N, Wen PY, Aizer AA. Epidemiology of brain metastases and leptomeningeal disease. *Neuro-Oncology*. 2021;23(9):1447-1456. doi:10.1093/neuonc/noab101

21. Cancer of the Brain and Other Nervous System - Cancer Stat Facts. SEER. Accessed October 8, 2024. https://seer.cancer.gov/statfacts/html/brain.html
22. Tabor JK, Onoichenco A, Narayan V, Wernicke AG, D'Amico RS, Vojnic M. Brain metastasis screening in the molecular age. *Neurooncol Adv*. 2023;5(1):vdad080. doi:10.1093/noajnl/vdad080
23. Kuksis M, Gao Y, Tran W, et al. The incidence of brain metastases among patients with metastatic breast cancer: a systematic review and meta-analysis. *Neuro Oncol*. 2021;23(6):894-904. doi:10.1093/neuonc/noaa285
24. Didier AJ, Nandwani SV, Watkins D, et al. Patterns and trends in melanoma mortality in the United States, 1999–2020. *BMC Cancer*. 2024;24(1):790. doi:10.1186/s12885-024-12426-z
25. Berghoff AS, Schur S, Füreder LM, et al. Descriptive statistical analysis of a real life cohort of 2419 patients with brain metastases of solid cancers. *ESMO Open*. 2016;1(2):e000024. doi:10.1136/esmoopen-2015-000024
26. Habbous S, Forster K, Darling G, et al. Incidence and real-world burden of brain metastases from solid tumors and hematologic malignancies in Ontario: a population-based study. *Neuro-Oncology Advances*. 2021;3(1):vdaa178. doi:10.1093/noajnl/vdaa178
27. Martin AM, Cagney DN, Catalano PJ, et al. Brain Metastases in Newly Diagnosed Breast Cancer: A Population-Based Study. *JAMA Oncology*. 2017;3(8):1069-1077. doi:10.1001/jamaoncol.2017.0001
28. Rangachari D, Yamaguchi N, VanderLaan PA, et al. Brain metastases in patients with *EGFR*-mutated or *ALK*-rearranged non-small-cell lung cancers. *Lung Cancer*. 2015;88(1):108-111. doi:10.1016/j.lungcan.2015.01.020
29. Jakob JA, Bassett RL, Ng CS, et al. NRAS mutation status is an independent prognostic factor in metastatic melanoma. *Cancer*. 2012;118(16):4014-4023. doi:10.1002/cncr.26724
30. Proescholdt M, Jünger ST, Schödel P, et al. Brain Metastases in Elderly Patients—The Role of Surgery in the Context of Systemic Treatment. *Brain Sciences*. 2021;11(1):123. doi:10.3390/brainsci11010123
31. Davis LE, Shalin SC, Tackett AJ. Current state of melanoma diagnosis and treatment. *Cancer Biol Ther*. 2019;20(11):1366-1379. doi:10.1080/15384047.2019.1640032
32. Wang Y, Lian B, Si L, et al. Cumulative incidence and risk factors of brain metastasis for acral and mucosal melanoma patients with stages I–III. *European Journal of Cancer*. 2022;175:196-203. doi:10.1016/j.ejca.2022.08.008
33. Melanoma of the Skin - Cancer Stat Facts. SEER. Accessed January 23, 2025. https://seer.cancer.gov/statfacts/html/melan.html
34. Navada S, Lai P, Schwartz AG, Kalemkerian GP. Temporal trends in small cell lung cancer: Analysis of the national Surveillance, Epidemiology, and End-Results (SEER) database. *JCO*. 2006;24(18_suppl):7082-7082. doi:10.1200/jco.2006.24.18_suppl.7082
35. Griesinger F, Roeper J, Pöttgen C, Willborn KC, Eberhardt WE. Brain metastases in ALK-positive NSCLC – time to adjust current treatment algorithms. *Oncotarget*. 2018;9(80):35181. doi:10.18632/oncotarget.26073
36. Tomasini P, Serdjebi C, Khobta N, et al. EGFR and KRAS Mutations Predict the Incidence and Outcome of Brain Metastases in Non-Small Cell Lung Cancer. *Int J Mol Sci*. 2016;17(12):2132. doi:10.3390/ijms17122132
37. Steindl A, Kreminger J, Moor E, et al. 363O Clinical characterization of a real-life cohort of 6001 patients with brain metastases from solid cancers treated between 1986-2020. *Annals of Oncology*. 2020;31:S397. doi:10.1016/j.annonc.2020.08.472
38. Sperduto PW, Jiang W, Brown PD, et al. The Prognostic Value of BRAF, C-KIT, and NRAS Mutations in Melanoma Patients With Brain Metastases. *Int J Radiat Oncol Biol Phys*. 2017;98(5):1069-1077. doi:10.1016/j.ijrobp.2017.03.030
39. Zhang W, Liu HT. MAPK signal pathways in the regulation of cell proliferation in mammalian cells. *Cell Res*. 2002;12(1):9-18. doi:10.1038/sj.cr.7290105
40. Proietti I, Skroza N, Bernardini N, et al. Mechanisms of Acquired BRAF Inhibitor Resistance in Melanoma: A Systematic Review. *Cancers*. 2020;12(10):2801. doi:10.3390/cancers12102801

41. Ascierto PA, Kirkwood JM, Grob JJ, et al. The role of BRAF V600 mutation in melanoma. *J Transl Med*. 2012;10(1):85. doi:10.1186/1479-5876-10-85
42. He Y, Sun MM, Zhang GG, et al. Targeting PI3K/Akt signal transduction for cancer therapy. *Sig Transduct Target Ther*. 2021;6(1):1-17. doi:10.1038/s41392-021-00828-5
43. Bucheit AD, Chen G, Siroy A, et al. Complete Loss of PTEN Protein Expression Correlates with Shorter Time to Brain Metastasis and Survival in Stage IIIB/C Melanoma Patients with BRAFV600 Mutations. *Clinical Cancer Research*. 2014;20(21):5527-5536. doi:10.1158/1078-0432.CCR-14-1027
44. Aksamitiene E, Kiyatkin A, Kholodenko BN. Cross-talk between mitogenic Ras/MAPK and survival PI3K/Akt pathways: a fine balance. *Biochem Soc Trans*. 2012;40(1):139-146. doi:10.1042/BST20110609
45. Hu X, Li J, Fu M, Zhao X, Wang W. The JAK/STAT signaling pathway: from bench to clinic. *Sig Transduct Target Ther*. 2021;6(1):1-33. doi:10.1038/s41392-021-00791-1
46. Santos G da C, Shepherd FA, Tsao MS. EGFR Mutations and Lung Cancer. *Annual Review of Pathology: Mechanisms of Disease*. 2011;6(Volume 6, 2011):49-69. doi:10.1146/annurev-pathol-011110-130206
47. Shreenivas A, Janku F, Gouda MA, et al. ALK fusions in the pan-cancer setting: another tumor-agnostic target? *npj Precis Onc*. 2023;7(1):1-20. doi:10.1038/s41698-023-00449-x
48. Computed Tomography (CT). National Institute of Biomedical Imaging and Bioengineering. Accessed October 15, 2024. https://www.nibib.nih.gov/science-education/science-topics/computed-tomography-ct
49. Magnetic Resonance Imaging (MRI). National Institute of Biomedical Imaging and Bioengineering. Accessed October 15, 2024. https://www.nibib.nih.gov/science-education/science-topics/magnetic-resonance-imaging-mri
50. Soffietti R, Abacioglu U, Baumert B, et al. Diagnosis and treatment of brain metastases from solid tumors: guidelines from the European Association of Neuro-Oncology (EANO). *Neuro-Oncology*. 2017;19(2):162-174. doi:10.1093/neuonc/now241
51. Kaufmann TJ, Smits M, Boxerman J, et al. Consensus recommendations for a standardized brain tumor imaging protocol for clinical trials in brain metastases. *Neuro-Oncology*. 2020;22(6):757-772. doi:10.1093/neuonc/noaa030
52. Delattre JY, Krol G, Thaler HT, Posner JB. Distribution of Brain Metastases. *Archives of Neurology*. 1988;45(7):741-744. doi:10.1001/archneur.1988.00520310047016
53. Derks SHAE, van der Veldt AAM, Smits M. Brain metastases: the role of clinical imaging. *British Journal of Radiology*. 2022;95(1130):20210944. doi:10.1259/bjr.20210944
54. Bonert M, Berzins A, Begum H, et al. Neuroanatomical location of brain metastases from solid tumours based on pathology: An analysis of 511 patients with a comparison to the provided clinical history. *PLoS One*. 2023;18(11):e0294154. doi:10.1371/journal.pone.0294154
55. Fink KR, Fink JR. Imaging of brain metastases. *Surg Neurol Int*. 2013;4(Suppl 4):S209-S219. doi:10.4103/2152-7806.111298
56. Schroeder T, Bittrich P, Kuhne JF, et al. Mapping distribution of brain metastases: does the primary tumor matter? *J Neurooncol*. 2020;147(1):229-235. doi:10.1007/s11060-020-03419-6
57. POPE WB. Brain metastases: neuroimaging. *Handb Clin Neurol*. 2018;149:89-112. doi:10.1016/B978-0-12-811161-1.00007-4
58. Chen XZ, Yin XM, Ai L, Chen Q, Li SW, Dai JP. Differentiation between Brain Glioblastoma Multiforme and Solitary Metastasis: Qualitative and Quantitative Analysis Based on Routine MR Imaging. *American Journal of Neuroradiology*. 2012;33(10):1907-1912. doi:10.3174/ajnr.A3106
59. Lee S, Bae H, Yun U, Hwang I, Kim SM. Atypical Hemorrhagic Brain Metastases Mimicking Cerebral Microbleeds. *J Neurocrit Care*. 2017;10(2):129-131. doi:10.18700/jnc.170019
60. Rhun EL, Guckenberger M, Smits M, et al. EANO–ESMO Clinical Practice Guidelines for diagnosis, treatment and follow-up of patients with brain metastasis from solid tumours☆. *Annals of Oncology*. 2021;32(11):1332-1347. doi:10.1016/j.annonc.2021.07.016

61. Vogelbaum MA, Brown PD, Messersmith H, et al. Treatment for Brain Metastases: ASCO-SNO-ASTRO Guideline. *Neuro-Oncology*. 2022;24(3):331-357. doi:10.1093/neuonc/noab262
62. Schackert G, Schmiedel K, Lindner C, Leimert M, Kirsch M. Surgery of recurrent brain metastases: retrospective analysis of 67 patients. *Acta Neurochir*. 2013;155(10):1823-1832. doi:10.1007/s00701-013-1821-y
63. Brenner AW, Patel AJ. Review of Current Principles of the Diagnosis and Management of Brain Metastases. *Front Oncol*. 2022;12. doi:10.3389/fonc.2022.857622
64. Nieder C, Andratschke NH, Grosu AL. Brain Metastases: Is There Still a Role for Whole-Brain Radiation Therapy? *Semin Radiat Oncol*. 2023;33(2):129-138. doi:10.1016/j.semradonc.2023.01.005
65. Soliman H, Das S, Larson DA, Sahgal A. Stereotactic radiosurgery (SRS) in the modern management of patients with brain metastases. *Oncotarget*. 2016;7(11):12318-12330. doi:10.18632/oncotarget.7131
66. Chang EL, Wefel JS, Hess KR, et al. Neurocognition in patients with brain metastases treated with radiosurgery or radiosurgery plus whole-brain irradiation: a randomised controlled trial. *The Lancet Oncology*. 2009;10(11):1037-1044. doi:10.1016/S1470-2045(09)70263-3
67. Pandit R, Chen L, Götz J. The blood-brain barrier: Physiology and strategies for drug delivery. *Advanced Drug Delivery Reviews*. 2020;165-166:1-14. doi:10.1016/j.addr.2019.11.009
68. Hargadon KM, Johnson CE, Williams CJ. Immune checkpoint blockade therapy for cancer: An overview of FDA-approved immune checkpoint inhibitors. *International Immunopharmacology*. 2018;62:29-39. doi:10.1016/j.intimp.2018.06.001
69. Tawbi HA, Forsyth PA, Hodi FS, et al. Long-term outcomes of patients with active melanoma brain metastases treated with combination nivolumab plus ipilimumab (CheckMate 204): final results of an open-label, multicentre, phase 2 study. *The Lancet Oncology*. 2021;22(12):1692-1704. doi:10.1016/S1470-2045(21)00545-3
70. Long GV, Atkinson V, Lo S, et al. Combination nivolumab and ipilimumab or nivolumab alone in melanoma brain metastases: a multicentre randomised phase 2 study. *The Lancet Oncology*. 2018;19(5):672-681. doi:10.1016/S1470-2045(18)30139-6
71. Ready NE, Audigier-Valette C, Goldman JW, et al. First-line nivolumab plus ipilimumab for metastatic non-small cell lung cancer, including patients with ECOG performance status 2 and other special populations: CheckMate 817. *J Immunother Cancer*. 2023;11(2):e006127. doi:10.1136/jitc-2022-006127
72. Nadal E, Rodriguez-Abreu D, Massuti B, et al. Updated analysis from the ATEZO-BRAIN trial: Atezolizumab plus carboplatin and pemetrexed in patients with advanced nonsquamous non–small cell lung cancer with untreated brain metastases. *JCO*. 2022;40(16_suppl):9010-9010. doi:10.1200/JCO.2022.40.16_suppl.9010
73. Tawbi HA, Forsyth PA, Hodi FS, et al. Safety and efficacy of the combination of nivolumab plus ipilimumab in patients with melanoma and asymptomatic or symptomatic brain metastases (CheckMate 204). *Neuro-Oncology*. 2021;23(11):1961-1973. doi:10.1093/neuonc/noab094
74. Langen AJ de, Johnson ML, Mazieres J, et al. Sotorasib versus docetaxel for previously treated non-small-cell lung cancer with KRASG12C mutation: a randomised, open-label, phase 3 trial. *The Lancet*. 2023;401(10378):733-746. doi:10.1016/S0140-6736(23)00221-0
75. Jänne PA, Riely GJ, Gadgeel SM, et al. Adagrasib in Non–Small-Cell Lung Cancer Harboring a KRASG12C Mutation. *New England Journal of Medicine*. 2022;387(2):120-131. doi:10.1056/NEJMoa2204619
76. Jaiyesimi IA, Leighl NB, Ismaila N, et al. Therapy for Stage IV Non–Small Cell Lung Cancer With Driver Alterations: ASCO Living Guideline, Version 2023.3. *JCO*. 2024;42(11):e1-e22. doi:10.1200/JCO.23.02744
77. Zhu W, Zhou L, Qian JQ, Qiu TZ, Shu YQ, Liu P. Temozolomide for treatment of brain metastases: A review of 21 clinical trials. *World J Clin Oncol*. 2014;5(1):19-27. doi:10.5306/wjco.v5.i1.19

78. He G, Xiao X, Zou M, Zhang C, Xia S. Pemetrexed/cisplatin as first-line chemotherapy for advanced lung cancer with brain metastases: A case report and literature review. *Medicine*. 2016;95(32):e4401. doi:10.1097/MD.0000000000004401
79. Winkler F. Anti-angiogenics in Brain Metastases: Perspectives and Experiences. In: Marmé D, ed. *Tumor Angiogenesis: A Key Target for Cancer Therapy*. Springer International Publishing; 2019:627-636. doi:10.1007/978-3-319-33673-2_49
80. Besse B, Lasserre SF, Compton P, Huang J, Augustus S, Rohr UP. Bevacizumab Safety in Patients with Central Nervous System Metastases. *Clinical Cancer Research*. 2010;16(1):269-278. doi:10.1158/1078-0432.CCR-09-2439
81. Qingdao Central Hospital. *Osimertinib Combined With Bevacizumab in Patients With Brain Metastasis Epidermal Growth Factor Receptor (EGFR) Mutation Positive Metastatic Non-Small Cell Lung Cancer*. clinicaltrials.gov; 2023. Accessed January 23, 2025. https://clinicaltrials.gov/study/NCT05104281
82. M.D. Anderson Cancer Center. *Phase II Study of BEvacizumab (Avastin) in Combination With Atezolizumab or Atezolizumab (Tencentriq) and Cobimetinib (Cotellic) in Patients With Untreated Melanoma Brain Metastases (TACo-BEAT-MBM)*. clinicaltrials.gov; 2024. Accessed January 23, 2025. https://clinicaltrials.gov/study/NCT03175432
83. Kluger H. *A Phase 2 Trial of Pembrolizumab Plus Bevacizumab in Patients With Metastatic Melanoma or Non-Small Cell Lung Cancer With Untreated Brain Metastases*. clinicaltrials.gov; 2024. Accessed January 23, 2025. https://clinicaltrials.gov/study/NCT02681549
84. Amaral T, Niessner H, Sinnberg T, et al. An open-label, single-arm, phase II trial of buparlisib in patients with melanoma brain metastases not eligible for surgery or radiosurgery—the BUMPER study. *Neurooncol Adv*. 2020;2(1):vdaa140. doi:10.1093/noajnl/vdaa140
85. Adjei AA, Bennouna J, Leighl NB, et al. Safety and efficacy of buparlisib (BKM120) and chemotherapy in advanced, squamous non-small cell lung cancer (sqNSCLC): Results from the phase Ib/II BASALT-2 and BASALT-3 studies. *JCO*. 2016;34(15_suppl):e20522-e20522. doi:10.1200/JCO.2016.34.15_suppl.e20522
86. Aasen SN, Parajuli H, Hoang T, et al. Effective Treatment of Metastatic Melanoma by Combining MAPK and PI3K Signaling Pathway Inhibitors. *Int J Mol Sci*. 2019;20(17):4235. doi:10.3390/ijms20174235
87. Leo AD, Johnston S, Lee KS, et al. Buparlisib plus fulvestrant in postmenopausal women with hormone-receptor-positive, HER2-negative, advanced breast cancer progressing on or after mTOR inhibition (BELLE-3): a randomised, double-blind, placebo-controlled, phase 3 trial. *The Lancet Oncology*. 2018;19(1):87-100. doi:10.1016/S1470-2045(17)30688-5
88. Redmer T, Schumann E, Peters K, et al. MET receptor serves as a promising target in melanoma brain metastases. *Acta Neuropathol*. 2024;147(1):44. doi:10.1007/s00401-024-02694-1
89. Stella GM, Corino A, Berzero G, Kolling S, Filippi AR, Benvenuti S. Brain Metastases from Lung Cancer: Is MET an Actionable Target? *Cancers*. 2019;11(3):271. doi:10.3390/cancers11030271
90. Fedorenko IV, Paraiso KHT, Smalley KSM. Acquired and intrinsic BRAF inhibitor resistance in *BRAF* V600E mutant melanoma. *Biochemical Pharmacology*. 2011;82(3):201-209. doi:10.1016/j.bcp.2011.05.015
91. Villanueva J, Vultur A, Lee JT, et al. Acquired Resistance to BRAF Inhibitors Mediated by a RAF Kinase Switch in Melanoma Can Be Overcome by Cotargeting MEK and IGF-1R/PI3K. *Cancer Cell*. 2010;18(6):683-695. doi:10.1016/j.ccr.2010.11.023
92. Nazarian R, Shi H, Wang Q, et al. Melanomas acquire resistance to B-RAF(V600E) inhibition by RTK or N-RAS upregulation. *Nature*. 2010;468(7326):973-977. doi:10.1038/nature09626
93. Whittaker S, Kirk R, Hayward R, et al. Gatekeeper Mutations Mediate Resistance to BRAF-Targeted Therapies. *Science Translational Medicine*. 2010;2(35):35ra41-35ra41. doi:10.1126/scitranslmed.3000758

94. Mehlman C, Cadranel J, Rousseau-Bussac G, et al. Resistance mechanisms to osimertinib in EGFR-mutated advanced non-small-cell lung cancer: A multicentric retrospective French study. *Lung Cancer*. 2019;137:149-156. doi:10.1016/j.lungcan.2019.09.019
95. Li Y, Mao T, Wang J, et al. Toward the next generation EGFR inhibitors: an overview of osimertinib resistance mediated by EGFR mutations in non-small cell lung cancer. *Cell Communication and Signaling*. 2023;21(1):71. doi:10.1186/s12964-023-01082-8
96. Oxnard GR, Hu Y, Mileham KF, et al. Assessment of Resistance Mechanisms and Clinical Implications in Patients With EGFR T790M–Positive Lung Cancer and Acquired Resistance to Osimertinib. *JAMA Oncology*. 2018;4(11):1527-1534. doi:10.1001/jamaoncol.2018.2969
97. Arvanitis CD, Ferraro GB, Jain RK. The blood–brain barrier and blood–tumour barrier in brain tumours and metastases. *Nat Rev Cancer*. 2020;20(1):26-41. doi:10.1038/s41568-019-0205-x
98. Ayloo S, Gu C. Transcytosis at the blood–brain barrier. *Current Opinion in Neurobiology*. 2019;57:32-38. doi:10.1016/j.conb.2018.12.014
99. Armulik A, Genové G, Mäe M, et al. Pericytes regulate the blood-brain barrier. *Nature*. 2010;468(7323):557-561. doi:10.1038/nature09522
100. Ben-Zvi A, Lacoste B, Kur E, et al. Mfsd2a is critical for the formation and function of the blood-brain barrier. *Nature*. 2014;509(7501):507-511. doi:10.1038/nature13324
101. Giaume C, Koulakoff A, Roux L, Holcman D, Rouach N. Astroglial networks: a step further in neuroglial and gliovascular interactions. *Nat Rev Neurosci*. 2010;11(2):87-99. doi:10.1038/nrn2757
102. Alvarez JI, Katayama T, Prat A. Glial influence on the Blood Brain Barrier. *Glia*. 2013;61(12):1939-1958. doi:10.1002/glia.22575
103. Syed NI. Neuron: Structure/Function, Cellular/Molecular. In: Binder MD, Hirokawa N, Windhorst U, eds. *Encyclopedia of Neuroscience*. Springer; 2009:2764-2768. doi:10.1007/978-3-540-29678-2_3907
104. Deng S, Gan L, Liu C, et al. Roles of Ependymal Cells in the Physiology and Pathology of the Central Nervous System. *Aging Dis*. 2023;14(2):468-483. doi:10.14336/AD.2022.0826-1
105. Bradl M, Lassmann H. Oligodendrocytes: biology and pathology. *Acta Neuropathol*. 2010;119(1):37-53. doi:10.1007/s00401-009-0601-5
106. Sofroniew MV, Vinters HV. Astrocytes: biology and pathology. *Acta Neuropathol*. 2010;119(1):7-35. doi:10.1007/s00401-009-0619-8
107. Escartin C, Galea E, Lakatos A, et al. Reactive astrocyte nomenclature, definitions, and future directions. *Nat Neurosci*. 2021;24(3):312-325. doi:10.1038/s41593-020-00783-4
108. Liddelow SA, Barres BA. Reactive Astrocytes: Production, Function, and Therapeutic Potential. *Immunity*. 2017;46(6):957-967. doi:10.1016/j.immuni.2017.06.006
109. Paolicelli RC, Bolasco G, Pagani F, et al. Synaptic Pruning by Microglia Is Necessary for Normal Brain Development. *Science*. 2011;333(6048):1456-1458. doi:10.1126/science.1202529
110. Gao C, Jiang J, Tan Y, Chen S. Microglia in neurodegenerative diseases: mechanism and potential therapeutic targets. *Sig Transduct Target Ther*. 2023;8(1):1-37. doi:10.1038/s41392-023-01588-0
111. Liddelow SA, Guttenplan KA, Clarke LE, et al. Neurotoxic reactive astrocytes are induced by activated microglia. *Nature*. 2017;541(7638):481-487. doi:10.1038/nature21029
112. Davalos D, Grutzendler J, Yang G, et al. ATP mediates rapid microglial response to local brain injury in vivo. *Nat Neurosci*. 2005;8(6):752-758. doi:10.1038/nn1472
113. Paolicelli RC, Sierra A, Stevens B, et al. Microglia states and nomenclature: A field at its crossroads. *Neuron*. 2022;110(21):3458-3483. doi:10.1016/j.neuron.2022.10.020
114. O'Callaghan JP, Sriram K, Miller DB. Defining "Neuroinflammation." *Annals of the New York Academy of Sciences*. 2008;1139(1):318-330. doi:10.1196/annals.1432.032
115. Louveau A, Smirnov I, Keyes TJ, et al. Structural and functional features of central nervous system lymphatic vessels. *Nature*. 2015;523(7560):337-341. doi:10.1038/nature14432
116. Croese T, Castellani G, Schwartz M. Immune cell compartmentalization for brain surveillance and protection. *Nat Immunol*. 2021;22(9):1083-1092. doi:10.1038/s41590-021-00994-2

117. Strik HM, Stoll M, Meyermann R. Immune Cell Infiltration of Intrinsic and Metastatic Intracranial Tumours. *Anticancer Research*. 2004;24(1):37-42.
118. Fares J, Fares MY, Khachfe HH, Salhab HA, Fares Y. Molecular principles of metastasis: a hallmark of cancer revisited. *Sig Transduct Target Ther*. 2020;5(1):1-17. doi:10.1038/s41392-020-0134-x
119. Castaneda M, den Hollander P, Kuburich NA, Rosen JM, Mani SA. Mechanisms of cancer metastasis. *Semin Cancer Biol*. 2022;87:17-31. doi:10.1016/j.semcancer.2022.10.006
120. Harper KL, Sosa MS, Entenberg D, et al. Mechanism of early dissemination and metastasis in Her2+ mammary cancer. *Nature*. 2016;540(7634):588-592. doi:10.1038/nature20609
121. Nieto MA, Huang RYJ, Jackson RA, Thiery JP. EMT: 2016. *Cell*. 2016;166(1):21-45. doi:10.1016/j.cell.2016.06.028
122. Batlle E, Sancho E, Francí C, et al. The transcription factor Snail is a repressor of E-cadherin gene expression in epithelial tumour cells. *Nat Cell Biol*. 2000;2(2):84-89. doi:10.1038/35000034
123. Bolós V, Peinado H, Pérez-Moreno MA, Fraga MF, Esteller M, Cano A. The transcription factor Slug represses E-cadherin expression and induces epithelial to mesenchymal transitions: a comparison with Snail and E47 repressors. *Journal of Cell Science*. 2003;116(3):499-511. doi:10.1242/jcs.00224
124. Yang J, Mani SA, Donaher JL, et al. Twist, a Master Regulator of Morphogenesis, Plays an Essential Role in Tumor Metastasis. *Cell*. 2004;117(7):927-939. doi:10.1016/j.cell.2004.06.006
125. Mani SA, Yang J, Brooks M, et al. Mesenchyme Forkhead 1 (FOXC2) plays a key role in metastasis and is associated with aggressive basal-like breast cancers. *Proceedings of the National Academy of Sciences*. 2007;104(24):10069-10074. doi:10.1073/pnas.0703900104
126. Thiery JP, Acloque H, Huang RYJ, Nieto MA. Epithelial-Mesenchymal Transitions in Development and Disease. *Cell*. 2009;139(5):871-890. doi:10.1016/j.cell.2009.11.007
127. Thiery JP, Sleeman JP. Complex networks orchestrate epithelial–mesenchymal transitions. *Nat Rev Mol Cell Biol*. 2006;7(2):131-142. doi:10.1038/nrm1835
128. Castaneda M, den Hollander P, Kuburich NA, Rosen JM, Mani SA. Mechanisms of cancer metastasis. *Seminars in Cancer Biology*. 2022;87:17-31. doi:10.1016/j.semcancer.2022.10.006
129. Kröger C, Afeyan A, Mraz J, et al. Acquisition of a hybrid E/M state is essential for tumorigenicity of basal breast cancer cells. *Proceedings of the National Academy of Sciences*. 2019;116(15):7353-7362. doi:10.1073/pnas.1812876116
130. Pastushenko I, Brisebarre A, Sifrim A, et al. Identification of the tumour transition states occurring during EMT. *Nature*. 2018;556(7702):463-468. doi:10.1038/s41586-018-0040-3
131. Lintz M, Muñoz A, Reinhart-King CA. The Mechanics of Single Cell and Collective Migration of Tumor Cells. *Journal of Biomechanical Engineering*. 2017;139(021005). doi:10.1115/1.4035121
132. Harada T, Swift J, Irianto J, et al. Nuclear lamin stiffness is a barrier to 3D migration, but softness can limit survival. *Journal of Cell Biology*. 2014;204(5):669-682. doi:10.1083/jcb.201308029
133. Mendez MG, Restle D, Janmey PA. Vimentin Enhances Cell Elastic Behavior and Protects against Compressive Stress. *Biophysical Journal*. 2014;107(2):314-323. doi:10.1016/j.bpj.2014.04.050
134. Yoshida K, Fujikawa T, Tanabe A, Sakurai K. Quantitative analysis of distribution and fate of human lung cancer emboli labeled with 125I-5-iodo-2′-deoxyuridine in nude mice. *Surg Today*. 1993;23(11):979-983. doi:10.1007/BF00308973
135. Labuschagne CF, Cheung EC, Blagih J, Domart MC, Vousden KH. Cell Clustering Promotes a Metabolic Switch that Supports Metastatic Colonization. *Cell Metabolism*. 2019;30(4):720-734.e5. doi:10.1016/j.cmet.2019.07.014
136. Kopp HG, Placke T, Salih HR. Platelet-derived transforming growth factor-beta down-regulates NKG2D thereby inhibiting natural killer cell antitumor reactivity. *Cancer Res*. 2009;69(19):7775-7783. doi:10.1158/0008-5472.CAN-09-2123
137. Fan J, Fu BM. Quantification of Malignant Breast Cancer Cell MDA-MB-231 Transmigration Across Brain and Lung Microvascular Endothelium. *Ann Biomed Eng*. 2016;44(7):2189-2201. doi:10.1007/s10439-015-1517-y

138. Alsabbagh R, Ahmed M, Alqudah MAY, Hamoudi R, Harati R. Insights into the Molecular Mechanisms Mediating Extravasation in Brain Metastasis of Breast Cancer, Melanoma, and Lung Cancer. *Cancers*. 2023;15(8):2258. doi:10.3390/cancers15082258
139. Peinado H, Zhang H, Matei IR, et al. Pre-metastatic niches: organ-specific homes for metastases. *Nat Rev Cancer*. 2017;17(5):302-317. doi:10.1038/nrc.2017.6
140. Geissler M, Jia W, Kiraz EN, et al. The Brain Pre-Metastatic Niche: Biological and Technical Advancements. *Int J Mol Sci*. 2023;24(12):10055. doi:10.3390/ijms241210055
141. Théry C, Witwer KW, Aikawa E, et al. Minimal information for studies of extracellular vesicles 2018 (MISEV2018): a position statement of the International Society for Extracellular Vesicles and update of the MISEV2014 guidelines. *J Extracell Vesicles*. 2018;7(1):1535750. doi:10.1080/20013078.2018.1535750
142. Welsh JA, Goberdhan DCI, O'Driscoll L, et al. Minimal information for studies of extracellular vesicles (MISEV2023): From basic to advanced approaches. *J Extracell Vesicles*. 2024;13(2):e12404. doi:10.1002/jev2.12404
143. Colombo M, Raposo G, Théry C. Biogenesis, Secretion, and Intercellular Interactions of Exosomes and Other Extracellular Vesicles. *Annual Review of Cell and Developmental Biology*. 2014;30(Volume 30, 2014):255-289. doi:10.1146/annurev-cellbio-101512-122326
144. Abels ER, Breakefield XO. Introduction to Extracellular Vesicles: Biogenesis, RNA Cargo Selection, Content, Release, and Uptake. *Cell Mol Neurobiol*. 2016;36(3):301-312. doi:10.1007/s10571-016-0366-z
145. van Niel G, D'Angelo G, Raposo G. Shedding light on the cell biology of extracellular vesicles. *Nat Rev Mol Cell Biol*. 2018;19(4):213-228. doi:10.1038/nrm.2017.125
146. Reiner AT, Witwer KW, van Balkom BWM, et al. Concise Review: Developing Best-Practice Models for the Therapeutic Use of Extracellular Vesicles. *Stem Cells Translational Medicine*. 2017;6(8):1730-1739. doi:10.1002/sctm.17-0055
147. Guerreiro EM, Øvstebø R, Thiede B, Costea DE, Søland TM, Galtung HK. Cancer cell line-specific protein profiles in extracellular vesicles identified by proteomics. *PLOS ONE*. 2020;15(9):e0238591. doi:10.1371/journal.pone.0238591
148. Xu R, Rai A, Chen M, Suwakulsiri W, Greening DW, Simpson RJ. Extracellular vesicles in cancer — implications for future improvements in cancer care. *Nat Rev Clin Oncol*. 2018;15(10):617-638. doi:10.1038/s41571-018-0036-9
149. Skotland T, Sagini K, Sandvig K, Llorente A. An emerging focus on lipids in extracellular vesicles. *Advanced Drug Delivery Reviews*. 2020;159:308-321. doi:10.1016/j.addr.2020.03.002
150. Balaj L, Lessard R, Dai L, et al. Tumour microvesicles contain retrotransposon elements and amplified oncogene sequences. *Nat Commun*. 2011;2(1):180. doi:10.1038/ncomms1180
151. Elzanowska J, Semira C, Costa-Silva B. DNA in extracellular vesicles: biological and clinical aspects. *Mol Oncol*. 2021;15(6):1701-1714. doi:10.1002/1878-0261.12777
152. Liu T, Zhang Q, Zhang J, et al. EVmiRNA: a database of miRNA profiling in extracellular vesicles. *Nucleic Acids Research*. 2019;47(D1):D89-D93. doi:10.1093/nar/gky985
153. Friedman RC, Farh KKH, Burge CB, Bartel DP. Most mammalian mRNAs are conserved targets of microRNAs. *Genome Res*. 2009;19(1):92-105. doi:10.1101/gr.082701.108
154. Kinoshita T, Yip KW, Spence T, Liu FF. MicroRNAs in extracellular vesicles: potential cancer biomarkers. *J Hum Genet*. 2017;62(1):67-74. doi:10.1038/jhg.2016.87
155. Tkach M, Théry C. Communication by Extracellular Vesicles: Where We Are and Where We Need to Go. *Cell*. 2016;164(6):1226-1232. doi:10.1016/j.cell.2016.01.043
156. Lattmann E, Levesque MP. The Role of Extracellular Vesicles in Melanoma Progression. *Cancers*. 2022;14(13):3086. doi:10.3390/cancers14133086
157. Li J, Lu S, Chen F, Zhu H. Unveiling the hidden role of extracellular vesicles in brain metastases: a comprehensive review. *Front Immunol*. 2024;15. doi:10.3389/fimmu.2024.1388574

158. Meneses KM, Pandya P, Lindemann JA, et al. RAB27B Drives a Cancer Stem Cell Phenotype in NSCLC Cells Through Enhanced Extracellular Vesicle Secretion. *Cancer Research Communications*. 2023;3(4):607-620. doi:10.1158/2767-9764.CRC-22-0425
159. Hanelova K, Raudenska M, Kratochvilova M, et al. Autophagy modulators influence the content of important signalling molecules in PS-positive extracellular vesicles. *Cell Commun Signal*. 2023;21(1):120. doi:10.1186/s12964-023-01126-z
160. Hoshino A, Costa-Silva B, Shen TL, et al. Tumour exosome integrins determine organotropic metastasis. *Nature*. 2015;527(7578):329-335. doi:10.1038/nature15756
161. Peinado H, Alečković M, Lavotshkin S, et al. Melanoma exosomes educate bone marrow progenitor cells toward a pro-metastatic phenotype through MET. *Nat Med*. 2012;18(6):883-891. doi:10.1038/nm.2753
162. Hsu YL, Hung JY, Chang WA, et al. Hypoxic lung cancer-secreted exosomal miR-23a increased angiogenesis and vascular permeability by targeting prolyl hydroxylase and tight junction protein ZO-1. *Oncogene*. 2017;36(34):4929-4942. doi:10.1038/onc.2017.105
163. Wieckowski EU, Visus C, Szajnik M, Szczepanski MJ, Storkus WJ, Whiteside TL. Tumor-Derived Microvesicles Promote Regulatory T Cell Expansion and Induce Apoptosis in Tumor-Reactive Activated CD8+ T Lymphocytes1. *The Journal of Immunology*. 2009;183(6):3720-3730. doi:10.4049/jimmunol.0900970
164. Liu C, Yu S, Zinn K, et al. Murine mammary carcinoma exosomes promote tumor growth by suppression of NK cell function. *J Immunol*. 2006;176(3):1375-1385. doi:10.4049/jimmunol.176.3.1375
165. Webber JP, Spary LK, Sanders AJ, et al. Differentiation of tumour-promoting stromal myofibroblasts by cancer exosomes. *Oncogene*. 2015;34(3):290-302. doi:10.1038/onc.2013.560
166. Ahmadi M, Hassanpour M, Rezaie J. Engineered extracellular vesicles: A novel platform for cancer combination therapy and cancer immunotherapy. *Life Sciences*. 2022;308:120935. doi:10.1016/j.lfs.2022.120935
167. Paget S. THE DISTRIBUTION OF SECONDARY GROWTHS IN CANCER OF THE BREAST. *The Lancet*. 1889;133(3421):571-573. doi:10.1016/S0140-6736(00)49915-0
168. Ewing J. Neoplastic Diseases, A Treatise on Tumors. *Can Med Assoc J*. 1924;14(5):466.
169. Kaplan RN, Riba RD, Zacharoulis S, et al. VEGFR1-positive haematopoietic bone marrow progenitors initiate the pre-metastatic niche. *Nature*. 2005;438(7069):820-827. doi:10.1038/nature04186
170. Fidler IJ, Nicolson GL. Organ selectivity for implantation survival and growth of B16 melanoma variant tumor lines. *J Natl Cancer Inst*. 1976;57(5):1199-1202. doi:10.1093/jnci/57.5.1199
171. Huang Y, Song N, Ding Y, et al. Pulmonary vascular destabilization in the premetastatic phase facilitates lung metastasis. *Cancer Res*. 2009;69(19):7529-7537. doi:10.1158/0008-5472.CAN-08-4382
172. Hiratsuka S, Goel S, Kamoun WS, et al. Endothelial focal adhesion kinase mediates cancer cell homing to discrete regions of the lungs via E-selectin up-regulation. *Proc Natl Acad Sci U S A*. 2011;108(9):3725-3730. doi:10.1073/pnas.1100446108
173. Maru Y. The lung metastatic niche. *J Mol Med*. 2015;93(11):1185-1192. doi:10.1007/s00109-015-1355-2
174. Gillot L, Baudin L, Rouaud L, Kridelka F, Noël A. The pre-metastatic niche in lymph nodes: formation and characteristics. *Cell Mol Life Sci*. 2021;78(16):5987-6002. doi:10.1007/s00018-021-03873-z
175. Krüger A. Premetastatic niche formation in the liver: emerging mechanisms and mouse models. *J Mol Med*. 2015;93(11):1193-1201. doi:10.1007/s00109-015-1342-7
176. Sleeman JP. The lymph node pre-metastatic niche. *J Mol Med (Berl)*. 2015;93(11):1173-1184. doi:10.1007/s00109-015-1351-6
177. Ren G, Esposito M, Kang Y. Bone metastasis and the metastatic niche. *J Mol Med (Berl)*. 2015;93(11):1203-1212. doi:10.1007/s00109-015-1329-4

178. Tominaga N, Kosaka N, Ono M, et al. Brain metastatic cancer cells release microRNA-181c-containing extracellular vesicles capable of destructing blood–brain barrier. *Nat Commun*. 2015;6(1):6716. doi:10.1038/ncomms7716
179. Zhou W, Fong MY, Min Y, et al. Cancer-Secreted miR-105 Destroys Vascular Endothelial Barriers to Promote Metastasis. *Cancer Cell*. 2014;25(4):501-515. doi:10.1016/j.ccr.2014.03.007
180. Wu D, Deng S, Li L, et al. TGF-β1-mediated exosomal lnc-MMP2-2 increases blood–brain barrier permeability via the miRNA-1207-5p/EPB41L5 axis to promote non-small cell lung cancer brain metastasis. *Cell Death Dis*. 2021;12(8):721. doi:10.1038/s41419-021-04004-z
181. Robador JR, Feinauer MJ, Schneider SW, et al. Involvement of platelet-derived VWF in metastatic growth of melanoma in the brain. *Neuro-Oncology Advances*. 2021;3(1):vdab175. doi:10.1093/noajnl/vdab175
182. Soto MS, Serres S, Anthony DC, Sibson NR. Functional role of endothelial adhesion molecules in the early stages of brain metastasis. *Neuro-Oncology*. 2014;16(4):540-551. doi:10.1093/neuonc/not222
183. Doron H, Pukrop T, Erez N. A Blazing Landscape: Neuroinflammation Shapes Brain Metastasis. *Cancer Research*. 2019;79(3):423-436. doi:10.1158/0008-5472.CAN-18-1805
184. Schwartz H, Blacher E, Amer M, et al. Incipient Melanoma Brain Metastases Instigate Astrogliosis and Neuroinflammation. *Cancer Research*. 2016;76(15):4359-4371. doi:10.1158/0008-5472.CAN-16-0485
185. Ye L, Wu Y, Zhou J, Xie M, Zhang Z, Su C. Influence of Exosomes on Astrocytes in the Pre-Metastatic Niche of Lung Cancer Brain Metastases. *Biological Procedures Online*. 2023;25(1):5. doi:10.1186/s12575-023-00192-4
186. Elias EG, Hasskamp JH, Sharma BK. Cytokines and Growth Factors Expressed by Human Cutaneous Melanoma. *Cancers*. 2010;2(2):794-808. doi:10.3390/cancers2020794
187. Abdul-Rahman T, Ghosh S, Badar SM, et al. The paradoxical role of cytokines and chemokines at the tumor microenvironment: a comprehensive review. *European Journal of Medical Research*. 2024;29(1):124. doi:10.1186/s40001-024-01711-z
188. Doron H, Amer M, Ershaid N, et al. Inflammatory Activation of Astrocytes Facilitates Melanoma Brain Tropism via the CXCL10-CXCR3 Signaling Axis. *Cell Reports*. 2019;28(7):1785-1798.e6. doi:10.1016/j.celrep.2019.07.033
189. Klein A, Schwartz H, Sagi-Assif O, et al. Astrocytes facilitate melanoma brain metastasis via secretion of IL-23. *The Journal of Pathology*. 2015;236(1):116-127. doi:10.1002/path.4509
190. Rodrigues G, Hoshino A, Kenific CM, et al. Tumour exosomal CEMIP protein promotes cancer cell colonization in brain metastasis. *Nat Cell Biol*. 2019;21(11):1403-1412. doi:10.1038/s41556-019-0404-4
191. Xu W, Patel N, Deng Y, Ding S, Wang T, Zhang H. Extracellular vesicle-derived LINC00482 induces microglial M2 polarization to facilitate brain metastasis of NSCLC. *Cancer Letters*. 2023;561:216146. doi:10.1016/j.canlet.2023.216146
192. Fong MY, Zhou W, Liu L, et al. Breast-cancer-secreted miR-122 reprograms glucose metabolism in premetastatic niche to promote metastasis. *Nat Cell Biol*. 2015;17(2):183-194. doi:10.1038/ncb3094
193. Sevenich L, Bowman RL, Mason SD, et al. Analysis of tumour- and stroma-supplied proteolytic networks reveals a brain-metastasis-promoting role for cathepsin S. *Nat Cell Biol*. 2014;16(9):876-888. doi:10.1038/ncb3011
194. Bos PD, Zhang XHF, Nadal C, et al. Genes that mediate breast cancer metastasis to the brain. *Nature*. 2009;459(7249):1005-1009. doi:10.1038/nature08021
195. Leenders WPJ, Küsters B, Verrijp K, et al. Antiangiogenic Therapy of Cerebral Melanoma Metastases Results in Sustained Tumor Progression via Vessel Co-Option. *Clinical Cancer Research*. 2004;10(18):6222-6230. doi:10.1158/1078-0432.CCR-04-0823
196. Valiente M, Obenauf AC, Jin X, et al. Serpins promote cancer cell survival and vascular co-option in brain metastasis. *Cell*. 2014;156(5):1002-1016. doi:10.1016/j.cell.2014.01.040

197. Lyle LT, Lockman PR, Adkins CE, et al. Alterations in Pericyte Subpopulations Are Associated with Elevated Blood-Tumor Barrier Permeability in Experimental Brain Metastasis of Breast Cancer. *Clin Cancer Res*. 2016;22(21):5287-5299. doi:10.1158/1078-0432.CCR-15-1836
198. Lockman PR, Mittapalli RK, Taskar KS, et al. Heterogeneous Blood–Tumor Barrier Permeability Determines Drug Efficacy in Experimental Brain Metastases of Breast Cancer. *Clinical Cancer Research*. 2010;16(23):5664-5678. doi:10.1158/1078-0432.CCR-10-1564
199. Nduom EK, Yang C, Merrill MJ, Zhuang Z, Lonser RR. Characterization of the blood-brain barrier of metastatic and primary malignant neoplasms. Published online August 1, 2013. doi:10.3171/2013.3.JNS122226
200. Tentori L, Lacal PM, Graziani G. Challenging resistance mechanisms to therapies for metastatic melanoma. *Trends in Pharmacological Sciences*. 2013;34(12):656-666. doi:10.1016/j.tips.2013.10.003
201. Kodack DP, Askoxylakis V, Ferraro GB, et al. The brain microenvironment mediates resistance in luminal breast cancer to PI3K inhibition through HER3 activation. *Science Translational Medicine*. 2017;9(391):eaal4682. doi:10.1126/scitranslmed.aal4682
202. Schulz M, Salamero-Boix A, Niesel K, Alekseeva T, Sevenich L. Microenvironmental Regulation of Tumor Progression and Therapeutic Response in Brain Metastasis. *Front Immunol*. 2019;10:1713. doi:10.3389/fimmu.2019.01713
203. Neman J, Termini J, Wilczynski S, et al. Human breast cancer metastases to the brain display GABAergic properties in the neural niche. *Proceedings of the National Academy of Sciences*. 2014;111(3):984-989. doi:10.1073/pnas.1322098111
204. Bjørnstad OV, Carrasco M, Finne K, et al. Global and single-cell proteomics view of the co-evolution between neural progenitors and breast cancer cells in a co-culture model. *eBioMedicine*. 2024;108. doi:10.1016/j.ebiom.2024.105325
205. Magnon C, Hall SJ, Lin J, et al. Autonomic nerve development contributes to prostate cancer progression. *Science*. 2013;341(6142):1236361. doi:10.1126/science.1236361
206. Shinonaga M, Chang CC, Suzuki N, Sato M, Kuwabara T. Immunohistological evaluation of macrophage infiltrates in brain tumors. Published online February 1, 1988. doi:10.3171/jns.1988.68.2.0259
207. Amit M, Laider-Trejo L, Shalom V, Shabtay-Orbach A, Krelin Y, Gil Z. Characterization of the melanoma brain metastatic niche in mice and humans. *Cancer Medicine*. 2013;2(2):155-163. doi:10.1002/cam4.45
208. Qiao S, Qian Y, Xu G, Luo Q, Zhang Z. Long-term characterization of activated microglia/macrophages facilitating the development of experimental brain metastasis through intravital microscopic imaging. *J Neuroinflammation*. 2019;16(1):4. doi:10.1186/s12974-018-1389-9
209. Chuang HN, van Rossum D, Sieger D, et al. Carcinoma cells misuse the host tissue damage response to invade the brain. *Glia*. 2013;61(8):1331-1346. doi:10.1002/glia.22518
210. Izraely S, Ben-Menachem S, Sagi-Assif O, et al. The metastatic microenvironment: Melanoma–microglia cross-talk promotes the malignant phenotype of melanoma cells. *International Journal of Cancer*. 2019;144(4):802-817. doi:10.1002/ijc.31745
211. Harter PN, Bernatz S, Scholz A, et al. Distribution and prognostic relevance of tumor-infiltrating lymphocytes (TILs) and PD-1/PD-L1 immune checkpoints in human brain metastases. *Oncotarget*. 2015;6(38):40836-40849.
212. Mustafa DAM, Pedrosa RMSM, Smid M, et al. T lymphocytes facilitate brain metastasis of breast cancer by inducing Guanylate-Binding Protein 1 expression. *Acta Neuropathol*. 2018;135(4):581-599. doi:10.1007/s00401-018-1806-2
213. Berghoff AS, Lassmann H, Preusser M, Höftberger R. Characterization of the inflammatory response to solid cancer metastases in the human brain. *Clin Exp Metastasis*. 2013;30(1):69-81. doi:10.1007/s10585-012-9510-4

214. Sugihara AQ, Rolle CE, Lesniak MS. Regulatory T cells actively infiltrate metastatic brain tumors. *International Journal of Oncology*. 2009;34(6):1533-1540. doi:10.3892/ijo_00000282
215. Burn L, Gutowski N, Whatmore J, Giamas G, Pranjol MZI. The role of astrocytes in brain metastasis at the interface of circulating tumour cells and the blood brain barrier. *FBL*. 2021;26(9):590-601. doi:10.52586/4969
216. Valiente M, Ahluwalia MS, Boire A, et al. The Evolving Landscape of Brain Metastasis. *Trends in Cancer*. 2018;4(3):176-196. doi:10.1016/j.trecan.2018.01.003
217. Chen Q, Boire A, Jin X, et al. Carcinoma–astrocyte gap junctions promote brain metastasis by cGAMP transfer. *Nature*. 2016;533(7604):493-498. doi:10.1038/nature18268
218. Xing F, Kobayashi A, Okuda H, et al. Reactive astrocytes promote the metastatic growth of breast cancer stem-like cells by activating Notch signalling in brain. *EMBO Molecular Medicine*. 2013;5(3):384-396. doi:10.1002/emmm.201201623
219. Lin Q, Balasubramanian K, Fan D, et al. Reactive Astrocytes Protect Melanoma Cells from Chemotherapy by Sequestering Intracellular Calcium through Gap Junction Communication Channels. *Neoplasia*. 2010;12(9):748-754. doi:10.1593/neo.10602
220. Zhang L, Zhang S, Yao J, et al. Microenvironment-induced PTEN loss by exosomal microRNA primes brain metastasis outgrowth. *Nature*. 2015;527(7576):100-104. doi:10.1038/nature15376
221. Priego N, Zhu L, Monteiro C, et al. STAT3 labels a subpopulation of reactive astrocytes required for brain metastasis. *Nat Med*. 2018;24(7):1024-1035. doi:10.1038/s41591-018-0044-4
222. Dirks WG. Ethical Challenges Using Human Tumor Cell Lines in Cancer Research. In: Bauer AW, Hofheinz RD, Utikal JS, eds. *Ethical Challenges in Cancer Diagnosis and Therapy*. Springer International Publishing; 2021:39-46. doi:10.1007/978-3-030-63749-1_4
223. Drouin Z, Lévesque F, Mouzakitis K, Labrie M. Current preclinical models of brain metastasis. *Clin Exp Metastasis*. 2024;42(1):5. doi:10.1007/s10585-024-10318-x
224. Idrisova KF, Simon HU, Gomzikova MO. Role of Patient-Derived Models of Cancer in Translational Oncology. *Cancers (Basel)*. 2022;15(1):139. doi:10.3390/cancers15010139
225. Daphu I, Sundstrøm T, Horn S, et al. In vivo animal models for studying brain metastasis: value and limitations. *Clin Exp Metastasis*. 2013;30(5):695-710. doi:10.1007/s10585-013-9566-9
226. Miarka L, Valiente M. Animal models of brain metastasis. *Neuro-Oncology Advances*. 2021;3(Supplement_5):v144-v156. doi:10.1093/noajnl/vdab115
227. Liu Z, Dong S, Liu M, et al. Experimental models for cancer brain metastasis. *Cancer Pathogenesis and Therapy*. 2024;2(1):15-23. doi:10.1016/j.cpt.2023.10.005
228. Cho JH, Robinson JP, Arave RA, et al. AKT1 Activation Promotes Development of Melanoma Metastases. *Cell Reports*. 2015;13(5):898-905. doi:10.1016/j.celrep.2015.09.057
229. Dankort D, Curley DP, Cartlidge RA, et al. BrafV600E cooperates with Pten loss to induce metastatic melanoma. *Nat Genet*. 2009;41(5):544-552. doi:10.1038/ng.356
230. Rebecca VW, Somasundaram R, Herlyn M. Pre-clinical modeling of cutaneous melanoma. *Nat Commun*. 2020;11(1):2858. doi:10.1038/s41467-020-15546-9
231. Russell WMS, Burch RL. *The Principles of Humane Experimental Technique*. Methuen; 1959.
232. Cekanova M, Rathore K. Animal models and therapeutic molecular targets of cancer: utility and limitations. *Drug Design, Development and Therapy*. 2014;8:1911-1922. doi:10.2147/DDDT.S49584
233. Balathasan L, Beech JS, Muschel RJ. Ultrasonography-Guided Intracardiac Injection: An Improvement for Quantitative Brain Colonization Assays. *The American Journal of Pathology*. 2013;183(1):26-34. doi:10.1016/j.ajpath.2013.03.003
234. Arifin DR, Witwer KW, Bulte JWM. Non-Invasive imaging of extracellular vesicles: Quo vaditis in vivo? *Journal of Extracellular Vesicles*. 2022;11(7):12241. doi:10.1002/jev2.12241
235. Li YJ, Wu JY, Wang JM, Hu XB, Xiang DX. Emerging strategies for labeling and tracking of extracellular vesicles. *Journal of Controlled Release*. 2020;328:141-159. doi:10.1016/j.jconrel.2020.08.056

236. Boudna M, Campos AD, Vychytilova-Faltejskova P, Machackova T, Slaby O, Souckova K. Strategies for labelling of exogenous and endogenous extracellular vesicles and their application for in vitro and in vivo functional studies. *Cell Commun Signal*. 2024;22(1):171. doi:10.1186/s12964-024-01548-3
237. Sundstrøm T, Daphu I, Wendelbo I, et al. Automated tracking of nanoparticle-labeled melanoma cells improves the predictive power of a brain metastasis model. *Cancer Res*. 2013;73(8):2445-2456. doi:10.1158/0008-5472.CAN-12-3514
238. Grover VPB, Tognarelli JM, Crossey MME, Cox IJ, Taylor-Robinson SD, McPhail MJW. Magnetic Resonance Imaging: Principles and Techniques: Lessons for Clinicians. *J Clin Exp Hepatol*. 2015;5(3):246-255. doi:10.1016/j.jceh.2015.08.001
239. Serai SD. Basics of magnetic resonance imaging and quantitative parameters T1, T2, T2*, T1rho and diffusion-weighted imaging. *Pediatr Radiol*. 2022;52(2):217-227. doi:10.1007/s00247-021-05042-7
240. Drew Z. Factors affecting T1 | Radiology Reference Article | Radiopaedia.org. Radiopaedia. doi:10.53347/rID-60741
241. Jin R, Lin B, Li D, Ai H. Superparamagnetic iron oxide nanoparticles for MR imaging and therapy: design considerations and clinical applications. *Current Opinion in Pharmacology*. 2014;18:18-27. doi:10.1016/j.coph.2014.08.002
242. Sceneay J, Smyth MJ, Möller A. The pre-metastatic niche: finding common ground. *Cancer Metastasis Rev*. 2013;32(3):449-464. doi:10.1007/s10555-013-9420-1
243. Lee W, Ko SY, Mohamed MS, Kenny HA, Lengyel E, Naora H. Neutrophils facilitate ovarian cancer premetastatic niche formation in the omentum. *Journal of Experimental Medicine*. 2018;216(1):176-194. doi:10.1084/jem.20181170
244. Morad G, Carman CV, Hagedorn EJ, et al. Tumor-Derived Extracellular Vesicles Breach the Intact Blood-Brain Barrier via Transcytosis. *ACS Nano*. 2019;13(12):13853-13865. doi:10.1021/acsnano.9b04397
245. Henrik Heiland D, Ravi VM, Behringer SP, et al. Tumor-associated reactive astrocytes aid the evolution of immunosuppressive environment in glioblastoma. *Nat Commun*. 2019;10(1):2541. doi:10.1038/s41467-019-10493-6
246. Zou Y, Watters A, Cheng N, et al. Polyunsaturated Fatty Acids from Astrocytes Activate PPARγ Signaling in Cancer Cells to Promote Brain Metastasis. *Cancer Discovery*. 2019;9(12):1720-1735. doi:10.1158/2159-8290.CD-19-0270
247. Forloni M, Dogra SK, Dong Y, et al. miR-146a promotes the initiation and progression of melanoma by activating Notch signaling. *Elife*. 2014;3:e01460. doi:10.7554/eLife.01460
248. Raimo M, Orso F, Grassi E, et al. miR-146a Exerts Differential Effects on Melanoma Growth and Metastatization. *Mol Cancer Res*. 2016;14(6):548-562. doi:10.1158/1541-7786.MCR-15-0425-T
249. Fares J, Cordero A, Kanojia D, Lesniak MS. The Network of Cytokines in Brain Metastases. *Cancers*. 2021;13(1):142. doi:10.3390/cancers13010142
250. Dhawan P, Richmond A. Role of CXCL1 in tumorigenesis of melanoma. *J Leukoc Biol*. 2002;72(1):9-18. doi:10.1189/jlb.72.1.9
251. Gril B, Paranjape AN, Woditschka S, et al. Reactive astrocytic S1P3 signaling modulates the blood–tumor barrier in brain metastases. *Nat Commun*. 2018;9(1):2705. doi:10.1038/s41467-018-05030-w
252. O'Connor T, Heikenwalder M. CCL2 in the Tumor Microenvironment. In: Birbrair A, ed. *Tumor Microenvironment: The Role of Chemokines – Part B*. Springer International Publishing; 2021:1-14. doi:10.1007/978-3-030-62658-7_1
253. Pozzi S, Scomparin A, Ben-Shushan D, et al. MCP-1/CCR2 axis inhibition sensitizes the brain microenvironment against melanoma brain metastasis progression. *JCI Insight*. 7(17):e154804. doi:10.1172/jci.insight.154804
254. Ciccone V, Terzuoli E, Ristori E, et al. ALDH1A1 overexpression in melanoma cells promotes tumor angiogenesis by activating the IL-8/Notch signaling cascade. *International Journal of Molecular Medicine*. 2022;50(1):1-17. doi:10.3892/ijmm.2022.5155
255. Xie T xin, Huang FJ, Aldape KD, et al. Activation of Stat3 in Human Melanoma Promotes Brain Metastasis. *Cancer Research*. 2006;66(6):3188-3196. doi:10.1158/0008-5472.CAN-05-2674

256. Marin J, Journe F, Ghanem GE, Awada A, Kindt N. Cytokine Landscape in Central Nervous System Metastases. *Biomedicines*. 2022;10(7):1537. doi:10.3390/biomedicines10071537
257. Liu X, Fang H, Chen H, et al. An Artificial miRNA against HPSE Suppresses Melanoma Invasion Properties, Correlating with a Down-Regulation of Chemokines and MAPK Phosphorylation. *PLOS ONE*. 2012;7(6):e38659. doi:10.1371/journal.pone.0038659
258. Wei H, Hu Y, Wang J, Gao X, Qian X, Tang M. Superparamagnetic Iron Oxide Nanoparticles: Cytotoxicity, Metabolism, and Cellular Behavior in Biomedicine Applications. *Int J Nanomedicine*. 2021;16:6097-6113. doi:10.2147/IJN.S321984
259. Toomajian VA, Tundo A, Ural EE, Greeson EM, Contag CH, Makela AV. Magnetic Particle Imaging Reveals that Iron-Labeled Extracellular Vesicles Accumulate in Brains of Mice with Metastases. *ACS Appl Mater Interfaces*. 2024;16(24):30860-30873. doi:10.1021/acsami.4c04920
260. Singh N, Jenkins GJS, Asadi R, Doak SH. Potential toxicity of superparamagnetic iron oxide nanoparticles (SPION). *Nano Reviews*. 2010;1(1):5358. doi:10.3402/nano.v1i0.5358
261. Yildirimer L, Thanh NTK, Loizidou M, Seifalian AM. Toxicology and clinical potential of nanoparticles. *Nano Today*. 2011;6(6):585-607. doi:10.1016/j.nantod.2011.10.001
262. Sancho-Albero M, Navascués N, Mendoza G, et al. Exosome origin determines cell targeting and the transfer of therapeutic nanoparticles towards target cells. *Journal of Nanobiotechnology*. 2019;17(1):16. doi:10.1186/s12951-018-0437-z
263. Hatzivassiliou G, Song K, Yen I, et al. RAF inhibitors prime wild-type RAF to activate the MAPK pathway and enhance growth. *Nature*. 2010;464(7287):431-435. doi:10.1038/nature08833
264. Heidorn SJ, Milagre C, Whittaker S, et al. Kinase-Dead BRAF and Oncogenic RAS Cooperate to Drive Tumor Progression through CRAF. *Cell*. 2010;140(2):209-221. doi:10.1016/j.cell.2009.12.040
265. Poulikakos PI, Zhang C, Bollag G, Shokat KM, Rosen N. RAF inhibitors transactivate RAF dimers and ERK signalling in cells with wild-type BRAF. *Nature*. 2010;464(7287):427-430. doi:10.1038/nature08902
266. Wagle N, Van Allen EM, Treacy DJ, et al. MAP Kinase Pathway Alterations in BRAF-Mutant Melanoma Patients with Acquired Resistance to Combined RAF/MEK Inhibition. *Cancer Discovery*. 2014;4(1):61-68. doi:10.1158/2159-8290.CD-13-0631
267. Girotti MR, Lopes F, Preece N, et al. Paradox-Breaking RAF Inhibitors that Also Target SRC Are Effective in Drug-Resistant BRAF Mutant Melanoma. *Cancer Cell*. 2015;27(1):85-96. doi:10.1016/j.ccell.2014.11.006
268. Huang S. Regulation of Metastases by Signal Transducer and Activator of Transcription 3 Signaling Pathway: Clinical Implications. *Clinical Cancer Research*. 2007;13(5):1362-1366. doi:10.1158/1078-0432.CCR-06-2313
269. Kujawski M, Cherryholmes G, Priceman SJ, Yu H. STAT3 and Src Signaling in Melanoma. In: Gajewski TF, Hodi FS, eds. *Targeted Therapeutics in Melanoma*. Springer; 2012:89-105. doi:10.1007/978-1-61779-407-0_7
270. Zeller SL, Spirollari E, Dicpinigaitis AJ, et al. Brain Metastases Are Regulated by Immuno-inflammatory Signaling Pathways Governed by STAT3, MAPK and Tumor Suppressor p53 Status: Possible Therapeutic Targets. *Anticancer Research*. 2024;44(1):13-22. doi:10.21873/anticanres.16783
271. Fu XQ, Liu B, Wang YP, et al. Activation of STAT3 is a key event in TLR4 signaling-mediated melanoma progression. *Cell Death Dis*. 2020;11(4):1-15. doi:10.1038/s41419-020-2440-1
272. Ceyzériat K, Abjean L, Carrillo-de Sauvage MA, Ben Haim L, Escartin C. The complex STATes of astrocyte reactivity: How are they controlled by the JAK–STAT3 pathway? *Neuroscience*. 2016;330:205-218. doi:10.1016/j.neuroscience.2016.05.043
273. Kenchappa RS, Dovas A, Argenziano MG, et al. Activation of STAT3 through combined SRC and EGFR signaling drives resistance to a mitotic kinesin inhibitor in glioblastoma. *Cell Reports*. 2022;39(12):110991. doi:10.1016/j.celrep.2022.110991
274. Wu D, Chen Q, Chen X, Han F, Chen Z, Wang Y. The blood–brain barrier: Structure, regulation and drug delivery. *Sig Transduct Target Ther*. 2023;8(1):1-27. doi:10.1038/s41392-023-01481-w

275. Deserpidine. Accessed January 14, 2025. https://go.drugbank.com/drugs/DB01089
276. Winsor T. Comparative Effects of Various Rauwolfia Alkaloids in Hypertension. *Dis Chest*. 1959;35(4):415-421. doi:10.1378/chest.35.4.415
277. Peri R, Mangipudy RS. Reserpine. In: Wexler P, ed. *Encyclopedia of Toxicology (Third Edition)*. Academic Press; 2014:94-96. doi:10.1016/B978-0-12-386454-3.00779-X
278. Saini N, Grewal AS, Lather V, Gahlawat SK. Natural alkaloids targeting EGFR in non-small cell lung cancer: Molecular docking and ADMET predictions. *Chemico-Biological Interactions*. 2022;358:109901. doi:10.1016/j.cbi.2022.109901
279. Gampa G, Kim M, Mohammad AS, et al. Brain Distribution and Active Efflux of Three panRAF Inhibitors: Considerations in the Treatment of Melanoma Brain Metastases. *J Pharmacol Exp Ther*. 2019;368(3):446-461. doi:10.1124/jpet.118.253708
280. Daphu I, Horn S, Stieber D, et al. In Vitro Treatment of Melanoma Brain Metastasis by Simultaneously Targeting the MAPK and PI3K Signaling Pathways. *International Journal of Molecular Sciences*. 2014;15(5):8773-8794. doi:10.3390/ijms15058773
281. Steeg PS. Targeting metastasis. *Nat Rev Cancer*. 2016;16(4):201-218. doi:10.1038/nrc.2016.25
282. Zhang Y, Xu H. Serum exosomal miR-378 upregulation is associated with poor prognosis in non–small-cell lung cancer patients. *Journal of Clinical Laboratory Analysis*. 2020;34(6):e23237. doi:10.1002/jcla.23237
283. Yokota Y, Noda T, Okumura Y, et al. Serum exosomal miR-638 is a prognostic marker of HCC via downregulation of VE-cadherin and ZO-1 of endothelial cells. *Cancer Science*. 2021;112(3):1275-1288. doi:10.1111/cas.14807
284. Chiabotto G, Gai C, Deregibus MC, Camussi G. Salivary Extracellular Vesicle-Associated exRNA as Cancer Biomarker. *Cancers*. 2019;11(7):891. doi:10.3390/cancers11070891
285. Khoo XH, Paterson IC, Goh BH, Lee WL. Cisplatin-Resistance in Oral Squamous Cell Carcinoma: Regulation by Tumor Cell-Derived Extracellular Vesicles. *Cancers (Basel)*. 2019;11(8):1166. doi:10.3390/cancers11081166
286. Zheng Y, Song A, Zhou Y, et al. Identification of extracellular vesicles-transported miRNAs in Erlotinib-resistant head and neck squamous cell carcinoma. *J Cell Commun Signal*. 2020;14(4):389-402. doi:10.1007/s12079-020-00546-7
287. Yan S, Dang G, Zhang X, et al. Downregulation of circulating exosomal miR-638 predicts poor prognosis in colon cancer patients. *Oncotarget*. 2017;8(42):72220-72226. doi:10.18632/oncotarget.19689
288. Kumar MA, Baba SK, Sadida HQ, et al. Extracellular vesicles as tools and targets in therapy for diseases. *Sig Transduct Target Ther*. 2024;9(1):1-41. doi:10.1038/s41392-024-01735-1
289. Bobrie A, Krumeich S, Reyal F, et al. Rab27a Supports Exosome-Dependent and -Independent Mechanisms That Modify the Tumor Microenvironment and Can Promote Tumor Progression. *Cancer Research*. 2012;72(19):4920-4930. doi:10.1158/0008-5472.CAN-12-0925
290. Anastasiadou E, Seto AG, Beatty X, et al. Cobomarsen, an Oligonucleotide Inhibitor of miR-155, Slows DLBCL Tumor Cell Growth In Vitro and In Vivo. *Clinical Cancer Research*. 2021;27(4):1139-1149. doi:10.1158/1078-0432.CCR-20-3139
291. Kara G, Calin GA, Ozpolat B. RNAi-based therapeutics and tumor targeted delivery in cancer. *Advanced Drug Delivery Reviews*. 2022;182:114113. doi:10.1016/j.addr.2022.114113
292. Golounina AV, Fedotcheva TA, Shimanovsky NL. Microrna-155 as a Possible Pharmacological Target. *Pharm Chem J*. 2024;58(4):547-553. doi:10.1007/s11094-024-03177-z
293. Kilikevicius A, Meister G, Corey DR. Reexamining assumptions about miRNA-guided gene silencing. *Nucleic Acids Research*. 2022;50(2):617-634. doi:10.1093/nar/gkab1256
294. Varkaris A, Medarova Z. 383P Clinical experience with TTX-MC138: A first-in-class therapy against metastatic cancer. *Annals of Oncology*. 2024;35:S379. doi:10.1016/j.annonc.2024.08.331
295. Wu YW, Lee DY, Lu YL, et al. Platelet extracellular vesicles are efficient delivery vehicles of doxorubicin, an anti-cancer drug: preparation and in vitro characterization. *Platelets*. 2023;34(1):2237134. doi:10.1080/09537104.2023.2237134

Received: 16 March 2023 | Revised: 4 August 2023 | Accepted: 20 August 2023

DOI: 10.1002/jev2.12363

RESEARCH ARTICLE

Inhibition of extracellular vesicle-derived miR-146a-5p decreases progression of melanoma brain metastasis via Notch pathway dysregulation in astrocytes

Emma Rigg[2] | **Jiwei Wang**[1,2,3] | **Zhiwei Xue**[2,3] | **Taral R. Lunavat**[2,4] | **Guowei Liu**[2,3] | **Tuyen Hoang**[1] | **Himalaya Parajuli**[1] | **Mingzhi Han**[1,2,3] | **Rolf Bjerkvig**[1] | **Petr V. Nazarov**[5] | **Nathalie Nicot**[6] | **Stephanie Kreis**[7] | **Christiane Margue**[7] | **Miléne Tetsi Nomigni**[7] | **Jochen Utikal**[8,9,10] | **Hrvoje Miletic**[1,11] | **Terje Sundstrøm**[12,13] | **Lars A. R. Ystaas**[1] | **Xingang Li**[2,3] | **Frits Thorsen**[1,2,12,14]

[1]Department of Neurosurgery, Qilu Hospital of Shandong University and Institute of Brain and Brain-Inspired Science, Cheeloo College of Medicine, Shandong University, Jinan, China

[2]Department of Biomedicine, University of Bergen, Bergen, Norway

[3]Shandong Key Laboratory of Brain Function Remodeling, Jinan, China

[4]Department of Neurology, Molecular Neurogenetics Unit-West, Massachusetts General Hospital, Harvard Medical School, Charlestown, Massachusetts, USA

[5]Bioinformatics Platform and Multiomics Data Science Research Group, Department of Cancer Research, Luxembourg Institute of Health, Luxembourg

[6]LuxGen Genome Center, Luxembourg Institute of Health, Laboratoire National de Santé, Dudelange, Luxembourg

[7]Department of Life Sciences and Medicine, University of Luxembourg, Luxembourg

[8]Skin Cancer Unit, German Cancer Research Center (DKFZ), Heidelberg, Germany

[9]Department of Dermatology, Venereology and Allergology, University Medical Center Mannheim, Ruprecht-Karl University of Heidelberg, Mannheim, Germany

[10]DKFZ Hector Cancer Institute at the University Medical Center Mannheim, Mannheim, Germany

[11]Department of Pathology, Haukeland University Hospital, Bergen, Norway

[12]Department of Neurosurgery, Haukeland University Hospital, Bergen, Norway

[13]Department of Clinical Medicine, University of Bergen, Bergen, Norway

[14]Molecular Imaging Center, Department of Biomedicine, University of Bergen, Bergen, Norway

Correspondence
Emma Rigg and Frits Thorsen, Department of Biomedicine, University of Bergen, Jonas Lies vei 91, 5009 Bergen, Norway. Email: emma.rigg@uib.no and frits.thorsen@uib.no

Funding information
Department of Science & Technology of Shandong Province, Grant/Award Number: ZR2020QH182; National Natural Science Foundation of China, Grant/Award Numbers: 82073219, 82203760; Helse Vest, Grant/Award Number: F-12856-D11661; Universitetet i Bergen; Norges Forskningsråd, Grant/Award Number: 315566; Kreftforeningen,

Abstract

Melanoma has the highest propensity of all cancers to metastasize to the brain with a large percentage of late-stage patients developing metastases in the central nervous system (CNS). It is well known that metastasis establishment, cell survival, and progression are affected by tumour-host cell interactions where changes in the host cellular compartments likely play an important role. In this context, miRNAs transferred by tumour derived extracellular vesicles (EVs) have previously been shown to create a favourable tumour microenvironment. Here, we show that miR-146a-5p is highly expressed in human melanoma brain metastasis (MBM) EVs, both in MBM cell lines as well as in biopsies, thereby modulating the brain metastatic

---

Emma Rigg and Jiwei Wang contributed equally.

This is an open access article under the terms of the Creative Commons Attribution License, which permits use, distribution and reproduction in any medium, provided the original work is properly cited.
© 2023 The Authors. *Journal of Extracellular Vesicles* published by Wiley Periodicals LLC on behalf of International Society for Extracellular Vesicles.

Grant/Award Number: 182716; Luxembourg National Research Fund, Grant/Award Number: C21/BM/15739125/DIOMEDES

niche. Mechanistically, miR-146a-5p was transferred to astrocytes via EV delivery and inhibited NUMB in the Notch signalling pathway. This resulted in activation of tumour-promoting cytokines (IL-6, IL-8, MCP-1 and CXCL1). Brain metastases were significantly reduced following miR-146a-5p knockdown. Corroborating these findings, miR-146a-5p inhibition led to a reduction of IL-6, IL-8, MCP-1 and CXCL1 in astrocytes. Following molecular docking analysis, deserpidine was identified as a functional miR-146a-5p inhibitor, both in vitro and in vivo. Our results highlight the pro-metastatic function of miR-146a-5p in EVs and identifies deserpidine for targeted adjuvant treatment.

KEYWORDS
brain metastasis, deserpidine, extracellular vesicles, melanoma, miR-146a-5p, normal human astrocytes (NHA)

1 | INTRODUCTION

The incidence of cutaneous melanoma is increasing world-wide where up to 60% of the patients with advanced disease will eventually be diagnosed with brain metastasis (Rishi & Yu, 2020). These patients often develop multiple metastases and even with modern therapies, the average survival is still quantified in months following diagnosis (Anvari et al., 2021). Treatment of melanoma brain metastasis (MBM) has proven to be a formidable clinical challenge. Tumours consistently acquire resistance to targeted therapies and immune checkpoint inhibitors. While having a good intracranial response in asymptomatic MBM patients, minimal effectiveness is seen in patients who are symptomatic (Boire et al., 2020; Larkin et al., 2019; Rishi & Yu, 2020; Tawbi et al., 2019). Given the role of putative tumour-host cell interactions, investigation into the MBM microenvironment is necessary to understand why current treatments are not working, and for the development of new and effective clinical treatment strategies.

The brain microenvironment (BME) consists of neurons and glial cells, in addition to extracellular matrix components. In brain metastasis, molecular interactions between tumour cells and the normal brain forms the brain metastatic niche. During niche establishment, the brain changes from being a hostile environment to one that promotes metastasis formation and growth.

Astrocytes are the most abundant cell type in the central nervous system (CNS), where they exert vital roles in glial-neuronal homeostasis and blood-brain barrier (BBB) maintenance (Cacho-Diaz et al., 2020). In the case of metastasis, astrocytes can be regarded as the first cell type that the extravasated tumour cells encounter, forming an activated phenotype that may promote MBM growth. This includes altered cytokine release, translational and transcriptional remodelling, as well as increased proliferative capacities (Placone et al., 2016). Thus, activated astrocytes have been found to surround brain metastases where they most likely contribute to tumour progression (Wasilewski et al., 2017).

A major contributing factor to niche remodelling is the transfer of small extracellular vesicles (EVs) of endocytic origin from tumour cells (Peinado et al., 2017; Tamas et al., 2022). The EVs shuttle proteins, DNA, and RNA, mostly in the form of miRNAs, to both local and distant cells (Cesi et al., 2016; Valadi et al., 2007). In brain metastasis, EV cargo has been found to both break down the BBB and alter the vascular environment to promote establishment of a secondary tumour (Rodrigues et al., 2019; Tominaga et al., 2015). It has been shown that EVs-delivered miRNAs from primary tumour cells can have important role in tumorigenesis, angiogenesis, metastasis, and drug resistance (Bartel, 2018; Cesi et al., 2018). However, their targets, transcriptional networks and direct role in BM development are unclear (Hanniford et al., 2015). It is known that miRNAs regulate 30% of the human genes and a majority of these have been found to be tumour-associated (Si et al., 2019). Therefore, a further understanding on how MBM EVs contributes to MBM niche establishment is warranted, as the mechanisms related to metastasis remain largely unknown.

Here, we show that MBM-EVs play a major role in the progression of MBM through upregulation of miR-146a-5p. We identified the mRNA *NUMB* as a direct binding partner of miR-146a-5p. This is important since Numb is an inhibitor protein in the Notch signalling pathway, known to be implicated in melanoma pathogenesis (Hristova et al., 2021). Therefore, our findings strongly suggest that miR-146a-5p is important in MBM development and thus represents a therapeutic target. We further identified, through molecular docking analysis, deserpidine, an antipsychotic and antihypertensive drug, to be a functional miR-146a-5p inhibitor, both in vitro and in vivo.

2 | MATERIALS AND METHODS

2.1 | Cell lines and cell culture conditions

Written consent was obtained from the patients before tumour material was collected and subsequently used to prepare cell lines. The Regional Ethical Committee (REC) approved tissue collection, biobank storage of tumour biopsies, as well as development and use of cell lines (REC Approvals 2013/720 and 2020/65185). Cell line authentication was verified by short tandem repeat (STR) fingerprinting and the cells were regularly tested for mycoplasma. The H1, H2, H3 and H10 cell lines were established in our laboratory from patient biopsies of human MBM. The BRAF mutation status of the H1, H2, H3 and H10 cell lines was investigated by performing massive parallel sequencing of the tumour DNA, according to published protocols (Bischof et al., 2019). The H1, H2 and H10 cell lines are $\mathrm{BRAF}^{\mathrm{V600E}}$ mutated, while the H3 cells are $\mathrm{BRAF}^{\mathrm{L577F}}$ mutated. Normal human astrocytes (NHA) were purchased from ABM (Applied Biological Materials, Vancouver, Canada) and human melanocytes were obtained from ATCC (American Type Culture Collection, Manassas, VA, USA).

The H1 cells were transduced with two lentiviral vectors, encoding Dendra (a green fluorescent protein (GFP) variant) and luciferase to obtain the H1_DL2 cell line. Flow cytometric isolation of cells by GFP expression was performed (BD FACS Aria, Becton Dickinson, Franklin Lakes, NJ, USA). All cell lines were grown in Dulbecco's Modified Eagle′s medium (DMEM; Sigma-Aldrich Inc., St. Louis, MO, USA), supplemented with 10% heat-inactivated new-born calf serum (Thermo Fischer Scientific, Waltham, MA, USA), 5 mg/mL plasmocin (Invivogen, Toulouse, France), 2% L-glutamine (BioWhittaker, Verviers, Belgium), penicillin (100 IU/mL) and streptomycin (100 mL/mL) (BioWhittaker). The cells were cultured in a standard tissue incubator at 37°C, 100% humidity and 5% CO_2, and trypsinated once they attained 75% confluency using 0.25% Trypsin/EDTA (BioWhittaker).

2.2 | EV isolation and characterization

All EVs were isolated and characterized according to MISEV 2018 guidelines (Théry et al., 2018). The H1, H2, H3, NHA and melanocyte cell lines were seeded in **eight** T175 flasks per isolation in DMEM growth medium as described above, supplemented with EV-depleted fetal bovine serum (FBS). FBS was depleted of EVs by centrifuging at 120,000 *g* for 18 h at 4°C. Conditioned medium (CM) was collected by pipetting after 48 h, and cells were reseeded for further EV production. The isolation of EVs was performed as previously described (Lunavat et al., 2017). Briefly, CM was centrifuged at 300 *g* for 5 min to remove cell debris. The collected supernatant was centrifuged again at 2000 *g* for 20 min at 4°C to remove apoptotic bodies, and then transferred to ultracentrifuge tubes and centrifuged at 16,500 *g* for 20 min to remove microvesicles. Finally, the supernatant was centrifuged at 120,000 *g* for 2 h to pellet exosomes termed as EVs and the supernatant was discarded. The remaining EV pellet was resuspended in 100–500 mL sterile-filtered PBS and frozen at −80°C until further use.

For particle size determination, EVs were diluted with filtered PBS at 1:100−1:1000. The sizes and relative intensities of EVs were quantified using a Zetasizer Nano ZS (Malvern Panalytical, Worcestershire, UK) or a Multiple–Laser ZetaView® f-NTA Nanoparticle Tracking Analyzer (Particle Metrix GmbH, Inning am Ammersee, Germany).

To visualize the cup-shaped morphology and the membrane structure of isolated EVs, transmission electron microscopy (TEM) was used. Approximately 10 μg of EVs were mounted on formvar carbon coated copper grids and post-fixed with 2.5% glutaraldehyde, followed by staining with 2% of uranyl acetate. Grids were dried and imaged using a Hitachi HT7800 transmission electron microscope (Hitachi High-Tech Corporation, Tokyo, Japan).

Other materials and methods used in this study are provided in the Supplementary materials.

3 | RESULTS

3.1 | EVs penetrate the mouse brain and increase brain metastatic growth

We first isolated EVs from two human MBM cell lines (H1, H2) as well as from normal human astrocytes (NHA) and melanocytes. Nanoparticle tracking revealed a mean EV diameter and concentration between 80 and 200 nm from NHA, H1, H2 and melanocytes (Figure 1a, Figure S1a), and the lipid bilayer membranes were verified by **TEM**(Figure 1a, Figure S1b). Additionally, Western blot (WB) analysis showed that the standard EV markers TSG101, CD9 and flotillin-1 were positive, whereas the ER marker calnexin, which is known to be absent in EVs (Zhao et al., 2022), was negative (Figure 1b, Figure S1c). These data thus confirm the isolation of EVs.

To study whether tumour MBM-EVs were taken up by the brain parenchyma in vivo, Cy7 labelled H1-EVs were injected intracardially (i.c.) into the left cardiac ventricle of one female nude mouse. After 24 h, fluorescence imaging both in vivo and in

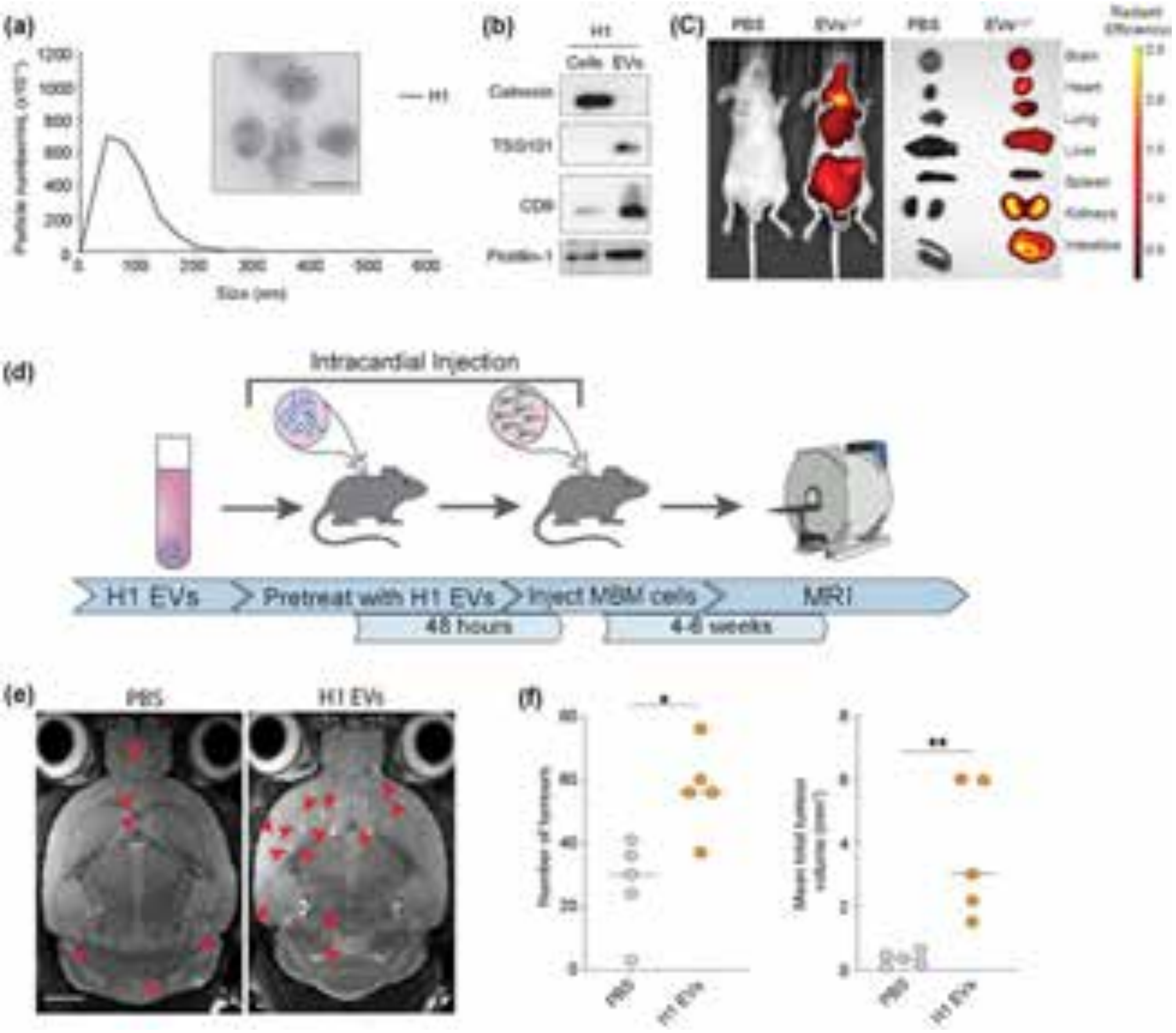

FIGURE 1 MBM-EVs contribute to increased metastatic burden. (a) Representative nanoparticle tracking analysis using Malvern Nanosight and transmission electron microscopy of H1-EVs. Size range 50–200 nm. Scale bar = 100 nm. (b) Western blot analysis of EV-characteristic markers on H1 cells and corresponding EVs. (c) In vivo and ex vivo NIR imaging of mice and harvested major organs after injection of Cy7 (excitation/emission: 745/820 nm) H1-EVs or PBS control. (d) Schematic workflow of the exosome-primed in vivo metastatic model. (e) Development of brain metastasis assessed by T2 weighted MRI at week 4 after priming with MBM-derived EVs or PBS prior to intracardial injection of MBM H1_DL2 cells. Scale bar = 2 mm. (f) Quantification of the total number and volume of brain metastasis at week 4 in exosome-primed animals compared to the control PBS group. n.s. = not significant, $^*p < 0.05$, $^{**}p < 0.01$.

organs ex vivo showed Cy7-labelled EVs to be incorporated into major organs including the brain (Figure 1c). To assess the role of the MBM-EVs in brain metastatic niche development, 5.0×10^9 H1-EVs were injected i.c into female NOD/SCID mice at 24 h intervals for 3 days (Figure 1d). 48 h after the final EV injection, 5.0×10^5 H1_DL2 cells were injected i.c. and MBM development was monitored by magnetic resonance imaging (MRI; Figure 1e). Mice pretreated with H1-EVs showed a significantly higher number of brain metastatic lesions at week 4 as well as significantly larger tumour volumes, compared to the control mice who received PBS pretreatment (Figure 1f).

These data show that circulating EVs from human MBM cells creates a brain metastatic niche that favours both brain metastatic initiation (number of brain metastases observed) as well as tumour growth.

3.2 | EVs derived from human MBM cells activate NHAs and elevate cytokine production

Astrocytes have major functions in maintaining BBB integrity and they consequently represent the first cells that the extravasating tumour cells will encounter within the CNS. Reactive astrocytes have been shown to be involved in numerous reciprocal interactions that brain metastatic cells require for their initiation and growth (Zhang et al., 2015). Therefore, we assessed to what

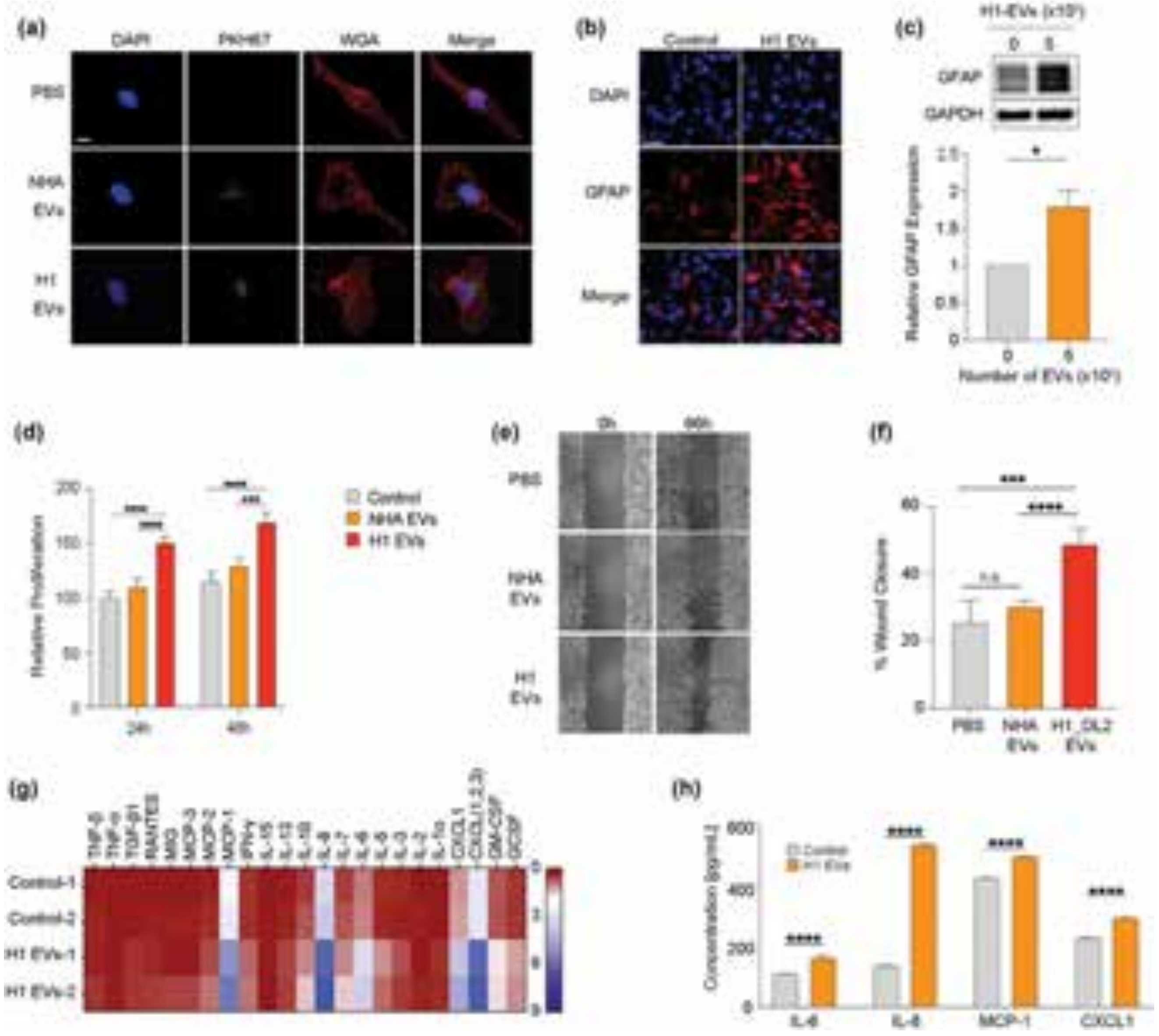

FIGURE 2 MBM-derived EVs induce activation in NHA. (a) NHA cultured with 5.0×10^9 EVs of PKH67-stained (green) NHA- or H1-EVs for 48 h to show uptake. Nuclei stained with DAPI (blue), membrane stained with WGA-Texas Red (red). Magnification (100X). Scale bar = 10 μm. (b) Representative images of ICC-stained NHA cells cultured with H1-EVs or PBS control for 48 h. Merged images of DAPI (blue) and GFAP (red). Magnification 20X. Scale bar = 20 μm. (c) Western blot analysis of GFAP in NHA cells after culturing with 5.0×10^9 H1-EVs or PBS for 48 h and subsequent quantification. (d) CCK8 proliferation assay of NHA cells cultured with 5.0×10^9 NHA- or H1-EVs over 48 h. (e) Representative micrographs at the start and completion of a 96 h NHA wound healing assay co-cultured with 5.0×10^9 NHA- or H1-EVs. Scale bar: 300 μm. (f) Quantification of wound healing assay as percentage wound closure after 96 h. (g) Heatmap of a cytokine array of NHA conditioned media after culturing with 5.0×10^9 H1-EVs or PBS for 48 h. (h) ELISA validation performed on NHA conditioned media after co-culture with 5.0×10^9 H1-EVs. ELISA of top four upregulated cytokines from cytokine array, IL-6, IL-8, MCP-1 and CXCL1, were used. n.s.= not significant $^*p < 0.05$, $^{***}p < 0.001$, $^{****}p < 0.0001$.

extent MBM-EVs could be taken up by NHAs and if they were activated. For this purpose, we labelled the NHA with Texas red-conjugated wheat germ agglutinin (WGA-Texas red) and the MBM-EVs with the membrane stain PKH67 (green). As shown in Figure 2(a) and Figure S2(a,b), the EVs derived from H1 and H2 MBM cells, as well as from NHAs, were taken up by the NHA cells. To assess a putative NHA activation, the cells were stained for the glial acidic fibrillary acidic protein (GFAP) known to be over-expressed in reactive astrocytes (Escartin et al., 2021). As shown in Figure 2(b,c), an exposure to H1-EVs led to an elevated expression of GFAP in the NHAs. This also resulted in an increased NHA cell proliferation (Figure 2d) as well as cell migration (Figure 2e,f). Interestingly, NHA EVs did not cause a stimulation of the NHAs (Figure 2d–f). NHA cells that were activated by H1 EVs where then co-cultured with H1_DL2 green, fluorescent cells. By counting the fluorescent cells, we observed an increased H1_DL2 cell proliferation (Figure S3a,b).

Previous studies have shown that activated astrocytes display altered cytokine expression levels in the brain (Zhang et al., 2018), which may contribute to MBM progression (Wasilewski et al., 2017). This, however, has not been determined in the context of EVs exposure and the establishment of the brain metastatic niche in melanoma. Therefore, we performed a cytokine array on conditioned media from NHAs that were activated by MBM-EVs. As shown in Figure 2(g), NHAs exposed to H1-EVs led to an upregulation of several cytokines that support MBM growth such as IL-6, IL-8, MCP-1 (CCL2) and CXCL1 (Dhawan & Richmond, 2002; Fares et al., 2021). These cytokines were also verified by enzyme-linked immunosorbent assays (ELISA, Figure 2h, Figure S4). Specifically, we found that neutralizing IL-8 and IL-6 activity significantly reversed the increased proliferation in H1 cells (Figure S5). Interestingly, these cytokines have previously been shown to increase melanoma cell migration and invasion through an activation of the mitogen-activated protein kinase (MAPK) and Notch signalling pathways (Alles et al., 2019; Dhawan & Richmond, 2002).

In conclusion, we show that MBM-EVs are taken up and activates NHAs, leading to increased proliferation and migration. Moreover, the activated NHAs show an increased expression of cytokines known to support MBM growth.

3.3 | MiR-146a-5p is expressed at high levels in EVs derived from MBMs and has a functional role in NHA activation

MiRNAs are known to be the most abundant RNA cargo in EVs, and it has been confirmed that EV packaged-miRNAs from tumour cells are involved in a microenvironmental modulation that may support tumour cell proliferation, metastasis, angiogenesis, chemoresistance and immune regulation (Kulkarni et al., 2019; Sun et al., 2018). Detailed knowledge of the EVs cargo provides an avenue for novel clinical biomarker discovery and potential therapeutic intervention. Therefore, we aimed to identify the miRNAs in MBM-EVs that could be responsible for the observed NHA stimulation.

For this purpose, we performed an Affymetrix array profiling on EVs collected from three MBM cell lines (H1, H2, H3), a cell line derived from a subcutaneous melanoma metastasis (Melmet 1), a lymph node metastasis from melanoma (Melmet 5), and NHA and melanocytes.

A detailed analysis of differentially expressed miRNAs (MBM-EVs vs. normal cell-EVs) revealed that miR-146a-5p was by far the most significantly upregulated miRNA across all MBM cell lines (Figure 3a,b).

In patient-derived cell lines derived from melanoma skin and lymph node metastases (Melmet 1 and Melmet 5), miR-146a-5p was elevated compared to the normal samples, but not to the same extent as observed in the MBMs (Figure S6a). RT-qPCR confirmed a 20-fold increase of miR-146a-5p in three MBM cell lines, and over 10-fold in their EVs, compared to NHA (Figure 3c). Comparison of miR-146a-5p expression between healthy melanocytes and NHA cells showed relatively low expression in both healthy cell types as well as EVs (Figure S6b). Furthermore, an RNA protection assay was performed to assess if miR-146a-5p was loaded inside the EVs. Over 65% of miR-146a-5p was retained following RNase treatment (Figure S6c).

We initially investigated miR-146a-5p by evaluating expression levels in EVs from blood serum from nine healthy volunteers, 26 melanoma patients without MBM and nine melanoma patients with confirmed MBM. No increase of miR-146a-5p expression was found in MBM patients versus healthy volunteers, and in fact healthy participants had the highest miR-146a-5p in their serum EVs compared to MBM patients (Figure S7a,b).

However, investigating further to confirm a putative role of miR-146a-5p in MBMs, in situ hybridization (ISH) was used to assess the expression levels of miR-146a-5p in 20 human MBM biopsies. Here, all tumour samples showed elevated expression levels compared to normal brain tissue. Moreover, 18 of the 20 clinical samples revealed a significantly higher expression of miR-146a-5p compared to healthy normal brain tissue (Figure 3d,e, Figure S8).

MiR-146a-5p has previously been shown to be implicated in melanoma growth and metastasis (Forloni et al., 2014; Pu et al., 2018; Raimo et al., 2016; Zhang et al., 2020); however, its role in EV delivery and niche establishment has not been determined. To determine if miR-146a-5p was responsible for the NHA activation mediated by the MBM EVs, NHAs were simultaneously co-cultured with H1-EVs and a single stranded RNA-miR-146a-5p inhibitor. We confirmed uptake of the inhibitor into NHAs by confocal microscopy (Figure S9). As shown in Figure 3(f), the inhibitor caused a reduced GFAP expression in NHAs following H1-EV exposure. Moreover, the inhibitor also reduced the effect of EVs on NHA cell proliferation and migration (Figure 3g–i, Figure S10a). By ELISA, we further show that miR-146a-5p inhibition caused reduced expression of IL-6, IL-8, MCP-1 and CXCL1 following exposure of H1-and H2-EVs to NHAs (Figure 3j, Figure S10b).

In conclusion, miR-146a-5p is expressed in human MBMs and MBM EVs and has a major role in the functional activation of NHAs following MBM EVs exposure.

3.4 | MiR-146a-5p increases Notch signalling through downregulation of NUMB expression

To assess how miR-146a-5p affects NHA activation at the transcription level, mRNA sequencing was performed on NHA cells exposed either to miR-146a-5p mimics or a scrambled control. MiR-146a-5p overexpression via a miRNA mimic led to 2330 differentially upregulated and 2591 differentially downregulated mRNAs (Figure 4a). We then performed online queries using

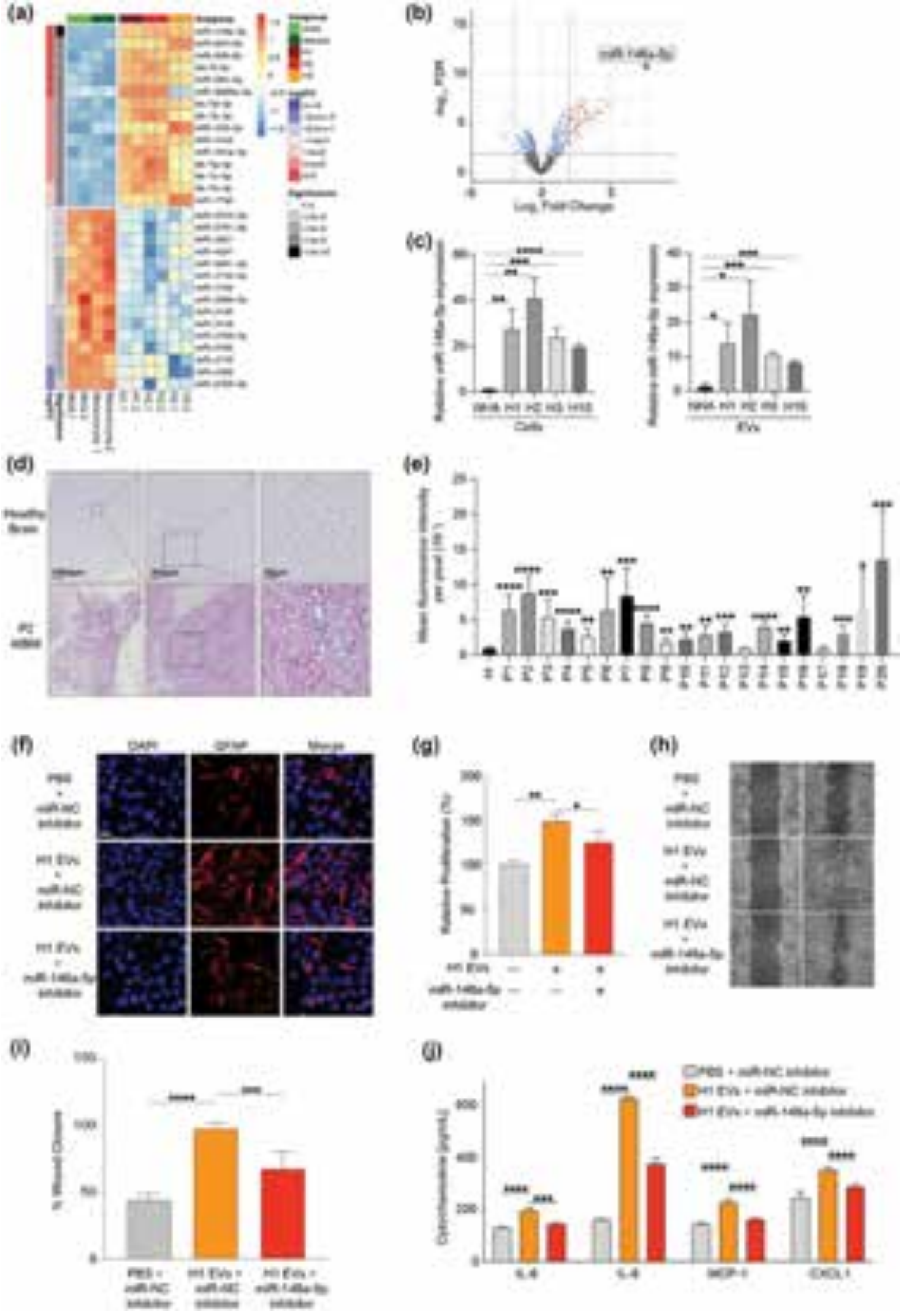

FIGURE 3 mir-146a-5p is significantly upregulated in H1-EVs compared to normal melanocytes and astrocytes and induces similar responses in NHA cells as H1-EVs. (a/b) Heatmap of the standardized expression for the top 15 up- and down-regulated miRNAs (a) and a volcano-plot (b) of differential miRNA expression in EVs derived from healthy (melanocytes and astrocytes) compared to MBM cell lines (H1, H2, H3). miR-146a-5p shows stable overexpression in MBM cell lines. (c) qPCR of miR-146a-5p expression in EVs and cells across multiple MBM cell lines (H1, H2, H3, H10) and normal cells (NHA). Cells normalized to endogenous control miR-103, and EVs normalized to spike-in *C-elegans* miR-39-3p. (d) MiRNAscope in situ hybridization assay of miR-146a-5p expression in patient MBM samples compared to healthy brain controls. Red dots indicate successful binding of the miR-146a-5p probe, tissues counterstained with haematoxylin (purple). (e) Quantification of miR-146a-5p expression across patient samples compared to three pooled healthy brain controls. Data

(Continues)

FIGURE 3 (Continued)
represented as mean fluorescence of 10 representative equal sized areas from each sample ± SE. (f) Representative images of ICC-stained NHA cells cultured with H1-EVs treated with miR-146a-5p inhibitor or miR-NC (negative control). Merged images of DAPI (blue) and GFAP (red). Magnification 20X. Scale bar = 20 μm. (g) CCK8 proliferation assay of NHA cells after co-culture with 5.0×10^9 H1-EVs in the presence or absence of a miR-146a-5p inhibitor. (h) Representative micrographs at the beginning and completion of a 96 h NHA wound healing assay co-cultured with H1-EVs with or without miR-146a-5p or scramble inhibitor. Scale bar = 300 μm. (i) Quantification of wound healing assay as percentage wound closure after 96 h. J ELISA of IL-6, IL-8, MCP-1 and CXCL1 levels from NHA cell conditioned media after co-culture with 5.0×10^9 H1-derived EVs in the presence or absence of miR-146a-5p inhibitor. $^*p < 0.05$, $^{**}p < 0.01$, $^{***}p < 0.001$, $^{****}p < 0.0001$.

databases predicting potential biological targets of miR-146a-5p (TargetScan, miRDB and microT-CDS online tools; Figure S11). By combining the downregulated sequencing data with the online queries, we identified 18 overlapping potential binding partners of miR-146a-5p (Figure 4b). A pulldown assay of NHA lysates followed by RT-qPCR was performed to quantify the enrichment of mRNA-miR-146a-5p complexes. As shown in Figure 4(c), NUMB was the most abundant binding partner, having around 6-fold more bound complexes compared to the scrambled control.

The Numb protein is an inhibitor in the Notch signalling pathway where it acts as a tumour suppressor. It has previously been shown that miR-146a-5p down-regulates NUMB leading to melanoma initiation and progression by activating the Notch signalling pathway (Forloni et al., 2014). Furthermore, data from The Cancer Genome Atlas (TCGA) also show a correlation between poor survival in melanoma patients and low NUMB expression levels (Hristova et al., 2021).

Based on this information, we aimed to study the putative role of EV enriched miR-146a-5p in NUMB inhibition in the context of MBM. As shown in Figure 4(d), RT-qPCR analysis revealed a significant down-regulation of Numb mRNA expression in NHA cells following a co-culture with H1-, H2- and H3-EVs. In contrast, EVs from melanocytes and NHAs did not have any effect. These findings were further substantiated at the protein level by WB analysis (Figure 4e). Moreover, the same results were observed by RT-qPCR and WB and in NHA cells after co-culture with a miR-146a-5p mimic (Figure 4f,g) indicating a causal relationship between miR-146a-5p and NUMB.

To further verify a putative target relationship between miR-146a-5p and NUMB, NHA cells were transfected with luciferase constructs containing either wild-type (WT) NUMB or a mutated version (Mut) of the miR-146a-5p binding site (Figure 4h). As shown in Figure 4(i), following an addition of miR-146a-5p mimic, luciferase activity was significantly reduced. In comparison, no significant difference was found between miR-146a-5p and miR-NC in mutated 3′ region samples, indicating a specific miR-146a-5p to NUMB binding.

In NHA, we performed a NUMB overexpression (Figure S12a) to determine the effects of miR-146a-5p on the previously studied cytokine production. An increased production of IL-6, IL-8, MCP-1 and CXCL1 were observed in the wild type NHA (NUMB-WT) when exposed to the miR-146a-5p mimic, whereas NHA overexpressing NUMB (NUMB-OE) did not show the same effect (Figure 4j) suggesting NUMB involvement in NHA activation/dysregulation.

In summary, NUMB is a direct miR-146a-5p target in NHAs, and its overexpression abrogates their cytokine production.

3.5 | MiR-146a-5p increases Notch expression levels and downstream proteins in NHAs

Next, we studied the expression of downstream proteins in the Notch signalling pathway. Expression levels of Notch, HES1, HEY2 and CCN1 increased in NHAs following addition of either H1-EVs or the miR-146-5p mimic (Figure 5a,b). NUMB inhibition via siRNA (Figure S12b) verified a causal relationship between NUMB and proteins of the Notch signalling pathway, as seen with increased expression of Notch, HES1, HEY2, and CCN1, compared to vector control (Figure 5c). In NHA cells overexpressing NUMB, the expression levels decreased, as assessed by qPCR (Figure 5d).

The γ-secretase inhibitor DAPT (N-[N-(3, 5-difluorophenacetyl)-l-alanyl]-s-phenylglycinet-butyl ester) is known to indirectly block Notch signalling activity (Geling et al., 2002). To further assess the effect of Notch signalling following miR-146a-5p mimic-induced NHA activation (assessed by GFAP expression), the cells were exposed to DAPT. As shown in Figure 5(e), the miR-146a-5p mimic increased GFAP expression levels significantly, as compared to NHA exposed to a scrambled miR negative control (miR-NC). DAPT treatment lowered GFAP levels regardless of whether miR-146a-5p mimic or a scrambled miR-NC control was added to the cultures.

Thereafter, we determined the expression levels of cytokines (IL-6, IL-8, MCP-1 and CXCL1) after miR-146a-5p and/or DAPT exposure to NHA cells. As expected, all four cytokines were elevated following miR-146a-5p mimic exposure, while after treatment with either DAPT alone or in combination with miR-146a-5p mimic cytokine expression remained the same as the control (Figure 5f). NHA were activated after silencing NUMB, as seen by elevated GFAP expression. However, this effect was reversed after treatment with DAPT alone or combined with si-NUMB (Figure 5g). The same effect was seen in a similar experiment where silencing of NUMB was induced in NHA cells with or without DAPT treatment. Upon silencing of NUMB, increased production of all four cytokines were observed, while combined treatment with DAPT decreased cytokine expression to normal levels (Figure 5h).

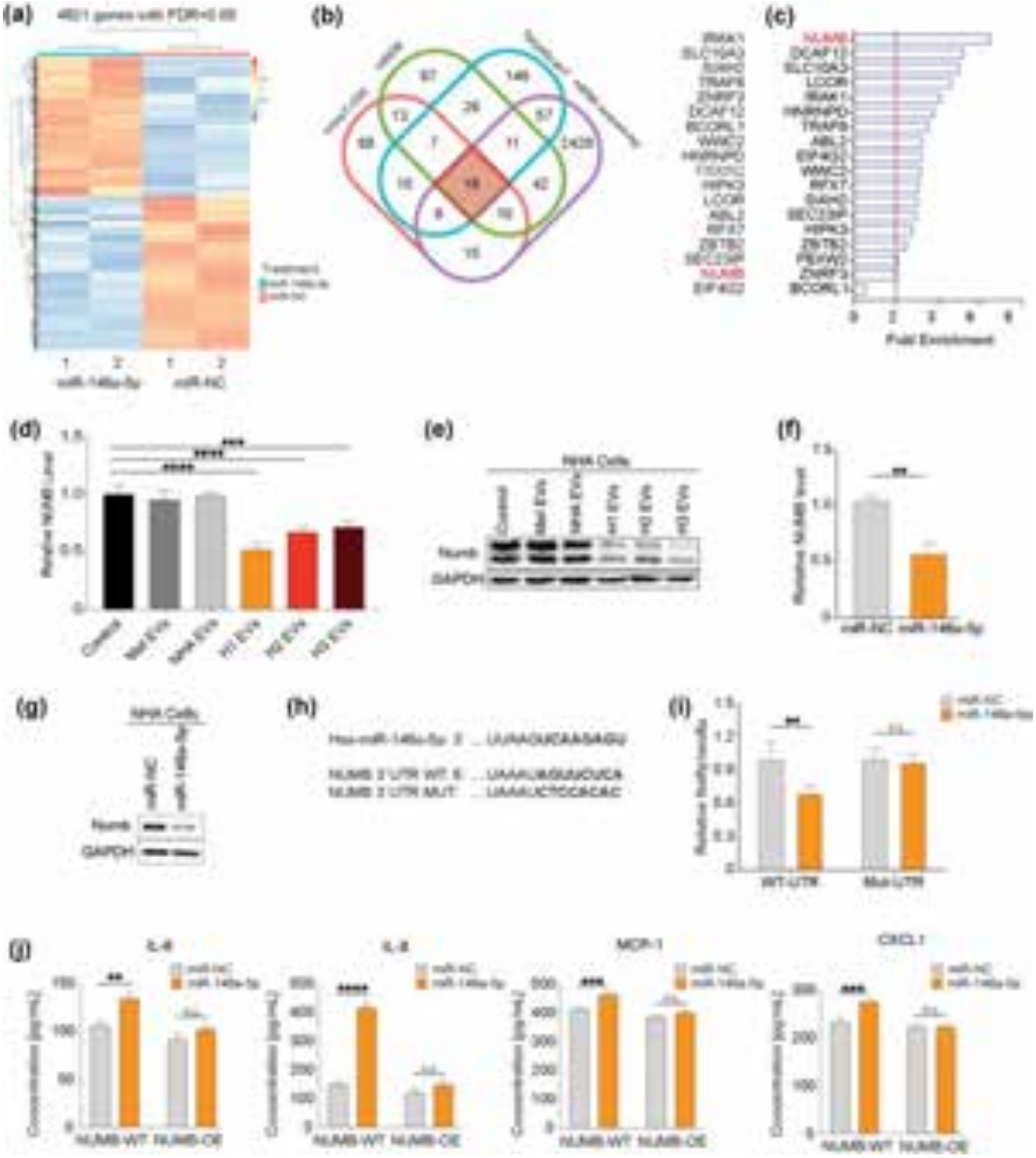

FIGURE 4 miR-146a-5p increased NOTCH signalling through interaction with and downregulation of NUMB expression. (a) Heatmap of significantly differentially expressed mRNA (FDR < 0.05) from NHA cells treated with a miR-146a-5p mimic for 48 h and compared to a scrambled control (miR-NC). (b) Significantly down-regulated mRNA results were compared to three databases (TargetScan 7.1, miRBD and microT-CDS) and 18 common genes were found as in situ projected binding partners. (c) mRNA-pulldown assay followed by qPCR quantification of bound mRNA-miR-146a-5p complexes from the common 18 binding partners. (d) qPCR of NUMB expression in NHA cells after co-culture with 5.0×10^9 EVs from melanocytes, NHA or MBM cell lines (H1, H2 and H3), normalized with U6 expression. (e) WB of Numb protein expression in NHA cells after co-culture with 5.0×10^9 EVs from melanocytes, NHA or MBM cell lines (H1, H2 and H3). (f) qPCR of NUMB expression in NHA cells after co-culture with miR-146a-5p mimic or a scrambled control, normalized to U6 expression. (g) Western blot of Numb protein expression in NHA cells after co-culture with miR-146a-5p mimic or a scrambled control. (h) Sequence of miR-146a-5p 3p binding site, and the comparison of NUMB 3′UTR-wild type (WT) and mutated (MUT) region. (i) Dual luciferase assay on the WT or MUT 3′UTR region with miR-146a-5p or a scrambled control in NHA cells, represented as the relative firefly to *Renilla* luciferase activity. (j) ELISA of top four upregulated cytokines released by NHA cells with WT or overexpression of NUMB in the presence of miR-146a-5p mimic or control. n.s.= not significant, $^{**}p < 0.01$, $^{***}p < 0.001$, $^{****}p < 0.0001$.

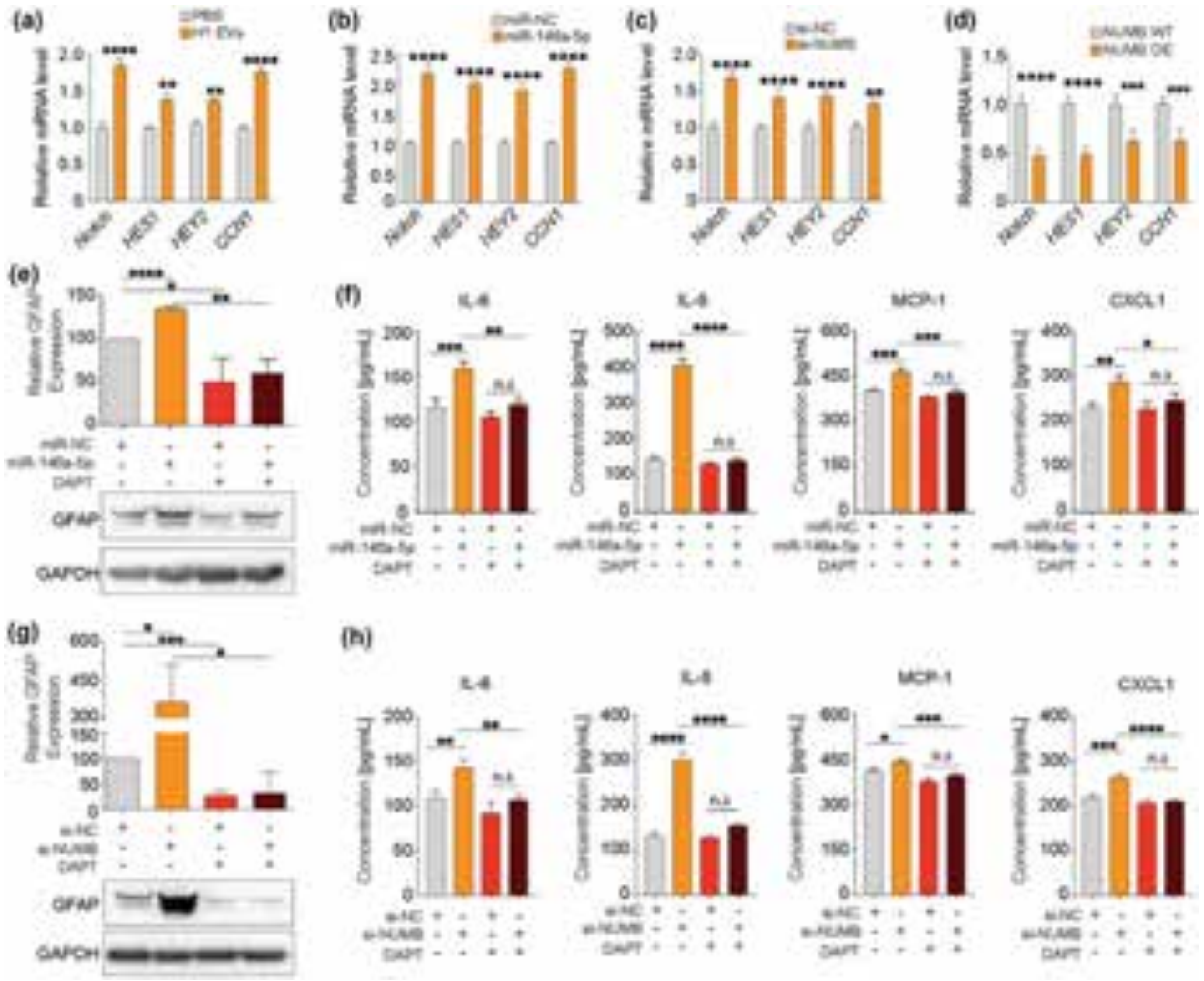

FIGURE 5 miR-146a-5p influences the activation of astrocytes through the upregulation of the Notch pathway via NUMB inhibition. (a–d) qPCR of relative mRNA expression of proteins involved in the Notch pathway from NHA cells after treatment with H1-derived EVs or PBS control, miR-146a-5p mimic or a scrambled control, NUMB siRNA or a scrambled control, and NUMB OE or WT control. (e) Western blot analysis of GFAP expression in NHA cells after treatment with miR-146a-5p mimic and/or Notch inhibitor DAPT and associated quantification. (f) ELISA of top four upregulated cytokines released by NHA cells after treatment with miR-146a-5p mimic with and without the Notch pathway inhibitor DAPT. (g) Western blot analysis of GFAP expression in NHA cells after treatment with NUMB siRNA and/or DAPT associated quantification. (h) ELISA of top four up regulated cytokines released by NHA cells after treatment with NUMB siRNA and/or DAPT. All data displayed from three independent experiments. n.s.= not significant, $^{*}p < 0.05$, $^{**}p < 0.01$, $^{***}p < 0.001$, $^{****}p < 0.0001$.

In summary, miR-146a-5p alters cytokine expression via NUMB silencing and dysregulates downstream proteins in the Notch signalling pathway including HES1, HEY2 and CCN1 suggesting a dysregulation of the overall Notch pathway.

3.6 | Mir-146a-5p knockdown (KD) in MBM cells decreases tumour burden and increases animal survival

A proof-of-concept study was performed with a miR-146a-5p knockdown model to investigate its effect on MBM development in vivo. MiR-146a-5p was knocked down by lentiviral transduction of a sponge mRNA in H1_DL2 cells (miR-146a-5p KD, Figure S13) and injected i.c. into female nude mice. As a control, mice were injected i.c. with H1_DL2 cells transduced with a scrambled miR-NC vector. Bioluminescence imaging showed a significantly reduced MBM burden at weeks 4 and 6 in mice injected with miR-146a-5p KD cells, as compared to control animals (Figure 6a,b). Furthermore, at week 6, a reduced tumour burden in the body of mice injected with miR-146a-5p KD cells was observed (Figure 6b). miR-146a-5p KD mice survived significantly longer than control mice (Figure 6c), and the miR-146a-5p KD tumours displayed a lower Ki67 expression indicating less tumour proliferation (Figure 6d,e).

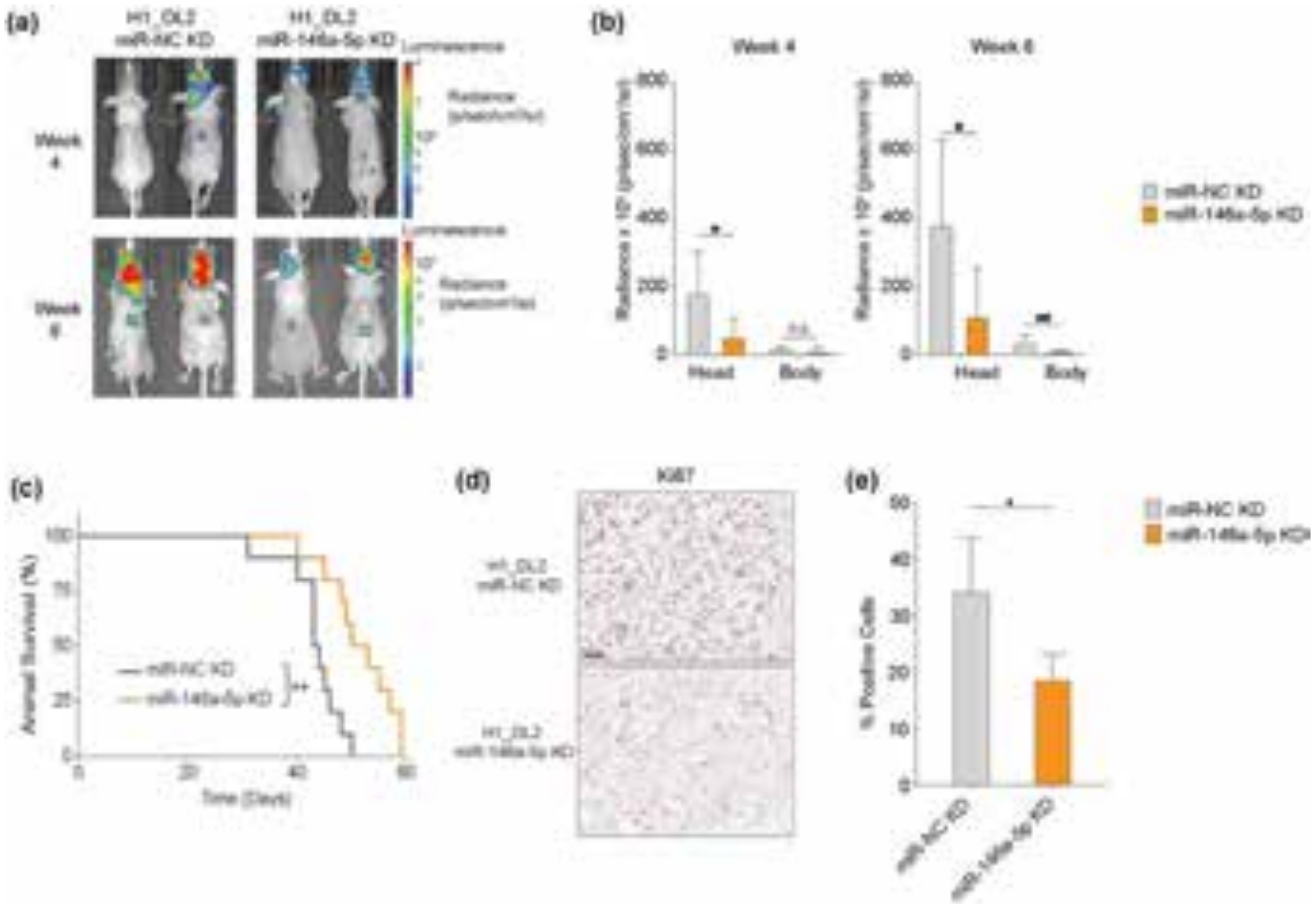

FIGURE 6 miR-146a-5p knockdown in MBM cells significantly decreased tumour burden and increased survival in a mouse brain metastasis model. (a) 5×10^5 H1_DL2 miR-NC KD (control) or H1_DL2 miR-146a-5pKD cells were injected intracardially into mice. Tumour burden was evaluated at week 4 and 6 with IVIS bioluminescent imaging. $n = 10$ mice per group. (b) Tumour distribution in head and body were quantified at week 4 and 6 by the average radiance in photons/s/cm^2/steradia (p/s/cm^2/sr). (c) Kaplan–Meier survival curves calculated for all animals in the treatment study. (d) Representative images of Ki67 staining of FFPE sections of brain tumour tissue from animal test subjects after sacrificing. Scale bar = 50 μm. (e) Quantification of Ki67 staining as a percentage of total cells in each tumour. n.s.= not significant, $^*p < 0.05$, $^{**}p < 0.01$.

Taken together, miR-146a-5p KD reduced MBM tumour burden and increased survival in a mouse model of human MBM, indicating its involvement in MBM development.

3.7 | Deserpidine inhibits miR-146a-5p activity and suppresses MBM development

In order to identify potential drugs that could suppress miR-146a-5p activity, we performed an *in silico* structure modelling to predict the 3-dimensional structure of the hairpin loop of the pre-miR-146a (Figure 7a), followed by a virtual screening of compounds with the potential to bind to the miR-146a-5p 3D-modelled structure (Figure 7b). The top three candidates predicted to cross the BBB were deserpidine, demecarium bromide (demecarium) and fosamprenavir. These drugs were chosen for further functional in vitro experiments. Both deserpidine and demecarium reduced miR-146a-5p levels significantly in both H1 cells and H1-EVs, while fosamprenavir did not alter the miRNA levels significantly (Figure 7c, Figure S14a). A viability screening on H1, H2, H3 and H10 cells determined the IC_{50} doses to be much lower for deserpidine (16.56–29.76 μM) (Figure 7d) than demecarium (97.79–271.33 μM) (Figure S14b,c), thus deserpidine was chosen for subsequent experiments.

Deserpidine is an ester alkaloid derived from Rauwolfa canescens and has been used in the treatment of psychosis and hypertension (Zhang et al., 2009). A dose-dependent inhibition of cell migration was observed in deserpidine-treated H1 cells (Figure 7e), as well as a dose-dependent induction of apoptosis in H1 cells (Figure 7f). Additionally, EVs derived from deserpidine-treated H1 cells did not activate NHAs (Figure S15), further confirming the role of MBM-EVs in NHA activation.

Here, deserpidine decreased miR-146a-5p expression levels in H1 MBM cells and in H1-EVs, subsequently leading to induction of apoptosis and inhibition of cell viability and migration in these cells.

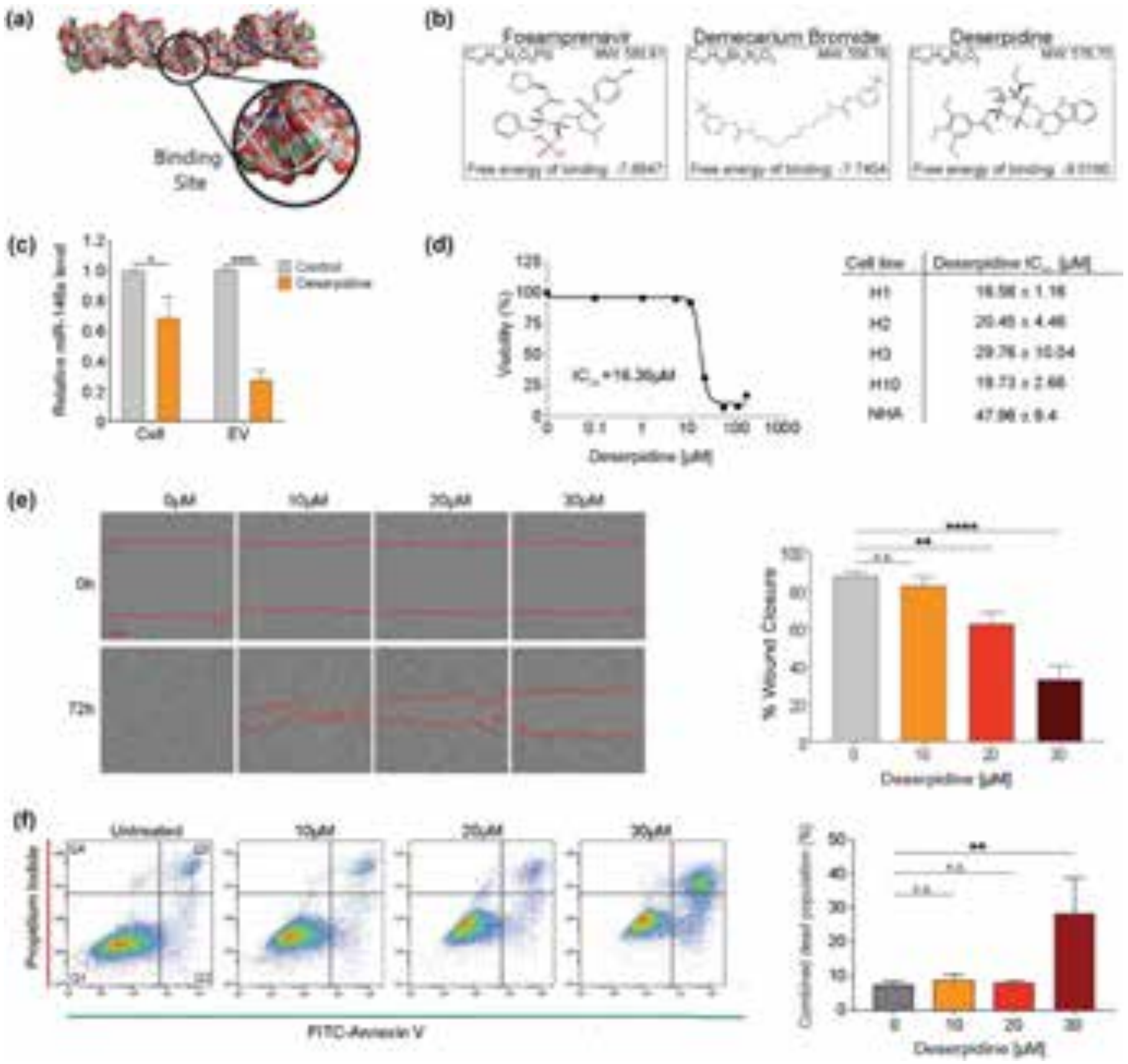

FIGURE 7 Deserpidine reduces the expression of miR-146a-5p in vitro and reduces the viability and proliferation of MBM cells. (a) Schematic representation of the 3D structure of the miR-146a-5p binding site for high-throughput molecular docking analysis. (b) Schematic representation of the top 3 binding partners of miR-146a-5p available for purchase and predicted to cross the blood brain barrier. (c) qPCR analysis of miR-146a-5p expression in H1 cells and EVs after deserpidine treatment. (d) Representative IC_{50} survival curve of H1 cells after treatment with increasing drug concentrations (0.01–150 μM) for 72 h and corresponding deserpidine IC_{50} doses of all MBM cell lines and NHA. (e) Representative images from wound healing assay of H1 cells after treatment with various concentrations of deserpidine and quantification of % wound closure at 72 h. Scale bar = 300 μm. (f) Annexin V-FITC and PI staining to assess apoptosis by flow cytometry in H1 cells treated with increasing concentrations of deserpidine for 72 h and corresponding quantification of live cell and apoptotic cell populations (Q2 + Q3) represented as percentage of total cell population. All data displayed from three independent experiments. Quadrant 1: Live cells. Quadrant 2: Early apoptosis. Quadrant 3: Late apoptosis. Quadrant 4: Necrosis. n.s.= not significant, $^{*}p < 0.05$, $^{**}p < 0.01$, $^{****}p < 0.0001$. $N = 3$.

3.8 | Deserpidine inhibits MBM tumour burden and increases animal survival

To determine the preclinical potential of deserpidine, female NOD/SCID mice were injected i.c. with 5.0×10^5 H1_DL2 cells and treated with either deserpidine or solvent only as control for 6–7 weeks. MRI showed that in mice treated with 0.15 mg/kg deserpidine, the numbers and volumes of MBM tumours were significantly reduced, compared to control mice (no treatment) (Figure 8a,b).

In a second experiment, bioluminescence imaging confirmed that mice injected with 0.5 mg/kg deserpidine had less tumour burden, compared to the control animals. No effects were observed on extracranial metastasis (Figure 8c,d). A Kaplan–Meyer

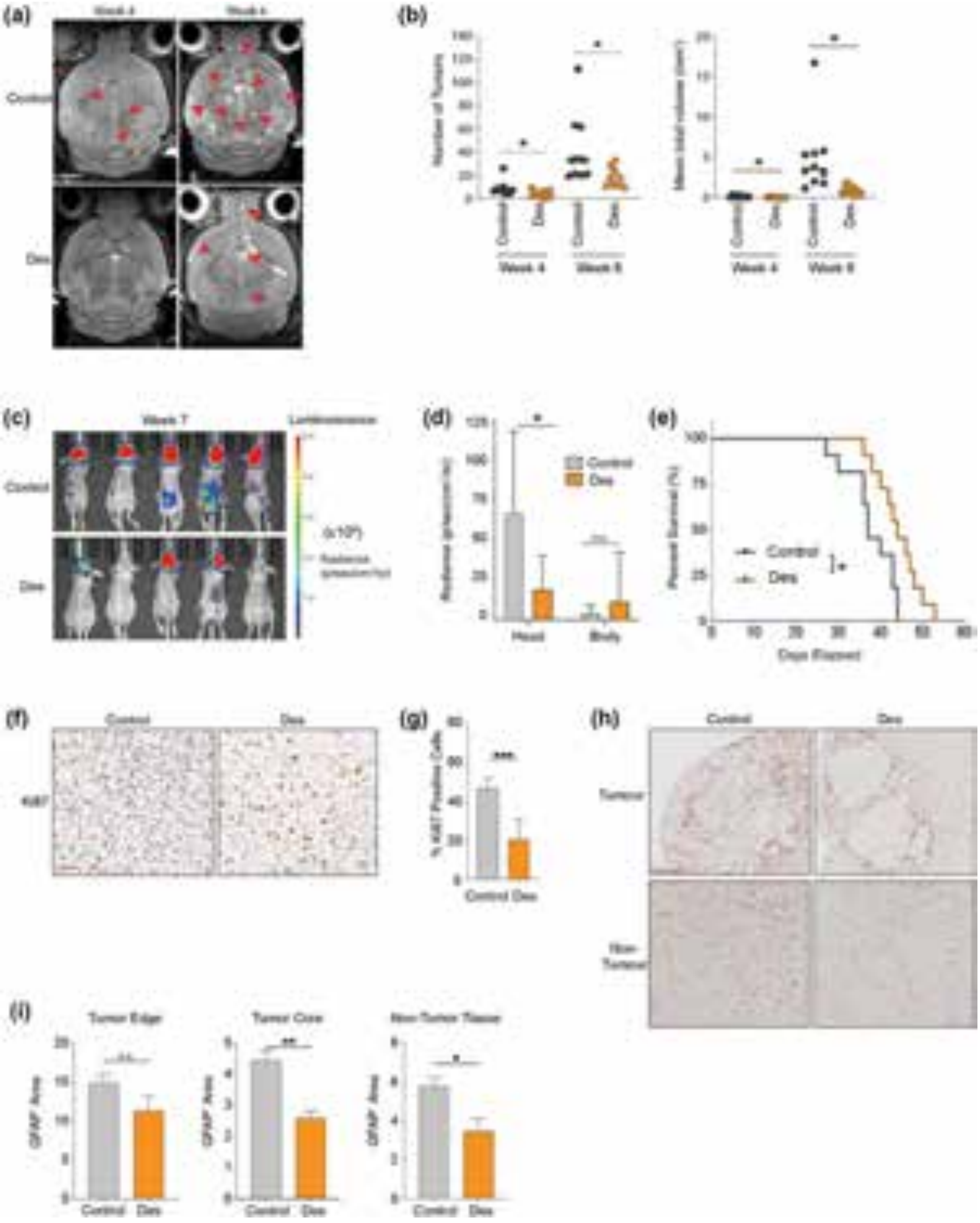

FIGURE 8 Deserpidine reduces tumour burden and increases mice overall survival in vivo. (a) Development of brain metastasis assessed by T2 weighted MRI at week 4 and 6 after intracardial injection of MBM H1_DL2 cells. Mice were either treated with 0.15 mg/kg deserpidine or solvent 3 days per week. $n = 10$ mice per group. (b) Quantification of the numbers and volumes of brain metastasis in 0.15 mg/kg deserpidine-treated and control animals. (c) Development of tumour burden evaluated week 4 and 6 with IVIS bioluminescent imaging after i.c. injection of MBM H1_DL2 cells. Mice were either treated with 0.5 mg/kg deserpidine or solvent every 3 days. $n = 10$ mice per group. (d) tumour distribution in head and body were quantified by the average radiance in photons/s/cm^2/steradia (p/s/cm^2/sr). (e) Kaplan–Meier survival curves calculated for all animals in the second treatment study. (f) Representative images of Ki67 staining of formalin fixed paraffin embedded (FFPE) sections of brain tumour tissue from animal test subjects after sacrificing. Scale bar: 50 μm. (g) Quantification of Ki67 staining as a percentage of total cells in each tumour. (h) Representative images of GFAP staining of FFPE sections of brain tumour tissue and brain non-tumour tissues from animal test subjects after sacrificing. Scale bar = 200 μm. (i) Quantification of GFAP staining as a percentage of intensity of GFAP in tumour edge, tumour core and non-tumour tissue areas. Data are displayed as mean ± SEM. Groups were compared using the Welch *t*-test. $^*p < 0.05$, $^{**}p < 0.01$, $^{***}p < 0.001$.

survival plot showed increased animal survival in deserpidine treated mice, compared to controls (Figure 8e). Cell proliferation was reduced in MBM tumours from deserpidine treated mice compared to control mice, as indicated by Ki67 expression (Figure 8f,g). GFAP staining showed a significant reduction of GFAP+ cells within the tumour mass and in normal brain tissue after deserpidine treatment, as well as a trend towards reduction in normal tissue close to the tumour edge (Figure 8h,i). Taken together, these results suggest that deserpidine shows inhibition of tumour growth which further adds to inhibition of miR146a-5p and therefore should be further exploited in a clinical context of MBM.

4 | DISCUSSION

Despite multimodal treatment, brain metastasis is a common complication in melanoma patients with advanced disease (Achrol et al., 2019). Thus, an improved molecular understanding of the metastatic process with the aim of discovering new adjuvant treatments is necessary. It has previously been shown that brain metastasis development is mediated by complex interactions between tumour cells and normal cells, facilitated in part by the transfer of EVs to establish a metastasis-promoting environment (Gowda et al., 2020; Tamas et al., 2022). To our knowledge this is the first study showing that MBM-EVs pretreatment increases brain metastasis burden in mice (Figure 1e,f), possibly due to increased transmigration of tumour cells through the BBB or improved survival of those cells already transmigrated. The importance of astrocytes in development of both primary and secondary neural malignancies is well documented, but the molecular mechanisms of astrocyte-tumour interactions are only just being discovered (Burn et al., 2021; Zou et al., 2019).

In the present study, we demonstrate that healthy astrocytes are remodelled via transfer of EV-packaged miR-146a-5p from MBM cells, which increases Notch signalling, stimulating MBM development. We also show, in a biological and therapeutic context, that a reduction of miR-146a-5p activity reduces MBM formation.

For melanomas, reports regarding the role of miR-146a-5p in metastatic development is conflicting. In a xenograft model by Hwang and colleagues, a loss of miR-146a-5p expression was seen in melanoma cells, where its overexpression reduced migration and invasion. In contrast, Pu and colleagues found that miR-146a-5p increased cell migration and invasion in melanomas (Hwang et al., 2012; Pu et al., 2018). Here, we show that miR-146a-5p is highly expressed across a number of human MBM cell lines, as well as in their secreted EVs, compared to healthy astrocytes and melanocytes. In addition, significantly higher miR-146a-5p levels were seen in clinical MBM samples, compared to healthy brain tissue (Figure 3i,j). In this context, prior clinical studies suggest that miR-146a-5p is overexpressed in both primary and metastatic lesions, but according to an in vivo melanoma progression model, it is reduced in circulating tumour cells (CTCs), indicating a site-specific mechanism of action (Dika et al., 2020; Raimo et al., 2016). This is in line with our findings, where we found low levels of miR-146a-5p in all melanoma patient blood EV samples compared to healthy individuals, but increased miR-146a-5p levels in metastasis samples, with the highest expression levels seen in MBM cell lines and clinical MBM samples. Our initial screening of human serum samples indicates that miR-146a-5p is not a suitable candidate as a liquid biopsy biomarker; however, this would need to be evaluated in a larger panel of blood samples. Given this, our data suggests that miR-146a-5p has a role in MBM-EVs by activating astrocytes that stimulates CTCs once they have reached the secondary organ.

A crosstalk between activated astrocytes and tumour cells in the brain may stimulate the progression of both primary and secondary brain tumours (Heiland et al., 2019; Zhang et al., 2015; Zou et al., 2019) through paracrine signalling as a main source of communication where cancer-induced cytokine profiles in astrocytes stimulate tumour growth and also protect them against immune responses (Heiland et al., 2019). Here we show that an increased production of key cytokines (IL-6, IL-8, MCP-1 and CXCL1), known to facilitate transmigration of breast cancer cells across the BBB (Fares et al., 2021), were increased following NHA exposure to MBM-EVs or miR-146a-5p mimic. In melanoma, these secreted factors have all been found to support growth and dissemination, as corroborated by our findings in Fig S5. IL-6 induced production of glutathione has been shown to stimulate MBM (Obrador et al., 2011) by triggering MMP-2 enzymatic activity in the tumour microenvironment (Rossi et al., 2018). Augmented IL-8 levels have been shown to increase cell migration, invasion, and adhesion capacities of metastatic melanoma cells by activating the MAPK signalling pathway (Liu et al., 2012). Compared to primary melanomas, MCP-1, and its corresponding receptors CCR2 and CCR4, have been shown to be overexpressed in MBM. An evoked MCP-1 expression and an altered astrocyte secretome has been reported to enhance MBM proliferation, migration, and invasion (Pozzi et al., 2022). Moreover, increased astrocyte secretion of MCP-1 can also contribute to an increased BBB permeability that may facilitate MBM establishment (Stamatovic et al., 2003; Weiss et al., 1998; Yao & Tsirka, 2014). Further, CXCL1 has been shown to constitutively increase expression of NF-κB in melanoma which contribute to melanoma progression via angiogenesis (Dhawan & Richmond, 2002). All these cytokines were triggered in NHAs following MBM-EV exposure, which suggest that they have a prominent role in MBM formation. The exact mechanisms on how they stimulate MBM progression remains to be elucidated.

Mechanistically we show, using *in silico* and in vitro methods, that NUMB, an inhibitory protein in the Notch signalling pathway, is a binding partner of miR-146a-5p in NHAs. MiR-146a-5p binding resulted in a targeted silencing of the Numb protein, with a subsequent activation of the several downstream signalling proteins and transcription factors associated with the Notch signalling pathway. Increased Notch signalling can have several effects on cancer development. This includes, among others, apoptosis inhibition, angiogenesis, induction of epithelial to mesenchymal transition (EMT) and formation of brain metastasis (Xing et al., 2013).

Numb has previously been described as a miR-146a-5p target in melanoma (Forloni et al., 2014; Raimo et al., 2016). Our research importantly shows an upregulation of the Notch pathway in surrounding astrocytes in vitro via EV transfer of miR-146a-5p from melanoma cells, that subsequently stimulates MBM development. To substantiate these results, we performed an in vivo proof-of-concept study, by injecting miR-146a-5p KD MBM cells i.c. using a reproducible and predictive human MBM animal model (Sundstrøm et al., 2013). A significant decrease in the subsequent brain metastatic burden with increased animal survival was observed after KD, supporting the important role of miR-146a-5p in MBM development.

Drugs targeting brain metastasis specifically are not available, and systemic therapies are usually ineffective (Kim et al., 2018). To find such drugs is a challenging task due to, among others, problems associated with BBB penetrance. From a therapeutic viewpoint, repurposing of drugs is an attractive strategy, as the time needed to bring such drugs to the clinic is shorter, less investments are needed, and the risk of failure is lower (Pushpakom et al., 2019). Using targeted *in silico* analysis, we screened commercially available compounds that could potentially bind to the 3D-modelled structure of miR-146a-5p, thus inhibiting its transcription. Subsequent in vitro and in vivo studies showed that deserpidine reduced the brain metastatic tumour burden, resulting in an inhibited MBM development and increased animal survival. Brain tumours dissected from these mice were found to have less penetrance of GFAP+ cells into the tumour mass, and in the overall brain, possibly indicating a reduced migration/invasion ability of the astrocytes via miR-146a-5p inhibition.

In conclusion, we show that MBM-EV-transferred miR-146a-5p is an important driver of MBM niche establishment, via the induction of a cancer-promoting activated astrocyte phenotype where Notch signalling, and cytokine production are elevated, leading to a feedback loop encouraging MBM growth. Through this novel discovery, we were able to inactivate the miRNA through both KD or deserpidine treatment and thereby decrease MBM growth in vivo. These findings encourage additional assessment of the role of MBM-EVs-stromal interactions in metastasis, and a further evaluation of deserpidine as an adjuvant treatment for patients with MBM or for melanoma patients at risk of developing brain metastasis.

AUTHOR CONTRIBUTIONS

Emma Rigg: Data curation; formal analysis; investigation; methodology; writing—original draft; writing—review and editing. **Jiwei Wang**: Data curation; formal analysis; investigation; methodology; writing—original draft; writing—review and editing. **Zhiwei Xue**: Data curation; formal analysis; investigation; writing—review and editing. **Taral R. Lunavat**: Conceptualization; data curation; formal analysis; methodology; writing—review and editing. **Guowei Liu**: Data curation; formal analysis; investigation; writing—review and editing. **Tuyen Hoang**: Data curation; formal analysis; investigation; writing—review and editing. **Himalaya Parajuli**: Data curation; formal analysis; investigation; writing—review and editing. **Mingzhi Han**: Data curation; formal analysis; investigation; writing—review and editing. **Rolf Bjerkvig**: Conceptualization; data curation; formal analysis; funding acquisition; investigation; supervision; writing—original draft; writing—review and editing. **Petr V. Nazarov**: Data curation; formal analysis; writing—review and editing. **Nathalie Nicot**: Data curation; formal analysis; writing—review and editing. **Stephanie Kreis**: Data curation; formal analysis; writing—review and editing. **Christiane Margue**: Data curation; formal analysis; writing—review and editing. **Miléne Tetsi Nomigni**: Data curation; formal analysis; writing—review and editing. **Jochen Utikal**: Data curation; formal analysis; writing—review and editing. **Hrvoje Miletic**: Data curation; formal analysis; writing—review and editing. **Terje Sundstrøm**: Data curation; formal analysis; writing—review and editing. **Lars A. R. Ystaas**: Formal analysis; writing—review and editing. **Xingang Li**: Conceptualization; funding acquisition; supervision; writing—review and editing. **Frits Thorsen**: Conceptualization; data curation; formal analysis; funding acquisition; investigation; project administration; supervision; writing—original draft; writing—review and editing. All authors performed the quality assurance of the paper and reviewed and approved the final versions of the manuscript and the figures.

ACKNOWLEDGEMENTS

The TEM, confocal and MR imaging was performed at The Molecular Imaging Centre, Department of Biomedicine, University of Bergen, Norway. Technical assistance from Aurea Castilho, Department of Biomedicine, University of Bergen, is highly appreciated. This work was supported by the Norwegian Cancer Society (182716), The Western Norway Regional Health Authority (F-12856-D11661), The Norwegian Research Council (315566), the University of Bergen, The National Natural Science Foundation of China (82073219, 82203760), the Department of Science & Technology of Shandong Province (ZR2020QH182), and Luxembourg National Research Fund (C21/BM/15739125/DIOMEDES).

CONFLICT OF INTEREST STATEMENT

The authors declare that there are no conflicts of interest.

ORCID

Emma Rigg https://orcid.org/0000-0003-3824-2040
Himalaya Parajuli https://orcid.org/0000-0001-7185-0844

REFERENCES

Achrol, A. S., Rennert, R. C., Anders, C., Soffietti, R., Ahluwalia, M. S., Nayak, L., Peters, S., Arvold, N. D., Harsh, G. R., Steeg, P. S., & Chang, S. D. (2019). Brain metastases. *Nature Reviews Disease Primers*, *5*, 5.

Alles, J., Fehlmann, T., Fischer, U., Backes, C., Galata, V., Minet, M., Hart, M., Abu-Halima, M., Grässer, F. A., Lenhof, H. P., Keller, A., & Meese, E. (2019). An estimate of the total number of true human miRNAs. *Nucleic Acids Research*, *47*, 3353–3364.

Anvari, A., Sasanpour, P., & Rajabzadeh Kheradmardi, M. (2021). Radiotherapy and immunotherapy in melanoma brain metastases. *Hematology/Oncology and Stem Cell Therapy*, *16*, 1–20.

Bartel, D. P. (2018). Metazoan microRNAs. *Cell*, *173*, 20–51.

Bischof, K., Knappskog, S., Hjelle, S. M., Stefansson, I., Woie, K., Salvesen, H. B., Gjertsen, B. T., & Bjorge, L. (2019). Influence of p53 isoform expression on survival in high-grade serous ovarian cancers. *Scientific Reports*, *9*, 5244.

Boire, A., Brastianos, P. K., Garzia, L., & Valiente, M. (2020). Brain metastasis. *Nature Reviews Cancer*, *20*, 4–11.

Burn, L., Gutowski, N., Whatmore, J., Giamas, G., & Pranjol, M. Z. I. (2021). The role of astrocytes in brain metastasis at the interface of circulating tumour cells and the blood brain barrier. *Frontiers in Bioscience (Landmark Ed)*, *26*, 590–601.

Cacho-Diaz, B., Garcia-Botello, D. R., Wegman-Ostrosky, T., Reyes-Soto, G., Ortiz-Sanchez, E., & Herrera-Montalvo, L. A. (2020). Tumor microenvironment differences between primary tumor and brain metastases. *Journal of Translational Medicine*, *18*, 1.

Cesi, G., Philippidou, D., Kozar, I., Kim, Y. J., Bernardin, F., Van Niel, G., Wienecke-Baldacchino, A., Felten, P., Letellier, E., Dengler, S., Nashan, D., Haan, C., & Kreis, S. (2018). A new ALK isoform transported by extracellular vesicles confers drug resistance to melanoma cells. *Molecular Cancer*, *17*, 145.

Cesi, G., Walbrecq, G., Margue, C., & Kreis, S. (2016). Transferring intercellular signals and traits between cancer cells: Extracellular vesicles as "homing pigeons". *Cell Communication and Signaling*, *14*, 13.

Dhawan, P., & Richmond, A. (2002). Role of CXCL1 in tumorigenesis of melanoma. *Journal of Leukocyte Biology*, *72*, 9–18.

Dika, E., Riefolo, M., Porcellini, E., Broseghini, E., Ribero, S., Senetta, R., Osella-Abate, S., Scarfi, F., Lambertini, M., Veronesi, G., Patrizi, A., Fanti, P. A., & Ferracin, M. (2020). Defining the prognostic role of MicroRNAs in cutaneous melanoma. *Journal of Investigative Dermatology*, *140*, 2260–2267.

Escartin, C., Galea, E., Lakatos, A., O'Callaghan, J. P., Petzold, G. C., Serrano-Pozo, A., Steinhäuser, C., Volterra, A., Carmignoto, G., Agarwal, A., Allen, N. J., Araque, A., Barbeito, L., Barzilai, A., Bergles, D. E., Bonvento, G., Butt, A. M., Chen, W. C., Cohen-Salmon, M., … Verkhratsky, A. (2021). Reactive astrocyte nomenclature, definitions, and future directions. *Nature Neuroscience*, *24*, 312–325.

Fares, J., Cordero, A., Kanojia, D., & Lesniak, M. S. (2021). The network of cytokines in brain metastases. *Cancers (Basel)*, *13*, 142.

Forloni, M., Dogra, S. K., Dong, Y., Conte D., Jr., Ou, J., Zhu, L. J., Deng, A., Mahalingam, M., Green, M. R., & Wajapeyee, N. (2014). miR-146a promotes the initiation and progression of melanoma by activating Notch signaling. *eLife*, *3*, e01460.

Geling, A., Steiner, H., Willem, M., Bally-Cuif, L., & Haass, C. (2002). A gamma-secretase inhibitor blocks Notch signaling in vivo and causes a severe neurogenic phenotype in zebrafish. *Embo Reports*, *3*, 688–694.

Gowda, R., Robertson, B. M., Iyer, S., Barry, J., Dinavahi, S. S., & Robertson, G. P. (2020). The role of exosomes in metastasis and progression of melanoma. *Cancer Treatment Reviews*, *85*, 101975.

Hanniford, D., Zhong, J., Koetz, L., Gaziel-Sovran, A., Lackaye, D. J., Shang, S., Pavlick, A., Shapiro, R., Berman, R., Darvishian, F., Shao, Y., Osman, I., & Hernando, E. (2015). A miRNA-based signature detected in primary melanoma tissue predicts development of brain metastasis. *Clinical Cancer Research*, *21*, 4903–4912.

Heiland, D. H., Ravi, V. M., Behringer, S. P., Frenking, J. H., Wurm, J., Joseph, K., Garrelfs, N. W. C., Strähle, J., Heynckes, S., Grauvogel, J., Franco, P., Mader, I., Schneider, M., Potthoff, A. L., Delev, D., Hofmann, U. G., Fung, C., Beck, J., Sankowski, R., … Prinz, M. (2019). Tumor-associated reactive astrocytes aid the evolution of immunosuppressive environment in glioblastoma. *Nature Communications*, *10*, 2541.

Hristova, D. M., Fukumoto, T., Takemori, C., Gao, L., Hua, X., Wang, J. X., Li, L., Beqiri, M., Watters, A., Vultur, A., Gimie, Y., Rebecca, V., Samarkina, A., Jimbo, H., Nishigori, C., Zhang, J., Cheng, C., Wei, Z., Somasundaram, R., … Herlyn, M. (2021). NUMB as a therapeutic target for melanoma. *The Journal of Investigative Dermatology*, *142*(7), 1882–1892.e5.

Hwang, S. J., Seol, H. J., Park, Y. M., Kim, K. H., Gorospe, M., Nam, D. H., & Kim, H. H. (2012). MicroRNA-146a suppresses metastatic activity in brain metastasis. *Molecules and Cells*, *34*, 329–334.

Kim, M., Kizilbash, S. H., Laramy, J. K., Gampa, G., Parrish, K. E., Sarkaria, J. N., & Elmquist, W. F. (2018). Barriers to effective drug treatment for brain metastases: A multifactorial problem in the delivery of precision medicine. *Pharmaceutical Research*, *35*, 177.

Kulkarni, B., Kirave, P., Gondaliya, P., Jash, K., Jain, A., Tekade, R. K., & Kalia, K. (2019). Exosomal miRNA in chemoresistance, immune evasion, metastasis and progression of cancer. *Drug Discovery Today*, *24*, 2058–2067.

Larkin, J., Chiarion-Sileni, V., Gonzalez, R., Grob, J.-J., Rutkowski, P., Lao, C. D., Cowey, C. L., Schadendorf, D., Wagstaff, J., Dummer, R., Ferrucci, P. F., Smylie, M., Hogg, D., Hill, A., Márquez-Rodas, I., Haanen, J., Guidoboni, M., Maio, M., Schöffski, P., … Wolchok, J. D. (2019). Five-year survival with combined nivolumab and ipilimumab in advanced melanoma. *New England Journal of Medicine*, *381*, 1535–1546.

Liu, X., Fang, H., Chen, H., Jiang, X., Fang, D., Wang, Y., & Zhu, D. (2012). An artificial miRNA against HPSE suppresses melanoma invasion properties, correlating with a down-regulation of chemokines and MAPK phosphorylation. *PLoS ONE*, *7*, e38659.

Lunavat, T. R., Cheng, L., Einarsdottir, B. O., Olofsson Bagge, R., Veppil Muralidharan, S., Sharples, R. A., Lässer, C., Gho, Y. S., Hill, A. F., Nilsson, J. A., & Lötvall, J. (2017). BRAF(V600) inhibition alters the microRNA cargo in the vesicular secretome of malignant melanoma cells. *PNAS*, *114*, E5930–e5939.

Obrador, E., Benlloch, M., Pellicer, J. A., Asensi, M., & Estrela, J. M. (2011). Intertissue flow of glutathione (GSH) as a tumor growth-promoting mechanism: Interleukin 6 induces GSH release from hepatocytes in metastatic B16 melanoma-bearing mice. *Journal of Biological Chemistry*, *286*, 15716–15727.

Peinado, H., Zhang, H., Matei, I. R., Costa-Silva, B., Hoshino, A., Rodrigues, G., Psaila, B., Kaplan, R. N., Bromberg, J. F., Kang, Y., Bissell, M. J., Cox, T. R., Giaccia, A. J., Erler, J. T., Hiratsuka, S., Ghajar, C. M., & Lyden, D. (2017). Pre-metastatic niches: Organ-specific homes for metastases. *Nature Reviews Cancer*, *17*, 302–317.

Placone, A. L., Quiñones-Hinojosa, A., & Searson, P. C. (2016). The role of astrocytes in the progression of brain cancer: Complicating the picture of the tumor microenvironment. *Tumor Biology*, *37*, 61–69.

Pozzi, S., Scomparin, A., Ben-Shushan, D., Yeini, E., Ofek, P., Nahmad, A. D., Soffer, S., Ionescu, A., Ruggiero, A., Barzel, A., Brem, H., Hyde, T. M., Barshack, I., Sinha, S., Ruppin, E., Weiss, T., Madi, A., Perlson, E., Slutsky, I., … Satchi-Fainaro, R. (2022). MCP-1/CCR2 axis inhibition sensitizes the brain microenvironment against melanoma brain metastasis progression. *JCI Insight*, *7*, e154804.

Pu, W., Shang, Y., Shao, Q., & Yuan, X. (2018). miR-146a promotes cell migration and invasion in melanoma by directly targeting SMAD4. *Oncology Letters*, *15*, 7111–7117.

Pushpakom, S., Iorio, F., Eyers, P. A., Escott, K. J., Hopper, S., Wells, A., Doig, A., Guilliams, T., Latimer, J., McNamee, C., Norris, A., Sanseau, P., Cavalla, D., & Pirmohamed, M. (2019). Drug repurposing: Progress, challenges and recommendations. *Nature Reviews Drug Discovery*, *18*, 41–58.

Raimo, M., Orso, F., Grassi, E., Cimino, D., Penna, E., De Pitta, C., Stadler, M. B., Primo, L., Calautti, E., Quaglino, P., Provero, P., & Taverna, D. (2016). miR-146a exerts differential effects on melanoma growth and metastatization. *Molecular Cancer Research*, *14*, 548–562.

Rishi, A., & Yu, H. M. (2020). Current treatment of melanoma brain metastasis. *Current Treatment Options in Oncology*, *21*, 45.

Rodrigues, G., Hoshino, A., Kenific, C. M., Matei, I. R., Steiner, L., Freitas, D., Kim, H. S., Oxley, P. R., Scandariato, I., Casanova-Salas, I., Dai, J., Badwe, C. R., Gril, B., Tešić Mark, M., Dill, B. D., Molina, H., Zhang, H., Benito-Martin, A., … Lyden, D. (2019). Tumour exosomal CEMIP protein promotes cancer cell colonization in brain metastasis. *Nature Cell Biology*, *21*, 1403–1412.

Rossi, S., Cordella, M., Tabolacci, C., Nassa, G., D'Arcangelo, D., Senatore, C., Pagnotto, P., Magliozzi, R., Salvati, A., Weisz, A., Facchiano, A., & Facchiano, F. (2018). TNF-alpha and metalloproteases as key players in melanoma cells aggressiveness. *Journal of Experimental & Clinical Cancer Research*, *37*, 326.

Si, W., Shen, J., Zheng, H., & Fan, W. (2019). The role and mechanisms of action of microRNAs in cancer drug resistance. *Clinical Epigenetics*, *11*, 25.

Stamatovic, S. M., Keep, R. F., Kunkel, S. L., & Andjelkovic, A. V. (2003). Potential role of MCP-1 in endothelial cell tight junction 'opening': Signaling via Rho and Rho kinase. *Journal of Cell Science*, *116*, 4615–4628.

Sun, Z., Shi, K., Yang, S., Liu, J., Zhou, Q., Wang, G., Song, J., Li, Z., Zhang, Z., & Yuan, W. (2018). Effect of exosomal miRNA on cancer biology and clinical applications. *Molecular Cancer*, *17*, 147.

Sundstrøm, T., Daphu, I., Wendelbo, I., Hodneland, E., Lundervold, A., Immervoll, H., Skaftnesmo, K. O., Babic, M., Jendelova, P., Sykova, E., Lund-Johansen, M., Bjerkvig, R., & Thorsen, F. (2013). Automated tracking of nanoparticle-labeled melanoma cells improves the predictive power of a brain metastasis model. *Cancer Research*, *73*, 2445–2456.

Tamas, F., Balasa, R., Manu, D., Gyorki, G., Chinezu, R., Tamas, C., & Bălaşa, A. (2022). The importance of small extracellular vesicles in the cerebral metastatic process. *International Journal of Molecular Sciences*, *23*(3), 1449.

Tawbi, H. A.-H., Forsyth, P. A. J., Hodi, F. S., Lao, C. D., Moschos, S. J., Hamid, O., Atkins, M. B., Lewis, K., Thomas, R. P., Glaspy, J. A., Jang, S., Algazi, A. P., Khushalani, N. I., Postow, M. A., Pavlick, A. C., Ernstoff, M. S., Reardon, D. A., Puzanov, I., Kudchadkar, R. R., … Margolin, K. A. (2019). Efficacy and safety of the combination of nivolumab (NIVO) plus ipilimumab (IPI) in patients with symptomatic melanoma brain metastases (CheckMate 204). *Journal of Clinical Oncology*, *37*, 9501.

Théry, C., Witwer, K. W., Aikawa, E., Alcaraz, M. J., Anderson, J. D., Andriantsitohaina, R., Antoniou, A., Arab, T., Archer, F., Atkin-Smith, G. K., Ayre, D. C., Bach, J. M., Bachurski, D., Baharvand, H., Balaj, L., Baldacchino, S., Bauer, N. N., Baxter, A. A., … Zuba-Surma, E. K. (2018). Minimal information for studies of extracellular vesicles 2018 (MISEV2018): A position statement of the International Society for Extracellular Vesicles and update of the MISEV2014 guidelines. *Journal of Extracellular Vesicles*, *7*, 1535750.

Tominaga, N., Kosaka, N., Ono, M., Katsuda, T., Yoshioka, Y., Tamura, K., Lötvall, J., Nakagama, H., & Ochiya, T. (2015). Brain metastatic cancer cells release microRNA-181c-containing extracellular vesicles capable of destructing blood–brain barrier. *Nature Communications*, *6*, 6716.

Valadi, H., Ekström, K., Bossios, A., Sjöstrand, M., Lee, J. J., & Lötvall, J. O. (2007). Exosome-mediated transfer of mRNAs and microRNAs is a novel mechanism of genetic exchange between cells. *Nature Cell Biology*, *9*, 654–659.

Wasilewski, D., Priego, N., Fustero-Torre, C., & Valiente, M. (2017). Reactive astrocytes in brain metastasis. *Frontiers in Oncology*, *7*, 298.

Weiss, J. M., Downie, S. A., Lyman, W. D., & Berman, J. W. (1998). Astrocyte-derived monocyte-chemoattractant protein-1 directs the transmigration of leukocytes across a model of the human blood-brain barrier. *Journal of Immunology*, *161*, 6896–6903.

Xing, F., Kobayashi, A., Okuda, H., Watabe, M., Pai, S. K., Pandey, P. R., Hirota, S., Wilber, A., Mo, Y. Y., Moore, B. E., Liu, W., Fukuda, K., Iiizumi, M., Sharma, S., Liu, Y., Wu, K., Peralta, E., & Watabe, K. (2013). Reactive astrocytes promote the metastatic growth of breast cancer stem-like cells by activating Notch signalling in brain. *EMBO Molecular Medicine*, *5*, 384–396.

Yao, Y., & Tsirka, S. E. (2014). Monocyte chemoattractant protein-1 and the blood-brain barrier. *Cellular and Molecular Life Sciences*, *71*, 683–697.

Zhang, H., Zhong, D., Zhang, Z., Dai, X., & Chen, X. (2009). Liquid chromatography/tandem mass spectrometry method for the quantification of deserpidine in human plasma: Application to a pharmacokinetic study. *Journal of Chromatography B, Analytical Technologies in the Biomedical and Life Sciences*, *877*, 3221–3225.

Zhang, L., Xie, H., & Cui, L. (2018). Activation of astrocytes and expression of inflammatory cytokines in rats with experimental autoimmune encephalomyelitis. *Experimental and Therapeutic Medicine*, *16*, 4401–4406.

Zhang, L., Zhang, S., Yao, J., Lowery, F. J., Zhang, Q., Huang, W. C., Li, P., Li, M., Wang, X., Zhang, C., Wang, H., Ellis, K., Cheerathodi, M., McCarty, J. H., Palmieri, D., Saunus, J., Lakhani, S., Huang, S., Sahin, A. A., … Yu, D. (2015). Microenvironment-induced PTEN loss by exosomal microRNA primes brain metastasis outgrowth. *Nature*, *527*, 100–104.

Zhang, Y., Zhao, J., Ding, M., Su, Y., Cui, D., Jiang, C., Zhao, S., Jia, G., Wang, X., Ruan, Y., Jing, Y., Xia, S., & Han, B. (2020). Loss of exosomal miR-146a-5p from cancer-associated fibroblasts after androgen deprivation therapy contributes to prostate cancer metastasis. *Journal of Experimental & Clinical Cancer Research*, *39*, 282.

Zhao, S., Mi, Y., Zheng, B., Wei, P., Gu, Y., Zhang, Z., Xu, Y., Cai, S., Li, X., & Li, D. (2022). Highly-metastatic colorectal cancer cell released miR-181a-5p-rich extracellular vesicles promote liver metastasis by activating hepatic stellate cells and remodelling the tumour microenvironment. *Journal of Extracellular Vesicles*, *11*, e12186.

Zou, Y., Watters, A., Cheng, N., Perry, C. E., Xu, K., Alicea, G. M., Parris, J. L. D., Baraban, E., Ray, P., Nayak, A., Xu, X., Herlyn, M., Murphy, M. E., Weeraratna, A. T., Schug, Z. T., & Chen, Q. (2019). Polyunsaturated fatty acids from astrocytes activate PPARγ signaling in cancer cells to promote brain metastasis. *Cancer Discovery*, *9*, 1720–1735.

SUPPORTING INFORMATION

Additional supporting information can be found online in the Supporting Information section at the end of this article.

How to cite this article: Rigg, E., Wang, J., Xue, Z., Lunavat, T. R., Liu, G., Hoang, T., Parajuli, H., Han, M., Bjerkvig, R., Nazarov, P. V., Nicot, N., Kreis, S., Margue, C., Nomigni, M. T., Utikal, J., Miletic, H., Sundstrøm, T., Ystaas, L. A. R., Li, X., & Thorsen, F. (2023). Inhibition of extracellular vesicle-derived miR-146a-5p decreases progression of melanoma brain metastasis via Notch pathway dysregulation in astrocytes. *Journal of Extracellular Vesicles*, *12,* e12363. https://doi.org/10.1002/jev2.12363

Supplementary Materials and Methods

2.3 Western blotting (WB)

Cells and EV lysates were isolated with RIPA lysis buffer supplemented with 10X protease and phosphatase inhibitor cocktail (Roche, Basel, Switzerland). Protein concentrations were measured using a Pierce BCA assay (Life Technologies, San Diego, CA, USA). Equal amounts of protein were diluted in NuPAGE™ 4X LDS Sample Buffer (Invitrogen, Waltham, MA, USA) and 10X Sample Reducing Agent (Invitrogen) and electrophoresed on a 10% or 12% Tris-Glycine SDS-polyacrylamide gel. Gels were run at 80V for stacking and 120V for separation until sample dye reached the bottom of the gel. Samples were transferred to a nitrocellulose membrane at 100 V for 1 h. Membranes were blocked for 1 h at room temperature (RT) with 5% skim milk in 1X TBS-T solution and incubated with primary immunoblotting antibodies: GAPDH (cat. no. 5174; Cell Signaling Technology, Inc., Danvers, MA, USA), GFAP (cat. no. 80788; Cell Signaling Technology), NUMB (cat. no. 2756; Cell Signaling Technology), CD9 (cat. no. 13118; Santa Cruz Biotechnology), Flotillin-1 (cat. no. 74566; Santa Cruz Biotechnology), TSG-101 (cat. no. 7964; Santa Cruz Biotechnology), Calnexin (cat. no. 46669; Santa Cruz Biotechnology) overnight at 4^0C. Membranes were washed and incubated with secondary antibodies (HRP anti-rabbit IgG; HRP 1:10,000, anti-mouse IgG 1:10 000; Santa Cruz Biotechnology, Inc, Dallas, TX, USA) for 2 h at room temperature. Signals were visualized with SuperSignal™ Pico/Femto Chemiluminescent Substrate (Thermo Fisher Scientific, Waltham, MA, USA) using a LAS-3000 imaging system (Fujifilm, Saitama, Japan).

2.4 Animals

Female NOD/SCID mice or female nude mice (6-8 weeks old) were fed a standard pellet diet and provided water *ad libitum*. Anesthesia was induced with 3% isoflurane (Abbott Laboratories, Chicago, IL, USA) in oxygen and maintained with 1.5% isoflurane in oxygen during all procedures unless stated otherwise. The mice were monitored daily and sacrificed when significant morbidity symptoms were observed. The Norwegian National Animal Research Authority (Application #14751, approved Feb 6th, 2018, and Application #28740, approved Dec 21st, 2021) and The Institutional Animal Care and Use Committee (IACUC) of Shandong University, Jinan, China (Approval number: KYLL-2020(KS)-515) approved all animal procedures prior to all experiments.

2.5 Visualization of EVs *in vivo*

EVs and Cy7 NHS ester (cat. no. A8109; APExBIO, Houston, TX, USA) were mixed at a mass ratio of 100:1 and incubated at 37^{0}C for 15 min in the dark. Cy7-stained EVs and unstained EVs (as negative control) were then transferred to 300 kDa Vivaspin centrifugal concentrators (Sigma-Aldrich, St. Louis, MO, USA). The samples were centrifuged at 4,000*g* and checked in between to ensure that a small part of the sample remained on top of the filter. Samples were washed with 5 ml PBS and the centrifugation procedure with subsequent washing step was repeated.

5 x 10^9 Cy7-labeled EVs in 100 μL PBS was injected intracardially into a nude mouse. Mice were fluorescently imaged after 24 h using the IVIS-200 optical imaging (OI) system (Xenogen, Alameda, CA, USA). The mice were then sacrificed by perfusion of 0.9% saline solution into the left cardiac ventricle. Brains, hearts, lungs, livers, spleens, kidneys, and intestines were removed, and *ex vivo* fluorescence imaging was done on the organs, using the IVIS-200 OI system (Xenogen, Alameda, CA, USA).

2.6 Assessment of H1_DL2 growth cocultured with activated NHA

NHA cells were seeded at 5.0×10^3 cells/well in 200 μL into each well of a 96 well dish (Nunc) and left for 24 h. Then, NHA were incubated with 5.0×10^9 EVs/mL from H1 or NHA cells or with PBS for 48 h, before being cocultured with H1_DL2 cells. Proliferation of H1_DL2 cells during 96 h was assessed *in vitro* using a Nikon TE2000 inverted microscope (Nikon Instruments Inc., Melville, NY. USA).

2.7 Assessment of MBM burden in mice after intracardial pre-injections of EVs

12 female NOD/SCID mice were anesthetized with 3% sevoflurane in oxygen and anesthesia was maintained with 1.5% sevoflurane in oxygen. The mice were fixed in a supine position on a heating pad to maintain a core temperature of 37^0C. The mice were randomized into two groups (6 mice per group). One group received 3 injections (once/day) with 5.0×10^9 EVs from H1 MBM cells in 100 μL PBS (in total 1.5×10^{10} EVs), while the second group received 3 injections (once/day) of 100 μL PBS. All injections were done intracardially, using a 30G insulin syringe (Omnican50, B. Brain Medical AS, Vestskogen, Norway), by ultrasound guidance (Vevo 2100 Imaging System, VisualSonics Inc., Toronto, Canada). After 2 days, 5.0×10^5 H1_DL2 MBM cells in 100 μL PBS were injected intracardially into all mice, by ultrasound guidance.

2.8 *In vivo* magnetic resonance imaging (MRI)

Brain metastasis development in the NOD/SCID mice after intracardiac injections of EVs and tumor cells was studied at weeks 4 and 6 using a 7 Tesla Pharmascan small-animal MR scanner (Bruker BioSpin MRI, Ettlingen, Germany) equipped with a 1-channel circular transmitter coil and a 4-channel receiver surface coil. T2 weighted (T2w) coronal images were obtained with the following RARE sequence scan parameters: FOV 20 mm × 20 mm, matrix size 256 × 256, 0.5 mm slice thickness, TR 3200 ms, TE 38 ms, FA 90^0, 4 averages, scan time 6 min 49 s.

Brain metastasis development in the NOD/SCID mice after intracardiac injections of tumor cells followed by deserpidine treatment was studied at weeks 4 and 6 using a 7 Tesla small-animal PET/MR scanner (MR Solutions Ltd., Guildford, UK) equipped with a 20mm inner diameter quadrature transmit/receive volume coil. T2w coronal images were obtained using the following fast spin echo sequence scan parameters: FOV 20 mm × 20 mm, matrix size 256 × 256, 0.5 mm slice thickness, TR 3000 ms, TE 45 ms, FA 90^0, 2 averages, scan time 3 min 41 s.

Visualization of MR images and quantification of tumor numbers and volumes ($V = 4/3 \times \pi \times r^3$) were performed using the 32-bit OsiriX freeware, version 5.8.1 (Pixmeo SARL, Geneva, Switzerland) in both studies.

2.9 *In vitro* uptake of EVs/miRNA inhibitors into normal human astrocytes (NHA)

Confocal imaging was used to visualize and confirm the uptake of either EVs or miRNA inhibitors into NHA cells.

For confirmation of uptake of EVs into NHA cells, EVs from H1, H2 and NHA cells were labeled using the PKH67 Green Fluorescent Cell Linker Kit (Sigma-Aldrich), as follows: 5.0×10^9 EVs, or equivalent volume PBS as control, were diluted up to 1mL in Diluent C and mixed with equal volume 4.0×10^{-6}M PKH67 dye for 5 min. Staining was quenched with 2 mL of 1% BSA solution for 1 min. Excess stain was removed by spinning samples in Vivaspin 300 kDa centrifugal filters (Sigma-Aldrich) at 4,000*g* and rinsed with 5 mL PBS 3 times. Final EV samples were diluted in growth medium and 5.0 x 10^9 EVs/mL of each were added to 2.0 x 10^4 NHA cells on coverslips in a 24-well plate.

To confirm the entry of miRNA inhibitors into NHA cells, a fluorescein-tagged fluorescent miR-146a-5p inhibitor (Qiagen, Düsseldorf, Germany) was added to 5.0 x 10^4 NHA cells on coverslips in a 24-well plate.

After 24 h, NHA cells were fixed with 4% PFA for 10 min at RT and stained sequentially with 5 μg/L Wheat Germ Agglutinin (WGA), Texas Red™-X Conjugate (Invitrogen) for 10 min and 300 nM DAPI (Invitrogen) for 5 min. Cells were rinsed and mounted on slides with ProLong™ Gold Antifade Mountant (Invitrogen). Fluorescent images were obtained by confocal laser scanning microscopy using a Leica TCS SP8 system (Leica Microsystems, Wetzlar, Germany) with a 100x NA1.4 HC PL APO STED White objective. Z-stacks were captured with a step size of 0.4 μm and presented as maximum intensity projections. The experiments were done in duplicate.

2.10 Immunofluorescence of GFAP expression

After co-culture with 3.0 x 10^8 EVs/mL for 48 h, NHA cells were either lysed for western blotting or were fixed with 3% paraformaldehyde (PFA) for 10 min at RT and permeabilized with 0.1% Triton X-100 for 10 min. After fixation, cells were incubated with 3% bovine serum albumin (BSA; Sigma-Aldrich) in PBS for 1 h to block nonspecific binding. NHA cells were then incubated with rabbit polyclonal antibody against GFAP (1:200, cat. no. 80788; Cell Signaling Technology) at 37^0C for 1 h. After washing with PBS containing Mg2+ and Ca2+, the cells were incubated with Alexa Fluor 594-conjugated anti-rabbit IgG (Invitrogen) for 1 h at 37^0C. Cell nuclei were then stained with DAPI (Thermo Fisher Scientific). Fluorescent images were obtained by confocal laser scanning microscopy using a Leica TCS SP8 system (Leica Microsystems).

2.11 Cell proliferation and viability

The Cell Counting Kit–8 (Sigma Aldrich 96992) was used to examine the effects of EVs from NHA and H1 on NHA, as well as to determine the IC_{50} doses of deserpidine, demecarium bromide and fosamprenavir on MBM cell lines. Drugs were all purchased from MedChemExpress, diluted in DMSO at recommended stock concentration according to the manufacturer and kept at -80°C for long term storage.

H1, H2, H3, H10 and NHA cells were seeded at 5.0 x 10^3 cells/well in 200µl in 96-well plates. After 24 h, cells were treated with 5.0 x 10^9 EVs/mL from NHA or H1 for 48 h, or deserpidine, demecarium or fosamprenavir (0, 0.1, 1, 5, 10, 20, 50, 100, and 150 µM) for 72 h. 10 µL of CCK-8 reagent was added to each well, and the plate was incubated for 4 h at 37^0C. Absorbance of plates was measured at 450 nm using a Multiskan FC Microplate Photometer (Thermo Fisher Scientific). IC_{50} doses were calculated using GraphPad Prism v7 software (GraphPad Software Inc., La Jolla, CA, USA). The experiments were done in triplicate.

2.12 Wound healing assays

Migration of cells was evaluated by two different wound healing assays.

First, NHA or H1 cells were seeded at 3.0 x 10^4 cells/well in a 96-well ImageLock plate (Essen BioScience Ltd., Welwyn Garden City, UK) and incubated for 48 h until confluency. A wound-maker tool (Essen BioScience Ltd.) was used to simultaneously create a uniform wound across all wells, after which H1 or NHA EVs, H1 EVs+miR-146a-5p inhibitor, H1 EVs+miR-146a-5p NC inhibitor or deserpidine (0, 10, 20, 30 µM) was added to the cells. The plates were imaged every 2 h for 72 h using the IncuCyte Live Cell Imaging System (Essen BioScience Ltd.), and subsequent analysis was done with the IncuCyte Scratch Wound Cell Migration Software Module (cat. no. 9600-0012; Essen BioScience Ltd.). The experiments were done in triplicate.

Second, NHA cells were seeded at 2.0 x 10^5 cells/well in 6-well, flat-bottomed plates and incubated at 37^0C overnight. A cell-free gap was generated by scratching with a 200 µL pipette tip. PBS or 5.0 x 10^9 EVs/mL from NHA or H1 cells were then added to the wells. The wound closure area was measured at 0 h, 24 h, 48 h, 72 h and 96 h using a Leica DMi8 microscope (Leica Microsystems) and quantified using ImageJ v1.53c freeware (National Institutes of Health, Bethesda, MD, USA). The experiments were done in triplicate.

2.13 Cytokine array and enzyme-linked immunosorbent assay (ELISA)

A human cytokine antibody array (ab133996; Abcam, Cambridge, UK) was used to screen for the secretion of 23 different cytokines in the supernatant of PBS or H1 EV treated NHA cells *in vitro* following the manufacturer´s protocol.

For ELISA, NHA were seeded at 5.0 x 10^4 cells/well in 6-well plates (Eppendorf) and incubated for 48 h with 5.0 x 10^9 EVs/mL; H1 and H2 EVs in the presence or absence of miR-146a-5p inhibitor, H1 cells with WT or overexpression of NUMB in the presence of miR-146a-5p mimics, miR-146a-5p mimics combined with the Notch inhibitor DAPT, or DAPT during silencing of NUMB with a siRNA. Quantitative ELISAs for IL-6 (ab46042; Abcam), IL-8 (ab46032; Abcam), MCP-1 (ab179886; Abcam) and CXCL-1 (ab190805; Abcam) were performed to verify and quantify cytokine secretion according to the manufacturer´s instructions. Absorbance was measured using a Multiskan FC Microplate Photometer (Thermo Fisher). The experiments were performed in triplicate.

2.14 Assessment of H1 growth cocultured with activation NHA conditioned media

To determine the specific cytokine affecting growth of H1 cells by activated NHA cells on H1 cells, NHA were seeded at 5.0 x 10^3 cells/well in 100 μL into a 96 well dish (Nunc) and left for 48 h. Then, NHA were incubated with 5.0 x 10^9 EVs/mL from H1 or with PBS for 48 h. After 48 h, EV containing media was exchanged with fresh media for another 48 h. Conditioned media was then sterile filtered and transferred to a 96-well plate containing 5.0 x 10^3 H1 cells/well. When transferring NHA-CM to H1 cells in a 96-well plate, 0.25μg/mL of either anti-CXCL1, anti-MCP-1, anti-IL-8 or anti-IL-6 (R&D Systems, Minneapolis, United States) antibodies were added. After 48 hours, proliferation of H1 cells was assessed by adding 10uL of the WST-1 cell proliferation reagent to each well and incubating for 3 h at 37^0C. Absorbance of plates was measured at 450 nm using a Multiskan FC Microplate Photometer (Thermo Fisher Scientific).

2.15 Microarray analysis of differentially expressed miRNAs in EVs

To determine miRNAs differentially expressed in EVs, a microarray profiling was done on EVs collected from 3 MBM cell lines (H1, H2, H3) and from NHA and melanocytes in duplicates. Total RNA was isolated from samples using the RNeasy Micro Kit (Qiagen, Düsseldorf, Germany).

Affymetrix GeneChip® miRNA Array v4.0 st (Thermo Fisher Scientific) were performed using 500 ng of total RNA, with RIN of >9, according to the manufacturer's user guide (FlashTag™ Biotin HSR RNA Labeling Kit For Affymetrix® GeneChip® miRNA Arrays P/N 703095 Rev3). Briefly, 500 ng of total RNA were subjected to a Poly (A) tailing with a PAP Enzyme, a biotin labeling was performed with a T4 DNA Ligase using the FlashTag™ Biotin RNA Labeling kit

(Thermo Fisher Scientific). Then, the labeling reaction was checked by an Elosa QC Assay before performing hybridization. GeneChip Eukaryotic Poly-A RNA Controls and Control Oligonucleotide B2 were added to the hybridization mix. 130 µl of the hybridization cocktail were injected onto the arrays. Arrays were incubated at 48^0C and 60 rpm in a GeneChip^{TM} Hybridization oven (Thermo Fisher Scientific) for 16 h. Then arrays were stained and washed with the GeneChip® Hybridization Wash and Stain kit using the Fluidic script FS450_0002 (GeneChip® Expression Wash, Stain and Scan User Guide for Cartridge Arrays P/N 702731).

Raw CEL files of Affymetrix miRNA v4 microarrays were processed using a standard pipeline in Transcriptome Analysis Console (TAC v.4.0.1.36). Microarray data were preprocessed using the "RMA+DABG" algorithm on human probes. Only mature miRNAs, which show $\log_2$ expression above 3 in at least one sample were considered for further analysis in R/Bioconductor v.4.1.0, similar to previously described (1). Differentially expressed miRNAs were detected using *limma* R/Bioconductor package. Statistical significance was assigned based Benjamini-Hochberg's false discovery rate (FDR). Volcano plot represents all considered miRNAs, the thresholds show FDR of 0.01 (horizontal) and log2FC of ±2 (vertical).

2.16 RNA Protection Assay of EVs

To evaluate the presence of miR-146a-5p internally in EVs, an RNA protection assay was performed. 5.0×10^9 EVs were diluted in equal volumes PBS. Samples were incubated with 0.05mg/mL RNase A only, 0.05mg/mL RNase A + 1% Triton X, or equal volumes PBS control for 20 minutes at 37^0C. RNA was extracted and qPCR quantification of miR-146a-5p was performed as described in Section 2.16.

2.17 Real-time quantitative PCR (RT-qPCR) of miR-146a-5p and NUMB levels in EVs and cells

Total RNA from EVs and cells were extracted using miRNeasy Tissue/Cells Advanced Kit (Qiagen). Quantification of RNA samples was done on the Nanodrop 1000 (Thermo Fisher Scientific). The relative quantifications of miRNAs of interest were performed by RT-qPCR. Extracted total RNA from EVs and cells underwent reverse transcriptase reaction using the miRCURY LNA RT Kit. 20 ng of RNA was used per reaction and spike in template RNA UniSp6 RNA/*C. elegans* cel-miR-39-3p (RNA Spike-In Kit, For RT; Qiagen) were added according to the manufacturer's protocol. miRCURY LNA SYBR® Green PCR Kit (Qiagen) was used for the PCR reaction. U6 or miR-103a-3p was used for normalization of cell RNA, but due to the instability of endogenous controls for EVs, *C. elegans* cel-miR-39-3p was used for normalization. ΔΔCt were calculated for relative quantification of expression.

Using the same protocol, relative NUMB expression levels normalized to U6, were analyzed in NHA cocultured with EVs derived from melanocytes, NHA or MBM cell lines H1, H2, and H3, or miR-146a-5p mimic. Downstream Notch, HES1, HEY1 and CCN1 were analyzed with the same method in NHA cells in the presence of H1-EVs, miR-146a-5p mimic, NUMB siRNA or NUMB overexpression. Primers used for the qPCR experiments are listed in Supplementary Table 1.

2.18 In-*situ* hybridization (ISH) on patient MBM

miRNAscope HD Assay Red (cat. no. 324500; Advanced Cell Diagnostics, La Jolla, CA, USA) was used to visualize miR-146a-5p in patient MBM tissue sections and *ex vivo* mouse brain tumors, according to the ACD formalin-fixed paraffin-embedded (FFPE) tissue protocol.

Slides were imaged using an Olympus VS120 S6 Slide scanner (Olympus Life Science Solutions, Shinjuku, Tokyo, Japan).

For quantification ISH images were taken with TRITC filter as Fast Red probe is fluorescent under rhodamine filters. Ten equally sized representative areas were selected from each patient sample using QuPath 0.23 and exported to ImageJ v1.53. The mean gray value was quantified from each and divided by the area for a normalized value. Final values were determined by calculating the mean of all ten areas for each sample. Data are displayed as mean ± SD. Groups were compared using the Welch t-test.

2.19 Analysis of miR-146a-5p levels in serum

Patient serum samples were collected at the Dermatology Clinic in Dortmund (Prof. Dorothée Nashan, Dr. Sonja Dengler), at the University Clinic in Mannheim (Prof. Jochen Utikal, Klinische Kooperationseinheit Dermato-Onkologie, DKFZ) and at the University of Luxembourg. Ethical approval from the respective ethics committees in Germany and Luxembourg was obtained before sample acquisition. Written informed consent was received from all healthy controls and melanoma patients. Additional information on patient samples is given in Supplementary Table 2. Serum was aliquoted and frozen immediately after collection and stored at -80^{0}C until further processing.

EVs were isolated from 250 µL of frozen patient serum using the Exoquick^{TM} Exosome Precipitation Solution (SBI, System Biosciences) according to the manufacturer's instructions. Precipitated EVs were resuspended in 200 µL PBS. Size distribution profiles (nm) and concentration measurements (particles/mL) of isolated EVs were obtained using the NanoSight NS300 instrument (NanoSight Technology, Malvern, UK). Samples were diluted

500- to 2000-fold in PBS to obtain the ideal particle-per-frame value (20–60 particles/frame). Sample injection was performed with a syringe pump set at 40 µL/s speed at RT. The camera (sCMOS) was set with a gain of 73 and a shutter of 696 (camera level 10) and a gain of 146 and a shutter of 890 (camera level 11). For each analysis, 3 1-min videos were captured, representing 4494 frames, and analyzed with the nanoparticle tracking software NTA 3.3 Dev Build 3.3.301 with a detection threshold set at 3. The capture and analysis settings used were manually set according to the manufacturer's instructions (Nanosight NS300 User manual MAN0541-02-EN).

Total RNA extraction from 200 µL isolated exosomes was performed using the miRNeasy serum/plasma kit (Qiagen) according to the manufacturer's instructions. As an internal calibrator and to control for variations in recovery and amplification efficiency between RNA preparations, a mix of cel-39 and cel-54 exogenous controls (Qiagen) was spiked into the samples. RNA was eluted with 14 µL of RNase-free water. 4 µL out of 12 µL total exosome RNA was reverse transcribed using the miScript RT II kit (Qiagen) with HiSpec buffer specifically amplifying only mature miRNAs.

Due to generally low amounts of miRNAs extracted from exosomes, a miRNA pre-amplification step was included before performing qPCR. The 1:5 diluted cDNA was pre-amplified with the miScript PreAMP PCR kit (Qiagen) according to the manufacturer's instructions, using specific primers: miRTC (internal Qiagen miRNA reverse transcription control), cel-54 and cel-39 (calibrators), miR-16-5p, miR-23a-3p, let7a, miR-223-3p and miR-451a (positive controls), and miR-146a-5p and miR-146b-5p. Quality controlled pre-amplified cDNA was diluted 1:20 and qPCR was carried out using specific 10X miScript primer assays (Qiagen) for individual miRNAs (mentioned above) and iTaq Universal SYBR Green Supermix (Biorad) on a CFX384 Detection System (Biorad). The spike-in controls and the target miRNAs were analyzed in parallel for each sample. Data were calibrated using cel-39 expression and normalized using global mean/miRNA (2).

2.20 mRNA sequencing of NHA and differential expression analysis

NHA were seeded at a concentration of 2 x 10^5 cells/well in a 6-well plate. mRNA sequencing of NHA either exposed to miR-146a-5p mimic or miR-NC mimic (negative control) was performed by Novogene (Beijing, China) according to company protocols. Briefly, 1µg of RNA per sample was used to create sequencing libraries generated with NEBNext®UltraTMRNA Library Prep Kit for Illumina® (NEB, USA) following manufacturer's recommendations. Sequencing was performed using 150 bases paired-end on an Illumina Novaseq sequencer with a targeted sequencing depth of 60 Million reads/samples. Differential expression analysis of NHA exposed to miR-146a-5p mimic or miR-NC was performed using the DESeq2 R package v1.16.1 (Bioconductor open-source software for bioinformatics). DESeq2 provide statistical routines for determining differential expression in digital gene expression data using a model based on the negative binomial distribution. The resulting P values were adjusted using the Benjamini and Hochbergh´s approach for controlling the false discovery rate (FDR). Genes with FDR-adjusted P-values < 0.05 found by DESeq 2 were assigned as differentially expressed.

2.21 In silico analysis of potential binding partners to miR-146a-5p

Three target prediction databases, TargetScan 7.1 (http://www.targetscan.org/vert_71/), miRDB (http://mirdb.org/), and microT-CDS (http://www.microrna.gr/microT-CDS) were used to determine predicted binding partners for miR-146a-5p. Each database provided a list of predicted mRNAs, which were combined with our own differential mRNA sequencing data to create a list of combined computed and experimental potential target genes of miR-146a-5p.

2.22 Pulldown assay

A miRNA pulldown assay was used to investigate the mRNA binding partners of miR-146a in NHA cells. Samples were sent to and processed by Shanghai Yunxu Biotechnology (Shanghai, China) according to their standard protocols. Briefly, biotinylated miR-146-5p and control miRNA were transfected into NHA cells and cell lysates were collected after 48 h. Lysates were incubated with M-280 streptavidin magnetic beads (Invitrogen) and 10 µL of yeast tRNA on a rotator at 4^0C overnight. The bound miRNA/mRNA complexes were purified by adding 750 µL of TrIzol (Invitrogen) per sample and 250 µL of water to the input and the pull-down beads for further RT-qPCR analysis. 3 wells were analyzed for each sample. The primers used for pulldown are shown in Supplementary Table 3.

2.23 Dual-luciferase reporter gene assays

To verify the target relationship between miR-146a-5p and NUMB**,** NHA cells were transfected with a luciferase construct containing NUMB with the wild-type (WT) or a mutated version of the binding site and then co-cultured with miR-146a-5p mimic or a scrambled control (miR-NC) (GenePharma Co., Ltd, Shanghai, China). Luciferase activities were detected after 48 h of transfection by using a Dual-Luciferase Reporter Assay System (Promega Corporation, Madison, USA) according to the manufacturer’s instructions.

Briefly, NHA were grown at a concentration of 1.0×10^4 cells/well in a 96-well dish. 75 µL Dual-Glo® Luciferase Assay Reagent was added to the wells and incubated at RT for 30 min.

Firefly luminescence was then measured by an Ensight Multi Mode plate reader (PerkinElmer). Dual-Glo® Stop & Glo® Reagent was then added to each well and incubated for 30 min. Finally, Renilla luminescence was measured using the Ensight Multi Mode plate reader (PerkinElmer).

2.24 Silencing and overexpression of NUMB in NHA

siRNAs (siNC, siNUMB) and overexpression plasmid vectors (PCDNA3.1, vector containing NUMB or empty vector) were prepared by GenePharma (Shanghai, China). 2.0 x 10^5 NHA cells/well were seeded in a 6-well plate overnight. The cells were then treated for 6 h, either with 6 µL siRNAS (20 µM of siNC or siNUMB) and 6 µL lipofectamine 2000 (Thermo Fisher), or overexpression plasmid vectors (1 µg of vector containing NUMB or empty vector) and 6 µL lipofectamine 2000 (Thermo Fisher). After 6 h, the growth medium was exchanged, and the NHA cells were cultured for another 48 h. The cells were then collected, and the proteins were extracted for WB according to standard protocols. siNUMB 5' to 3': GGUUAAGUACCUUGGCCAUTT. siNC 5' to 3': UUCUCCGAACGUGUCACG.

2.25 Construction of a miR-146a-5p knockdown (KD) H1_DL2 cell line

Mcherry-hsa-miR-146a-5p inhibitor sponge (5' to 3'): TAACCCATGGAATTCAGTTCTCACGATAACCCATGGAATTCAGTTCTCAACCGGTAACCCATGGAATTCAGTTCTCATCACAACCCATGGAATTCAGTTCTCATTTTTTC) and mcherry-control lentiviruses (5' to 3': TTCTCCGAACGTGTCACGT) with a neomycin resistant region were synthesized by Genechem (Shanghai, China). For transfection, H1_DL2 cells were seeded in 6-well plates overnight and transfected using Lipofectamine 3000 (Invitrogen, CA, USA) according to the manufacturer’s instructions. Knockdown was confirmed with qPCR of miR-146a-5p levels in H1-DL2 cells normalized to U6 transcripts. Flow cytometry was used to sort mCherry-labeled, stably transfected cells. Cells were harvested for WB analysis 48 h after transfection, and the H1_DL2 KD cells were scaled up and frozen down for subsequent experiments.

2.26 Studies of *in vivo* effects of miR-146a-5p knock-down in H1_DL2 cells

Female nude mice were injected intracardially with 5.0 x 10^5 MBM cells using ultrasound guidance, either H1_DL2 cells where miR-146a-5p was knocked down (H1_DL2 miR-146a-5p KD), or with H1_DL2 cells where a scrambled miRNA was used (H1_DL2 miR-NC KD; n = 10 mice in each group). The mice were imaged with BLI at weeks 4 and 6. The radiance values in regions of interest (ROIs) were registered in ROIs placed over the head and the body regions. Mean radiance values for head and body were calculated in GraphPad Prism v9.0 software (GraphPad Software Inc.). Animal survival was recorded, Kaplan-Meyer survival curves were plotted in GraphPad Prism v9.0 software (GraphPad Software Inc.), and a log-rank analysis was performed to determine the statistical significance of the differences in survival.

2.27 *Ex* vivo immunohistochemical analysis of tumors from mice

Paraffin-embedded mouse brain samples from either miR-146a-5p KD or deserpidine study were sectioned (4 µm) and mounted onto microscopic slides. For immunohistochemistry, deparaffinized sections were incubated with Ki67 (dilution 1:800; Cell Signaling Technology, Beverly, MA, USA) or GFAP (1:250; Abcam, Cambridge, UK) primary antibody at 4^{O}C overnight, rinsed with PBS, and incubated with goat anti-rabbit secondary antibody (dilution

1:200; ZSGB Biotechnology, Beijing, China). One representative image from 5-6 mice in each group was taken using a Leica DMi8 microscope (Leica Microsystems). For each Ki67 image, positively stained nuclei were counted using QuPath v0.2.3 software's cell classification (3). Positively Ki67-stained cells are presented as a percentage of a total number of cells counted.

For GFAP quantification whole slide images were acquired using an Olympus V120 slide scanner (Olympus Corporation, Tokyo, Japan). Using QuPath software a neural network pixel classifier was trained to separate the image into tumor, non-tumor tissue, cerebellum, and background/non-tissue. These preliminary classifications were then manually optimized. Tumor edge was defined as a 300 µm border around the tumors. Inside the different regions, all pixels with an intensity of DAB staining above a fixed threshold were considered positive for the antigen, and the total area of positive staining was quantified. Statistical analysis of image analysis data was done using Rstudio software (RStudio 2022.07.1+554). Data are displayed as mean ± SEM. Groups were compared using the Welch t-test.

2.28 3D structure modeling of miRNA and virtual screening of drug candidates

The Homo sapiens RNA mir-146a-5p stem-loop sequence was acquired from miRBase database (http://www.mirbase.org) with accession ID of MI0000477. The sequence was submitted to MC-Fold/MC-Sym, a service for RNA secondary and tertiary structure prediction. MC-Fold outputs the secondary structures, and the hairpin loop of the pre-miRNA was subsequently submitted to MC-Sym to predict the 3D structure.

The dock module in Molecular Operating Environment (MOE v2015.1001) was used for structure-based virtual screening. The modeled 3D structure of mir-146a-5p were defined as receptor. The DrugBank database were defined as VS library for miR-146a-5p. Prior to docking, the force field of AMBER12: EHT and the implicit solvation model of Reaction Field (R-field) were selected. The orientation of the hydrogens was optimized by LigX module at pH = 7.0 and T = 300^0K. For flexible docking, the docked poses were ranked by London dG scoring first, then a force field refinement was carried out on the top 10 poses followed by a rescoring of GBVI/WSA dG. After flexible docking, the ranked top 100 hits of each compound library were finally identified.

2.29 Apoptosis study after *in vitro* deserpidine treatment

To assess the effects of deserpidine on H1 cells, apoptosis was studied using a Dead Cell Apoptosis Kit with Annexin V for flow cytometry (Thermo Fisher Scientific), according to the manufacturer's instructions. 1.5 x 10^6 H1 cells were plated in 6-well plates and left for 24 h before treating with 0 μM (negative control), 10 μM, 20 μM or 30 μM deserpidine for 72 h. Then, cells were washed with cold PBS and trypsinized using 0.25% Trypsin/EDTA, collected and centrifuged at 1200 rpm for 5 min. Cells were washed with cold PBS and resuspended in 100μL 1X Annexin V binding buffer. 5μL of AlexaFluor®488 and 1μL of 100 μg/mL propidium iodide (PI) was added and cells were incubated for 15 min in the dark at room temperature. 400 μL of 1X Annexin-binding buffer was added after incubation, cells were transferred to ice and immediately analyzed using BD LSR Fortessa Flow cytometer (Becton Dickinson, NJ, USA). FITC-A (530 nm, Annexin V) and PE-A (>575 nm, PI) channels were used in a two-parameter histogram. FlowJo software v10.7.1 (Tree Star Inc., Ashland, OR, USA) was used to analyze raw data using the following cell populations: Q1: live cells (Annexin V−/PI−), Q2: early apoptosis (Annexin V+/PI−) Q3: late apoptosis (Annexin V+/PI+), Q4: necrosis (Annexin V−/PI+).

2.30 *In vivo* drug studies

First, an animal study was performed at the Shandong University, certified by the Association for Assessment and Accreditation of Laboratory Animal Care International. 6-8 weeks old female nude mice were anesthetized with 3% sevoflurane and maintained with 1.5% sevoflurane during the injection procedure. The mice were fixed in a supine position on a 37^0C heating pad to maintain core temperature. 5.0 x 10^5 cells in 0.1 mL sterile PBS were injected during 20 s into the left cardiac ventricle of each mouse using a 30G insulin syringes (Omnican50, B. Brain Medical AS, Vestskogen, Norway), by ultrasound guidance (Vevo 225 2100 Imaging System, VisualSonics Inc.). After tumor cell injection, the mice were divided into two groups (n = 10 mice in each group). One group received intraperitoneal (i.p.) injections of 0.5 mg/kg deserpidine in 100 μL solvent according to the manufacturer's description, every 3rd day for 7 weeks, the other group received 100 μL solvent i.p. every 3rd day for 7 weeks. The mice were monitored daily after injection and BLI was carried out every week for 4 weeks to evaluate tumor burden. Animal survival was recorded and analyzed using GraphPad Prism v7 software (GraphPad Software, Inc.). The brains were harvested, fixed in 4% paraformaldehyde, and embedded in paraffin for subsequent analysis.

Next, the animal study was repeated at the University of Bergen, using MRI to study MBM tumor development in detail. 20 female NOD/SCID mice were injected i.c. with tumor cells with the procedure as described above and divided into 2 groups. 10 mice received i.p. injections of 0.15 mg/kg deserpidine in 100 μL solvent 3 days per week, while 10 mice received i.p. injections of 100 μL solvent 3 days per week. The mice were monitored daily after injection and MRI was carried out at weeks 4 and 6 to evaluate tumor burden. The brains were harvested, fixed in 4% paraformaldehyde, and embedded in paraffin for subsequent miR-146a-5p expression analysis.

2.31 Statistical Analysis

All statistical analyses including one and two way-ANOVAs, Student T-tests, IC_{50} calculations and Kaplan-Meier survival curves were generated using Prism 9 (Version 9.0.2 for Mac OS, GraphPad Software, San Diego, California USA). $P < 0.05$ was regarded as being statistically significant for all tests.

References

1. Nazarov PV, Reinsbach SE, Muller A, Nicot N, Philippidou D, Vallar L*, et al.* Interplay of microRNAs, transcription factors and target genes: linking dynamic expression changes to function. Nucleic Acids Res **2013**;41:2817-31
2. Margue C, Reinsbach S, Philippidou D, Beaume N, Walters C, Schneider JG*, et al.* Comparison of a healthy miRNome with melanoma patient miRNomes: Are microRNAs suitable serum biomarkers for cancer? Oncotarget **2015**;6:12110-27
3. Bankhead P, Loughrey MB, Fernández JA, Dombrowski Y, McArt DG, Dunne PD*, et al.* QuPath: Open source software for digital pathology image analysis. Scientific Reports **2017**;7:16878

Supplementary Fig. S1: Characterization of isolated EVs. A Representative nanoparticle tracking analysis of H2-, NHA- and Mel-EVs. **B** Electron micrograph of NHA- and H2-EVs. Scale bar = 100μm. **C** Western blot analysis of EV-characteristic markers on H3, H2 and NHA cells and corresponding EVs.

Supplementary Fig. 2: Visualization of MBM-EV uptake in NHAs. A Confocal images of NHA cultured with 5.0 x 10^9 EVs of PKH67-stained (green) H2-EVs for 48 h to show uptake. Nuclei stained with DAPI (blue), membrane stained with WGA-Texas Red (red). The images were obtained in X-Y orientation. Magnification (100X). Scale bar = 10 μm **B** Z-stack images of NHA cells after co-culture with PBS or H1-, H2-, and NHA-EVs to show EVs inside the plasma membrane. Images I, III, V, and VII show Z-stack in Z-X orientation. Images II, IV, VI, and VIII show corresponding images in X-Y orientation with white line indicating the slice orientation shown in the top images.

Supplementary Fig. 3: NHA activated by H1-EVs increase MBM growth *in vitro*. A Schematic of workflow for *in vitro* co-culture experiment. **B** Number of H1_DL2 cells at 0, 2 or 4 days after co-culture with PBS, NHA- or H1-EVs co-cultured with NHA. Cell numbers were determined by counting number of fluorescent green cells with a Nikon TE2000 inverted microscope. n.s.= not significant, ***$p < 0.001$.

Supplementary Fig. 4: H2-EVs increase cytokine production in NHA cells. ELISA validation performed on conditioned media from NHA cells co-cultured with H2-EVs. ELISA was done on the top four upregulated cytokines, IL-6, IL-8, MCP-1 and CXCL1. ***$p < 0.001$; ****$p < 0.0001$.

Supplementary Fig. 5: Conditioned medium from NHA treated with H1-EV increases H1 growth due to cytokine upregulation. WST-1 proliferation assay of H1 cells cultured in CM from NHA cells treated H1-EVs or PBS for 48 h. H1 cells were treated with antibodies for either CXCL1, MCP-1, IL-8 or IL-6 for 48 h. **$p < 0.01$, ****$p < 0.0001$.

Supplementary Fig. 6: miR-146a-5p expression in normal cell- and MBM cell-EVs A Dot plot presenting $\log_2$ expression of miRNA 146a in normal controls (left), brain metastases (middle) and skin and lymph node metastases (right). **B** qPCR comparing expression levels of miR-146a-5p in healthy melanocyte and NHA cells and EVs. **C** RNA protection assay of H1-EVs after treatment with RNase, RNase and Triton X compared to no treatment showing RNA concentration (left) after treatment, and qPCR of miR-146a levels (right).

Supplementary Fig. 7: MiR-146a-5p expression levels in clinical serum EV samples.
A Overall concentrations of EVs isolated from patient samples 1-54 quantified by NanoSight NS300 instrument. **B** Normalized miR-146a-5p expression in EVs from serum of healthy volunteers, melanoma patients without brain metastases, and melanoma patients with brain metastases. Data were acquired via RT qPCR analysis, results were calibrated with spike-in *C. elegans* miR-39-3p and normalized using global mean/miRNA.

Supplementary Fig. 8: *In situ* hybridization of clinical MBM samples and normal brain tissue. miRNAscope *in situ* hybridization assay of miR-146a-5p expression in patient MBM samples and healthy brain controls. Red dots indicate successful binding of the miR-146a probe, tissues counterstained with hematoxylin (purple). Scale bar = 200μm.

Supplementary Fig. 9: Visualization of FAM-tagged miR-146a inhibitor in NHA cells. Confocal images of NHA uptake of FAM-tagged miR-146a inhibitor (green) after 24 h. Nuclei stained with DAPI (blue), membrane stained with WGA-Texas Red (red). The images were obtained in X-Y orientation. Magnification (100X). Scale bar = 10 μm **B** Z-stack image of NHA cells after addition of inhibitor to confirm presence inside the plasma membrane in Z-Y orientation.

Supplementary Fig. 10: A CCK8 proliferation assay of NHA cells after co-culture with 5.0 x 10^9 H2-EVs in the presence or absence of a miR-146a-5p inhibitor. **B** ELISA of IL-6, IL-8, MCP-1 and CXCL1 levels from NHA cell conditioned media after co-culture with 5.0 x 10^9 H2-derived EVs in the presence or absence of miR-146a-5p inhibitor. $^*p < 0.05$, $^{**}p < 0.01$, $^{***}p < 0.001$; $^{****}p < 0.0001$.

Supplementary Fig. 11: 18 common predicted miR-146a-5p binding partners. Log fold change (logFC) and false discovery rate (FDR) of 18 predicted binding partners of miR-146a-5p from three online databases (TargetScan, miRDB, and microT-CDS) combined with sequencing data in Figure 4a.

Supplementary Fig. 12: Overexpression and silencing of NUMB in NHA cells. A Western blot confirming NUMB overexpression in NHA cells. Overexpression performed by transfection of an overexpression plasmid vector. **B** Western blot confirming NUMB silencing. Silencing performed by addition of NUMB-siRNA treatment of NHA cells.

Supplementary Fig. 13: A MiR-146a-5p is knocked down in H1_DL2 cells. qPCR confirming successful knockdown of miR-146-5p in H1_DL2 cells via transfection of a miRNA sponge lentiviral vector. $^{***}p < 0.001$.

Supplementary Fig. 14: Screening of drug candidates demecarium bromide and fosamprenavir. A qPCR analysis of miR-146a-5p expression in H1 cells and H1 EVs after demecarium bromide and fosamprenavir treatment. **B and C** Representative IC_{50} survival curves of H1, H2, H3 and H10 cells after treatment with increasing demecarium bromide concentrations (0.1 μM–1000 μM) for 72 h and corresponding IC_{50} doses of all MBM cell lines and NHA. n.s.= not significant $^*p < 0.05$, $^{**}p < 0.01$.

Supplementary Fig. 15: **EVs derived from deserpidine-treated H1 cells do not activate NHA. A** Western blot of NHA cells after 48 h co-culture with either PBS, H1-EV or 20 μM deserpidine treated H1-EV (Des-H1-EV). **B** Subsequent quantification of western blot normalized to PBS control. n.s.= not significant $^*p < 0.05$, $^{**}p < 0.01$.

Supplementary Figure S1

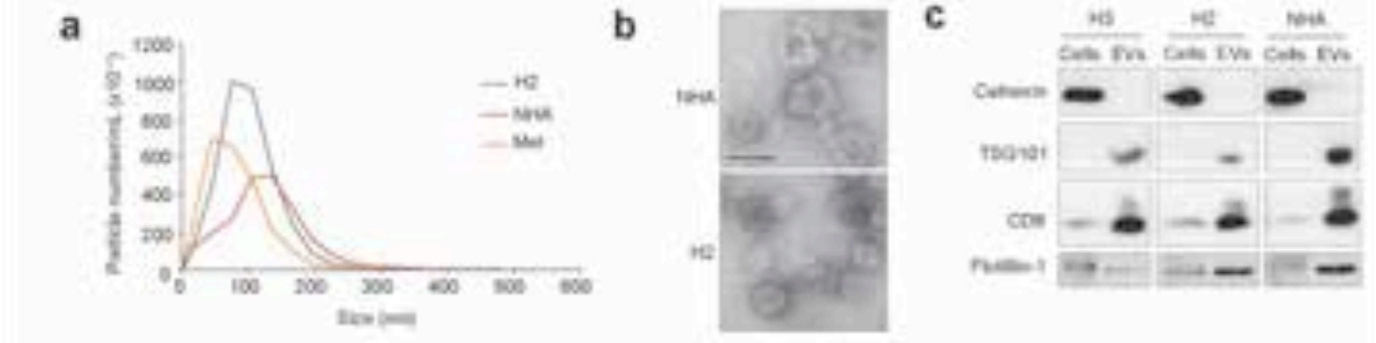

Supplementary Figure 2

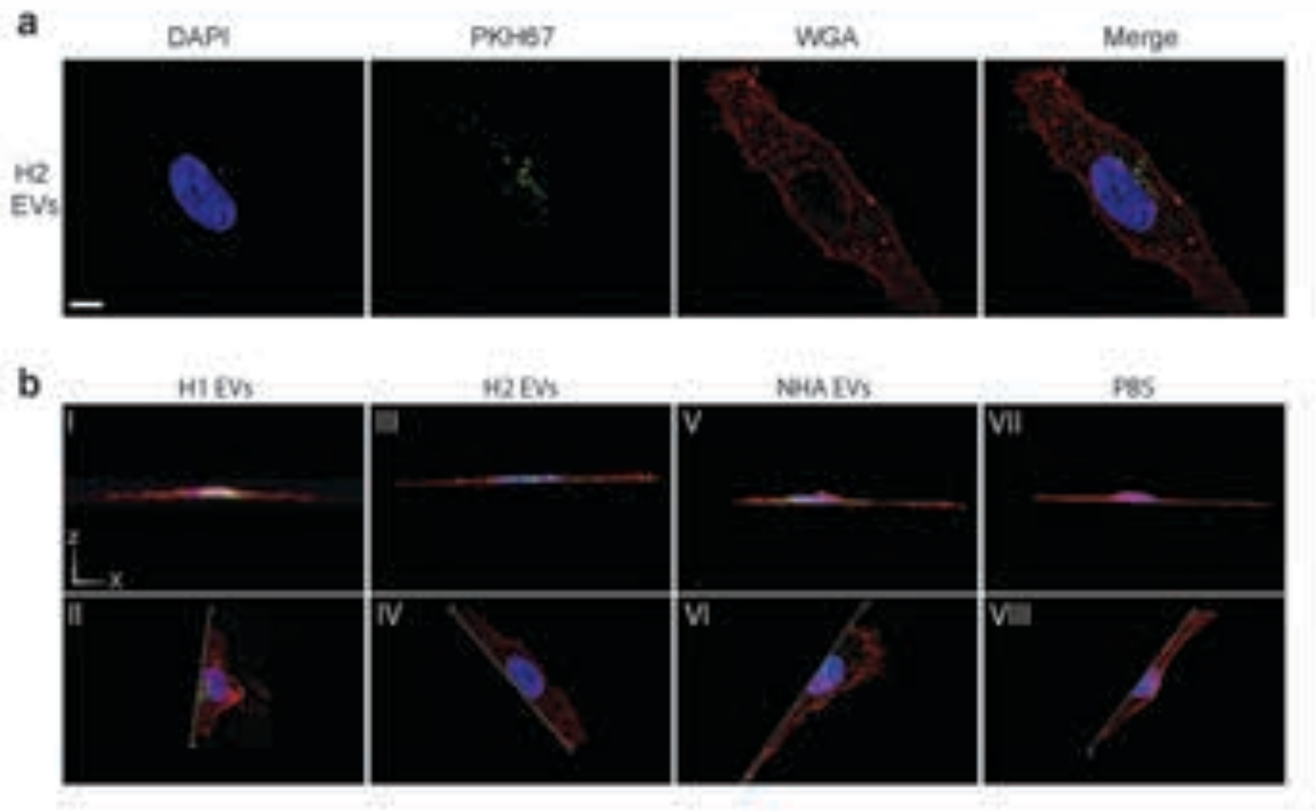

Supplementary Figure S3

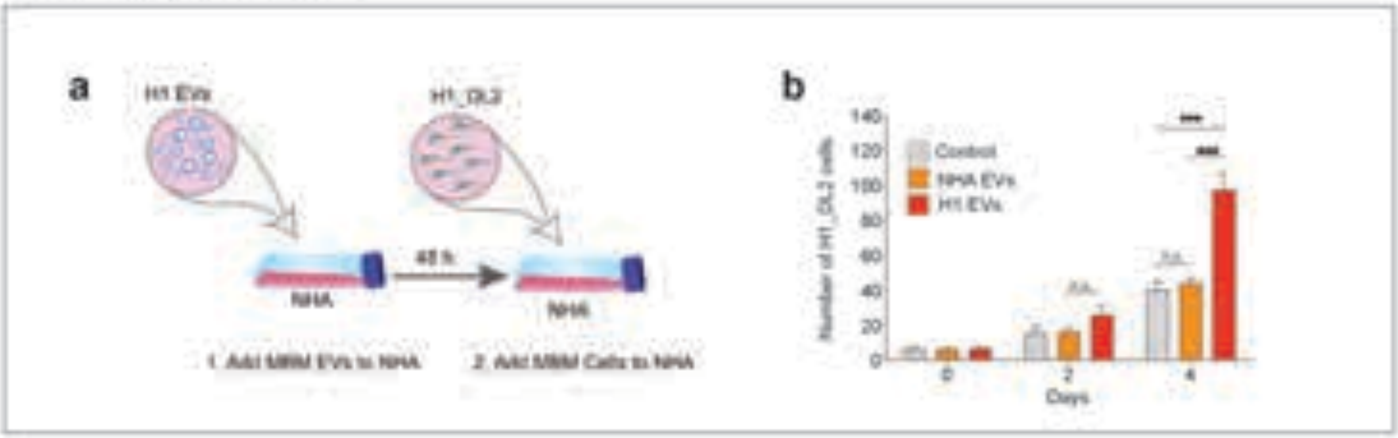

Supplementary Figure S4

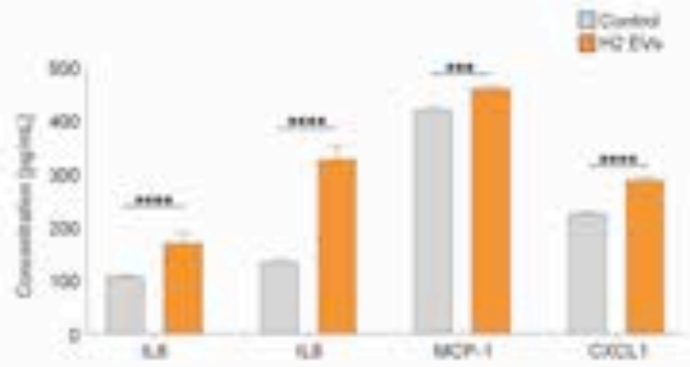

Supplementary Figure S5

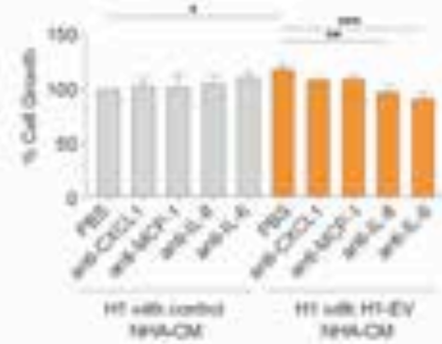

Supplementary Figure S6

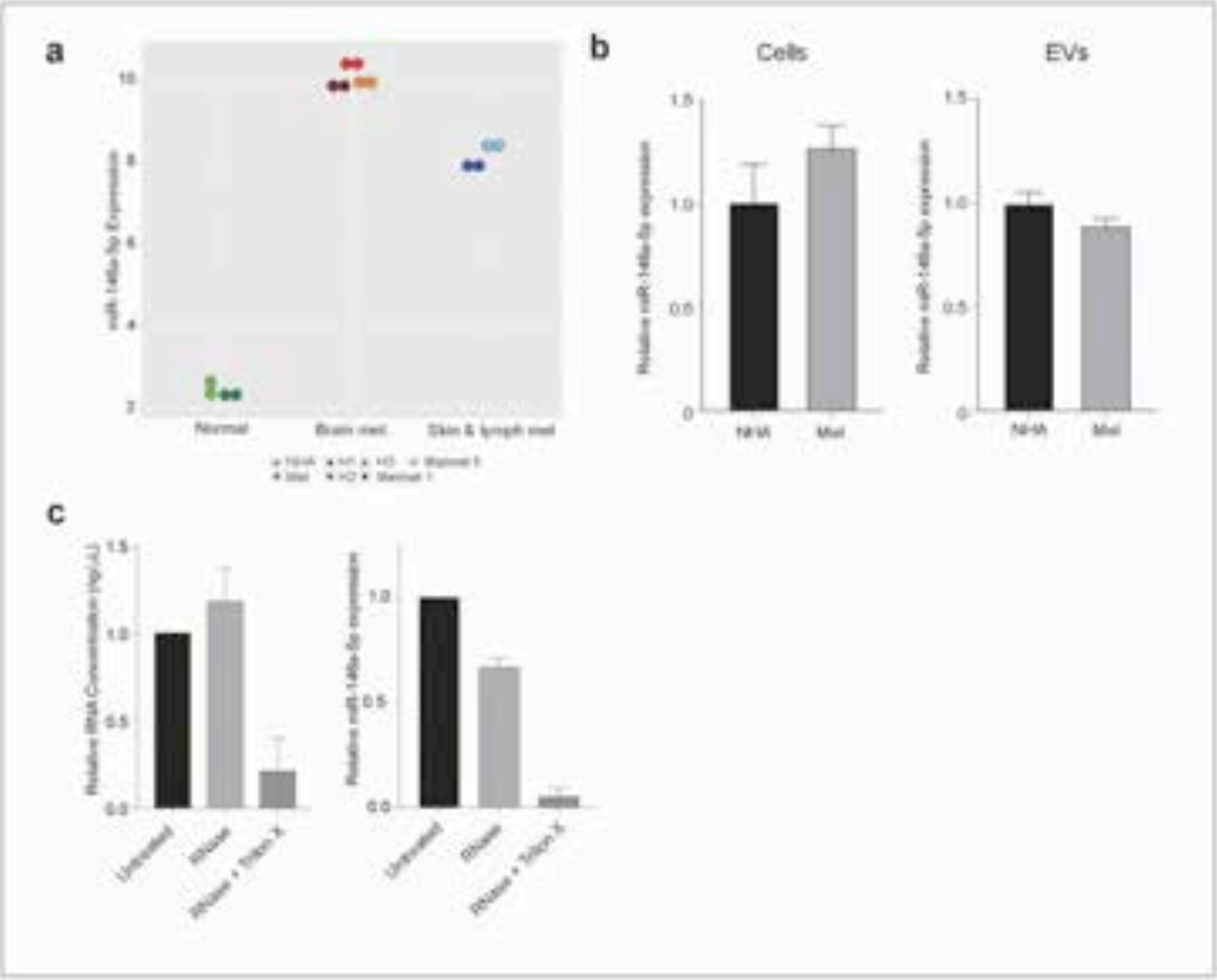

Supplementary Figure S7

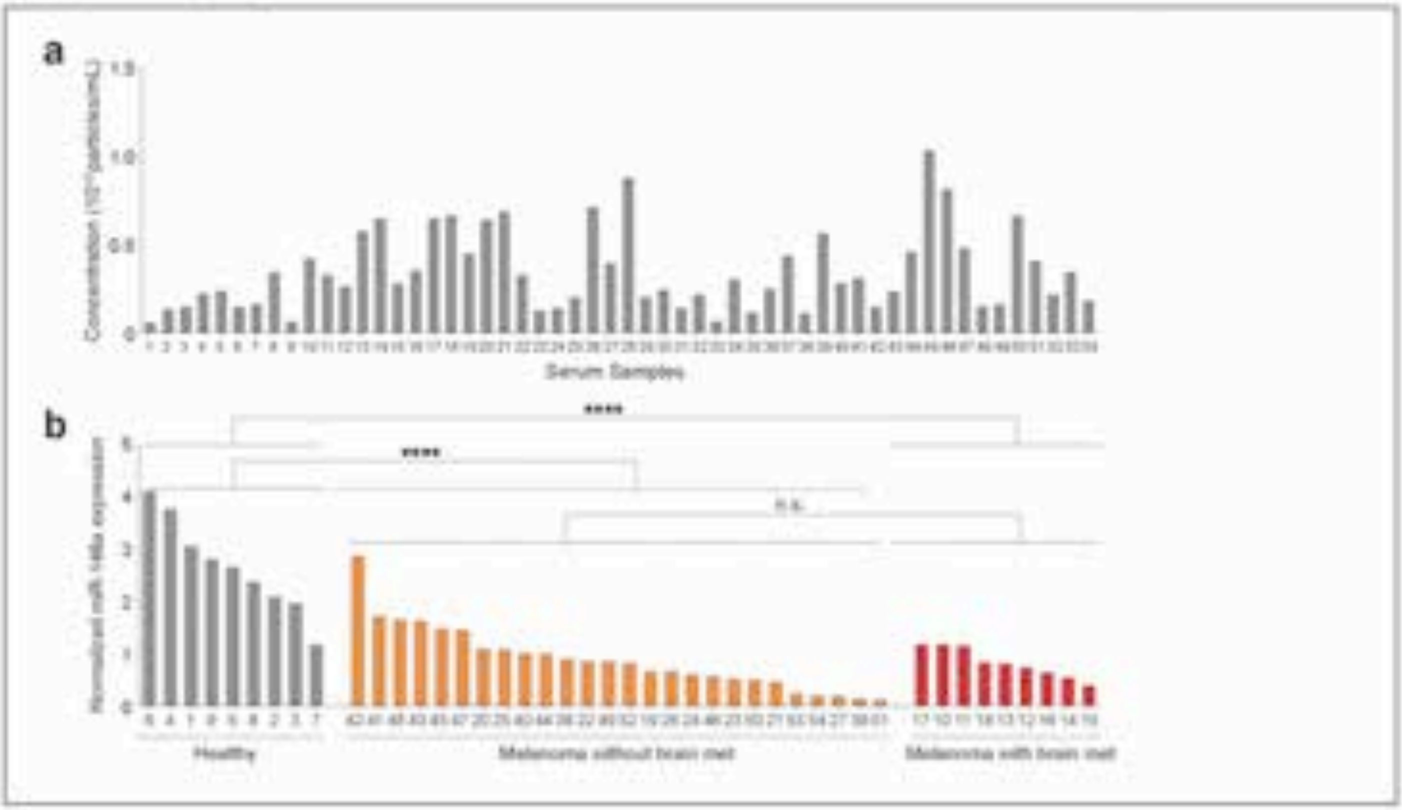

Supplementary Fig S8

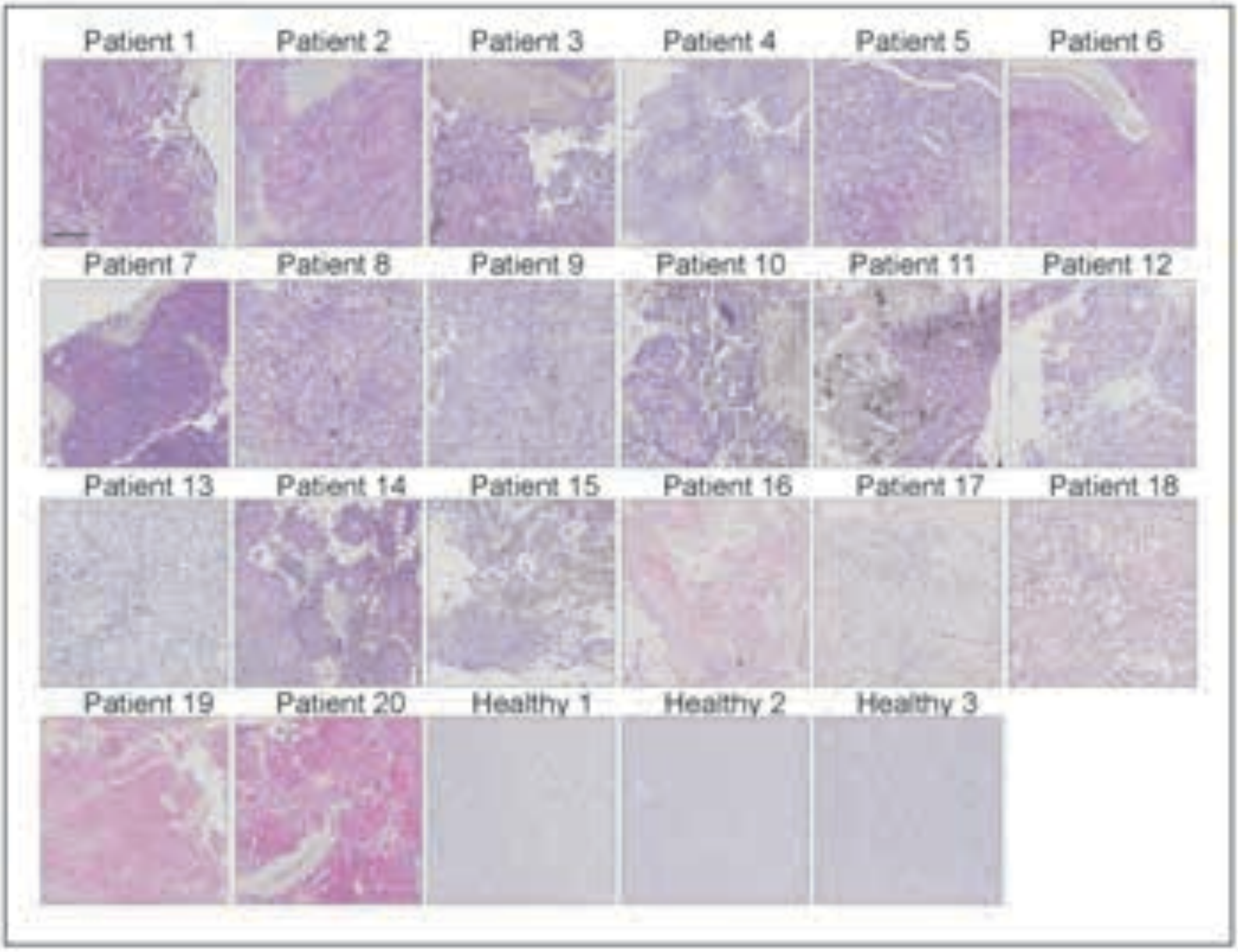

Supplementary Figure S9

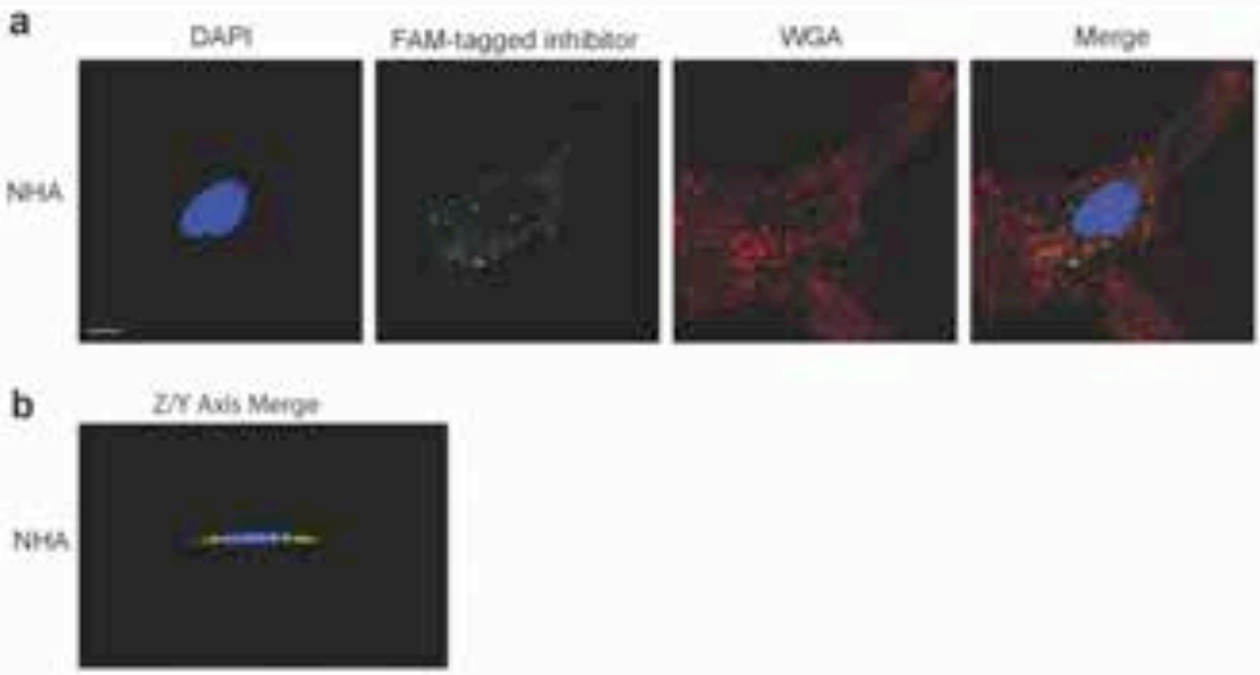

Supplementary Figure S10

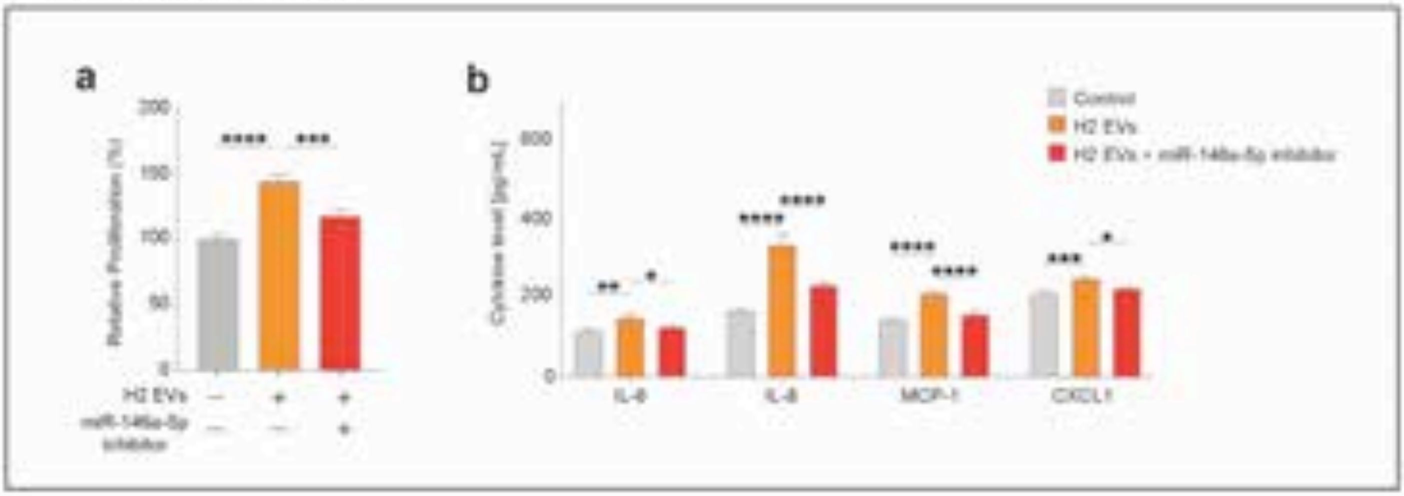

Supplementary Figure S11

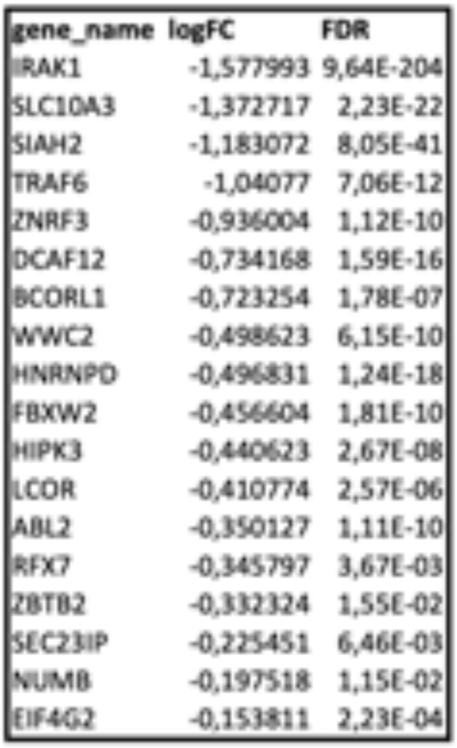

gene_name	logFC	FDR
IRAK1	-1,577993	9,64E-204
SLC10A3	-1,372717	2,23E-22
SIAH2	-1,183072	8,05E-41
TRAF6	-1,04077	7,06E-12
ZNRF3	-0,936004	1,12E-10
DCAF12	-0,734168	1,59E-16
BCORL1	-0,723254	1,78E-07
WWC2	-0,498623	6,15E-10
HNRNPD	-0,496831	1,24E-18
FBXW2	-0,456604	1,81E-10
HIPK3	-0,440623	2,67E-08
LCOR	-0,410774	2,57E-06
ABL2	-0,350127	1,11E-10
RFX7	-0,345797	3,67E-03
ZBTB2	-0,332324	1,55E-02
SEC23IP	-0,225451	6,46E-03
NUMB	-0,197518	1,15E-02
EIF4G2	-0,153811	2,23E-04

Supplementary Figure S12

Supplementary Figure S13

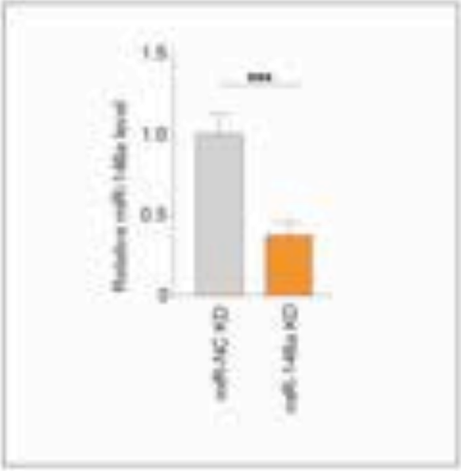

Supplementary Figure S14

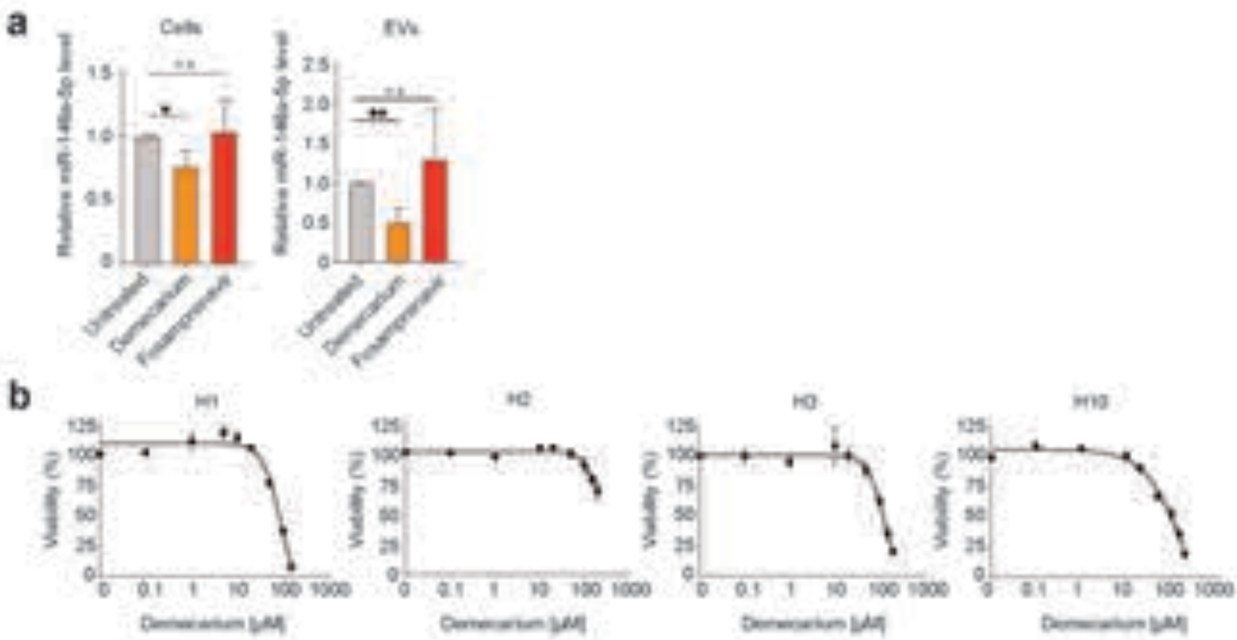

c

Cell line	Demecarium IC_{50} (µM)
H1	97.78 ± 37.49
H2	174.75 ± 34.74
H3	133.42 ± 41.50
H10	271.33 ± 104.97
NHA	79.33 ± 20.45

Supplementary Figure S15

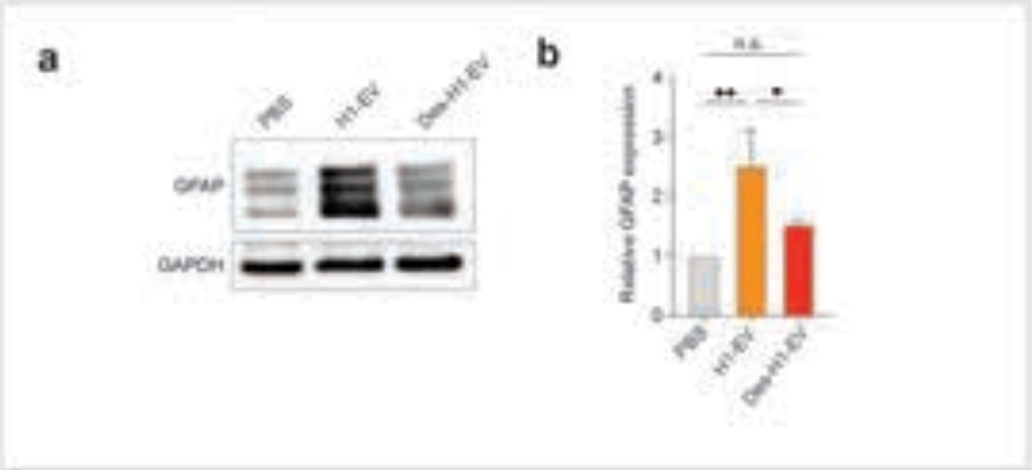

Supplementary Table 1. Primers used for qPCR experiments.

	Company	miRBase Accessio	Gene name	GeneGlobe ID (Cataloge #)
miRNA primers	Qiagen	MIMAT0000101	hsa-miR-103a-3p	YP00204063 (339306)
	Qiagen	MIMAT0000449	hsa-miR-146a-5p	YP00204688 (339306)
	Qiagen	MIMAT0000010	cel-miR-39-3p	YP00203952 (339306)
	Company	**Gene name**	**Forward Primer**	**Reverse Primer**
miRNA primers	BioSune	*Hey2*	5'- CAGGCAACAGGGGGGTAAAGG -3'	5'- CAGGTACCGCGCAACTTCTG -3'
	BioSune	*Hes1*	5'- TGGCCAGTTTGCTTTCCTCA -3'	5'- GGAAGGTGACACTGCGTTGG -3'
	BioSune	*CCDN1*	5'- TTTGGCGTTTCCCAGAGTCA -3'	5'- AAGGAAGGGGGCAGGGGATAA -3'
	BioSune	*Notch*	5'-TCAGCGGGATCCACTGTGAG-3'	5'-ACACAGGCAGGTGAAGTTG-3'
	BioSune	*NUMB*	5'-TGGCACTGACTCAGCCTTCC-3'	5'-CTGGAGAGGCAGCACCAGAA-3'

Supplementary Table 2: Overview of clinical serum samples

Patient	Sample description	Disease stage
1	healthy control	-
2	healthy control	-
3	healthy control	-
4	healthy control	-
5	healthy control	-
6	healthy control	-
7	healthy control	-
8	healthy control	-
9	healthy control	-
10	melanoma patient with brain metastasis (Cohort A)	IV
11	melanoma patient with brain metastasis (Cohort A)	IV
12	melanoma patient with brain metastasis (Cohort A)	IV
13	melanoma patient with brain metastasis (Cohort A)	IV
14	melanoma patient with brain metastasis (Cohort A)	IV
15	melanoma patient with brain metastasis (Cohort A)	IV
16	melanoma patient with brain metastasis (Cohort A)	IV
17	melanoma patient with brain metastasis (Cohort A)	IV
18	melanoma patient with brain metastasis (Cohort A)	IV
19	melanoma patient without brain metastasis (Cohort A)	IV
20	melanoma patient without brain metastasis (Cohort A)	IV
21	melanoma patient without brain metastasis (Cohort A)	IV
22	melanoma patient without brain metastasis (Cohort A)	IV
23	melanoma patient without brain metastasis (Cohort A)	IV
24	melanoma patient without brain metastasis (Cohort A)	IV
25	melanoma patient without brain metastasis (Cohort A)	IV
26	melanoma patient without brain metastasis (Cohort A)	IV
27	melanoma patient without brain metastasis (Cohort A)	IV
28	melanoma patient with brain metastasis (Cohort B): 22 months before BM diagnosis	IIIB-IV
29 (same as 28)	melanoma patient with brain metastasis (Cohort B): 10 months after BM diagnosis	IIIB-IV
30	melanoma patient with brain metastasis (Cohort B): 14 months before BM diagnosis	IV
31 (same as 30)	melanoma patient with brain metastasis (Cohort B): 4 months before BM diagnosis	IV
32	melanoma patient with brain metastasis (Cohort B): 12 months before BM diagnosis	IV
33 (same as 32)	melanoma patient with brain metastasis (Cohort B): 1 month before BM diagnosis	IV
34	melanoma patient with brain metastasis (Cohort B): 2 months after BM diagnosis	IV
35 (same as 34)	melanoma patient with brain metastasis (Cohort B): 9 months after BM diagnosis	IV
36 (same as 34)	melanoma patient with brain metastasis (Cohort B): 13 months after BM diagnosis	IV
37	melanoma patient with brain metastasis (Cohort B): 10 months before BM diagnosis	IIIC (at 1st diagnosis)
38	melanoma patient without brain metastasis (Cohort B)	IIA
39	melanoma patient without brain metastasis (Cohort B)	IIIC
40	melanoma patient without brain metastasis (Cohort B)	IIIB
41	melanoma patient without brain metastasis (Cohort B)	IIIB
42	melanoma patient without brain metastasis (Cohort B)	IV
43	melanoma patient without brain metastasis (Cohort B)	IIA
44	melanoma patient without brain metastasis (Cohort B)	IB
45	melanoma patient without brain metastasis (Cohort B)	IIB
46	melanoma patient without brain metastasis (Cohort B)	IV
47	melanoma patient without brain metastasis (Cohort B)	IIA
48	melanoma patient without brain metastasis (Cohort B)	IA
49	melanoma patient without brain metastasis (Cohort B)	IIA
50	melanoma patient without brain metastasis (Cohort B)	IIB
51	melanoma patient without brain metastasis (Cohort B)	IB
52	melanoma patient without brain metastasis (Cohort B)	IIIB
53	melanoma patient without brain metastasis (Cohort B)	IV
54	melanoma patient without brain metastasis (Cohort B)	IB

Supplementary Table 3. Primers for RT-qPCR after pulldown

Gene number	Gene name	Type of primer	Primer sequence
Gene1	WWC2	1-Forward	TGATGAGTCTGTGGCTGGAG
		1-Reverse	GATTCTGTGGGCGGATGAAC
Gene2	NUMB	2-Forward	CCCTTCTCATCTGCTCCGAT
		2-Reverse	GGGAGTACGTCTATGACCGG
Gene3	SLC10A3	3-Forward	CATTGAGGTAGGGGTGCAGA
		3-Reverse	GCTGCTGTAGATGAAGTGGC
Gene4	ZBTB2	4-Forward	CCGCTTGAAACCAACTGACA
		4-Reverse	TGGGAAAACTTGGTCAGGGT
Gene5	HNRNPD	5-Forward	CTTCCGTCGGCCATTTTAGG
		5-Reverse	CGAACCGAAACTAGCAGCAA
Gene6	LCOR	6-Forward	CGTCTGTCATACTGGGAGCT
		6-Reverse	GTGCACATTTTCCACCACCT
Gene7	HIPK3	7-Forward	AGTCTGGATGATGTAGCGCA
		7-Reverse	GATGGTTCAGGGTCTCAGCT
Gene8	RFX7	8-Forward	CCTCTACCTTCAGCTGCCTT
		8-Reverse	CCTTCCAACCCATCTCCAGT
Gene9	TRAF6	9-Forward	GTGACAACTGTGCTGCATCA
		9-Reverse	GCATGGAATTGGGGCTGTAG
Gene10	FBXW2	10-Forward	TTCTGTGCCTCTTCCTCTGG
		10-Reverse	GGCTTCTCCCCTATCCTGAC
Gene11	SEC23IP	11-Forward	AGAATTGGAGAAGGTGGCCA
		11-Reverse	CTGGGGCTGTTCTGGACTAA
Gene12	DCAF12	12-Forward	TGCAAAGTGATCCAGCCCTA
		12-Reverse	CAGGTCTTGAGGGGAAGGAG
Gene13	ZNF652	13-Forward	GTGCTCCCTCTCTGTCAGTT
		13-Reverse	TCTGTGCCTGGTATTGCTCA
Gene14	IRAK1	14-Forward	ATCTCTTTGGACAGTGGCCA
		14-Reverse	TGGCTGGTCTTGACCTACTG
Gene15	ABL2	15-Forward	CCGAGAATGCAACCGAGAAG
		15-Reverse	AAGACTCTCTGGTGCTGTCC
Gene16	BCORL1	16-Forward	CCCAACAAAGTCCAGGGGAT
		16-Reverse	AGAACAACATCCTTTGCCTCTT
Gene17	EIF4G2	17-Forward	TGCAAGGACAGTCGAAGGAT
		17-Reverse	CAGAGGTGGTGTTTGAGTGC
Gene18	SIAH2	18-Forward	GCCCACAAGAGCATTACCAC
		18-Reverse	GGTGGCCTTCGTACTTCTCT

Multimodal imaging of brain metastasis-derived extracellular vesicles using superparamagnetic iron oxide nanoparticle labeling

Birgitte Feginn Berle[1,*], Sunniva Juliussen[1,*], Aurea Castilho[1], Ege Solel[1], Halala Sdik Saed[1], Oliver Vanderpoorten[2], Taral R. Lunavat[1], Emma Rigg[1,#], Frits Thorsen[1,3,4,5,#]

[1]Department of Biomedicine, University of Bergen, Jonas Lies vei 91, 5009 Bergen, Norway [2]Department of Physics and Technology, UiT The Arctic University of Norway, Tromsø, Norway [3]Department of Neurosurgery, Haukeland University Hospital, Haukelandsveien 22, 5021 Bergen, Norway [4]Molecular Imaging Center, Department of Biomedicine, University of Bergen, Jonas Lies vei 91, 5009 Bergen, Norway [5]Department of Neurosurgery, Qilu Hospital of Shandong University and Shandong Key Laboratory of Brain Health and Function Remodeling, Jinan, China

*These authors contributed equally to this work
#Shared last authorship

Correspondence: Emma Rigg; Frits Thorsen, Department of Biomedicine, University of Bergen, Jonas Lies vei 91, 5009 Bergen, Norway. Email emma.rigg@uib.no, frits.thorsen@uib.no

---

Background: Extracellular vesicles (EVs) are crucial mediators in brain metastasis (BM), facilitating pre-metastatic niche formation and metastatic progression. However, tracking their distribution and interactions *in vivo* remains challenging.

Objective: To develop and validate a method for labeling BM-derived EVs using superparamagnetic iron oxide nanoparticles (SPIONs) that enables their visualization and tracking through magnetic resonance imaging (MRI).

Methods: Three SPION variants with different coatings and sizes were evaluated using two patient-derived BM cell lines. The labeled EVs were characterized using transmission electron microscopy (TEM), colorimetric iron assays, dynamic light scattering and nanoparticle tracking analysis (NTA) in Nanospacer devices. The functionality and visualization of SPION-labeled EVs were assessed in fetal rat brain organoids (FRBOs) using Prussian blue staining, TEM, and MRI. Detection sensitivity was determined using agar phantoms, and in vivo tracking was validated through intramuscular injections in mice.

Results: Uncoated 5 nm SPIONs demonstrated superior labeling efficiency, successfully marking over 90% of cells within 24 hours without significantly affecting cell growth. These SPIONs were effectively incorporated into BM-derived EVs while maintaining their original size distribution. The labeled EVs were successfully internalized by FRBOs and could be visualized using multiple imaging modalities. Agar phantom studies revealed significant changes in T2 and T2* relaxation times, which was further confirmed through *in vivo* MRI following intramuscular injections.

Conclusions: This study establishes a reliable protocol for labeling BM-derived EVs with SPIONs, enabling their visualization across various biological contexts, from subcellular to tissue levels. This proposed model facilitates a valuable tool for spatially tracking BM-EVs *in vivo*, identifying specific target cells, and investigating their functional role in metastatic progression.

Keywords: Extracellular vesicles, brain metastasis, pre-metastatic niche, magnetic resonance imaging, superparamagnetic iron oxide particles, transmission electron microscopy

Introduction

Metastatic spread of cancers to the brain is significantly affected by the release of tumor-derived extracellular vesicles (EVs)[1]. These nanosized particles, less than 200 nm in diameter, play an important role in intercellular communication through the transfer of various biomolecules such as lipids, proteins, carbohydrates, DNA and RNA[2]. Although EVs are released from almost all cell types, tumor cells discharge them in much larger quantities compared to normal cells[3,4]. In brain metastasis (BM), EVs have been shown to disrupt the blood-brain barrier (BBB), cause vascular and metabolic remodeling, promote neutrophil recruitment, and induce astrocyte dysregulation[5–8]. These alterations prepare the brain microenvironment for the onset of metastasis and promote invasion by creating a pre-metastatic niche (PMN), where cells and mechanisms that typically protect from malignancies become more hospitable to incoming tumor cells[9].

Although we have begun to understand the effects of EVs on BM and the PMN, a significant knowledge gap remains regarding the dynamic pathology of these brain metastasis-derived EVs (BM-EVs). Improved model systems are required to further understand their homing, spatial distribution, and interactions with specific cell types in the brain.

Magnetic resonance imaging (MRI) facilitates accurate clinical diagnosis of cancer patients and metastatic spread through its ability to differentiate between soft tissues, making it an ideal tool for detecting and visualizing tumors. This imaging technique offers detailed cross-sectional images of the brain, which are crucial for identifying the exact location, extent, size, shape, and potential invasiveness of cancerous growths[10]. However, detecting single cells and EVs by MRI is challenging without using reliable contrast agents or labeling techniques.

Superparamagnetic iron oxide nanoparticles (SPIONs) have previously been used as stable, non-radioactive, and biocompatible contrast agents, producing strong, hypointense (dark) contrast in MRI[11]. SPIONs are non-toxic at low doses and can remain in the body for weeks after administration depending on the coating, enabling long-term imaging in both pre-clinical and clinical settings[12–14]. Due to the high electron density of SPIONs, iron is also easily detected by transmission electron microscopy (TEM), enabling detailed visualization of EVs within cells and tissue sections.

Given the strong signal and cost-effectiveness of SPIONs, bulk labeling of EVs allows for efficient visualization and tracking in imaging studies, both in cell culture and preclinical MRI[15–17]. However, this approach has yet to be applied to BM-EVs for investigating their role in targeting healthy brain cells. By developing a model to track these BM-EVs *in vitro* and *in vivo*, we can gain insights into the specific cells and regions they target for PMN establishment. This knowledge could increase our understanding of their role in metastasis progression and highlight their potential as therapeutic targets.

In this study, we demonstrate that BM cell lines can be effectively prelabeled with SPIONs. Furthermore, we show that EVs derived from these cells incorporate SPIONs, enabling their visualization by MRI in both *in vitro* and *in vivo* settings.

Materials and Methods

Cell lines and cell culture conditions

The H16 cell line was derived from a BM of a patient with a BRAF$^{\text{wild-type}}$ malignant melanoma, while the LBM1 cell line was developed from a BM of a patient with non-small cell lung carcinoma. Both cell lines were grown in Dulbecco's Modified Eagle's medium (DMEM; Sigma-Aldrich Inc., St. Louis, MO, USA), supplemented with 10% heat-inactivated fetal bovine serum (Sigma-Aldrich Inc.), 5 mg/mL plasmocin (Invivogen, Toulouse, France), 2% L-glutamine (Sigma-Aldrich Inc.), 3.2% Nonessential amino acids, penicillin (100 IU/mL) and streptomycin (100 m L/mL) (Sigma-Aldrich Inc.). Cells were grown in a tissue incubator at 37^0C, 5% CO_2, and 100% humidity. For maintenance of the cell lines, short tandem repeat fingerprinting (STR) and mycoplasma testing were performed regularly.

Generation of fetal rat brain organoids (FRBOs)

3D fetal rat brain organoids (FRBOs) are a well-established *in vitro* model for mimicking the brain environment for differentiation and therapeutic studies[18]. Briefly, pregnant Sprague Dawley rats (Janvier Laboratories, Le Genest-Saint-Isle, France) were sacrificed on gestational day 18, and fetuses were surgically removed. The fetal brain tissue was excised, homogenized with scalpel blades, and washed with 1x PBS (Sigma-Aldrich Inc) under sterile conditions. Homogenized tissue was then enzymatically dissociated twice with StemPro Accutase (Thermo Fisher Scientific) for 20 min at 37^0C. Meninges and other floating debris were removed and dissociated cells were filtered through a 70 µm cell strainer (Thermo Fisher Scientific), washed with cell culture medium (DMEM supplemented with 10 % heat-inactivated FBS) and counted. Cells were seeded in 24-well agar-coated plates (Thermo Fisher Scientific) at 2.0×10^6 cells/well. Aggregated cells were transferred to agar-coated T25 flasks (Thermo Fisher Scientific) on day 3 of culture and placed on an orbital shaker to ensure 3D growth. Cell culture medium was exchanged regularly and mature FRBOs were used for experiments on day 21.

Labelling of cell lines with SPIONs

To label H16 and LBM1 cell lines with SPIONs, cells were first seeded in either 24-well plates, T75 flasks or T175 flasks (Thermo Fisher Scientific) and incubated overnight to reach 70% confluency. Three different commercially available SPIONs were individually added to separate H16 and LBM1 cell cultures at increasing concentrations of 0 µg/mL, 50 µg/mL, 100 µg/mL or 200 µg/mL diluted in cell culture medium. These included Molday 35 nm dextran-coated SPIONs (BioPAL Inc., Worcester, MA, USA), uncoated 5 nm SPIONs (Sigma-Aldrich, Burlington, MA, USA), and carboxyl-coated 5 nm SPIONs (Ocean Nanotech, San Diego, CA, USA). The cells were then incubated for either 24 h or 48 h. After incubation, the cells were washed three times with pre-warmed PBS prior to downstream analyses.

Prussian Blue staining

To confirm uptake of SPIONs by BM cell lines or SPION-loaded EVs by FRBOs, Prussian blue staining was performed. For staining of monolayer cell cultures after incubation with SPIONs for either 24 h or 48 h, the cell culture medium was removed and excess SPIONs were discarded by washing the cells three times with 1x PBS. The cells were then fixed in 4% paraformaldehyde (PFA) for 20 min at room temperature. The fixative was removed, and the cells were rinsed gently three times with 1x PBS. The cells were then rinsed once with dH_2O, once with 70% EtOH, and again with dH_2O before incubating with Prussian Blue stain (1 % potassium ferrocyanide (Sigma-Aldrich) + 0.5 % HCl in dH_2O) for 20 min. To remove excess stain, cells were rinsed three times with dH_2O. Brightfield images of cells and histological sections were obtained using a Nikon Eclipse Ti2 inverted microscope (Nikon Instruments, Inc., Melville, NY, USA). The percentage of cells that contained SPIONS (blue spots) were quantified using Fiji freeware (version 2.14.0).

FRBOs were fixed overnight in 4% PFA and embedded in paraffin after being co-cultured with 50 mg/mL SPION-loaded LBM1-EVs for 24 h. Sections were deparaffinized with xylene for 2 x 5 min. Sections were then re-hydrated with decreasing percentages of ethanol and finally distilled water before staining for 10 min in Prussian Blue stain. Sections were washed in running water before counterstaining briefly for 1 min in Nuclear Fast Red (Thermo Fisher Scientific) and again washed in running water. Sections were incrementally dehydrated with an increasing percentage of ethanol before submerging in xylene and mounting coverslips. Images were taken using an Olympus VS120 S6 Slide scanner (Olympus Corporation, Tokyo, Japan).

Transmission Electron Microscopy (TEM)

TEM was utilized to visualize the uptake of SPIONs or SPION-labelled EVs into cells, EVs, and FRBOs. The cells or FRBOs were incubated with either 0 µg/mL, 50 µg/mL, or 100 µg/mL uncoated SPIONs or SPION-labeled LBM1-EVs for 24 h. The samples were then rinsed, harvested, and fixed overnight at 4°C in Karnovsky's fixative, prepared as 2.5% glutaraldehyde (Electron Microscopy Sciences, Hatfield, USA) and 2% paraformaldehyde in 0.1 M sodium cacodylate buffer (Electron Microscopy Sciences). Samples were post-fixed for 1 h in 1% osmium tetroxide (Electron Microscopy Sciences) in 0,1 M Na cacodylate buffer (Electron Microscopy Sciences), followed by a serial dehydration in ethanol (50 - 100%), a 1:1 mixture of EtOH and propylene oxide, and finally 100% propylene oxide. The samples were then solidified in Agar 100 resin and sectioned. Ultrathin sections (60 nm) were placed on 200 mesh formvar-coated copper grids (Electron Microscopy Sciences), stained with 2% uranyl acetate (Electron Microscopy Sciences) and lead citrate (Electron Microscopy Sciences).

For EVs, 10 µg of EVs were fixed in Karnovsky's fixative overnight at 4°C. After mounting on formvar carbon-coated copper grids, samples were post-fixed with 2.5% glutaraldehyde, followed by staining with 2% of uranyl acetate.

Final images were captured using a Hitachi HT7800 transmission electron microscope (Hitachi High-Tech Corporation, Tokyo, Japan).

Proliferation Assay

A proliferation assay was performed on H16 and LBM1 cells after 24 h incubation with both dextran-coated and uncoated SPIONs to assess their effects on cell growth. Cells were washed three times with PBS, and fresh cell culture medium was added to the cells. Plates were imaged every 2 h for 48 h using the IncuCyte Live-Cell Analysis System (Sartorius, Göttingen, Germany), and subsequent growth curves were generated using the IncuCyte S3 software (Essen Bioscience, Ltd.). The experiments were performed in triplicates.

Separation and Characterization of EVs

EVs were separated from serum EV-free cell culture medium using qEV columns (Izon Science, Christchurch, New Zealand). H16 and LBM1 cells were cultured in T175 flasks containing EV-free cell culture medium for 48 h until ~90% confluency. Conditioned medium (CM) was collected and centrifuged at 300 x g for 5 min to remove cell debris, and at 2000 x g for 20 min to remove larger apoptotic bodies. CM was concentrated in Amicon Ultra-15 100 kDa centrifugal filters (MilliporeSigma, Burlington, MA, USA) and immediately added to qEV Gen2 70nm series column. EVs were separated based on the manufacturer's recommendations. EV-rich fractions (6-11) were collected, pooled, and concentrated further using AmiconTM Ultra-0.5 Centrifugal Filter Units (MilliporeSigma) to a final volume of ~300 µL. Size distribution of isolated EV populations was quantified using dynamic light scattering (DLS) with a Zetasizer Nano ZS instrument (Malvern Panalytical, Malvern, Worcestershire, UK). Further characterization was performed through Western blotting for marker confirmation (and TEM for morphology) prior to further experimentation.

Western Blotting

Cells and EV lysates were isolated with RIPA lysis buffer supplemented with 10X protease and phosphatase inhibitor cocktail (Roche, Basel, Switzerland). Protein samples were electrophoresed on 4-12% NuPAGE Bis-Tris Protein gels (Invitrogen, Thermo Fisher), followed by a transfer to nitrocellulose membranes. Membranes were blocked for 1 h at room temperature (RT) with 5% skim milk in 1X TBS-T solution and incubated with primary immunoblotting antibodies: Calnexin (cat. no. 2679S; Cell Signaling Technology, Inc., Danvers, MA, USA), FLOT1 (cat. 18634S; Cell Signaling Technology), CD9 (cat. 13174S; Cell Signaling Technology), CD81 (cat. 56039S; Cell Signaling Technology) overnight at 4^0C. Membranes were washed and incubated with secondary antibodies (HRP anti-rabbit IgG; Immunotech, Beckman Coulter) for 1 h at room temperature. Signals were visualized with SuperSignal™ Pico/Femto Chemiluminescent Substrate (Thermo Fisher Scientific) using a LAS-3000 imaging system (Fujifilm, Saitama, Japan).

Labeling BM cell line-derived EVs with SPIONs

6.0 x 10^6 H16 and LBM1 cells were seeded in T175 flasks with EV-free cell culture media and incubated overnight. Fresh EV-free media with 0 µg/mL, 50 µg/mL, or 100 µg/mL SPIONs was exchanged in the flasks and incubated for 24 h. Cells were washed gently three times with 1x PBS to remove excess SPIONs and incubated for another 48 h. Cell-conditioned culture medium was then collected and EVs were separated as described above in section *"Separation and Characterization of EVs"*.

Iron Assay

Iron content within EV samples was quantified using the Iron Assay Kit (Sigma-Aldrich). 60 µg/well of EV samples in triplicates were processed according to the manufacturer's recommendations. Briefly, samples and iron kit standards (0 nmol/well, 2 nmol/well, 4 nmol/well, 6 nmol/well, 8 nmol/well, and 10 nmol/well) were added to 96-well plates in triplicates and iron assay buffer was added to all wells prior to a 1 h incubation at RT. 100 mL of Iron Probe was then added to all wells and the plate was incubated for 60 min at RT. Absorbance values at 593 nm were measured using a Multiskan FC Microplate Photometer (Thermo Fisher Scientific).

Nanospacer Assay

Nanoparticle tracking analysis (NTA) was conducted on control and SPION-EVs after isolation using Nanospacer devices (Norinnova, Norway). The device consists of a transparent coverslip precisely attached to a microscope slide - creating a nano space between the layers. Devices were filled by manual pipetting 2µl of sample onto the edge of the device (Supp. Fig. 1a). The capillary force pulls the liquid sample into a thin layer under the glass coverslip which then immediately after is used for NTA analysis. EV samples were imaged with darkfield-microscopy using an Olympus bench-top industrial microscope (Model BX53M, Olympus) equipped with a FLIR industrial camera (BFS-U3-200S6C-C, FLIR IIS Inc.) and standard white LED illumination. Movies were acquired using a 50x 0.5NA objective (LMPlanFL 50x BD, Olympus) at a frame rate of 10 Hz and same illumination condition to allow comparative intensity measurements between samples. Movies were identically processed using standard FIJI (version v1.54g) software functions before further analysis (e.g. binning, FFT filter, background removal). Open-source software Trackmate (FIJI) was used to trace EVs' movements under flow and measure scattering intensity levels (quality parameter) of single particles (Supp. Fig. 1b)[19,20]. The TraJClassifier FIJI plugin (version v0.8.1) was then used for mean square displacement (MSD) analysis to obtain diffusion coefficients from single particle tracks and estimate their hydrodynamic size according to their Brownian motion using the Stokes-Einstein relation (Supp. Fig. 1c)[21].

In vitro MR relaxometry of cell and EV phantoms

To investigate the effects of SPION-labeled cells on relaxation time, H16 and LBM1 cells were incubated with 100 μg/mL SPIONS as described above. A 2% Difco Noble agar solution (Becton Dickinson, Franklin Lakes, NJ, USA) was prepared in autoclaved water and mixed 1:1 with cell culture medium containing prelabeled cells in increasing concentrations. 2 mL from agar/cell dilution was transferred to 2 mL eppendorf tubes (Eppendorf SE, Hamburg, Germany) at final concentrations 500 cells/μL, 1000 cells/μL or 2000 cells/μL. Negative controls were prepared the same way with unlabeled cells. The experiments were performed in triplicates.

For EV phantoms, 10 and 20 μg of control or SPION-EVs were resuspended (1 mg/mL) and injected into semi-solidified 1% Difco Noble agar in PBS in 2 mL Eppendorf tubes and allowed to harden.

The tubes were examined by MRI at 21^{0}C using a 7T small animal PET/MR scanner (MR Solutions Ltd, Guildford, UK). First, a T2 weighted fast spin echo sequence was performed (repetition time (TR) 3000 ms, echo time (TE) 45 ms, field of view (FOV) 3 cm, matrix 256 x 252, slice thickness 1 mm, 12 slices, number of averages (NA) 2) to verify homogeneity of the agar/cell solution. Next, a multiple gradient echo T2 mapping sequence was performed (TR 2000 ms, TE 6 ms, 12 echoes, FOV 3 cm, matrix 64 x 64, slice thickness 1 mm, 12 slices, NA 1). Last, a multiple gradient echo T2* mapping sequence was performed (TR 1000 ms, TE 2 ms, 6 echoes, FOV 3 cm, matrix 64 x 64, slice thickness 1 mm, 12 slices, NA 1). Within the images of each tube, a region of interest covering approximately 75% of the tube was defined in the scanning software (Powerscan, MR Solutions Ltd), and T2 as well as T2* mapping values of the tubes were calculated. MR images were visualized using the Horos software (version 3.3.6, Annapolis, MA, USA) and graphs, statistical calculations and linear regression were performed using Graphpad Prism software version 10 (Graphpad Software, Inc., Boston, MA, USA).

Intracardial injections of LBM1 and H16 cell lines

Five 6-8-week-old female NOD/SCID mice per group were anesthetized with 3% sevoflurane in oxygen and anesthesia was maintained with 1.5% sevoflurane in oxygen. The mice were fixed in a supine position on a heating pad to maintain a core temperature of 37^{0}C. 5 x 10^5 of either LBM1 or H16 cells in 100 μL PBS were injected into the left cardiac ventricle using an insulin syringe by ultrasound guidance (Vevo 2100 Imaging System, VisualSonics Inc., Toronto, Canada). Brain tumor development was monitored with MRI every two weeks. T2 weighted coronal MR images were obtained using the following fast spin echo sequence scan parameters: FOV 20 mm × 20 mm, matrix size 256 × 256, 0.5 mm slice thickness, TR 3000 ms, TE 45 ms, FA 900, NA 2, scan time 3 min 41 s. Visualization of MR images were performed using the 32-bit OsiriX freeware, version 5.8.1 (Pixmeo SARL, Geneva, Switzerland).

In vivo injections of SPION-EVs and MRI

To visualize SPION-EVs *in vivo*, two 12-week-old C57BL/6 mice were scanned by MRI before and after intramuscular injection of 50 μg of LBM1 SPION-EVs in 100 mL of PBS into the right hind limb and 50 μg of control LBM1 EVs into the left hind limb. T2 weighted fast spin echo MRI scans (TR 3000 ms, TE 45 ms, FOV 3 cm, matrix 256 x 252, slice thickness 1 mm, 12 slices, NA 2) were performed to assess anatomical structures prior to injection and at, and 10 min post-injection. The imaging aimed to confirm the feasibility of MRI to detect small amounts of free, iron-labeled EVs.

Ethics Statement

For patient-derived cell lines used in this publication, written informed consent was obtained from all patients prior to tumor collection and tissue culture. Tissue collection, and generation, storage and use of cell lines from patient samples was approved by The Regional Committee for Medical and Health Research Ethics (REC; REC Approvals 2013/720 and 2020/65185).
For all *in vivo* work in this publication, mice were maintained on standard pellet feed with unrestricted water access. All mice experiments were approved by The Norwegian National Animal Research Authority under the Norwegian Food Safety Authority (Mattilsynet-Forsøksdyrutvalget; FOTS ID #30011) in accordance with the Norwegian Animal Welfare Act.

Results

SPIONs of different sizes are effectively internalized by LBM1 and H16 cell lines

We first tested the labeling of LBM1 and H16 cell lines using three different variants of commercially available superparamagnetic iron oxide nanoparticles (SPIONs); one measuring 35 nm and two measuring 5 nm in diameter, at concentrations of 50 µg/mL, 100 µg/mL, and 200 µg/mL. Prussian blue staining confirmed efficient SPION labeling within 24 h when using both dextran-coated 35 nm and uncoated 5 nm particles (Fig 1a, 1b). After 48 h of incubation, both cell lines exhibited reduced cell numbers and altered morphology (Supp. Fig. 2). Analysis indicated that over 90% of the cells were labeled with SPIONs at the highest concentrations after 24 h (Fig 1a, 1b). No uptake was observed when carboxyl-coated 5 nm particles were used, and therefore, no further experiments were performed (Supp. Fig. 3).
To quantify the effect of SPION labeling on cell growth, a proliferation assay was performed. For both cell lines, treatment with 35 nm SPIONs significantly inhibited cell growth already after 24 h of incubation for all iron concentrations tested (Fig 1c), as did 200 µg/mL of uncoated 5 nm SPIONs (Fig. 1d). In contrast, lower concentrations of uncoated 5 nm SPIONs had minimal effects on cell proliferation. TEM further confirmed the presence of uncoated 5 nm SPIONs within perinuclear vesicles in both H16 and LBM1 cells (Fig. 1e).

EVs are successfully loaded with 5nm SPIONs without altering population size distribution

EVs from LBM1 and H16 cells were isolated using Izon AFC and qEV columns. The presence of EV markers CD9, CD81, and flotilin-1, and the absence of the cell marker calnexin confirmed the successful extraction of EVs (Fig. 2a).
TEM was employed to confirm the labeling of BM-EVs with SPIONs. EV samples from both cell lines were collected after 24 h incubation with 5 nm and 35 nm SPIONS. SPION-labeled EVs displayed a distinct dark center within the vesicles, suggesting incorporation of 5 nm SPIONs into the EVs, though labeling was less consistent with the 35 nm SPIONs (Fig. 2b). Further, TEM verified the cup-shaped morphology and the sizes of EVs, as well as their iron content (Fig. 2b).

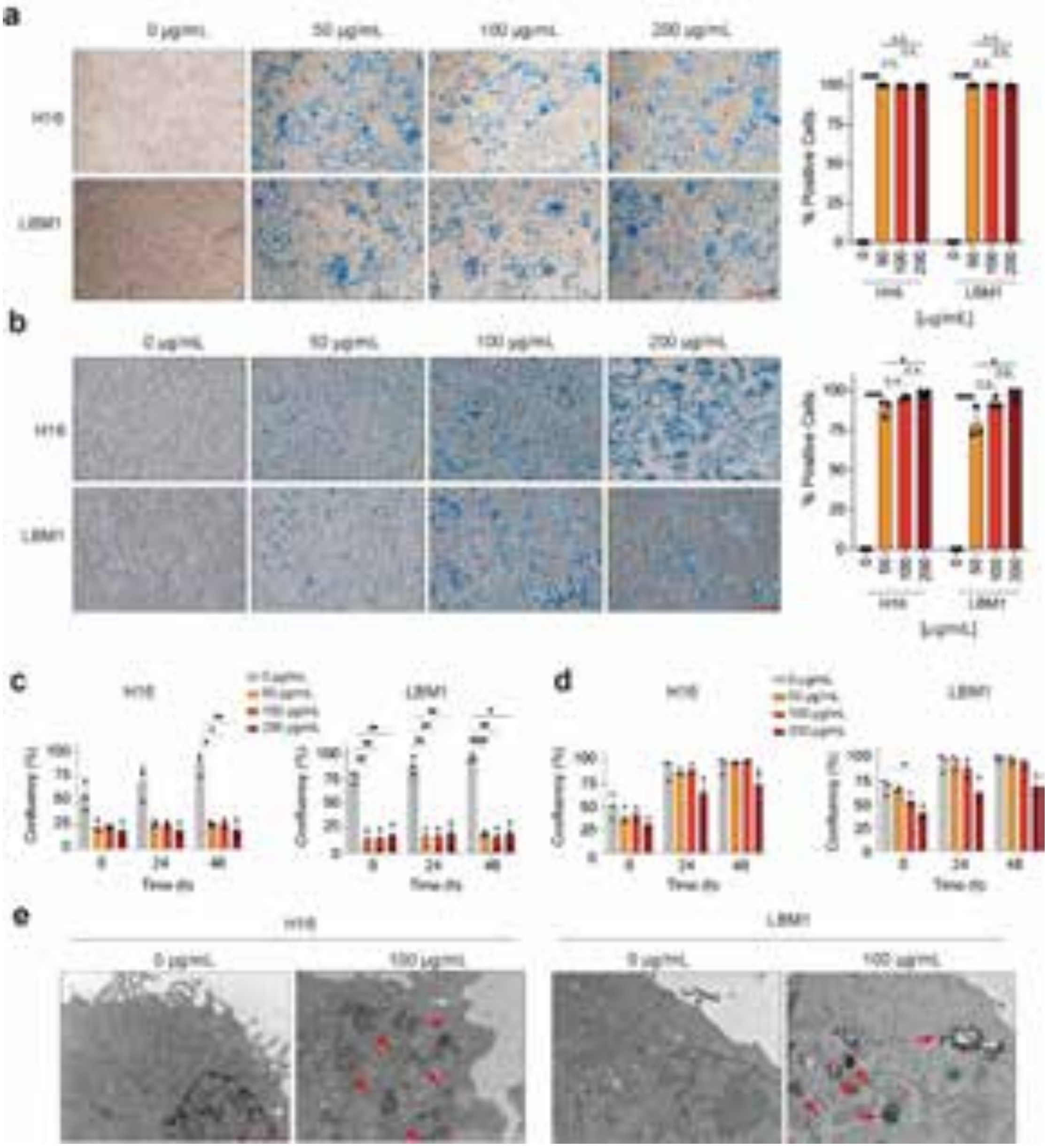

Fig. 1: Evaluating uptake and growth effects of commercially available SPIONs in LBM1 and H16 cell lines. (a,b) Prussian blue staining and subsequent quantification of H16 and LBM1 cells incubated with increasing doses of 35 nm **(a)** or 5 nm **(b)** SPIONS after 24 h. Scale bar = 100 µm. Blue spots show the presence of iron, and quantification is represented as percentage of blue-stained cells relative to the total cell number. **(c,d)** Incucyte proliferation assay of H16 and LBM1 cells following 24 h incubation with increasing doses of 35 nm **(c)** or 5 nm **(d)** SPIONs. **(e)** TEM micrographs of H16 and LBM1 cells after 24 h incubation with 5 nm SPIONs. Red arrows indicate SPIONs, localized in clusters in the cytoplasm of the cells. Scale bar = 1 µm. n.s. non-significant, $^*p < 0.05$, $^{**}p < 0.01$, $^{****}p < 0.0001$

A quantitative colorimetric iron assay showed that EVs labeled with 5 nm uncoated SPIONs or dextran-coated 35 nm SPIONs had comparable iron concentrations per µg EV protein, however labeling with 5 nm SPIONs was more consistent between batches (Fig. 2c).

The size distribution of the control EV population was confirmed to be between 50-200 nm through dynamic light scattering (DLS) analysis and remained unchanged after cell incubation with uncoated 5nm SPIONs (Fig. 2d). EVs collected from cells incubated with 35 nm SPIONs exhibited an altered size distribution compared to the control (Fig. 2d), suggesting either a change in EV production after incubation with SPIONs, or co-isolation of free SPIONs.

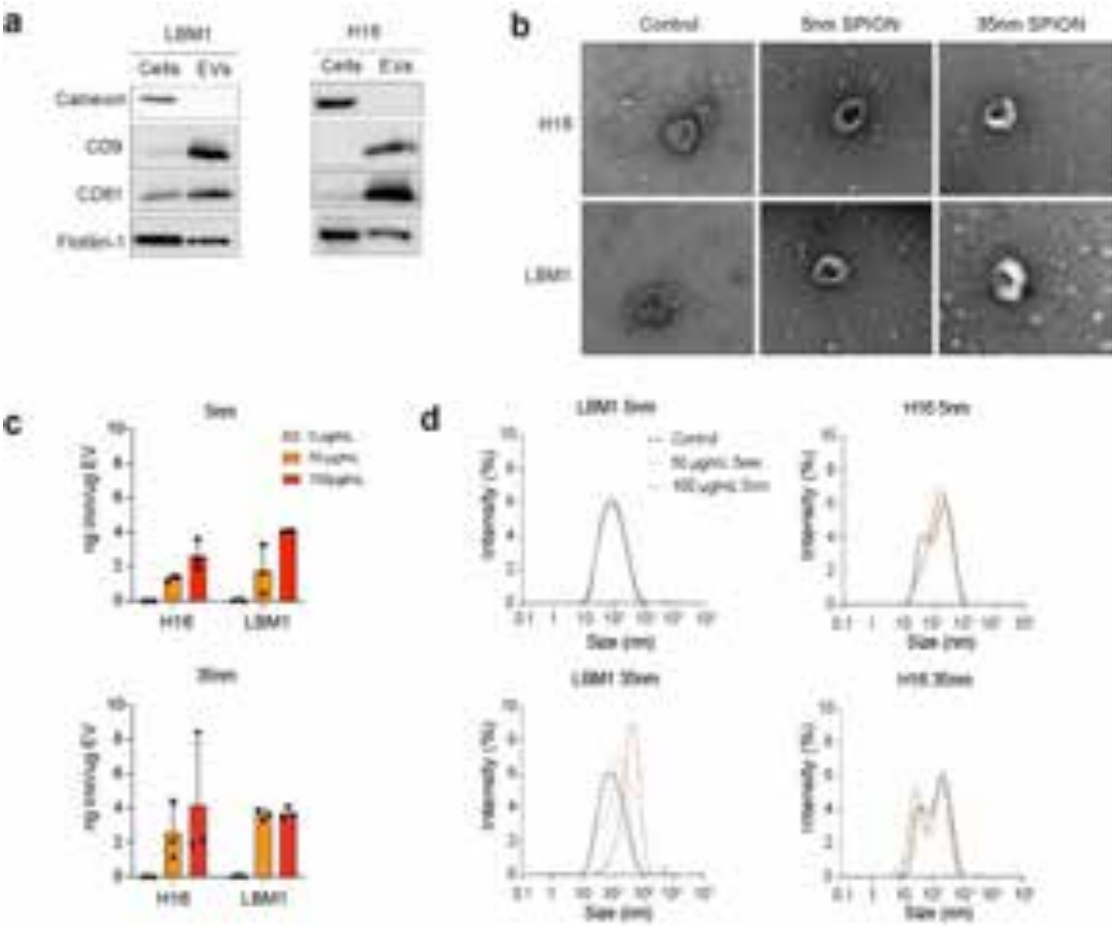

Fig. 2: Characterization of LBM1- and H16-EV markers, size, morphology, and iron content after SPION labeling. (a) Western blot analysis of positive (CD9, CD81 and FLOT-1) and negative marker (calnexin) on LBM1 and H16 cells and corresponding EVs. **(b)** TEM of unlabeled and labeled EVs extracted from H16 and LBM1 cells. Scale bar = 100 nm. **(c)** Quantification of iron content in EVs from H16 and LBM1 cells after labeling with SPIONs. **(d)** DLS analysis of H16- and LBM1-EV samples after SPION labeling, showing size distribution compared to unlabeled controls.

Based on the results from cell and EV labeling experiments (Fig. 1 and 2), 100 µg/mL of 5 nm uncoated SPIONs with a 24 h incubation time was determined to be the optimal conditions for further experiments. LBM1 cells were chosen for subsequent studies due to their rapid growth rate and high EV production. Nanoparticle tracking analysis using Nanospacer demonstrated a clear population shift in H16 EV light scattering intensity after iron incubation (Supp. Fig. 4a), while maintaining similar average particle sizes (124.44 nm control vs. 135.81 nm SPION), confirming successful iron incorporation (Supp. Fig. 4b).

SPION-EVs are effectively taken up by normal cells in FRBOs

To determine the bioactivity and feasibility of using SPION-EVs for iron delivery to organs, we conducted an *in vitro* co-culture assay by incubating 21-day-old FRBOs with LBM1 and H16 SPION-EVs to evaluate iron uptake.

After 24 h of incubation, Prussian blue staining revealed distinct blue spots within cells of FRBOs treated with LBM1-EVs, but not those treated with H16-EVs (Fig. 3a). This pattern reflects the differential brain-colonizing capacity of their parent cells, as LBM1 cells form brain tumors in mice, whereas H16 cells do not. (Supp. Fig. 5) The iron-positive spots initially appeared concentrated at the FRBO periphery before progressively spreading inward, suggesting a time-dependent pattern of EV internalization (Fig. 3a). TEM confirmed the

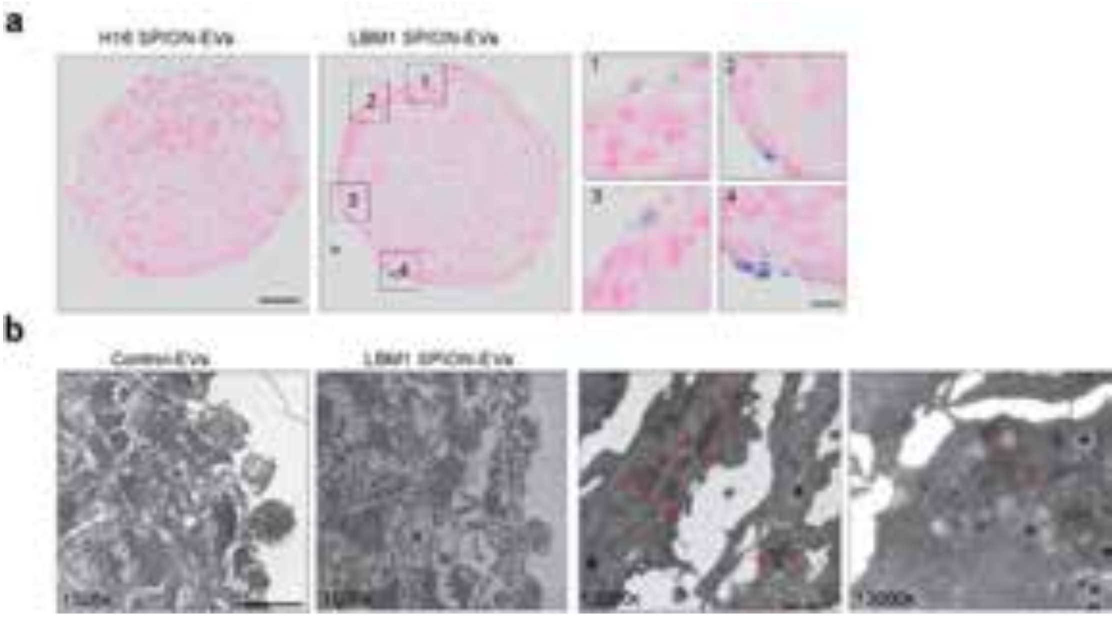

Fig. 3: Visualization of uptake of EV labeled SPIONs in FRBOs. (a) Prussian blue staining of FRBOs after 24 h co-culture with LBM1 SPION-EVs or H16 SPION-EVs. Blue dots show the presence of SPIONs within brain cells in FRBOs. The pink color is nuclear fast red stain. Scale bar = 50 µm, zoomed scale bar = 12.5 µm **(b)** Negative stained TEM images of FRBOs after co-culture with LBM1 SPION-EVs. Red encircled areas and red arrows indicate SPIONs. 1500x Scale bar = 10 µm, 12000x Scale bar = 1 µm.

presence of SPIONs within cell membranes, providing direct evidence of successful EV uptake (Fig. 3b).

BM cells and EVs labeled with SPIONs were successfully detected by in vitro MRI

Detection limits and optimal scanning parameters of SPION-labeled EVs and cells were established using agar phantoms. These phantoms contained both unlabeled and SPION-labeled BM cells at varying concentrations, along with SPION-EVs. Initial imaging of the phantoms, which included both SPION-labeled and unlabeled cells, used T2 weighted and T2* mapping scans (Fig. 4a-f).

The phantoms with SPION-labeled cells appeared as hypointense areas compared to the label-free controls (Fig. 4 a, d). T2 weighted MRI scans showed that the unlabeled phantoms displayed a T2 relaxation times of 120-140 ms, regardless of cell concentration (500, 1000 or 2000 cells/mL in agar). In phantoms labeled with uncoated 5 nm SPIONs, a significant change in T2 relaxation times was found for the two highest concentrations (2000 and 1000 cells/mL agar) (Fig. 4a, b). Further, a linear correlation between T2 relaxation values and the concentration of SPION-labeled cells were found (Fig. 4c).

The T2* mapping was shown to be more sensitive in detecting labeled cells, since there was a significant change in T2* mapping values also for 500 cells (Fig. 4d, 4e). Additionally, there was a linear correlation between T2* values and cell concentration (Fig. 4f).

In phantoms where SPIONs-labeled EVs were injected directly into the agar, their location was clearly visible in T2 weighted images, as well as T2 and T2* mapping images compared to the control-EVs (Fig. 4g), confirming successful visualization of labeled EVs *in vitro* using MRI.

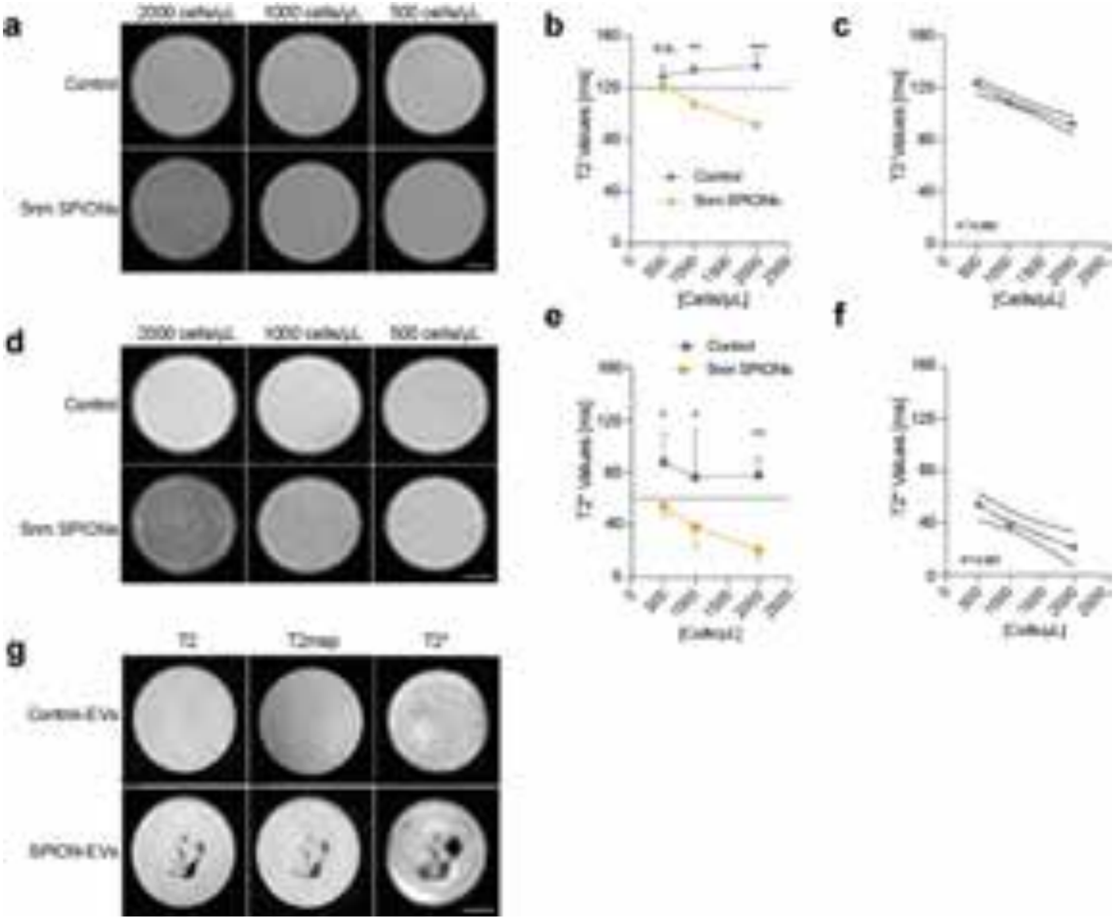

Fig. 4: Detection of cells and EVs labeled with SPIONs *in vitro* using MRI. Representative MR images of T2 **(a)** and T2* weighted **(d)** scanning of LBM1 cell phantoms with or without SPION labeling immobilized in 1% agarose at varying cell concentrations. **(b,c)** Quantification of MRI signal from SPION-labeled cells compared to controls with T2 **(b)** or T2* weighted **(e)** scanning. **(c,f)** Linear regression of LBM1 cell phantom signal quantification with T2 **(c)** or T2* weighted **(f)** scanning and corresponding R2 value. **(g)** MR images of LBM1 SPION-EV or control-EV samples injected into 1% agarose with T2 weighted, T2 mapping and T2* weighted scans. Hypointense areas indicate the presence of iron. n.s., non-significant, *p < 0.05, **p < 0.01, ***p < 0.001

SPION-labeled EVs injected intramuscularly were successfully detected by in vivo MRI

After confirming the bioactivity of SPION-EVs in organoids *in vitro* and their feasibility for visualization with MRI, we next visualized the SPION-EVs in complex tissues using an *in vivo* model. As a proof of concept, bulk intramuscular injections of LBM1 SPION-EVs and control EVs were administered into the thighs of two mice. MRI clearly visualized the injection areas in both legs, with the control injection producing a hyperintensive area, likely due to the presence of PBS (Fig. 5a). However, the SPION-EVs produced a notable hypointense area (indicated by red arrows) in the center of the injection site, confirming the presence of SPIONs and thus a loss of signal. Ten min post-injection, the injection sites were more dispersed but remained clearly visible.

Discussion

While EVs are known to play crucial roles in PMN formation and metastasis development, current methods lack the capability to track their dynamic distribution and cellular targeting in real-time[6,8,22]. To address this critical gap, we developed a SPION-based labeling system that

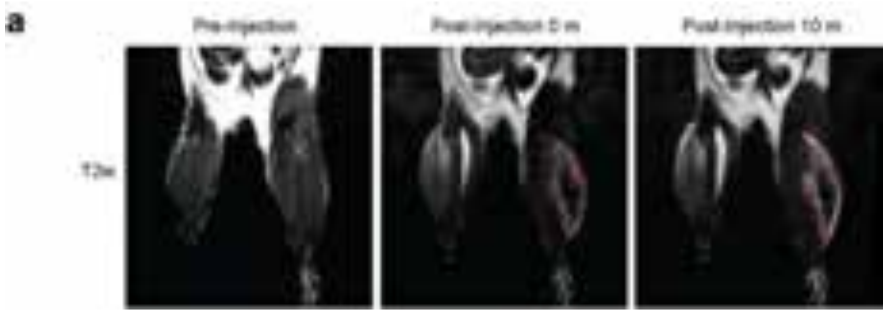

Fig. 5: SPION-EVs are clearly detected in mouse tissues. T2 weighted MR images of mice quadricep muscles pre- and post- injection of either LBM1 control-EVs (left leg) or SPION-EVs (right leg). Injection areas are marked by either green (control) or red (SPION) dashed lines, and hypointense areas indicating SPION presence are marked with red arrows.

enables multiscale visualization of EVs from subcellular imaging to *in vivo* distribution. Our approach builds on existing methods by, for the first time to our knowledge, combining passive SPION labeling of EVs and size exclusion chromatography for greater purity and maintenance of tissue-tropism properties. Through extensive characterization and optimization with multimodal imaging, we establish a robust and reliable labeling system for both *in vivo* and *in vitro* applications.

Labeling of EVs has proven to be a challenging task. Given their nanoscale size and bioactivity, labels must also be nanosized, capable of penetrating tissue, stable, and non-interfering with the activity of the EVs themselves. Although many labeling techniques are available, labels are typically restricted to a single imaging modality and can have limited imaging time windows, such as with fluorescence or radionuclide tags[23]. In contrast, SPIONs are detectable across a range from large-scale *in vivo* imaging to *ex vivo* cellular and sub-cellular imaging[24,25]. While fluorescence-based methods are restricted to approximately 2 mm imaging depth, our approach enables deep-tissue visualization through MRI while simultaneously allowing detailed analysis at the subcellular and cellular level[26]. This dual-capability system provides a comprehensive platform to study the temporal and spatial dynamics of EV distribution in PMN formation.

Uncoated 5 nm SPIONs emerged as the optimal choice among three commercially available formulations, demonstrating superior cellular uptake and preserving cell viability in our systematic evaluation. This specific size appears to represent an ideal balance between efficient cellular incorporation and minimal disruption of EV biology at a concentration that mediates cell toxicity[27]. The SPION-labeled EVs exhibited an iron concentration of 4 ng iron/µg EV, which is comparable to previous reports in stem cells (6.43 ng iron/µg EV) after incubation with 200 µg/mL SPIONs, whereas our study used 100 µg/mL[15]. Importantly, our labeling technique offers broad applicability across diverse cell types without requiring extensive protocol optimization or genetic modification of cell lines. By combining passive labeling with size exclusion chromatography, we achieved highly pure SPION-EVs while minimizing free SPION contamination—a persistent challenge when using larger particles with traditional ultracentrifugation-based isolation methods[28]. Dynamic light scattering and Nanospacer analysis confirmed consistent EV size distributions (100-150 nm) before and after SPION loading, with a clear shift in light scattering intensity post-loading. This shift, occurring without significant size alterations, provides strong evidence for successful nanoparticle incorporation while preserving vesicle structural integrity.

A key concern when loading EVs with nanoparticles is the potential disruption of their biological function and natural behavior. Our results demonstrate that LBM1-EVs maintain their brain tropism, while EVs from H16 cells—which do not colonize the brain *in vivo*—showed no uptake in brain organoids. These findings align with previous research indicating that EV tropism is determined by the parent cell signature, and importantly, confirms that our SPION-loading process preserves the EVs' targeting capabilities[29]. This preservation of natural targeting behavior is a pre-requisite for studying PMN formation, ensuring EV distribution patterns reflect genuine biological processes rather than artifacts of the labeling method. The maintained functionality of SPION-labeled EVs also suggests preservation of their membrane proteins and surface markers, essential components for crossing the blood-brain barrier, and cellular recognition and uptake in the brain[30].

While much of SPION-EV research has focused on therapeutic delivery, we aim to use this model for a novel application: understanding the fundamental biology of PMN formation before tumor cell arrival [31–33]. We have successfully demonstrated that SPION-EVs are clearly visible following intramuscular injection, setting the stage for optimizing brain delivery methods. Moving forward, comprehensive dosing studies, time-course analyses, and biodistribution investigations will be essential to advance this work. Optimization of MRI detection techniques would enhance sensitivity for tracking physiologically relevant EV concentrations *in vivo*. While T2* was optimal for *in vitro* SPION detection, T2 proved more feasible for mouse tissue imaging, as the increased sensitivity of T2* also heightened shimming requirements. Particular attention should be paid to understanding the kinetics of EV distribution in the brain microenvironment and their interactions with specific cell types involved in PMN formation. Additionally, future studies should explore the potential of combining this tracking system with therapeutic interventions to both monitor and modulate PMN development.

Our results on the SPION-based EV labeling may have potential clinical applications in diagnostics as well as in therapeutics. A non-invasive tracking strategy using SPION-labeled EVs and MRI could help monitor metastatic progression and evaluate therapeutic responses in patients with BM SPIONs can effectively label EVs without changing their biological properties is particularly significant, as certain iron oxide nanoparticles have already received FDA approval for clinical imaging applications[34,35]. Our results could facilitate translation to clinical studies aiming to understand EV-mediated PMN formation in patients. This labeling approach could also support the development of EV-based therapies, enabling real-time visualization of therapeutic EV delivery and distribution clinically.

Conclusion

In this study, we developed a reproducible, trackable, and straightforward protocol for labeling BM-EVs, enabling their visualization in complex environments such as brain organoids and tissues and even at subcellular localization within individual cells. This model not only facilitates spatial tracking of EVs *in vivo* but also aids in identifying specific target cell types, paving the way for functional studies that may explore the impact of BM-EVs. This approach can be applied to investigate the role of EVs in shaping the pre-metastatic niche, providing insights into their contributions to tumor progression and metastasis.

Data Availability Statement

Data available upon reasonable request to the corresponding authors.

Acknowledgments

All light microscopy, TEM, and MR imaging was performed at The Molecular Imaging Center, Department of Biomedicine, University of Bergen, Norway. This work was supported by the Norwegian Cancer Society (182716), The Western Norway Regional Health Authority

(F-12856-D11661) and the University of Bergen and the Horizon Europe Program (101064246), UiT Talent Innovation grant.

Disclosure

Oliver Vanderpoorten has filed a patent application on Nanospacer technology.

Author Contributions

Birgitte Feginn Berle: Data curation; formal analysis; investigation; methodology; writing—review and editing. **Sunniva Juliussen**: Data curation; formal analysis; investigation; methodology; writing—review and editing. **Aurea Castilho**: Data curation; formal analysis; investigation; methodology; writing—review and editing. **Ege Solel**: Data curation; investigation; methodology; writing—review and editing. **Halala Sdik Saed**: Data curation; investigation; methodology; writing—review and editing. **Oliver Vanderpoorten**: Data curation; formal analysis; investigation; methodology; writing—review and editing. **Taral R. Lunavat**: Methodology; supervision; writing—review and editing. **Emma Rigg**: Conceptualization; data curation; formal analysis; investigation; project administration; supervision; writing—original draft; writing—review and editing. **Frits Thorsen**: Conceptualization; data curation; formal analysis; funding acquisition; investigation; project administration; supervision; writing—original draft; writing—review and editing.

References

1. Li J, Lu S, Chen F, Zhu H. Unveiling the hidden role of extracellular vesicles in brain metastases: a comprehensive review. *Front Immunol*. 2024;15. doi:10.3389/fimmu.2024.1388574
2. Welsh JA, Goberdhan DCI, O'Driscoll L, et al. Minimal information for studies of extracellular vesicles (MISEV2023): From basic to advanced approaches. *J Extracell Vesicles*. 2024;13(2):e12404. doi:10.1002/jev2.12404
3. Hanelova K, Raudenska M, Kratochvilova M, et al. Autophagy modulators influence the content of important signalling molecules in PS-positive extracellular vesicles. *Cell Commun Signal*. 2023;21(1):120. doi:10.1186/s12964-023-01126-z
4. Walbrecq G, Margue C, Behrmann I, Kreis S. Distinct Cargos of Small Extracellular Vesicles Derived from Hypoxic Cells and Their Effect on Cancer Cells. *IJMS*. 2020;21(14):5071. doi:10.3390/ijms21145071
5. Wu D, Deng S, Li L, et al. TGF-β1-mediated exosomal lnc-MMP2-2 increases blood-brain barrier permeability via the miRNA-1207-5p/EPB41L5 axis to promote non-small cell lung cancer brain metastasis. *Cell Death Dis*. 2021;12(8):721. doi:10.1038/s41419-021-04004-z
6. Rigg E, Wang J, Xue Z, et al. Inhibition of extracellular vesicle-derived miR-146a-5p decreases progression of melanoma brain metastasis via Notch pathway dysregulation in astrocytes. *J Extracell Vesicles*. 2023;12(10):e12363. doi:10.1002/jev2.12363
7. Rodrigues G, Hoshino A, Kenific CM, et al. Tumour exosomal CEMIP protein promotes cancer cell colonization in brain metastasis. *Nat Cell Biol*. 2019;21(11):1403-1412. doi:10.1038/s41556-019-0404-4
8. Tominaga N, Kosaka N, Ono M, et al. Brain metastatic cancer cells release microRNA-181c-containing extracellular vesicles capable of destructing blood–brain barrier. *Nat Commun*. 2015;6(1):6716. doi:10.1038/ncomms7716
9. Geissler M, Jia W, Kiraz EN, et al. The Brain Pre-Metastatic Niche: Biological and Technical Advancements. *Int J Mol Sci*. 2023;24(12):10055. doi:10.3390/ijms241210055
10. Chourmouzi D, Papadopoulou E, Marias K, Drevelegas A. Imaging of Brain Tumors. *Surgical Oncology Clinics*. 2014;23(4):629-684. doi:10.1016/j.soc.2014.07.004
11. Rahman M. Magnetic Resonance Imaging and Iron-oxide Nanoparticles in the era of Personalized Medicine. *Nanotheranostics*. 2023;7(4):424-449. doi:10.7150/ntno.86467
12. Thakor AS, Jokerst JV, Ghanouni P, Campbell JL, Mittra E, Gambhir SS. Clinically Approved Nanoparticle Imaging Agents. *J Nucl Med*. 2016;57(12):1833-1837. doi:10.2967/jnumed.116.181362
13. Wei H, Hu Y, Wang J, Gao X, Qian X, Tang M. Superparamagnetic Iron Oxide Nanoparticles: Cytotoxicity, Metabolism, and Cellular Behavior in Biomedicine Applications. *Int J Nanomedicine*. 2021;16:6097-6113. doi:10.2147/IJN.S321984

14. Wang HH, Wang YXJ, Leung KCF, et al. Durable Mesenchymal Stem Cell Labelling by Using Polyhedral Superparamagnetic Iron Oxide Nanoparticles. *Chemistry – A European Journal*. 2009;15(45):12417-12425. doi:10.1002/chem.200901548
15. Busato A, Bonafede R, Bontempi P, et al. Magnetic resonance imaging of ultrasmall superparamagnetic iron oxide-labeled exosomes from stem cells: a new method to obtain labeled exosomes. *IJN*. 2016;11:2481-2490. doi:10.2147/IJN.S104152
16. Kutchy NA, Ma R, Liu Y, Buch S, Hu G. Extracellular Vesicle-Mediated Delivery of Ultrasmall Superparamagnetic Iron Oxide Nanoparticles to Mice Brain. *Front Pharmacol*. 2022;13:819516. doi:10.3389/fphar.2022.819516
17. Han Z, Liu S, Pei Y, et al. Highly efficient magnetic labelling allows MRI tracking of the homing of stem cell-derived extracellular vesicles following systemic delivery. *Journal of Extracellular Vesicles*. 2021;10(3):e12054. doi:10.1002/jev2.12054
18. Bjerkvig R, Steinsvåg SK, Laerum OD. Reaggregation of fetal rat brain cells in a stationary culture system I: Methodology and cell identification. *In Vitro Cell Dev Biol*. 1986;22(4):180-192. doi:10.1007/BF02623302
19. Ershov D, Phan MS, Pylvänäinen JW, et al. TrackMate 7: integrating state-of-the-art segmentation algorithms into tracking pipelines. *Nat Methods*. 2022;19(7):829-832. doi:10.1038/s41592-022-01507-1
20. Tinevez JY, Perry N, Schindelin J, et al. TrackMate: An open and extensible platform for single-particle tracking. *Methods*. 2017;115:80-90. doi:10.1016/j.ymeth.2016.09.016
21. Wagner T, Kroll A, Haramagatti CR, Lipinski HG, Wiemann M. Classification and Segmentation of Nanoparticle Diffusion Trajectories in Cellular Micro Environments. *PLOS ONE*. 2017;12(1):e0170165. doi:10.1371/journal.pone.0170165
22. Zhang Y, Chen Y, Shi L, et al. Extracellular vesicles microRNA-592 of melanoma stem cells promotes metastasis through activation of MAPK/ERK signaling pathway by targeting PTPN7 in non-stemness melanoma cells. *Cell Death Discov*. 2022;8(1):1-10. doi:10.1038/s41420-022-01221-z
23. Almeida S, Santos L, Falcão A, Gomes C, Abrunhosa A. In Vivo Tracking of Extracellular Vesicles by Nuclear Imaging: Advances in Radiolabeling Strategies. *Int J Mol Sci*. 2020;21(24):9443. doi:10.3390/ijms21249443
24. Arifin DR, Witwer KW, Bulte JWM. Non-Invasive imaging of extracellular vesicles: Quo vaditis in vivo? *Journal of Extracellular Vesicles*. 2022;11(7):12241. doi:10.1002/jev2.12241
25. Zhuo Z, Wang J, Luo Y, et al. Targeted extracellular vesicle delivery systems employing superparamagnetic iron oxide nanoparticles. *Acta Biomaterialia*. 2021;134:13-31. doi:10.1016/j.actbio.2021.07.027
26. Ochiai H, Sakamoto N, Fujita K, et al. Zinc-finger nuclease-mediated targeted insertion of reporter genes for quantitative imaging of gene expression in sea urchin embryos. *Proceedings of the National Academy of Sciences*. 2012;109(27):10915-10920. doi:10.1073/pnas.1202768109
27. Singh N, Jenkins GJS, Asadi R, Doak SH. Potential toxicity of superparamagnetic iron oxide nanoparticles (SPION). *Nano Reviews*. 2010;1(1):5358. doi:10.3402/nano.v1i0.5358
28. Toomajian VA, Tundo A, Ural EE, Greeson EM, Contag CH, Makela AV. Magnetic Particle Imaging Reveals that Iron-Labeled Extracellular Vesicles Accumulate in Brains of Mice with Metastases. *ACS Appl Mater Interfaces*. 2024;16(24):30860-30873. doi:10.1021/acsami.4c04920
29. Sancho-Albero M, Navascués N, Mendoza G, et al. Exosome origin determines cell targeting and the transfer of therapeutic nanoparticles towards target cells. *Journal of Nanobiotechnology*. 2019;17(1):16. doi:10.1186/s12951-018-0437-z
30. Morad G, Carman CV, Hagedorn EJ, et al. Tumor-Derived Extracellular Vesicles Breach the Intact Blood-Brain Barrier via Transcytosis. *ACS Nano*. 2019;13(12):13853-13865. doi:10.1021/acsnano.9b04397
31. Hu WJ, Wei H, Cai LL, et al. Magnetic targeting enhances the neuroprotective function of human mesenchymal stem cell-derived iron oxide exosomes by delivering miR-1228-5p. *J Nanobiotechnol*. 2024;22(1):665. doi:10.1186/s12951-024-02941-3
32. Ji C, Zhang J, Shi L, et al. Engineered extracellular vesicle-encapsulated CHIP as novel nanotherapeutics for treatment of renal fibrosis. *npj Regen Med*. 2024;9(1):1-11. doi:10.1038/s41536-024-00348-0
33. Tian T, Qiao S, Tannous BA. Nanotechnology-Inspired Extracellular Vesicles Theranostics for Diagnosis and Therapy of Central Nervous System Diseases. *ACS Appl Mater Interfaces*. 2023;15(1):182-199. doi:10.1021/acsami.2c07981
34. Pellico J, Ruiz-Cabello J, Herranz F. Radiolabeled Iron Oxide Nanomaterials for Multimodal Nuclear Imaging and Positive Contrast Magnetic Resonance Imaging (MRI): A Review. *ACS Appl Nano Mater*. 2023;6(22):20523-20538. doi:10.1021/acsanm.3c04269
35. Oberdick SD, Jordanova KV, Lundstrom JT, et al. Iron oxide nanoparticles as positive T1 contrast agents for low-field magnetic resonance imaging at 64 mT. *Sci Rep*. 2023;13(1):11520. doi:10.1038/s41598-023-38222-6

Supplementary Information

Supp. Figure 1: The Nanospacer methodology. (a) Schematic overview of the Nanospacer concept. A glass capillary confines nanoparticles or biomolecules into a thin liquid layer (approx. 1 mm) under a glass coverslip which is then imaged using dark-field microscopy. (**b**) EV tracking in Nanospacer confinement using the Trackmate plugin. Particle tracks are color-coded based on Trackmate parameters (quality, speed, shape). Different scattering intensities at the same hydrodynamic size indicate varying EV cargos, enabling single-particle subpopulation analysis. (**c**) TraJ analysis of EV motion. Single particle tracking results in a trajectory of EV movement over time (left) and provides data for MSD analysis (right). Experimental data (blue line) is fit to a theoretical model (orange dots) to determine the particle's diffusion coefficient. The coefficient is used with the Stokes-Einstein equation to estimate EV size.

Supp. Figure 2: Evaluating uptake and growth effects of multiple commercially available SPIONs in LBM1 and H16 cell lines after 48 h. (a,b) Prussian blue staining of H16 and LBM1 cells incubated with increasing doses of both 35 nm **(a)** or 5nm **(b)** SPIONS after 24 h. Scale bar = 100 µm. Blue spots indicate the presence of iron.

Supp. Figure 3 Evaluating uptake of carboxyl coated-SPIONs in LBM1 and H16 cell lines. Prussian blue staining of H16 and LBM1 cells incubated with increasing doses of both 5 nm carboxyl-coated SPIONS after 24 h. Scale bar = 100µm.

Supp. Figure 4 Nanospacer Analysis of H16 EVs after SPION loading. (a) Intensity distribution histograms of EVs isolated from H16 control and SPION-treated cells. (**b**) Size distribution histograms of H16-derived EVs.

Supp. Figure 5: MRI Evaluation of tumor burden in mice after injection of LBM1 or H16 cells. T2 weighted MRI brain scans of NOD-SCID mice 2 and 4 weeks after injection with $5x10^5$ LBM1 or H16 cells. Red arrows indicate tumors.

Supp. Figure 1

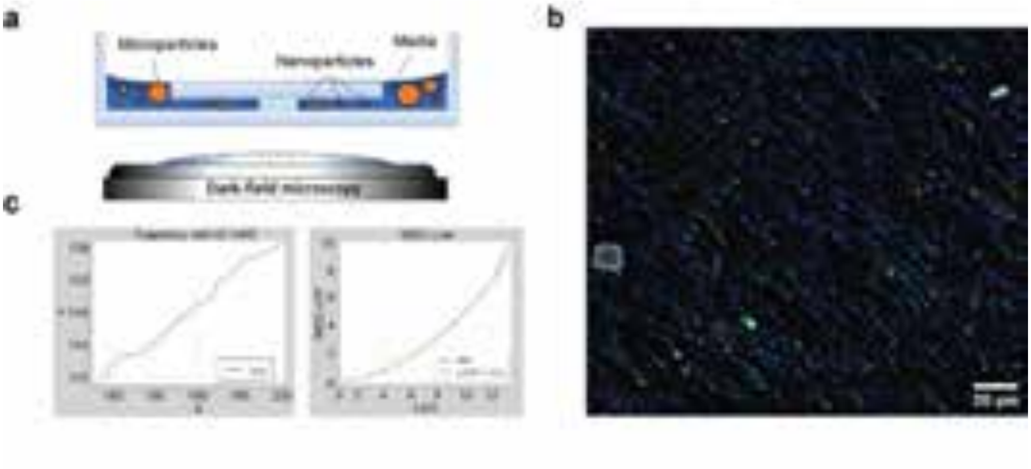

Supp. Figure 2

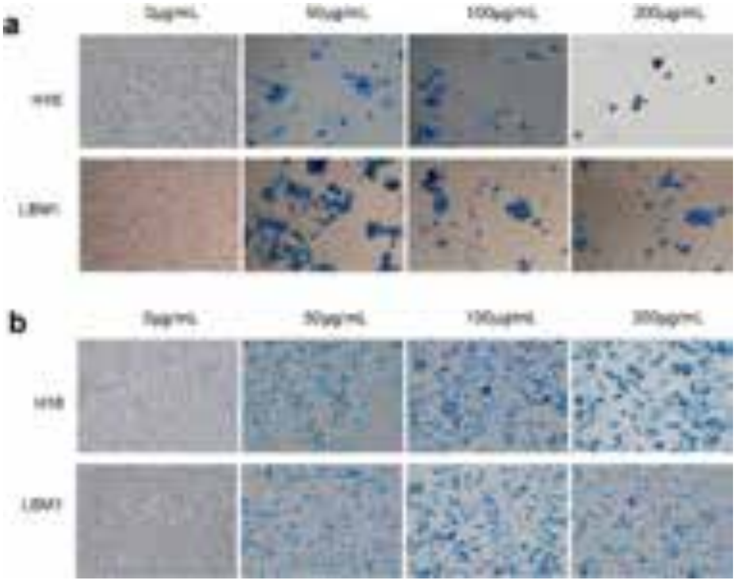

Supp. Figure 3

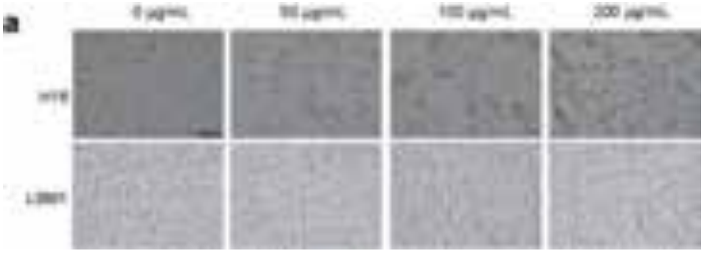

Supp. Figure 4

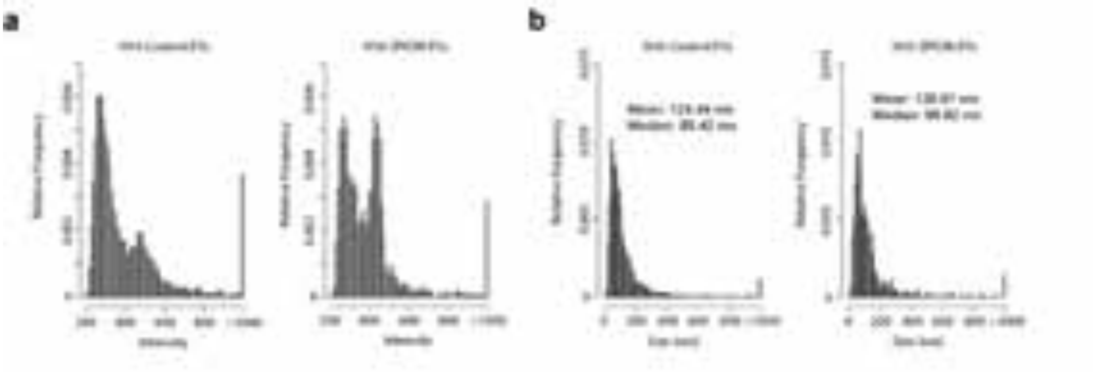

Supp. Figure 5

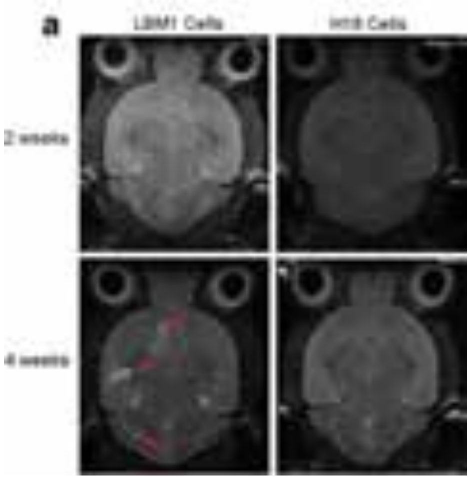

RESEARCH ARTICLE

CCT196969 effectively inhibits growth and survival of melanoma brain metastasis cells

Agathe Reigstad[1], Christina Frantzen Herdlevær[1], Emma Rigg[1], Tuyen Hoang[1], Ole Vidhammer Bjørnstad[1], Synnøve Nymark Aasen[1,2], Jasmin Preis[3], Claude Haan[3], Terje Sundstrøm[4,5], Frits Thorsen[1,6]*

1 Department of Biomedicine, University of Bergen, Bergen, Norway, **2** Faculty of Health and Social Sciences, Western Norway University of Applied Sciences, Bergen, Norway, **3** Department of Life Sciences and Medicine, University of Luxembourg, Belvaux, Luxembourg, **4** Department of Neurosurgery, Haukeland University Hospital, Bergen, Norway, **5** Department of Clinical Medicine, University of Bergen, Bergen, Norway, **6** Molecular Imaging Center, Department of Biomedicine, University of Bergen, Bergen, Norway

* frits.thorsen@uib.no

Check for updates

OPEN ACCESS

Citation: Reigstad A, Herdlevær CF, Rigg E, Hoang T, Bjørnstad OV, Aasen SN, et al. (2022) CCT196969 effectively inhibits growth and survival of melanoma brain metastasis cells. PLoS ONE 17(9): e0273711. https://doi.org/10.1371/journal.pone.0273711

Editor: Suzie Chen, Rutgers University, UNITED STATES

Received: March 18, 2022

Accepted: August 11, 2022

Published: September 9, 2022

Copyright: © 2022 Reigstad et al. This is an open access article distributed under the terms of the Creative Commons Attribution License, which permits unrestricted use, distribution, and reproduction in any medium, provided the original author and source are credited.

Data Availability Statement: All relevant data files will be available after acceptance of the manuscript.

Funding: F.T. has been supported by The Norwegian Cancer Society (grant no 182716) (https://kreftforeningen.no/en/) and The Western Norway Regional Health Authority (grant no F-11970)(https://helse-vest.no/en/research-and-co-operation). A.R. and C.F.H. has been supported by The Medical Student Research Programme at The Faculty of Medicine, University of Bergen (https://www.uib.no/en/med/71062/medical-student-

Abstract

Melanomas frequently metastasize to the brain. Despite recent progress in the treatment of melanoma brain metastasis, therapy resistance and relapse of disease remain unsolved challenges. CCT196969 is a SRC family kinase (SFK) and Raf proto-oncogene, serine/threonine kinase (RAF) inhibitor with documented effects in primary melanoma cell lines *in vitro* and *in vivo*. Using *in vitro* cell line assays, we studied the effects of CCT196969 in multiple melanoma brain metastasis cell lines. The drug effectively inhibited proliferation, migration, and survival in all examined cell lines, with viability IC_{50} doses in the range of 0.18–2.6 μM. Western blot analysis showed decreased expression of p-ERK, p-MEK, p-STAT3 and STAT3 upon CCT196969 treatment. Furthermore, CCT196969 inhibited viability in two *B-Raf Proto-Oncogene* (BRAF) inhibitor resistant metastatic melanoma cell lines. Further *in vivo* studies should be performed to determine the treatment potential of CCT196969 in patients with treatment-naïve and resistant melanoma brain metastasis.

Introduction

The incidence of melanoma is rising faster than any other cancer [1], and 44–75% of patients with metastatic melanoma will develop brain metastases during the course of their disease [2–4]. Melanoma brain metastasis (MBM) is associated with a poor prognosis. If left untreated, the median patient survival is only a few months [5–7]. Aberrant activation of the mitogen-activated protein kinase (MAPK) signalling pathway represents a central step in melanoma development by providing increased proliferation and survival of melanoma cells [8]. Mutations are frequently seen in the *NRAS proto-oncogene* (*NRAS*; 28%) and *BRAF* (52%) genes [9], and 80% of *BRAF*-mutated melanomas display the $BRAF^{V600E}$ mutation [10].

Treatment of metastatic melanoma has improved over the last decade due to the use of targeted inhibitors and immunotherapies. Although targeted therapies offer a promising avenue for treatment of patients with *BRAF*-mutated melanoma, most patients experience relapse of

research-programme-faculty-medicine). The funders had no role in study design, data collection and analysis, decision to publish or preparation of the manuscript.

Competing interests: The authors declare that no competing interests exist.

disease within a few months [11]. There are major challenges with intrinsic and acquired resistance to BRAF inhibitors [8, 11], and use of BRAF inhibitors may cause paradoxical activation of the MAPK pathway, leading to increased tumour growth [12, 13].

Mechanisms of resistance to BRAF inhibitors include MAPK-dependent mechanisms such as novel *NRAS* mutations or *BRAF* amplifications, and MAPK-independent mechanisms [14] such as upregulation of the epidermal growth factor receptor (EGFR)-SFK-signal transducer and activator of transcription 3 (STAT3) pathway and the phosphoinositide 3-kinase (PI3K) pathway [15, 16]. The STAT3 pathway is frequently upregulated in BRAF inhibitor resistant melanoma [15], which can drive invasion and metastasis [15, 17]. Furthermore, SFKs are known to promote a neoplastic and metastatic phenotype [18] and is commonly upregulated in BRAF inhibitor resistant cells [19, 20]. Patients often develop BRAF inhibitor resistance shortly after single drug treatment with BRAF inhibitors [21]. Therefore, the median survival is only modestly increased for patients with MBM upon treatment with MAPK inhibitors [22, 23]. Thus, there is an urgent need for novel therapeutic options through targeting multiple signalling pathways besides MAPK to improve patient outcome.

It has been shown that the pan-RAF and SFK inhibitor CCT196969 targets mutated $\mathrm{BRAF}^{\mathrm{V600E}}$, C-Raf Proto-Oncogene (CRAF) and SFKs in primary melanoma cell lines [24]. Furthermore, the drug inhibited cell proliferation more effectively than the vemurafenib analogue PLX4720 and hampered growth of *RAS* mutant melanomas [24]. Here, we report for the first time that CCT196969 effectively inhibits cell growth of MBM cell lines *in vitro*.

Materials and methods

Cell lines and cell culture

The H1, H2, H3, H6 and H10 cell lines were established in our laboratory from patient biopsies of human MBM, as previously described [25]. Written, informed consent was obtained from all patients before collection of tumour material. The Regional Ethical Committee (REC) approved tissue collection, storage of tumour material, and generation and use of cell lines (REC Approvals 2013/720 and 2020/65185). The H1 and H2 cell lines harbour the $BRAF^{V600E}$ mutation, while the H3 cell line is $BRAF^{L577F}$ mutated [26]. In addition, H3 possesses $NRAS^{Q61H}$ and *EGFR* mutations, while the H6 and H10 cell lines also harbour the $BRAF^{V600E}$ mutation (unpublished data from our lab). The cells were cultured in Dulbecco's Modified Eagle's Medium (DMEM, Sigma-Aldrich Inc., St. Louis, MO, USA) supplemented with 10% heat-inactivated fetal calf serum (FCS) (Thermo Fischer Scientific, Waltham, MA, USA), 4 times the prescribed amount of non-essential amino acids, 2% L-Glutamine, 100 IU/mL penicillin and 100 μL/mL streptomycin (all reagents from BioWhittaker, Verviers, Belgium).

The $BRAF^{V600E}$-mutated melanoma cell line Wm3248 was purchased from Rockland (Limerick, PA, USA). The cells were cultured in RPMI-1640 Glutamax™ (Thermo Fischer Scientific) supplemented with 10% heat-inactivated FCS (Thermo Fischer Scientific), 50 IU/mL penicillin and 50 μL/mL streptomycin (BioWhittaker).

All cell cultures were maintained in a standard tissue culture incubator at 37˚C with 100% humidity and 5% CO_2. Cells were subcultured to 70–90% confluency before passaging, and the growth medium was exchanged twice a week. Cells were tested and found mycoplasma free before use and authenticated using short tandem repeat profiling within 6 months of use.

Drug

CCT196969 and vemurafenib were purchased from ChemieTek (Indianapolis, IN, USA). Both drugs were dissolved in dimethylsulfoxide (DMSO, Sigma-Aldrich Inc.) at a stock concentration of 50 mM and stored as aliquots at -20˚C until use.

Monolayer cell viability assay

Monolayer MTS assays were performed to study cell viability upon exposure to different concentrations of CCT196969. H1, H2, H3, H6, H10 and Wm3248 cells were seeded in 96-well plates (Nunc, Roskilde, Denmark) at a cell density of 5 x 10^3 cells/well in 100 μL growth medium. After 24 h, 100 μL growth medium containing CCT196969 was applied to the wells in final concentrations of 0.0001, 0.001, 0.005, 0.01, 0.05, 0.1, 1, 10 and 50 μM for all cell lines except H2. For H2, 100 μL growth medium containing CCT196969 was applied to the wells in final concentrations of 0.001, 0.005, 0.01, 0.05, 0.1, 1, 5, 10 and 50 μM. After 72 h of incubation, morphology pictures were captured using a Nikon TE2000 inverted microscope (Nikon Instruments Inc., Melville, NY, USA). Floating cells were removed and 100 μL fresh DMEM was added prior to morphology imaging. 20 μL of MTS solution (CellTiter 96™ Aqueous One Solution Cell Proliferation Assay, Promega Corporation, Fitchburg, WI, USA) was then added to each well, and absorbance was measured at 490 nm 4 h later, using a Multiskan FC Microplate photometer (Thermo Fischer Scientific), equipped with SkanIt software. Cell viability curves were generated using Prism 8 Software (GraphPad Software Inc., San Diego, CA, USA), and IC_{50} doses were calculated; i.e., the drug concentrations at which 50% of the cell viability was inhibited. The experiments for the H1, H2, H3, H6 and H10 were done in triplicates. The Wm3248 experiment was performed in duplicate.

Tumour sphere viability assay

To study the effects of treatment on 3-dimensional tumour growth, a tumour sphere viability assay was performed. A base agar was prepared by mixing 2.4% of Difco Noble Agar in purified water (Becton Dickinson and Company, Sparks, USA) with growth medium to a final concentration of 0.6%. The agar was kept warm by a block heater (Grant QBT2 Digital Block Heater, Gran Instruments, Cambridge, England) to prevent it from solidifying. 50 μL of agar solution was plated into each well of a 96-well plate (Nunc).

A soft agar top layer was prepared by mixing 1 part low melting point agarose in purified water (Sigma-Aldrich Inc.) with 3 parts of growth medium at 50˚C in a water bath. The liquid agar was temporarily kept at 40˚C. H1, H2 and H3 cells were trypsinised and quantified using a Countess Automated Cell Counter (Invitrogen, Waltham, MA, USA). A suspension of 8 x 10^4 cells/mL in pre-warmed growth medium was prepared and mixed with equal parts of soft agar. The cell-containing soft agar was then transferred to a petri dish on a 37˚C heat block and added on top of the base agar at 50 μL per well (2 x 10^3 cells/well). The 96-well plates were kept in the fridge for 30 min before adding 100 μL growth medium containing CCT196969 in final concentrations of 0.01, 0.05, 0.1 and 1 μM for H1 and H2 and 0.05, 0.1, 0.5 and 1 μM for H3. After 10 days, microscopic images were captured with a Nikon TE2000 inverted microscope (Nikon Instruments Inc) using 10x and 20x objectives. Then, 20 μL of 0.1 mg/mL resazurin (Sigma-Aldrich Inc.) was added to each well and incubated for 4 h. The absorbance was measured at dual mode 560/590 nm using a scanning multi-well spectrophotometer (Victor 3 1420 multi-label counter, Perkin Elmer, Waltham, MA, USA), equipped with WorkOut 2.5 data analysis software. Each experiment was performed in triplicates (n = 6 per experiment per drug concentration). The results were analysed and IC_{50} doses were calculated using Prism 8 software (GraphPad Prism). Sphere diameters were measured in ImageJ software version 2.0.0 (National Institute of Health, Bethesda, MD; USA). Volumes were calculated in Excel (Microsoft) using the following formula: $\frac{4\pi r^3}{3}$.

Cell migration assay

H1, H2 and H3 cells were seeded at a density of 3 x 10^4 cells/well in Essen Bioscience Image-Lock 96-well plates (Essen Bioscience Ltd., Hertfordshire, UK). After 48 h, a wound maker tool was employed to simultaneously create a consistent wound with a uniform width across the wells. All wells were washed with pre-heated growth medium before drug solutions were added to the wells in concentrations of 0.1, 0.5 and 1 μM. Imaging was performed every 2 h using the 10x objective in the IncuCyte Live Cell Imaging System (Essen BioScience Ltd.) for 72 h. Resulting images were analysed to find the wound width in μm using the IncuCyte Cell Migration Software Module (Essen BioScience Ltd.). The experiments were done in triplicates.

Apoptosis assay by flow cytometry

Flow cytometry was performed to study drug effects on apoptosis. H1, H2 and H3 cell lines were plated in 6-well plates (Nunc) with a concentration of 3×10^5 cells/well in 4 mL growth medium. After 24 h, CCT196969 was added to the wells in final concentrations of 1, 2 and 4 μM. Untreated cells were used as controls. 4 h before the collecting of cells, 4.08 μL of 30% H_2O_2, equivalent to a concentration of 10 μM, was added in one well to induce apoptosis and serve as an apoptotic control. After 72 h of incubation, growth medium was collected from the wells into tubes, and the cells were washed with phosphate buffered saline (PBS), trypsinated and added to the growth medium before centrifuging at 900 rpm for 5 min. After removal of the supernatant, cells from each sample were resuspended in 100 μL Annexin V binding buffer (Invitrogen), and 2 μL of Annexin V and propidium iodide (PI; AlexaFluor®488 Annexin v/dead cell apoptosis kit; Molecular Probes, Life Technologies, Waltham, MA, USA) were added to the samples. After 20 min incubation the samples were vortexed and analysed using a BD Accuri C6 flow cytometer (BD Bioscience, San Jose, CA, USA). Fluorescence in the FITC-A and PE-A channels were gated to a two-parameter histogram, and analysed using FloJo software (Tree Star Inc., Ashland, OR, USA). The experiment was repeated 3 times for each cell line.

Western blot analysis

Western blots were performed to study change in protein levels in the MAPK, STAT3 and PI3K pathways after treatment with CCT196969. 1×10^6 H1 and H3 cells were seeded into T25 culture flasks (Nunc). After 24 h cells were treated with 1, 2 and 4 μM CCT196969. Untreated cells were used as control. The cells were then incubated for 24 h, before collecting both floating and attached cells. The cells were lysed in 100 μL lysis buffer (radioimmunoprecipitation assay (RIPA) based buffer (Thermo Fischer Scientific) containing 10% PhosSTOP and CompleteMini protease inhibitors (Sigma-Aldrich Inc.)). Lysates were centrifuged at 13 000 rpm in 4°C for 5 min, and the resulting supernatants were used as final lysates. Protein levels were quantified using BCA protein assay (ThermoFischer Scientific) according to the manufacturer user guide. Lysates were electrophoresed on 10% or 15% SDS-polyacrylamide gel electrophoresis according to target protein sizes. Proteins were transferred to nitrocellulose membranes (GE Healthcare Life Science, Chicago, Illinois, USA), and then blocked in Tris-Buffered Saline (TBS), 0.1% Tween and 5% skim-milk for 1 h at room temperature. The membranes were incubated at 4°C overnight in antibody diluent (Thermo Fischer Scientific) mixed with the relevant antibody. The primary antibodies used were: p-ERK1/2 (Cell Signaling Technology, Inc, Danvers, MA, USA, cat. #4370, monoclonal, rabbit, dilution 1:1000, RRID:AB_2315112), p-MEK1/2 (Cell Signaling Technology, cat. #9154, monoclonal, rabbit, dilution 1:1000, RRID: AB_2138017), Stat3 (Cell Signaling Technology, cat. #4904, monoclonal, rabbit, dilution 1:2000, RRID:AB_331269), p-Stat3 (Cell Signaling Technology, cat. #9134, polyclonal, rabbit, dilution 1:1000, RRID:AB_331589), p-AKT (Cell Signaling Technology, cat. #4056, monoclonal, rabbit, dilution 1:1000, RRID:AB_331163), cleaved caspase-3 (Cell Signaling Technology, cat. #9664, monoclonal, rabbit, dilution 1:1000, RRID:AB_2070042) and loading control

GAPDH (Abcam, Cambridge, UK, cat. #ab9485, polyclonal, rabbit, dilution 1:4000, RRID: AB_307275). The membranes were then washed in TBS-Tween 3 times before being incubated with a secondary antibody, Goat anti-Rabbit IgG (Invitrogen, cat. #31462, polyclonal, dilution 1:10 000, RRID:AB_228338), diluted in a blocking buffer. After 3 washing steps, proteins were detected using an enhanced chemiluminescence kit (Thermo Fischer Scientific) and a LAS3000 imaging system (FujiFilm, Saitama, Japan). Quantification of protein expression levels was based on band density measured in ImageJ software version 2.0.0 (National Institute of Health). The protein levels were normalised against the loading control and compared to the untreated controls. The experiments were performed in triplicates.

Development of resistant cell lines and monolayer cell viability assay on resistant cell lines

To study the effect of CCT196969 on a BRAF inhibitor resistant cell line, H1 cells were seeded in increasing concentrations of vemurafenib until resistance was established. H1 cells of the equivalent passage were seeded in two separate T75 flasks (Nunc), one untreated as control, the other initially treated with 0.05 μM vemurafenib (Chemietek). The cells in both flasks were passaged 6 times in total, but in the latter flask the vemurafenib concentration was increased for each passage; 0.1, 0.25, 0.5, 1.0, 2.0 and 3.0 μM.

To verify the development of resistance towards vemurafenib, monolayer resazurin assays were performed for the H1 vemurafenib-naïve (H1) and H1 vemurafenib-resistant (H1-R) cell lines using increasing concentrations of vemurafenib. Thereafter, monolayer resazurin assays were performed on the H1 and H1-R cell lines of the same passage using 0.1, 0.5, 1 and 2 μM CCT196969. The experiments were performed in triplicates.

A Wm3248-DR (double resistant) BRAF-inhibitor resistant cell line was generated from the parental Wm3248 cell line by long-term culturing under continuous drug presence of the BRAF inhibitor encorafenib and the MEK inhibitor binimetinib, corresponding to approximately 10x IC_{50} concentration. Drug-naïve and drug-resistant cell lines were authenticated by STR profiling. After generation, resistant cell lines were maintained under continuous exposure to encorafenib and binimetinib. Monolayer resazurin assays, as previously described, were then performed on the cell lines using vemurafenib and CCT196969. The experiments were done in duplicates.

Statistical analysis

Unpaired, 2-tailed t-tests were performed in Excel (Microsoft). A 2-tailed $p<0.05$ was considered statistically significant. Values presented in the figures represent means ± standard error of the mean (SEM) calculated in Prism 8 Software (GraphPad Software Inc).

Results

CCT196969 decreases viability of MBM cells in monolayer cultures

To explore whether CCT196969 affected cell growth in monolayer cultures, we performed cell viability assays. Changes in cell morphology after treatment were observed. In the 1 μM treatment group, H1 cells appeared elongated and more spindle-like, while H2 and H3 cells had a flatter, wider form and loss of structural integrity. Hardly any viable cells were present at 4 μM of CCT196969, and all cell lines displayed cell shrinkage and intracellular fragmentation (Fig 1A).

Treatment with CCT196969 reduced viability in a dose-dependent manner in the H1, H2, H3, H6, H10 and Wm3248 cell lines (Fig 1B, S1 Fig). The IC_{50} doses were calculated to be 0.7,

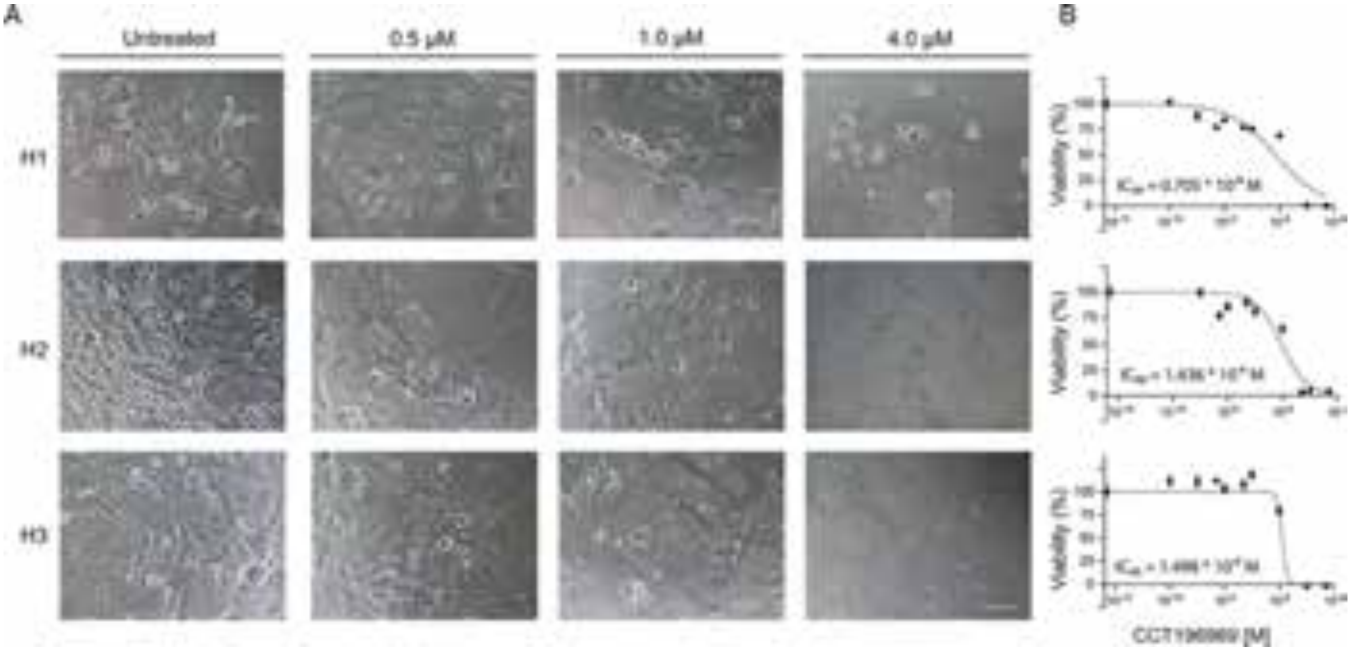

Fig 1. CCT196969 treatment reduces viability in MBM cell lines in a dose-dependent manner. (A) Representative microscopic images (20x objective) of H1, H2 and H3 cells grown in monolayers, exposed to increasing concentrations of CCT196969; untreated, 0.5, 1.0 and 4 μM, for 72 h. Scale bar = 100 μm. (B) Representative viability curves of the cell lines grown as monolayers, exposed to increasing concentrations of CCT196969. The mean IC_{50} dose value for CCT196969 was calculated from the experimental triplicate and is presented in the graph.

https://doi.org/10.1371/journal.pone.0273711.g001

1.4, 1.5, 2.6, 1.2 and 0.18 μM, respectively. At a concentration of 10–50 μM, no viable cells were detected in any cell line (Fig 1B, S1 Fig).

CCT196969 decreases viability of MBM cells grown as tumour spheres

To examine the effects of CCT196969 on colony formation and anchorage-independent growth, we conducted a tumour sphere assay. After 10 days of culturing in agar, the untreated cells formed spheres ranging from 100–200 μm in diameter (Fig 2A). The sphere sizes in treated groups were negatively correlated with increasing doses when compared to untreated spheres (Fig 2A and 2C). The calculated IC_{50} values for the H1, H2 and H3 cell lines were 0.02, 0.03 and 0.1 μM, respectively, showing that tumour spheres were more drug sensitive than the monolayer cultures (Fig 2B).

CCT196969 decreases MBM cell migration

We performed a scratch wound assay to demonstrate drug effects on cell migration. CCT196969 treatment decreased the migratory abilities of the H1, H2 and H3 cell lines in a dose-dependent manner (Fig 3). The wounds closed completely within 72 h in the untreated H1 and H3 cell lines. Wound confluency after 72 h was between 20–40% and 20% in 1 μM-treated H1 and H3 cells, respectively. The untreated H2 cells had a wound confluency of 65% after 72 h, whereas cells treated with 1 μM had confluency of approximately 20%.

CCT196969 induces apoptosis in MBM cells

To assess drug effects on apoptosis and cell survival, we performed an apoptosis assay by flow cytometry. CCT196969 induced apoptosis in the H1, H2 and H3 cell lines (Fig 4A, S2 Fig). 4 μM CCT196969 induced early and late apoptosis in about 90%, 94%, and 94% of each of the

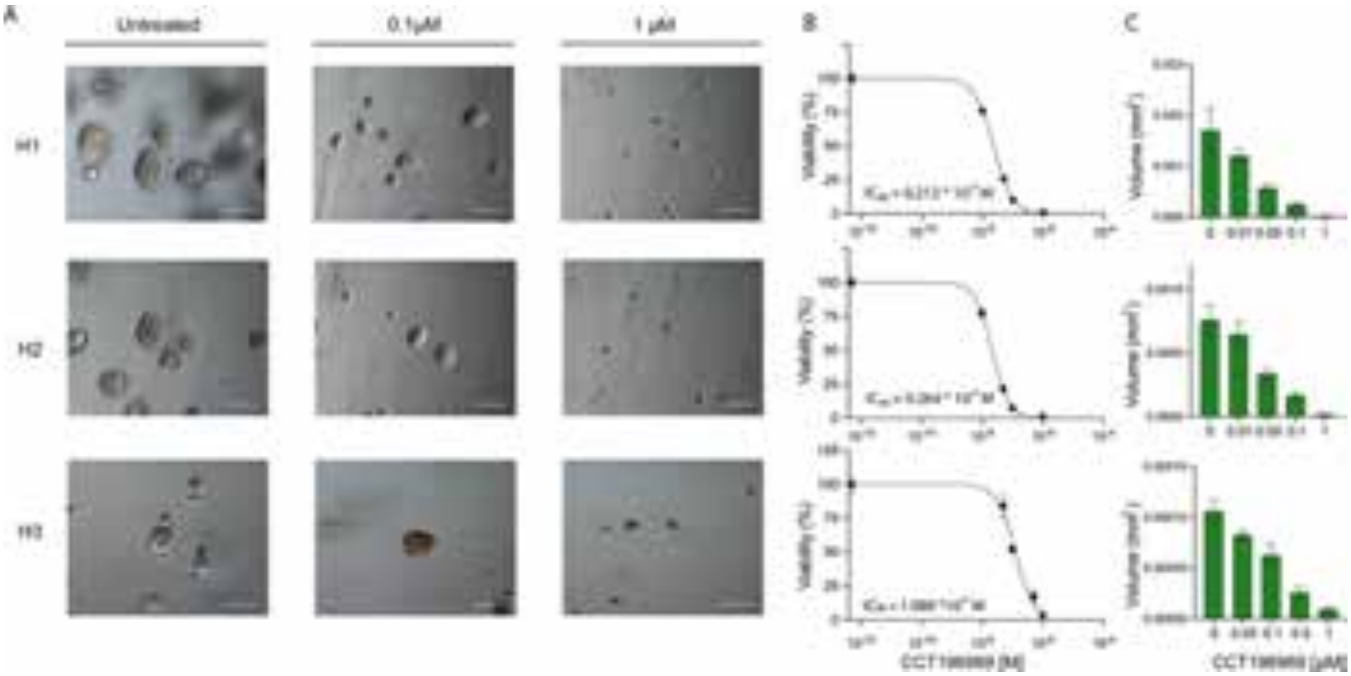

Fig 2. CCT196969 treatment reduces tumour sphere growth in MBM cell lines in a dose-dependent manner. (A) Representative phase-contrast microscopic images (20x objective) of the H1, H2 and H3 cell lines at different concentrations of CCT196969; untreated, 0.1 and 1 μM. Scale bars = 100 μm. (B) Representative viability curves of the 3 cell lines with the mean IC_{50} dose of the triplicates. (C) Mean tumour sphere volumes (in mm^3) measured after 10 days exposure to different CCT196969 concentrations: untreated, 0.01, 0.05, 0.1 and 1 μM for the H1 and H2 cell lines, and untreated, 0.05, 0.1, 0.5 and 1 for the H3 cell line.

https://doi.org/10.1371/journal.pone.0273711.g002

cell lines, respectively, compared to 14%, 7%, and 10% apoptotic cells in untreated controls. For untreated cells, between 86–92% of the cells were viable in the cell lines, compared to 5–10% after treatment with 4 μM CCT196969. The increase in apoptosis after treatment was significant, compared to untreated controls (Fig 4B). Flow cytometry results were validated by Western blots showing an increase in cleaved caspase-3 after CCT196969 treatment of H1 and H3 cells with CCT196969 (Fig 5). Cleaved caspase-3 was not detected in the untreated groups.

CCT196969 reduces phosphorylation of key kinases in the MAPK, STAT3 and PI3K signalling pathways

To investigate the effects on MAPK, STAT3 and PI3K signalling pathways upon treatment with CCT196969, H1 and H3 cells were treated with CCT196969 for 24 h and analysed by Western blotting. We observed a significant decrease in expression of STAT3, p-STAT3, p-MEK and p-ERK in both cell lines upon treatment with CCT196969 (Fig 6). In addition, p-AKT protein level was downregulated in the H1 cell line (S3 Fig).

CCT196969 reduces viability of BRAF inhibitor resistant cells

To assess the effects of CCT196969 on BRAF inhibitor resistant cell lines, we first developed BRAF inhibitor resistance in the H1 and Wm3248 cell lines. Viability studies confirmed significant differences in vemurafenib sensitivity between the H1 and H1-R cell lines, and for the Wm3248 and Wm3248-DR cell lines (Fig 7A and 7C).

To the investigate the effects of CCT196969 on vemurafenib-naïve metastatic melanoma cell lines and their drug-resistant counterparts, viability studies were performed. For the lowest

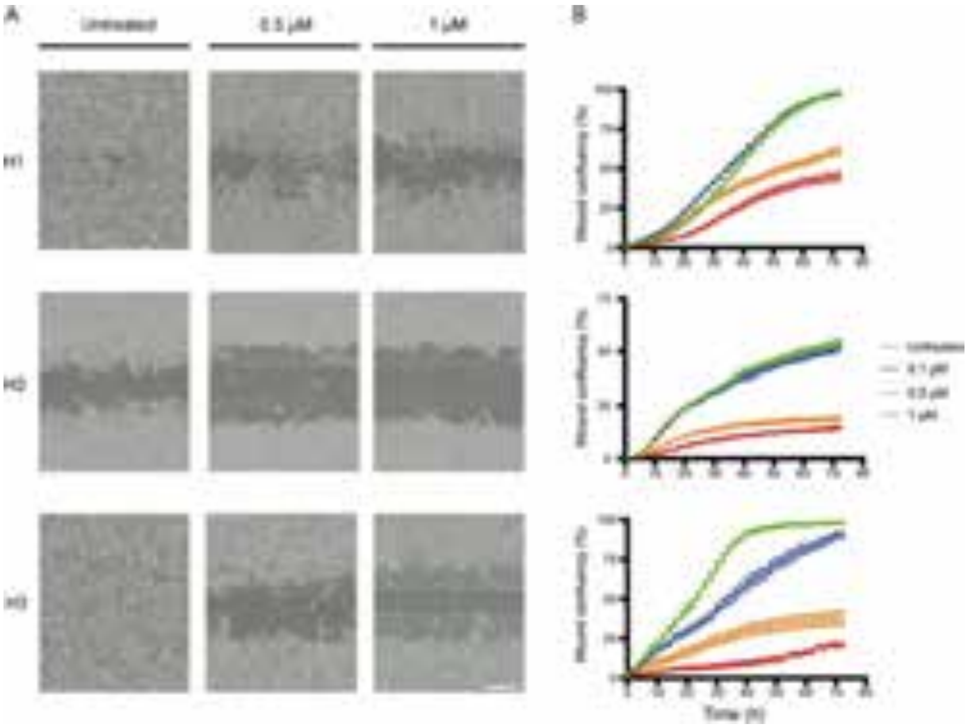

Fig 3. CCT196969 reduces migration in MBM cell lines. (A) Representative microscopic images (10x objective) of the H1, H2 and H3 cell lines displaying differences in wound confluency at 72 h, untreated or exposed to 0.5 or 1 μM of CCT196969. Scale bar = 300 μm. (B) Representative graphs of the wound confluency in the H1, H2 and H3 cell lines during 72 h. The experiments were done in triplicates.

https://doi.org/10.1371/journal.pone.0273711.g003

concentrations of CCT196969, significant differences in viability were observed for the H1 and H1-R cell lines, similar to what was also found for Wm3248 and Wm3248-DR cell lines (S1 Table). Both the vemurafenib-naïve and the resistant cell lines showed a dose-dependent reduction of viability when treated with CCT196969 (Fig 7B and 7D), although the effect on the resistant cell lines were less compared to the vemurafenib-naïve cells when treated with 0.1, 0.5 and 1 μM CCT196969. There were no significant differences in viability between the sensitive and resistant cell lines when treated with 2 μM CCT196969 (Fig 7B and 7D).

Discussion

Around 90% of melanomas express abnormal activation of the MAPK pathway [8], providing a strong rationale for clinical use of BRAF and MEK inhibitors. However, primary and secondary resistance mechanisms significantly impede the clinical utility of these drugs, and second-line treatments are scarce. Developing new therapies, one should also take into account that MBMs have distinct expression patterns as compared to extracranial metastases [27]. PI3K and STAT3 pathway overexpression drive development of MBM and also confers survival and resistance during MAPK treatment [28, 29]. Here, we show for the first time that CCT196969 targets multiple key signalling pathways in MBM and effectively inhibits growth, migration, and induces apoptosis in several BRAF inhibitor sensitive and resistant MBM cell lines *in vitro*.

Viability studies demonstrated that the IC_{50} doses were in the range of 0.18–2.6 μM, which is in line with previous studies using CCT196969 and other SFK inhibitors in primary melanoma cell lines [15, 24, 30] and metastatic melanoma [31]. Interestingly, the H3 cell line,

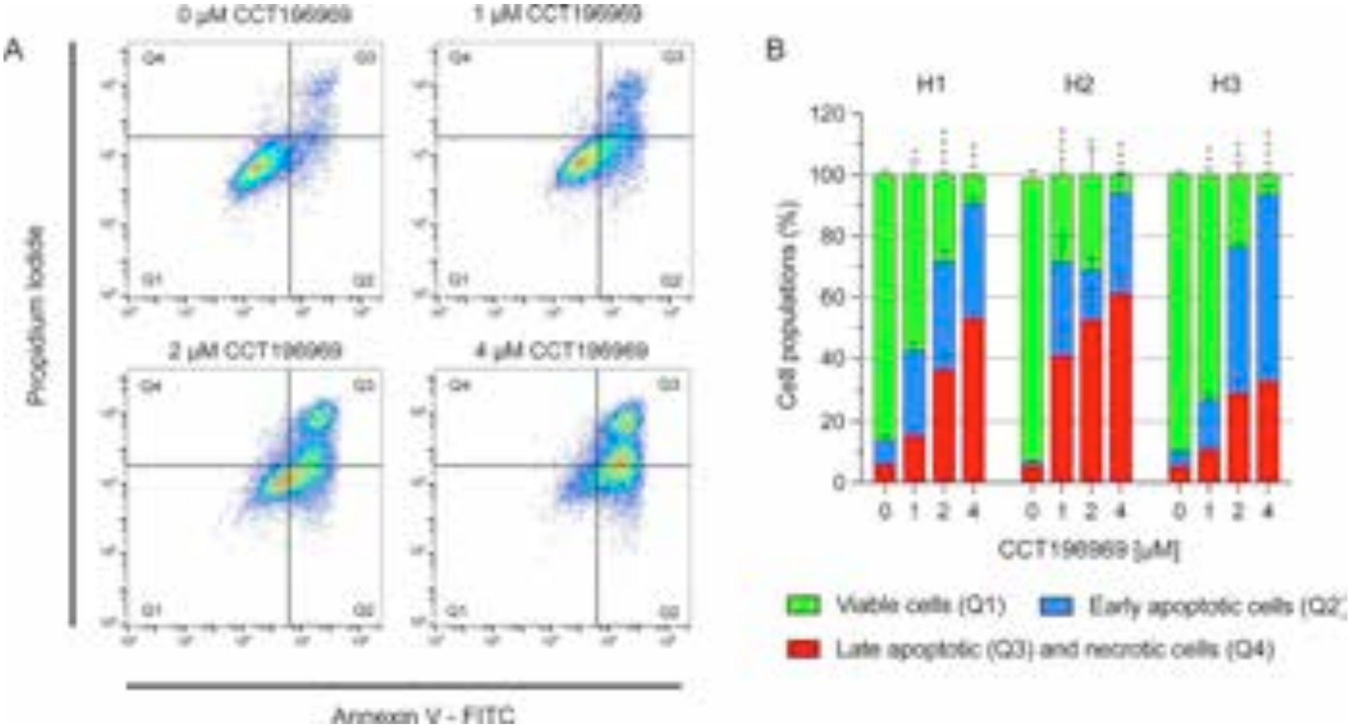

Fig 4. CCT196969 induces apoptosis in MBM cell lines. Annexin V labels apoptotic cells and propidium iodide labels necrotic cells. (A) Representative dot plots of the H1 cell line treated with selected concentrations of CCT196969; untreated, 1, 2 and 4 μM. (B) Percentage of viable cells, early apoptotic and late apoptotic and dead cells in the H1, H2 and H3 cell lines. The experiments were done in triplicates. Abbreviations: Q1: Viable cells, Q2: Early apoptotic cells, Q3: Late apoptotic cells, Q4: Necrotic cells. *: $p < 0.05$, **: $p < 0.01$, ***: $p < 0.001$, ****: $p < 0.0001$.

https://doi.org/10.1371/journal.pone.0273711.g004

which harbours a $BRAF^{L577F}$ mutation of unknown clinical relevance and mutations in *NRAS* and *EGFR*, displayed an IC_{50} dose similar to the $BRAF^{V600E}$ mutated cell lines. It has previously been shown that the IC_{50} dose of the BRAF inhibitor vemurafenib was around 10-fold higher in the H3 cell line compared to the H1 cells [32]. This suggests that CCT196969 may be an effective treatment in melanomas that carry other pathogenic mutations than $BRAF^{V600E}$. In addition, treatment of *NRAS*-mutated cell lines with BRAF inhibitors is known to reactivate the MAPK pathway through BRAF/CRAF dimerisation [12, 13], thereby inducing increased signalling and proliferation. This reactivation may be avoided by simultaneously targeting SFK and several RAFs using CCT196969.

Tumour spheres are generally more representative than monolayers in mimicking tumour growth *in vivo* [33]. CCT196969 treatment of tumour spheres inhibited growth with IC_{50} doses around 15–47 times lower as compared to monolayers. This is in line with other findings [34] and indicates that the MBM cells are more drug sensitive when grown in an anchorage independent manner.

Melanoma is well known for its unique metastatic properties, exhibiting increased migration and invasiveness, as well as aggressive local invasion and early metastatic dissemination [35]. It has been shown that MBMs may be found in more than 70% of autopsies in patients with advanced melanoma [36]. At doses less than the IC_{50} doses, we found that CCT196969 inhibited MBM cell migration in H1, H2 and H3 cells. This indicates that CCT196969 at lower concentrations inhibits migration but may also be partly due to reduced cell proliferation.

Previous reports have also suggested that SFK inhibitors decreased migration and invasion in melanoma cells [37, 38]. The Src/Abl inhibitor dasatinib eliminated all SFK activity in

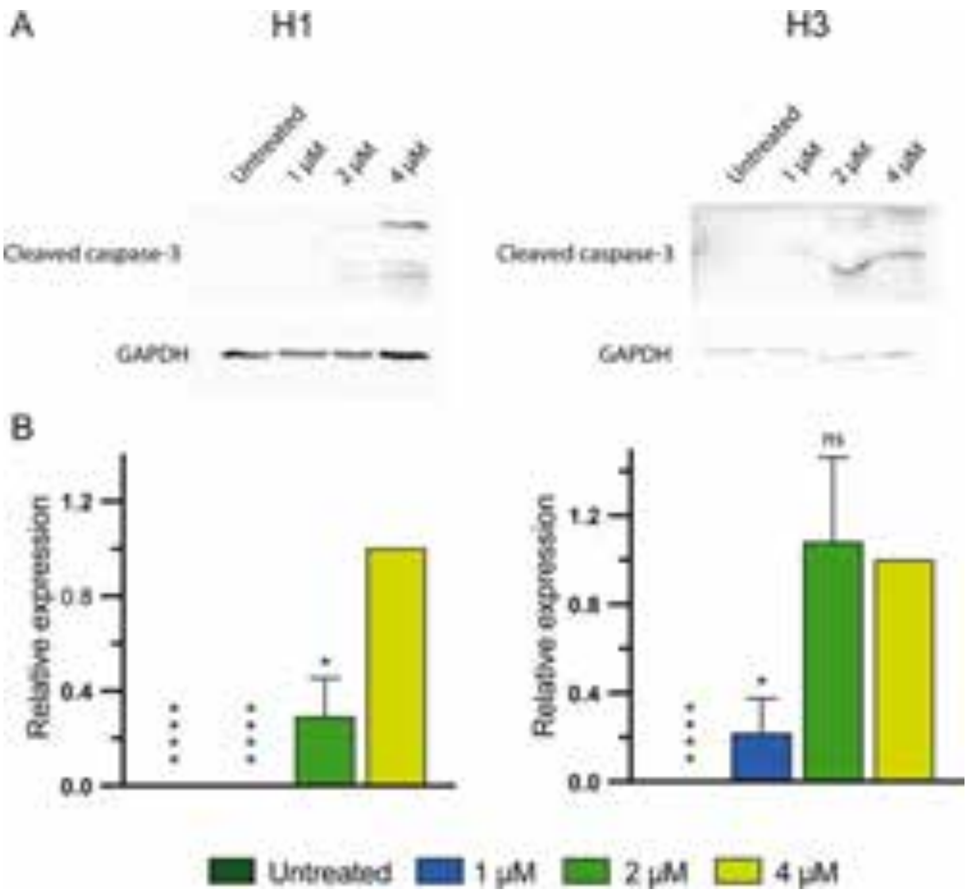

Fig 5. CCT196969 upregulates expression of cleaved caspase-3 in MBM cell lines. (A) Western blots showing cleaved caspase-3 from H1 and H3 cells, untreated or treated with 1, 2 or 4 μM CCT196969 for 24 h. (B) Quantification of Western blots against the loading control GAPDH in ratio with the bands of the highest concentration of CCT196969. Due to no expression of cleaved caspase-3 in the untreated groups, expression of cleaved caspase-3 in the highest concentration group was set to 1.0. The experiments were done in triplicates. Abbreviations: ns: not significant, *: $p < 0.05$, ****: $p < 0.0001$.

https://doi.org/10.1371/journal.pone.0273711.g005

primary melanoma, with no concurrent effects on ERK1/2 protein kinases. Cell migration and invasion were inhibited before affecting cell viability or cell proliferation [39]. Inhibition of cell migration by SFKs and effects on melanoma cell proliferation have also been demonstrated [15, 30], yet the literature remains inconclusive as to possible *in vivo* effects [40]. Taken together, SFK activity seems to inhibit cell migration in MBM cells and in primary melanoma, at doses below IC_{50} and without affecting cell proliferation.

CCT196969 effectively induced apoptosis in the H1, H2 and H3 cell lines in a dose dependent manner, with 90% to 95% of the cells being apoptotic at a concentration of 4 μM. Morphological examinations demonstrated typical apoptotic traits. Morphologically, the H1 cell line displayed an elongated, spindle-like shape after treatment, while the H2 and H3 cells appeared wider with reduced focal adhesion. Changes observed in the H1 cells resemble an epithelial-mesenchymal transition (EMT), which has been previously reported for MBM cells treated with MAPK inhibitors [26, 41].

Apoptosis was confirmed by Western blotting, showing increased levels of the apoptotic marker cleaved caspase-3 in cells treated with 2 μM and 4 μM CCT196969. Cleavage of caspase-3 leads to activation of the caspase cascade, which plays a crucial role in both the intrinsic

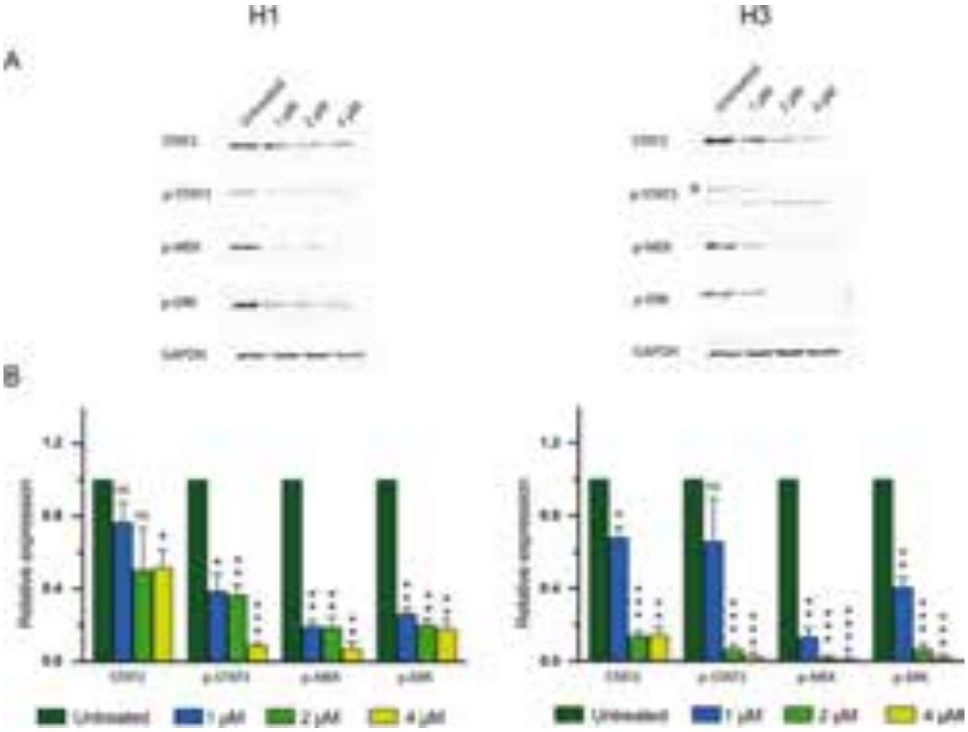

Fig 6. CCT196969 downregulates expression of STAT3, p-STAT3, p-MEK and p-ERK in MBM cell lines. (A) Western blots from H1 and H3 cells, untreated or treated with selected doses of CCT196969; 1, 2 and 4 μM. (B) Quantification of Western blots normalised against the loading control GAPDH and in ratio with the untreated control. The experiments were done in triplicates. The graphs show the mean with SEM. Abbreviations: ns: not significant, *: $p < 0.05$, **: $p < 0.01$, ***: $p < 0.001$, ****: $p < 0.0001$.

https://doi.org/10.1371/journal.pone.0273711.g006

and extrinsic apoptotic pathways, and thus execution of apoptosis [42]. Previous work has shown increase in cleaved caspase-3 in vemurafenib-resistant melanoma cell lines after treatment with 1 μM CCT196969 [24].

CCT196969 is a pan-RAF and SFK inhibitor, targeting both the MAPK and STAT3 pathways. CCT196969 has been shown to target mutated BRAF, CRAF and SFKs in *BRAF*-mutated primary melanoma cell lines, resulting in decreased expression levels of p-MEK and p-ERK [24]. In our study, CCT196969 downregulated p-ERK, p-MEK, p-STAT3 and STAT3 in the H1 and H3 cell lines. The H3 cell line has mutations in *NRAS* and *EGFR*, making both the MAPK and STAT3 pathways relevant targets. Targeting of the STAT3 pathway is a crucial point, as activation leads to increased production of vascular endothelial growth factor (VEGF), an angiogenic factor important for tumour development, invasion, and metastasis [15, 43]. Both pathways have also been shown to be upregulated in BRAF inhibitor resistant cells [15, 44]. Due to STAT3 and MAPK pathway crosstalk, inhibition of one pathway may lead to upregulation of the other; targeting both pathways simultaneously would likely exhibit a stronger inhibitory effect on tumours [45].

Our results also indicate that CCT196969 may have an inhibitory effect in the PI3K pathway in MBM through downregulation of p-AKT (S3 Fig). Hyperactivation of the PI3K pathway is more common in intracranial than extracranial metastases [46], and is therefore a key target in MBM patients. Whether CCT196969 would be effective against tumours gaining resistance through PI3K-signalling remains unknown. As CCT196969 has been suggested as a potential second line treatment for BRAF inhibitor resistant melanoma and first line therapy

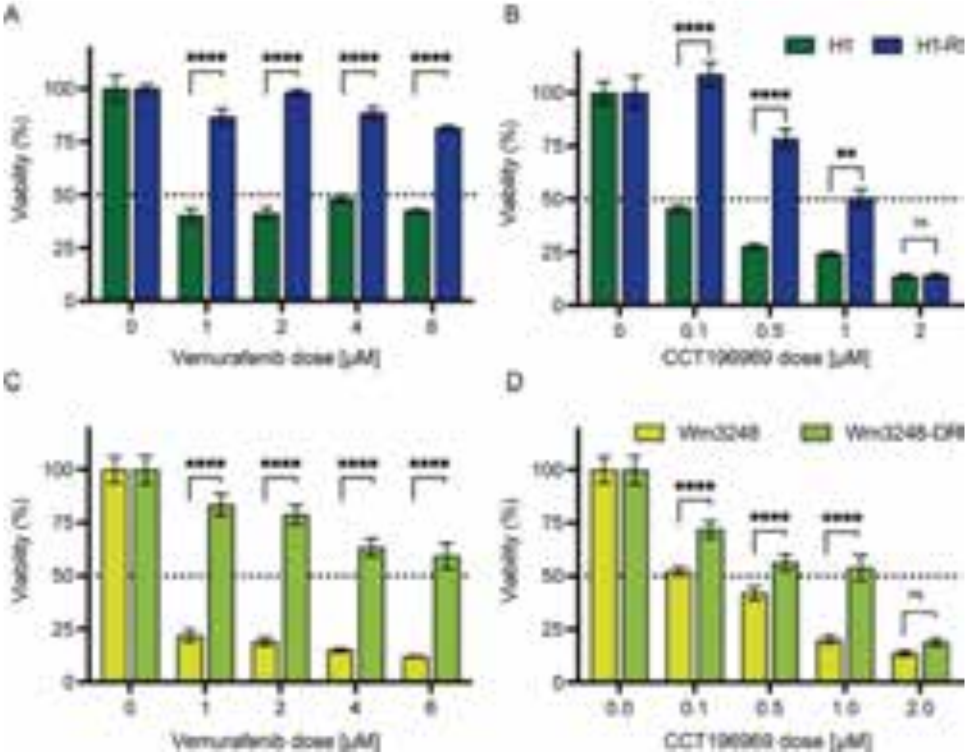

Fig 7. Cell viability in the vemurafenib-naïve and resistant cell lines after exposure to increasing concentrations of vemurafenib (A, C) and CCT196969 (B, D). (A) Dose response curves after exposure to vemurafenib for H1 and H1-R using the following concentrations: untreated, 1, 2, 4 and 6 μM. (B) Dose response curves for H1 and H1-R after exposure to CCT196969 using the following concentrations: untreated, 0.1, 0.5, 1 and 2 μM. (C) Dose response curves after exposure to vemurafenib for Wm3248 and Wm3248-DR using the following concentrations: untreated, 1, 2, 4 and 6 μM. (D) Dose response curves for Wm3248 and Wm3248-DR after exposure to CCT196969 using the following concentrations: untreated, 0.1, 0.5, 1 and 2 μM. Abbreviations: ns: not significant, **: $p < 0.01$, ****: $p < 0.0001$.

https://doi.org/10.1371/journal.pone.0273711.g007

for *NRAS*- and *BRAF*-mutated melanoma [24], combination therapy with PI3K inhibitors should be investigated in the future.

CCT196969 inhibited cell viability in a dose-dependent manner in our vemurafenib resistant metastatic cell lines. There were no significant differences in cell viability between the BRAF inhibitor resistant and sensitive cell lines at 2 μM, indicating that CCT196969 could be effective against BRAF inhibitor resistant melanoma. We did not investigate the mechanisms responsible for the acquired resistance, but upregulation of the MAPK, STAT3 or PI3K pathways all serve as likely mechanisms. A clinical study using patient-derived xenografts from patients obtained before and after receiving vemurafenib treatment, found elevated levels of p-SFK and p-ERK in the vemurafenib resistant tumours after treatment [24]. The resistant tumours were not sensitive to the vemurafenib analogue PLX4720 but were still responsive to treatment with CCT196969 [24].

In a previous study, EGFR was hyperphosphorylated in 4 out of 5 tumours from patients with acquired or intrinsic resistance to vemurafenib, leading to a hyperactivation of the STAT3 pathway [15]. In the present study, CCT196969 displayed anti-proliferative and apoptotic effects in the H3 cell line harbouring an *EGFR* pathogenic mutation, and treatment with CCT196969 downregulated p-STAT3. CCT196969 seems to be an effective inhibitor of cell viability in *EGFR*-mutated melanoma, as well as in BRAF inhibitor resistant melanoma which has achieved resistance with upregulation of the STAT3 pathway.

Drug penetrance through the blood brain barrier (BBB) is a central challenge in treatment of intracranial metastases. Previous studies on CCT196969 have demonstrated conflicting results on BBB penetrability [31]. *In vitro* experiments showed that CCT196969 was not a substrate for two important efflux transporters (P-glycoprotein (P-gp) and breast cancer resistance protein (Bcrp)), but in vivo studies found enhanced brain distribution without these transporters [31]. To establish the potential clinical value of CCT196969, toxicity issues, drug dosage, penetrance of the BBB and the significance of drug efflux pumps in drug delivery should be investigated before further *in vivo* treatment experiments are carried out.

In conclusion, we found CCT196969 to be an effective inhibitor of MBM proliferation, growth, and survival *in vitro*. Further *in vivo* studies should be performed to determine its therapeutic potential, as it has been shown to have good bioavailability and to be well tolerated in mice [24]. CCT196969 may serve as a potential first line treatment for patients with *NRAS*- or *EGFR*-mutated MBMs, and as second line treatment for patients with intrinsic or acquired resistance towards MAPK inhibitors.

Supporting information

S1 Fig. Viability curves of cells grown as monolayers after treatment with increasing doses of CCT196969. (A) Representative graph of the H6 cell line treated with increasing doses of CCT196969 (0.0001–50 μM) for 72 h. (B) Representative graph of the H10 cell line treated with increasing doses of CCT196969 (0.0001–50 μM) for 72 h. The experiments were performed in triplicates. (C) Representative graph of the Wm3248 cell line treated with increasing doses of CCT196969 (0.0001–50 μM) for 72 h. The experiments were performed in duplicates.
(TIF)

S2 Fig. Flow cytometric analysis of apoptosis in the H2 and H3 MBM cell lines after treatment with CCT196969. Annexin V marks apoptotic cells and Propidium Iodide marks necrotic cells. (A) Dot plots of the H2 cell line treated with selected concentrations of CCT196969; untreated, 1, 2 and 4 μM. (B) Dot plots of the H3 cell line treated with selected concentrations of CCT196969; untreated, 1, 2 and 4 μM. The experiments were done in triplicates. Abbreviations: Q1: Viable cells, Q2: Early apoptotic cells, Q3: Late apoptotic cells, Q4: Necrotic cells.
(TIF)

S3 Fig. CCT196969 downregulates expression of p-AKT in the H1 cell line. (A) Western blot bands from H1 cells treated with selected doses CCT196969; untreated, 1, 2 and 4 μM. (B) Quantification of protein bands normalised against the loading control GAPDH and in ratio with the untreated control. The experiments were done in triplicates. Abbreviations: *: $p < 0.05$, ***: $p < 0.001$.
(TIF)

S1 Table. Statistical testing of the effects of single drug treatment on cell lines. Statistical testing of cell survival, comparing untreated cells with cells treated with either CCT196969 or vemurafenib at different concentrations. Results show p-values from T-test comparisons of cells treated with the given concentrations vs untreated control of corresponding cell line.
(TIF)

S1 Raw images.
(TIF)

Acknowledgments

Imaging in this project was performed at the Molecular Imaging Centre (MIC), Department of Biomedicine, University of Bergen. Flow cytometry was performed at the Flow Cytometry Core Facility, Department of Clinical Science, University of Bergen.

Author Contributions

Conceptualization: Agathe Reigstad, Christina Frantzen Herdlevær, Frits Thorsen.

Formal analysis: Agathe Reigstad, Christina Frantzen Herdlevær, Frits Thorsen.

Funding acquisition: Frits Thorsen.

Investigation: Agathe Reigstad, Christina Frantzen Herdlevær, Emma Rigg.

Methodology: Agathe Reigstad, Christina Frantzen Herdlevær, Emma Rigg, Tuyen Hoang, Ole Vidhammer Bjørnstad, Synnøve Nymark Aasen, Jasmin Preis, Claude Haan.

Supervision: Terje Sundstrøm, Frits Thorsen.

Visualization: Agathe Reigstad, Christina Frantzen Herdlevær, Frits Thorsen.

Writing – original draft: Agathe Reigstad, Christina Frantzen Herdlevær, Frits Thorsen.

Writing – review & editing: Agathe Reigstad, Christina Frantzen Herdlevær, Emma Rigg, Tuyen Hoang, Ole Vidhammer Bjørnstad, Synnøve Nymark Aasen, Jasmin Preis, Claude Haan, Terje Sundstrøm, Frits Thorsen.

References

1. Ali Z., Yousaf N., and Larkin J., Melanoma epidemiology, biology and prognosis. EJC Suppl, 2013. 11 (2): p. 81–91.
2. Chason J.L., Walker F.B., and Landers J.W., Metastatic carcinoma in the central nervous system and dorsal root ganglia. A prospective autopsy study. Cancer, 1963. 16: p. 781–7.
3. Davies M.A., et al., Prognostic factors for survival in melanoma patients with brain metastases. Cancer, 2011. 117(8): p. 1687–96.
4. Budman D.R., Camacho E., and Wittes R.E., The current causes of death in patients with malignant melanoma. Eur J Cancer, 1978. 14(4): p. 327–30.
5. Lagerwaard F.J., et al., Identification of prognostic factors in patients with brain metastases: a review of 1292 patients. Int J Radiat Oncol Biol Phys, 1999. 43(4): p. 795–803.
6. Fife K.M., et al., Determinants of outcome in melanoma patients with cerebral metastases. J Clin Oncol, 2004. 22(7): p. 1293–300. https://doi.org/10.1200/JCO.2004.08.140 PMID: 15051777
7. Zhang D., et al., Incidence and prognosis of brain metastases in cutaneous melanoma patients: a population-based study. Melanoma Res, 2019. 29(1): p. 77–84.
8. Leonardi G.C., et al., Cutaneous melanoma: From pathogenesis to therapy (Review). Int J Oncol, 2018. 52(4): p. 1071–1080. https://doi.org/10.3892/ijo.2018.4287 PMID: 29532857
9. Cancer Genome Atlas N., Genomic Classification of Cutaneous Melanoma. Cell, 2015. 161(7): p. 1681–96.
10. Davies H., et al., Mutations of the BRAF gene in human cancer. Nature, 2002. 417(6892): p. 949–54.
11. Davies M.A., et al., Dabrafenib plus trametinib in patients with BRAF(V600)-mutant melanoma brain metastases (COMBI-MB): a multicentre, multicohort, open-label, phase 2 trial. Lancet Oncol, 2017. 18 (7): p. 863–873. https://doi.org/10.1016/S1470-2045(17)30429-1 PMID: 28592387
12. Heidorn S.J., et al., Kinase-dead BRAF and oncogenic RAS cooperate to drive tumor progression through CRAF. Cell, 2010. 140(2): p. 209–21.
13. Kaplan F.M., et al., Hyperactivation of MEK-ERK1/2 signaling and resistance to apoptosis induced by the oncogenic B-RAF inhibitor, PLX4720, in mutant N-RAS melanoma cells. Oncogene, 2011. 30(3): p. 366–71.

14. Manzano J.L., et al., Resistant mechanisms to BRAF inhibitors in melanoma. Ann Transl Med, 2016. 4 (12): p. 237. https://doi.org/10.21037/atm.2016.06.07 PMID: 27429963

15. Girotti M.R., et al., Inhibiting EGF receptor or SRC family kinase signaling overcomes BRAF inhibitor resistance in melanoma. Cancer Discov, 2013. 3(2): p. 158–67.

16. Shi H., et al., Acquired resistance and clonal evolution in melanoma during BRAF inhibitor therapy. Cancer Discov, 2014. 4(1): p. 80–93.

17. Wheeler S.E., et al., Epidermal growth factor receptor variant III mediates head and neck cancer cell invasion via STAT3 activation. Oncogene, 2010. 29(37): p. 5135–45.

18. Irby R.B. and Yeatman T.J., Role of Src expression and activation in human cancer. Oncogene, 2000. 19(49): p. 5636–42.

19. Vergani E., et al., Identification of MET and SRC activation in melanoma cell lines showing primary resistance to PLX4032. Neoplasia, 2011. 13(12): p. 1132–42.

20. Krayem M., et al., Kinome Profiling to Predict Sensitivity to MAPK Inhibition in Melanoma and to Provide New Insights into Intrinsic and Acquired Mechanism of Resistance. Cancers (Basel), 2020. 12(2).

21. Wagle N., et al., Dissecting therapeutic resistance to RAF inhibition in melanoma by tumor genomic profiling. J Clin Oncol, 2011. 29(22): p. 3085–96. https://doi.org/10.1200/JCO.2010.33.2312 PMID: 21383288

22. McArthur G.A., et al., Vemurafenib in metastatic melanoma patients with brain metastases: an open-label, single-arm, phase 2, multicentre study. Ann Oncol, 2017. 28(3): p. 634–641. https://doi.org/10.1093/annonc/mdw641 PMID: 27993793

23. Long G.V., et al., Dabrafenib in patients with Val600Glu or Val600Lys BRAF-mutant melanoma metastatic to the brain (BREAK-MB): a multicentre, open-label, phase 2 trial. Lancet Oncol, 2012. 13(11): p. 1087–95. https://doi.org/10.1016/S1470-2045(12)70431-X PMID: 23051966

24. Girotti M.R., et al., Paradox-breaking RAF inhibitors that also target SRC are effective in drug-resistant BRAF mutant melanoma. Cancer Cell, 2015. 27(1): p. 85–96.

25. Wang J., et al., A novel brain metastases model developed in immunodeficient rats closely mimics the growth of metastatic brain tumours in patients. Neuropathol Appl Neurobiol, 2011. 37(2): p. 189–205.

26. Aasen S.N., et al., Effective Treatment of Metastatic Melanoma by Combining MAPK and PI3K Signaling Pathway Inhibitors. Int J Mol Sci, 2019. 20(17). https://doi.org/10.3390/ijms20174235 PMID: 31470659

27. Brastianos P.K., et al., Genomic Characterization of Brain Metastases Reveals Branched Evolution and Potential Therapeutic Targets. Cancer Discov, 2015. 5(11): p. 1164–1177. https://doi.org/10.1158/2159-8290.CD-15-0369 PMID: 26410082

28. Xie T.X., et al., Activation of stat3 in human melanoma promotes brain metastasis. Cancer Res, 2006. 66(6): p. 3188–96.

29. Niessner H., et al., Targeting hyperactivation of the AKT survival pathway to overcome therapy resistance of melanoma brain metastases. Cancer Med, 2013. 2(1): p. 76–85.

30. Halaban R., et al., A novel anti-melanoma SRC-family kinase inhibitor. Oncotarget, 2019. 10(23): p. 2237–2251. https://doi.org/10.18632/oncotarget.26787 PMID: 31040916

31. Gampa G., et al., Brain Distribution and Active Efflux of Three panRAF Inhibitors: Considerations in the Treatment of Melanoma Brain Metastases. J Pharmacol Exp Ther, 2019. 368(3): p. 446–461.

32. Daphu I., et al., In vitro treatment of melanoma brain metastasis by simultaneously targeting the MAPK and PI3K signaling pathways. Int J Mol Sci, 2014. 15(5): p. 8773–94. https://doi.org/10.3390/ijms15058773 PMID: 24840574

33. Duval K., et al., Modeling Physiological Events in 2D vs. 3D Cell Culture. Physiology (Bethesda), 2017. 32(4): p. 266–277.

34. Sundstrom T., et al., Inhibition of mitochondrial respiration prevents BRAF-mutant melanoma brain metastasis. Acta Neuropathol Commun, 2019. 7(1): p. 55.

35. Arozarena I. and Wellbrock C., Targeting invasive properties of melanoma cells. FEBS J, 2017. 284 (14): p. 2148–2162. https://doi.org/10.1111/febs.14040 PMID: 28196297

36. de la Monte S.M., Moore G.W., and Hutchins G.M., Patterned distribution of metastases from malignant melanoma in humans. Cancer Res, 1983. 43(7): p. 3427–33.

37. Eustace A.J., et al., Preclinical evaluation of dasatinib, a potent Src kinase inhibitor, in melanoma cell lines. J Transl Med, 2008. 6: p. 53.

38. Ferguson J., et al., Combination of MEK and SRC inhibition suppresses melanoma cell growth and invasion. Oncogene, 2013. 32(1): p. 86–96.

39. Buettner R., et al., Inhibition of Src family kinases with dasatinib blocks migration and invasion of human melanoma cells. Mol Cancer Res, 2008. 6(11): p. 1766–74.

40. Gangadhar T.C., et al., Phase II study of the Src kinase inhibitor saracatinib (AZD0530) in metastatic melanoma. Invest New Drugs, 2013. 31(3): p. 769–73. https://doi.org/10.1007/s10637-012-9897-4 PMID: 23151808

41. Cordaro F.G., et al., Phenotype characterization of human melanoma cells resistant to dabrafenib. Oncol Rep, 2017. 38(5): p. 2741–2751.

42. Ghavami S., et al., Apoptosis and cancer: mutations within caspase genes. J Med Genet, 2009. 46(8): p. 497–510.

43. Chen Z. and Han Z.C., STAT3: a critical transcription activator in angiogenesis. Med Res Rev, 2008. 28(2): p. 185–200. https://doi.org/10.1002/med.20101 PMID: 17457812

44. Degirmenci U., Wang M., and Hu J., Targeting Aberrant RAS/RAF/MEK/ERK Signaling for Cancer Therapy. Cells, 2020. 9(1).

45. Zhao K., et al., Dual Inhibition of MAPK and JAK2/STAT3 Pathways Is Critical for the Treatment of BRAF Mutant Melanoma. Mol Ther Oncolytics, 2020. 18: p. 100–108.

46. Chen G., et al., Molecular profiling of patient-matched brain and extracranial melanoma metastases implicates the PI3K pathway as a therapeutic target. Clin Cancer Res, 2014. 20(21): p. 5537–46.

Supplementary Information

S1 Fig. Viability curves of cells grown as monolayers after treatment with increasing doses of CCT196969.

(A) Representative graph of the H6 cell line treated with increasing doses of CCT196969 (0.0001–50 µM) for 72 h. (B) Representative graph of the H10 cell line treated with increasing doses of CCT196969 (0.0001–50 µM) for 72 h. The experiments were performed in triplicates. (C) Representative graph of the Wm3248 cell line treated with increasing doses of CCT196969 (0.0001–50 µM) for 72 h. The experiments were performed in duplicates.

S2 Fig. Flow cytometric analysis of apoptosis in the H2 and H3 MBM cell lines after treatment with CCT196969.

Annexin V marks apoptotic cells and Propidium Iodide marks necrotic cells. (A) Dot plots of the H2 cell line treated with selected concentrations of CCT196969; untreated, 1, 2 and 4 µM. (B) Dot plots of the H3 cell line treated with selected concentrations of CCT196969; untreated, 1, 2 and 4 µM. The experiments were done in triplicates. Abbreviations: Q1: Viable cells, Q2: Early apoptotic cells, Q3: Late apoptotic cells, Q4: Necrotic cells.

S3 Fig. CCT196969 downregulates expression of p-AKT in the H1 cell line.

(A) Western blot bands from H1 cells treated with selected doses CCT196969; untreated, 1, 2 and 4 µM. (B) Quantification of protein bands normalised against the loading control GAPDH and in ratio with the untreated control. The experiments were done in triplicates. Abbreviations: *: $p < 0.05$, ***: $p < 0.001$.

S4 Raw WB images

S1 Table. Statistical testing of the effects of single drug treatment on cell lines.

Statistical testing of cell survival, comparing untreated cells with cells treated with either CCT196969 or vemurafenib at different concentrations. Results show p-values from T-test comparisons of cells treated with the given concentrations vs untreated control of corresponding cell line.

S1

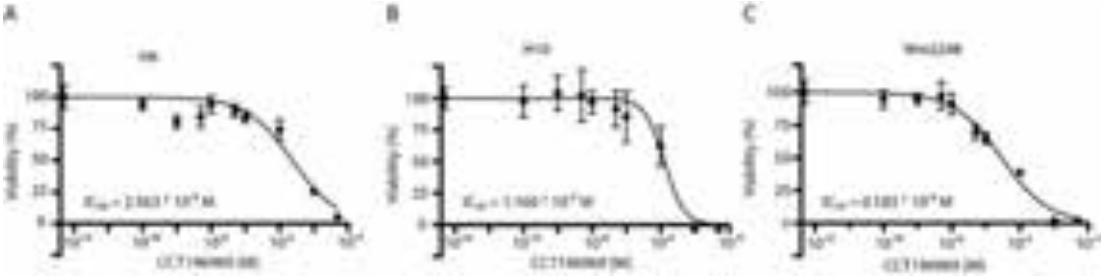
A
B
C
Viability (%)
100
75
50
25
0
CCT196969 (M)

S2

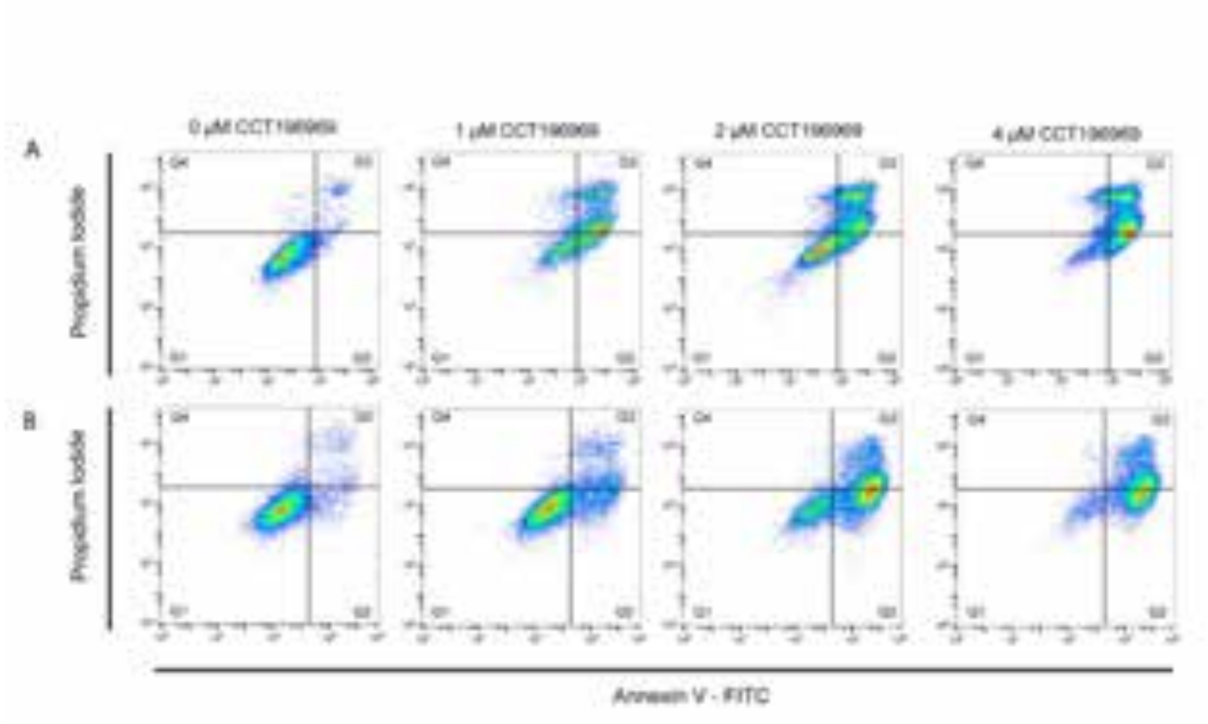
0 µM CCT196969
1 µM CCT196969
2 µM CCT196969
4 µM CCT196969
A
B
Propidium Iodide
Propidium Iodide
Q1
Q2
Q3
Q4
Annexin V - FITC

S3

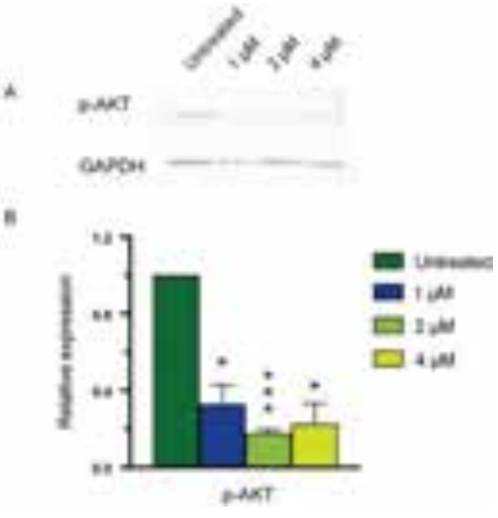
Untreated
1 µM
2 µM
4 µM
A
p-AKT
GAPDH
B
1.2
0.8
0.4
0.0
Relative expression
*
*
*
*
*
*
p-AKT
Untreated
1 µM
2 µM
4 µM

S4

* Fig 5A

+ Fig 6A

S3 fig

The images were captured using the LAS3000 imaging system (FujiFilm, Saitama, Japan).
All blots were used in the making of the graphs.

S1 Table

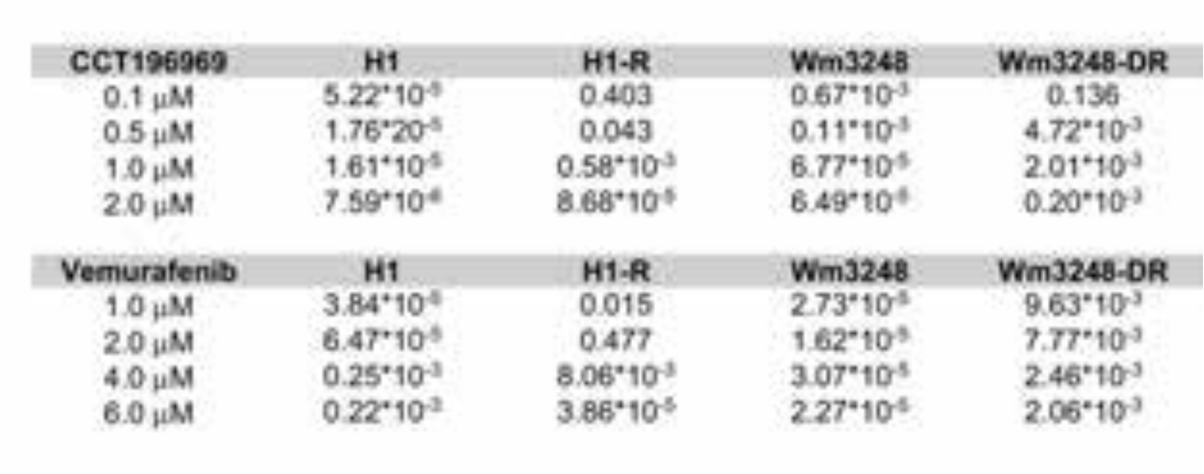

CCT196969	H1	H1-R	Wm3248	Wm3248-DR
0.1 µM	$5.22*10^{-5}$	0.403	$0.67*10^{-3}$	0.136
0.5 µM	$1.76*20^{-5}$	0.043	$0.11*10^{-3}$	$4.72*10^{-3}$
1.0 µM	$1.61*10^{-5}$	$0.58*10^{-3}$	$6.77*10^{-5}$	$2.01*10^{-3}$
2.0 µM	$7.59*10^{-6}$	$8.68*10^{-5}$	$6.49*10^{-6}$	$0.20*10^{-3}$

Vemurafenib	H1	H1-R	Wm3248	Wm3248-DR
1.0 µM	$3.84*10^{-5}$	0.015	$2.73*10^{-5}$	$9.63*10^{-3}$
2.0 µM	$6.47*10^{-5}$	0.477	$1.62*10^{-5}$	$7.77*10^{-3}$
4.0 µM	$0.25*10^{-3}$	$8.06*10^{-3}$	$3.07*10^{-5}$	$2.46*10^{-3}$
6.0 µM	$0.22*10^{-3}$	$3.86*10^{-5}$	$2.27*10^{-5}$	$2.06*10^{-3}$